FRAME SELECTION PERFORMANCE LIMITS
FOR STATISTICAL IMAGE RECONSTRUCTION
OF ADAPTIVE OPTICS COMPENSATED IMAGES

THESIS
Stephen D. Ford
Captain, USAF

AFIT/GEO/ENP/94D-03

DEPARTMENT OF THE AIR FORCE

AIR UNIVERSITY

AIR FORCE INSTITUTE OF TECHNOLOGY

Wright-Patterson Air Force Base, Ohio

FRAME SELECTION PERFORMANCE LIMITS
FOR STATISTICAL IMAGE RECONSTRUCTION
OF ADAPTIVE OPTICS COMPENSATED IMAGES

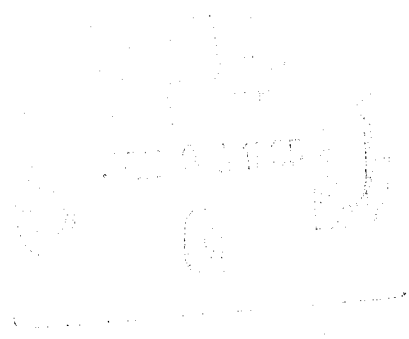THESIS
Stephen D. Ford
Captain, USAF

AFIT/GEO/ENP/94D-03

Approved for public release; distribution unlimited

REPORT DOCUMENTATION PAGE

Public reporting burden for this collection of information is estimated to average 1 hour per response, including the time for reviewing instructions, searching existing data sources, gathering and maintaining the data needed, and completing and reviewing the collection of information. Send comments regarding this burden estimate or any other aspect of this collection of information, including suggestions for reducing this burden. to Washington Headquarters Services, Directorate for Information Operations and Reports, 1215 Jefferson Davis Highway, Suite 1204, Arlington, VA 22202-4302, and to the Office of Management and Budget, Paperwork Reduction Project (0704-0188), Washington, DC 20503.

1. AGENCY USE ONLY (Leave blank)	2. REPORT DATE December 1994	3. REPORT TYPE AND DATES COVERED Master's Thesis

4. TITLE AND SUBTITLE
Frame selection performance limits for statistical image reconstruction of adaptive optics compensated images

5. FUNDING NUMBERS

6. AUTHOR(S)
Stephen D. Ford, Capt, USAF

7. PERFORMING ORGANIZATION NAME(S) AND ADDRESS(ES)
Air Force Institute of Technology, WPAFB OH 45433-6583

8. PERFORMING ORGANIZATION REPORT NUMBER
AFIT/GEO/ENP/94D-03

9. SPONSORING/MONITORING AGENCY NAME(S) AND ADDRESS(ES)
Capt Andy Suzuki
PL/LIMA, 535 Lipoa Pkwy, Suite 200
Kihei, HI 96753

10. SPONSORING/MONITORING AGENCY REPORT NUMBER

11. SUPPLEMENTARY NOTES

12a. DISTRIBUTION/AVAILABILITY STATEMENT
Approved for Public Release; Distribution Unlimited

12b. DISTRIBUTION CODE

13. ABSTRACT (Maximum 200 words)

The Air Force uses adaptive optics systems to collect images of extended objects beyond the atmosphere. These systems use wavefront sensors and deformable mirrors to compensate for atmospheric turbulence induced aberrations. Adaptive optics greatly enhance image quality, however, wavefront aberrations are not completely eliminated. Therefore, post-detection processing techniques are employed to further improve the compensated images. Typically, many short exposure images are collected, recentered to compensate for tilt, and then averaged to overcome randomness in the images and improve signal-to-noise ratio. Experience shows that some short exposure images in a data set are better than others. Frame selection exploits this fact by using a quality metric to discard low quality frames. A composite image is then created by averaging only the best frames. Performance limits associated with the frame selection technique are investigated in this thesis. Limits imposed by photon noise result in a minimum object brightness of visual magnitude +8 for point sources and +4 for a typical satellite model. Effective average point spread functions for point source and extended objects after frame selection processing are almost identical across a wide range of conditions. This discovery allows the use of deconvolution techniques to sharpen images after using the frame selection technique. A new post-detection processing method, frame weighting, is investigated and may offer some improvement for dim objects during poor atmospheric seeing. Frame selection is demonstrated for the first time on actual imagery from an adaptive optics system. Data analysis indicates that signal-to-noise ratio improvements are degraded for exposure times longer than that allowed to "freeze" individual realizations of the turbulence effects.

14. SUBJECT TERMS
Frame Selection, Adaptive Optics, Image Processing

15. NUMBER OF PAGES
197

16. PRICE CODE

17. SECURITY CLASSIFICATION OF REPORT UNCLASSIFIED	18. SECURITY CLASSIFICATION OF THIS PAGE UNCLASSIFIED	19. SECURITY CLASSIFICATION OF ABSTRACT UNCLASSIFIED	20. LIMITATION OF ABSTRACT UL

The views expressed in this thesis are those of the author and do not reflect the official policy or position of the Department of Defense or the U. S. Government.

Accesion For

NTIS CRA&I ☒
DTIC TAB ☐
Unannounced ☐
Justification

By
Distribution /

Availability Codes

Dist   Avail and / or
Special

A-1

FRAME SELECTION PERFORMANCE LIMITS
FOR STATISTICAL IMAGE RECONSTRUCTION
OF ADAPTIVE OPTICS COMPENSATED IMAGES

THESIS

Presented to the Faculty of the School of Engineering

of the Air Force Institute of Technology

Air University

In Partial Fulfillment of the

Requirements for the Degree of

Master of Science in Electrical Engineering

Stephen D. Ford, B.S.E.E.

Captain, USAF

December 1994

Preface

This thesis presents the results of an investigation into the application of frame selection as a post-detection processing technique for Air Force adaptive optics systems. The key result is that frame selection improves the signal-to-noise ratio and visible resolution of actual imagery from the Air Force Maui Optical Station. In addition, this effort has demonstrated that the effective point spread functions for both point source references and extended objects are almost identical across a wide range of seeing conditions. This fact allows for the application of deconvolution techniques to further sharpen images improved via frame selection. I hope this thesis contributes to the national defense by improving the Air Force's space surveillance mission effectiveness.

I'd like to thank my faculty advisor, Major Michael C. Roggemann, for his assistance throughout this project. His constant encouragement and active interest in this subject area made this work enjoyable.

I'd also like to thank my thesis committee members, Dr. Byron M. Welsh and Dr. Theodore E. Luke, for their many suggestions and comments which greatly contributed to the quality of this thesis.

Finally, I'd like to thank my wife and two sons. Their love and support will always teach me more than any class or research project.

<div align="right">Stephen D. Ford</div>

Table of Contents

List of Figures

viii

xiv

List of Tables

Abstract

The U. S. Air Force uses adaptive optics systems to collect images of extended objects beyond the atmosphere. These systems use wavefront sensors and deformable mirrors to compensate for atmospheric turbulence induced aberrations. Adaptive optics greatly enhance image quality, however, wavefront aberrations are not completely eliminated. Therefore, post-detection processing techniques are employed to further improve the compensated images. Typically, many short exposure images are collected, recentered to compensate for tilt, and then averaged to overcome randomness in the images and improve signal-to-noise ratio. Experience shows that some short exposure images in a data set are better than others. Frame selection exploits this fact by using a quality metric to discard low quality frames. A composite image is then created by averaging only the best frames. Performance limits associated with the frame selection technique are investigated in this thesis. Limits imposed by photon noise result in a minimum object brightness of visual magnitude +8 for point sources and +4 for a typical satellite model. Effective average point spread functions for point source and extended objects after frame selection processing are almost identical across a wide range of conditions. This discovery allows the use of deconvolution techniques to sharpen images after using the frame selection technique. A new post-detection processing method, frame weighting, is investigated and may offer some improvement for dim objects during poor atmospheric seeing. Frame selection is demonstrated for the first time on actual imagery from an adaptive optics system. Data analysis indicates that signal-to-noise ratio improvements are degraded for exposure times longer than that allowed to "freeze" individual realizations of the turbulence effects.

FRAME SELECTION PERFORMANCE LIMITS FOR STATISTICAL IMAGE RECONSTRUCTION OF ADAPTIVE OPTICS COMPENSATED IMAGES

I. Introduction

1.1 Motivation

Astronomers have long realized that atmospheric turbulence limits the capability of ground-based telescopes to properly resolve objects beyond the Earth's atmosphere. Prior to the space age, this problem was purely a concern of astronomers. The post-World War II era brought the limitations of atmospheric imaging to the forefront of cold war national defense as our nation grappled with the Soviet Union's space advances. Today, the United States faces an ever growing number of potential adversaries with satellite launch capability. Clear, resolvable images of space objects from ground-based telescopes are an absolute requirement to determine an opponent's intentions in space.

The U.S. Air Force obtains some of its space surveillance imagery from the Air force Maui Optical Station (AMOS) located on the island of Maui, Hawaii [31]. The 1.6 meter telescope uses adaptive optics to compensate for atmospheric turbulence effects. Unfortunately, adaptive optics cannot completely counter these effects; therefore, linear reconstruction is used to improve the compensated images [31].

Linear reconstruction consists of collecting many short exposure images of a given object. The use of short exposure images offers an opportunity to "freeze" an individual realization of the turbulence effects [32]. Individual images are also recentered to eliminate random image motion due to tilt. Many recentered images are then averaged to improve the image frequency spectrum signal-to-noise ratio (SNR).

A single, SNR-improved image is then sharpened using deconvolution methods such as the inverse filter or Weiner filter [31]. Computer simulation has shown that it is possible to increase the SNR of a reconstructed image by implementing a simple data sifting method on a data set of short exposure images [32]. Two questions naturally come to mind: "Under what range of conditions can frame selection be applied to images?" and "Will SNR improvements translate to visibly superior deconvolved images?"

1.2 Problem Statement

This thesis develops performance limits for the frame selection image reconstruction technique and then demonstrates the technique on actual and simulated images.

1.3 Approach

This thesis addresses the problem statement by investigating the performance limits of frame selection as they relate to improved image spectrum SNR and the visible quality of deconvolved images. In addition, several new frame weighting methods are investigated from an image spectrum SNR perspective. To achieve these goals, the following research questions are addressed:

1. What are the performance limits associated with frame selection as a function of key optical parameters?

2. What optical parameters have the greatest effect on the average point spread function (PSF)? Under what conditions are these PSFs similar for point source and extended objects?

3. Under what conditions do improvements in image spectrum SNR due to frame selection translate to visibly superior deconvolved images?

4. Does frame weighting improve image spectrum SNR performance? Under what conditions does this improvement take place?

5. Does frame selection improve image spectrum SNR for AMOS data in a similar manner as seen in computer simulation?

This research effort relies on both computer simulation and actual data from the AMOS surveillance site. Michael C. Roggemann developed a simulation package known as HYSIM which models the effects of atmospheric turbulence with a series of random phase screens and incorporates complete models for each element of an adaptive optics system [32]. Recent research at the Air Force Institute of Technology (AFIT) by Craig A. Stoudt resulted in a modification of HYSIM to incorporate statistical frame selection and a charge coupled device (CCD) camera model [32]. This modified computer simulation was renamed HYSIMS [32]. AMOS data is processed using computer code known as REDSEL. REDSEL is a modified version of FORTRAN code written by Roggemann that reconstructs an improved image from an ensemble of AMOS imagery. The modification consists of adding frame selection subroutines. Deconvolution is accomplished using simple FORTRAN routines, also provided by Roggemann, which implement the modified inverse filter and pseudo-Weiner filter [31].

1.4   Scope

Performance limits associated with the frame selection post-detection processing technique are presented in this thesis. In addition, frame weighting will be investigated as a possible complementary technique to frame selection. The primary parameters are the adaptive optics system configuration, atmospheric seeing conditions, frame selection rate, object type, and object brightness.

Linear reconstruction of short exposure images is the central theme of this research effort. While computer simulation and actual data from an adaptive optics system are essential, no adaptive optics system design is proposed. In addition, opti-

cal design issues, development of new frame quality metrics, and real time processing concerns are not addressed.

1.5 Summary of Key Results

Performance limits associated with frame selection are demonstrated as a function of key independent parameters over a wide range of test conditions. As a result, a minimum object brightness threshold has been established for point source objects. In addition, a satellite model was used to investigate this limit representing a generalized extended object. Expressed in terms of the apparent visual magnitude, m_ν, these limits are $m_\nu = +8$ for a point source and $m_\nu = +4$ for the given satellite model. More general statements are made regarding the effect of atmospheric seeing conditions on frame selection performance.

The PSFs for point source and satellite objects were nearly identical after applying frame selection over a wide range of conditions. This discovery points to the successful application of deconvolution techniques to sharpen images after frame selection. This thesis documents the first successful application of deconvolution on images benefiting from frame selection processing. Frame selection was also applied to actual imagery from AMOS. Experimental results were inconclusive in terms of SNR performance because excessively long exposure times were used to collect the data. Without adequately short exposures, frame selection cannot properly discard the worst manifestations of the turbulence effects.

Finally, the first investigation of simple frame weighting on short exposure images was shown to provide no improvement in SNR performance, except for dim objects. Further investigation is needed to determine if frame weighting can complement frame selection in this dim object regime.

1.6 Chapter Outlines

The following is a brief summary of the information found in each chapter of the thesis.

1.6.1 Chapter 2.
This chapter provides a short overview of the atmospheric turbulence problem, the use of adaptive optics and post-detection image processing to compensate for atmospheric turbulence, and the limitations of the typical adaptive optics system. Frame selection and frame weighting principles are discussed in detail. Finally, image sharpening through deconvolution is discussed with emphasis on the inverse and Weiner filters.

1.6.2 Chapter 3.
The methodology for conducting the research is presented in this chapter. Basic terminology is defined, the optical system model is outlined, the computer simulation approach is justified, performance metrics are defined, experimental independent parameters are outlined, and an approach for handling AMOS data is developed.

1.6.3 Chapter 4.
The results of four simulation experiments designed to explore frame selection performance limits and frame weighting are presented in Chapter 4. A fifth experiment demonstrates frame selection on AMOS imagery. The experiments and results are discussed in detail.

1.6.4 Chapter 5.
Conclusions based on the results presented in Chapter 4 are presented in this chapter. Chapter 5 concludes with recommendations for future research efforts.

II. Background

2.1 Introduction

This chapter provides the background necessary to understand the fundamental limitations imposed by atmospheric turbulence on Air Force optics systems, and the need for image reconstruction techniques to improve image quality. Theory associated with frame selection, frame weighting, and image sharpening through deconvolution are presented in detail.

2.2 Atmospheric Turbulence

A continuing problem for the U.S. Air Force and the optical astronomy community is imaging through the turbulent atmosphere. Atmospheric turbulence places a fundamental limit on the resolution of optical systems by imposing random phase aberrations on the incoming light [27]. These aberrations are caused by propagation through random layers of turbulence which create a non-uniform index of refraction. The result is a general broadening of the image point spread function (PSF) which manifests itself as blurring and lowered resolution when compared to an ideal system.

The atmospheric turbulence problem begins with the heating and cooling of the Earth by the sun. Large air masses gain heat directly from the sun during the day. At night, heat is also coupled to these air masses as the Earth cools. As a result, large scale temperature variations are produced. These temperature variations lead to pressure differences which result in large scale motion of the air masses. Initial large scale air motions break down into smaller and smaller scale motions until the atmosphere is distributed into randomly sized pockets of air, each with its own temperature. These pockets of air are called turbulent eddies [27]. Since the index of refraction of air is dependent on temperature, the atmosphere has a non-uniform index of refraction.

Three key individuals, Kolomogorov, Tatarskii, and Fried, laid the theoretical groundwork for research into atmospheric turbulence. Kolomogorov developed a model for how large scale turbulent eddies break down and transfer their energy into small scale turbulent eddies as part of his work in fluid mechanics [11]. Tatarskii then used Kolomogorov's model as a basis for his solution of the wave equation for propagation through weak random index fluctuations [33]. Finally, Fried used Tatarskii's work to derive expressions for the atmospheric coherence length, r_o, as well as the turbulence induced long and short exposure optical transfer functions (OTFs) [5].

2.2.1 Atmospheric Coherence Length, r_o. The atmospheric coherence length, r_o, first introduced by Fried in 1966 [5], is a useful parameter describing the image degrading effects of atmospheric turbulence. He determined the Strehl resolution [11] achieved by an imaging system looking through turbulence to be

$$\mathcal{R} = 4 \left(\frac{D}{\bar{\lambda}}\right)^2 \int_0^1 u[cos^{-1}u - u\sqrt{1 - u^2}] \exp\left\{-3.44 \left(\frac{D}{r_o}\right)^{\frac{5}{3}} u^{\frac{5}{3}}\right\} du, \qquad (2.1)$$

where D is the diameter of the aperture, $\bar{\lambda}$ is the wavelength of the incoming light, and u is a normalized spatial frequency variable. The parameter r_o is defined as

$$r_o = 0.185 \left[\frac{\bar{\lambda}^2}{\int_0^z C_n^2(\xi)d\xi}\right]^{\frac{3}{5}} \qquad (2.2)$$

where z is the total path length through all turbulence layers and C_n is the structure constant, a measure of turbulence strength.

Fried evaluated Equation 2.1 numerically for various values of $\frac{D}{r_o}$. He determined that the resolution of a diffraction limited system looking through turbulence increases as D increases until D is approximately the same as r_o for long exposure times. Any further increase in D above the r_o value does not result in any significant increase in system resolution. Therefore, it is clear that atmospheric turbulence

imposes a fundamental limit on optical system performance, and the parameter r_o is a measure of this performance limit. Typical values of r_o for astronomical viewing at a good observatory vary between 5 centimeters for relatively poor seeing to 20 centimeters for good seeing [11]. A typical value for good seeing is around 10 centimeters [11].

2.2.2 Long and Short Exposure OTFs. As indicated in the previous section, the r_o parameter provides a good indication of the level of image degradation expected under the corresponding atmospheric turbulence. Atmospheric turbulence contributes to image degradation by attenuating the OTF at high spatial frequencies. Image exposure time is a key factor in determining the characteristics of the OTF. To better understand the effects of exposure time on image quality, Fried [5] developed the following expressions for the average long and short exposure atmospheric OTFs

$$\langle H_{LE}(u) \rangle = \exp\left[-3.44\left(\frac{\bar{\lambda}fu}{r_o}\right)^{\frac{5}{3}}\right] H_o(u), \tag{2.3}$$

$$\langle H_{SE}(u) \rangle = \exp\left\{-3.44\left(\frac{\bar{\lambda}fu}{r_o}\right)^{\frac{5}{3}}\left[1-\left(\frac{\bar{\lambda}fu}{D}\right)^{\frac{1}{3}}\right]\right\} H_o(u) \tag{2.4}$$

where f is the focal length of the telescope, $H_o(u)$ is the OTF of the diffraction limited telescope, and u is a normalized spatial frequency variable. The short exposure and long exposure OTFs exhibit markedly different characteristics. The long exposure OTF is narrow and smooth, while its instantaneous short exposure counterpart is wider with fluctuations in magnitude and phase [11]. In addition, Fried determined that long exposures result, in part, from random image motion, also known as tilt. Tilt manifests itself in a broadened PSF and narrowed OTF. On the other hand, Fried noted that sufficiently short exposures (on the order of 10 milliseconds or less) were not significantly degraded by tilt. Instead, successive short exposure images appear to move randomly in the image plane. Simply recentering these images during post-detection processing or mechanically removing tilt with a fast steering mirror

eliminates the tilt effects. This method of using the short exposure image to eliminate tilt is used in many post-detection processing schemes. While the elimination of tilt is important, it does not produce a diffraction limited image due to the remaining phase aberration. Dealing with random phase effects due to atmospheric turbulence is left to the more ambitious techniques described later in this chapter.

Based on the work of Kolomogorov, Tatarskii, and Fried, much research has been expended in attempts to improve astronomical images taken through the atmosphere. Three classes of techniques have emerged: (1) pre-detection processing, consisting of adaptive optics, which rely on purely mechanical means to correct atmospheric effects before the light reaches the image plane; (2) post-detection processing which relies on specialized measurements from a large ensemble of images to correct for atmospheric effects after the data is collected; and (3) hybrid methods which combine both adaptive optics and post-detection processing.

2.3 Adaptive Optics

Adaptive optics compensate for turbulence induced wavefront aberrations in real time before the light is detected at the image plane. The key components of an adaptive optics system are the deformable mirror (DM), wavefront sensor (WFS), and actuator control computer [29]. Voltages applied to the DM actuators allow its figure to be changed in real time to match an estimate of the conjugate of the input wavefront phase. The WFS senses the aberrations in the incoming wave by measuring gradients in small subapertures of the telescope pupil [34]. This information is then sent to the actuator control computer which adjusts the DM to apply an estimate of the conjugate of the wavefront aberration. The correction imposed by the DM cancels out the aberration leading to a narrower PSF and an improved image. This process must occur at speeds on the order of the rate of change of the wavefront aberration to be effective [34]. Typically, these speeds range from approximately tens of Hertz to a few hundred Hertz [34].

Fully compensated adaptive optics systems have individual subaperture area approximately the square of the atmospheric coherence length, r_o, and DM actuators placed on a square grid with grid spacing approximately r_o [30]. Fully compensated systems for large telescopes are complex and expensive to build. A cheaper, lower performance alternative is to build a DM with fewer actuators and use a WFS with larger subapertures. Such a system is referred to as partially compensated [30].

Unfortunately, even a fully compensated system cannot completely eliminate turbulence induced wavefront aberrations [34]. Some limitations include finite WFS signal and measurement noise, finite WFS sampling, a limited number of degrees-of-freedom in the DM, and control system time delays [30].

2.4 Post-detection Processing

Post-detection processing refers to a large variety of image reconstruction techniques which attempt to overcome atmospheric turbulence after data collection. The first attempts to post-process astronomical images relied on processing large numbers of short exposure images without the benefit of adaptive optics. These techniques are referred to as speckle imaging due to the fact that the data consists of an ensemble of uncompensated, short exposure, speckled images [19].

Labeyrie invented an important form of speckle imaging, referred to as speckle interferometry [15], by showing that the energy spectrum of an object could be estimated from a large data set of short exposure images. The energy spectrum, or modulus squared of the Fourier transform, encodes unique information about an object. However, the phase of the Fourier transform (phase spectrum) is also needed to create an image [19]. Two common techniques for obtaining the phase spectrum are the Knox-Thompson [14] and bispectrum methods [16].

Speckle imaging techniques are limited by low signal-to-noise ratio (SNR) performance due to randomness in the OTF and the photon-limited nature of many astronomical images. This limit is so severe that the SNR at mid and high spatial

frequencies for a single frame reaches a maximum of unity for an infinitely bright point source and is typically smaller for extended objects [11]. Averaging many frames can be used to improve SNR performance but only at the expense of handling several hundred to a few thousand frames of independent data.

An alternative post-detection processing method that does not suffer from such severe SNR limitations is deconvolution from wavefront sensing (DFWS) [7, 26]. This method uses simultaneous measurements from a WFS and a single, short exposure image of the desired object. The WFS data provides an estimate of the instantaneous system OTF that generated the short exposure image. This reference is used in a deconvolution scheme to remove the degrading effect of the combined atmosphere-optical system OTF from the image. Unlike speckle interferometry, DFWS provides the modulus and the phase of the object directly but with the added expense of WFS hardware and processing equipment.

In contrast to both speckle imaging techniques and DFWS, linear reconstruction relies on AO compensation and averaging to overcome randomness in short exposure images resulting in higher SNR [31]. Deconvolution can then be used to lessen image blurring by boosting previously attenuated high spatial frequencies [31]. Past experience with linear reconstruction has shown that some images in a given short exposure data set are better than others [32]. This observation suggests two related linear reconstruction methods, frame selection and frame weighting, which seek to process high and low resolution images differently to further improve SNR performance. The next section deals with the first step in both the frame selection and frame weighting methods, calculating image quality.

2.5   Quality Metrics

In order to properly apply frame selection or frame weighting, it is essential to have a well understood metric that attaches a numerical value to the quality of

each frame. Many such metrics exist, but it is logical to turn first to common optical system quality metrics.

One such quality metric is the Strehl ratio [25] defined as

$$\mathcal{S} = \frac{\int \tau(f)df}{\int \tau_o(f)df} \tag{2.5}$$

where τ is the OTF of the atmosphere-optical system, τ_o is the OTF of the optical system with no atmosphere present, and f is a spatial frequency variable. $\mathcal{S}$ is best understood as the ratio of Fried's resolution parameter, $\mathcal{R}$ of Equation 2.1, in the presence of atmospheric turbulence versus the ideal case of no atmospheric turbulence. As reported by Stoudt [32], Marechal developed a convenient relationship between $\mathcal{S}$ and mean squared phase distortion over the optical system aperture, Δ^2:

$$\mathcal{S} \approx \left(1 - \frac{1}{2}\Delta^2\right)^2 \tag{2.6}$$

where Δ^2 must be less than unity. Mahajan [17] conducted error analysis on Equation 2.6 as well as deriving his own approximate relationship between $\mathcal{S}$ and Δ^2:

$$\mathcal{S} \approx \exp\left(\Delta^{-2}\right). \tag{2.7}$$

Mahajan's error analysis showed that Marechal's Equation 2.6 gives $\mathcal{S}$ with less than 10 percent error as long as $\mathcal{S} \geq 0.6$. Mahajan's Equation 2.7 has a broader allowable range of $\mathcal{S}$ such that it provides 10 percent error if $\mathcal{S} \geq 0.3$. One important drawback to using $\mathcal{S}$ as a frame quality metric is its dependence on the OTF, τ. τ can be determined using

$$\tau(f) = \frac{I(f)}{O(f)} \tag{2.8}$$

where I is the image spectrum and O is the object spectrum [10]. To determine τ, it is necessary to have knowledge of both I and O. In practice, only the image spectrum is usually available.

O'Neill [25] provides a discussion of three additional image quality metrics:

Relative Structural Content, T

$$T = \frac{\overline{i^2(x,y)}}{\overline{o^2(x,y)}} \tag{2.9}$$

Correlation Quality, Q

$$Q = \frac{\overline{i(x,y)o(x,y)}}{\overline{o^2(x,y)}} \tag{2.10}$$

Fidelity Defect, F

$$F = 1 - D \tag{2.11}$$

$$D = \frac{\overline{[o(x,y) - i(x,y)]^2}}{\overline{o^2(x,y)}} \tag{2.12}$$

where $i(x,y)$ is the measured image, $o(x,y)$ is the original object, (x,y) are image plane coordinates, and the bar indicates averaging. These three metrics are related by the following equation:

$$Q = \frac{1}{2}(T + F). \tag{2.13}$$

Fidelity Defect differs from Strehl ratio due to the fact that it is a normalized measure of mean squared error between object and measured image. Some research indicates that mean squared error is not a good representative of human visual quality assessments [18, 24]. This discrepancy between mean squared error and human vision is not well understood [24].

Unfortunately, O'Neill's quality metrics also require prior knowledge of the object. In 1974, Muller and Buffington [22] developed eight quality metrics, seven of which do not require any prior knowledge of the object. They define these quality metrics, also known as "sharpness functions", as functions which reach a maximum value for unaberrated images. Muller and Buffington's eight sharpness functions are

$$S_1 = \int \int i^2(x,y)dxdy \qquad (2.14)$$

$$S_2 = i(0,0) \qquad (2.15)$$

$$S_3 = \int \int m(x,y)i(x,y)dxdy \qquad (2.16)$$

$$S_4 = \int \int \left| \frac{\partial^{m+n} i(x,y)}{\partial x^m \partial y^n} \right|^2 dxdy \qquad (2.17)$$

$$S_5 = \int \int i^n(x,y)dxdy \qquad (2.18)$$

$$S_6 = -\int \int i(x,y)r^2 dxdy, \; r^2 = x^2 + y^2 \qquad (2.19)$$

$$S_7 = -\int \int ln[i(x,y)]i(x,y)dxdy \qquad (2.20)$$

$$S_8 = -\int \int |i(x,y) - o(x,y)|^2 dxdy \qquad (2.21)$$

where $m(x,y)$ is known as the mask function. If $m(x,y)$ is a good replica of the undistorted image, S_3 is a good sharpness definition which reduces to S_1 when distortion is removed [22]. Muller and Buffington were able to prove that S_1, S_3, S_4, S_5, and S_8 reach maximum values for an unaberrated image. In addition, they provide evidence that S_2, S_6, and S_7 also reach maximum values for an unaberrated image under typical imaging conditions. The next section provides examples of frame selection implementations using some of the quality metrics discussed above.

2.6 Frame Selection

The basis of frame selection is to choose the best quality or highest resolution frames for averaging such that

$$I_S(u, v) = \frac{1}{M} \sum_{i=1}^{M} I_i(u, v) \qquad (2.22)$$

where $I_S(u, v)$ is the average image frequency spectrum due to frame selection, $I_i(u, v)$ is the image frequency spectrum of an individual frame in the frame selection subset, M is the number of frames in the selected subset, and (u, v) is a spatial frequency. Figure 2.1 provides a visual representation of the process associated with Equation 2.22. N images are collected and each transformed to the frequency spectrum with the Fourier transform. An image quality metric, such as those developed by Muller and Buffington [22], is used to provide a numerical representation of frame quality. The images are then ranked based on the quality metric determination, with the worst images being discarded. SNR is calculated to aid in comparison between image quality averaging all N frames and image quality averaging just the M frames in the selected subset. The rest of this section provides a historical review of frame selection research as well as key results associated with a more recent application of the frame selection technique to astronomical objects of interest to the Air Force.

*   Distant
          Object

Aberrated
Light

Telescope
Pupil

Image
Detector

| Image Recorder (N Images) | → | Sifting Algorithm (Select M Images, M < N) |
| Fourier Transform N Images | | Accumulate Statistical Quantities | → | Compute SNR of M and N Data Sets |
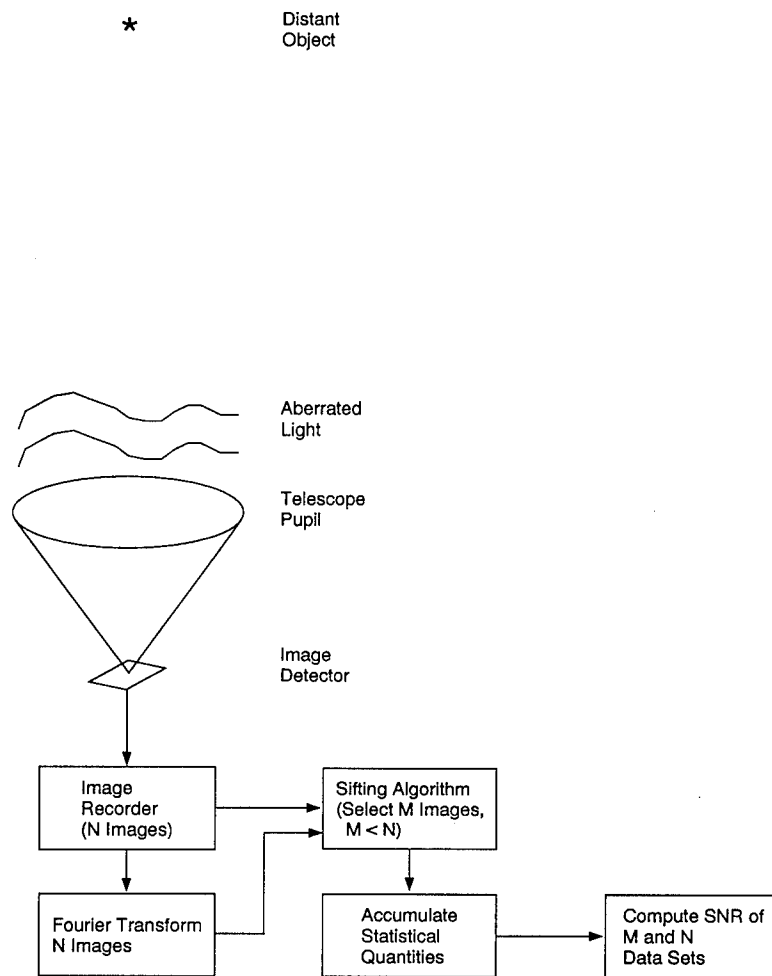
Figure 2.1   Block Diagram of the Frame Selection Technique

2.6.1 Early Applications of Frame Selection. In 1978, Fried [6] determined that there is a finite probability of obtaining a diffraction limited short exposure image through the atmosphere due to the possibility that the wavefront distortion is negligible during the exposure. He derived the following expression for the probability of getting a "good" short exposure image

$$Prob \approx 5.6 \ \exp\left[-0.1557\left(\frac{D}{r_o}\right)^2\right] \tag{2.23}$$

for $\frac{D}{r_o} \geq 3.5$. Fried used mean squared phase distortion over the aperture, Δ^2, of 1 rad^2 or less as his measure of a "good" image. His work showed that the probability of a diffraction limited short exposure decreases as the diameter of the aperture increases. In fact, $\frac{D}{r_o}$ is limited to approximately 7 to 8 for probabilities on the order of 10^{-3}. This rapidly decreasing probability limits the aperture size of telescopes, which degrades the ability to image dim objects. In addition, collecting enough short exposure images to realize a high probability of collecting a single high quality image would be a burden on most data collection systems. For example, a 1 meter telescope at a site with an average r_o of 10 centimeters would require the collection of 1 million short exposure images to have a high probability of getting just one diffraction limited image. Fried's work is important because it was among the first research efforts to rigorously demonstrate that the correct choice of aperture for seeing conditions and proper selection of short exposure images can significantly improve optical system performance through atmospheric turbulence [6].

Corteggiani [3] addressed two limitations to Fried's Equation 2.23 making the following expression valid for all values of $\frac{D}{r_o}$ and $\Delta^2 < 1 \ rad^2$:

$$\log Pr\left[\left(\frac{D}{r_o}\right), 1\right] = \frac{-0.1557\left(\frac{D}{r_o}\right)^2}{exp\left[\frac{11.014}{\left(\frac{D}{r_o}\right)^2} + \frac{35.35}{18.907 + \left(\frac{D}{r_o}\right)^2}\right]} \tag{2.24}$$

The notation $Pr\left[\left(\frac{D}{r_o}\right),1\right]$ denotes the probability, at a given $\frac{D}{r_o}$ ratio, of collecting a diffraction limited short exposure image through the atmosphere with $\Delta^2 = 1\ rad^2$. In addition, Corteggiani related the quality metric Δ^2 to the atmospheric coherence length, r_o, through the relation

$$Pr\left(\frac{D}{r_o}, \Delta^2\right) = Pr\left(\frac{D}{r_o\Delta^{\frac{6}{5}}}, 1\right). \tag{2.25}$$

Equation 2.25 indicates that relaxing the quality metric Δ^2 is equivalent to collecting a short exposure image at a smaller value of r_o.

The work of Fried and Corteggiani established a relationship between frame quality and optical system performance but only using the mean squared phase aberration metric, Δ^2. Hequet and Coupinout provided the first experimental validation of the frame selection technique [12]. Their method involved collecting a large set of short exposure images of an object, selecting the best frames using the Strehl ratio as a quality metric, recentering the images to compensate for tilt effects, and averaging the frames in the recentered subset to create an image of the original object. Using Equation 2.7 and Corteggiani's model of Equation 2.25, Hequet and Coupinout determined that the Strehl ratio of an image can be improved by a factor of two when selecting the best 10 percent of the images from the original ensemble. This technique does not account for photon and detector shot noise. In addition, Corteggiani's model only indirectly considers imaging wavelength since r_o is proportional to the $\frac{6}{5}$ power of the imaging wavelength.

With frame selection firmly established as a post-processing technique by Hequet and Coupinout, other researchers demonstrated similar performance improvements with Muller and Buffington's quality metrics. In 1987, Nieto and others [23] demonstrated frame selection on the binary stars 48Vir and HRS10 using a 4 meter telescope. They showed that the full width, half maximum (FWHM) value of the average system PSF improved by a factor of 2.18 when selecting 10 percent of the

images using the S_3 quality metric of Equation 2.16 and the long exposure image as the mask, $m(x, y)$. In 1988, Fuensalida and others [8] performed a similar experiment applying frame selection to produce high resolution images of the binary star AG Peg using a 2.5 meter telescope. They reported qualitative improvements in the high frequency structure of the images with S_3 as the quality metric and the long exposure autocorrelation function as the mask. Also in 1988, Devaney and others [4] performed a frame selection experiment with a Gaussian function the width of the diffraction limit of the telescope as the mask. They reported very similar results to those presented by the two previous research teams.

The results of these three research teams agree well with those presented by Hequet and Coupinout. This agreement indicates that Muller and Buffington's quality metrics have great potential for application on Air Force adaptive optics systems. This fact led to more recent frame selection research at the Air Force Institute of Technology (AFIT).

2.6.2 Recent Developments in Frame Selection. In 1993, Craig A. Stoudt, an AFIT graduate student, investigated frame selection of adaptive optics compensated images [32]. Stoudt's work relied on computer simulation of both point source and extended objects over a range of seeing conditions and light levels. He evaluated three of Muller and Buffington's original quality metrics, S_1, S_4, and S_8, as well as a new metric S_{S1} defined as

$$S_{S1} = \int \int S_{OTF}(u, v) |I(u, v)|^2 du\, dv \qquad (2.26)$$

where $S_{OTF}(u, v)$ is the support of the OTF. Stoudt's use of computer simulation allowed a much broader examination of the effects of key independent parameters than those conducted by earlier researchers. Image spectrum SNR was used as the primary performance measure. The independent parameters included r_o, object brightness, frame selection rate (FSR), and CCD camera noise.

Stoudt made the following conclusions by simulating a 1 meter fully compensated adaptive optics telescope [32]:

1. Frame selection with the Muller and Buffington quality metrics increases noise reduction, thereby boosting the image spectrum SNR of the reconstructed image. Ten to Fifteen percent improvement in image spectrum SNR is possible for FSRs of 60-75 percent. In general, there is an optimum FSR where SNR gain is maximized.

2. For equivalent seeing conditions and light levels, frame selection is of greater benefit to point sources than extended objects. This is especially true with respect to object brightness where extended objects are limited to a minimum brightness. Stoudt concluded that at low light levels photon noise and shot noise dominate over the randomness of the average system OTF. He suggested frame weighting as a possible alternative approach to better improve image quality of dim objects.

3. Frame selection improves image quality when seeing conditions limit performance, but not when photon noise and CCD camera noise are the dominate effects.

4. The S_{S1} quality metric produced the highest overall image spectrum SNR gain compared to the other metrics in the investigation.

These important conclusions and their grounding in accurate and convenient computer simulation made this work an important step in the understanding of frame selection performance.

2.7 Frame Weighting

Frame weighting is a method to improve image spectrum SNR by weighting each frame based on frame quality. This thesis provides an extension of Stoudt's work by conducting the first investigation into combining adaptive optics compensation and frame weighting. This technique is best understood by examining its governing

equation

$$I_W(u,v) = \frac{1}{N}\sum_{i=1}^{N} W_i I_i(u,v),\qquad(2.27)$$

where $I_W(u,v)$ is the average image frequency spectrum of the weighted image, W_i is a frame weighting vector associated with the ith frame, $I_i(u,v)$ is the image frequency spectrum of an individual frame, N is the number of frames in the entire data set, and (u,v) is a spatial frequency. Equation 2.27 is simply a weighted average based on individual frame quality. The following sections present a discussion of an optimum frame weighting approach followed by a more intuitive, sub-optimal weighting scheme.

2.7.1 Optimal Frame Weighting. As the previous discussion demonstrates, some knowledge is already in hand regarding the frame selection technique. It is clear that frame selection is not the best reconstruction method under certain conditions, notably dim, extended objects. Determination of the optimal weighting matrix, W_i, is a key step in the application of frame weighting on these objects.

Linear minimum variance (LMV) and least squares (LS) methods have the potential to yield optimal weighting matrices. In this case, both methods are based on a linear degradation model cast in linear algebra notation such that

$$\boldsymbol{I_i = HO + N}\qquad(2.28)$$

where $\boldsymbol{I_i}$ is a vector containing all the images in the ensemble, $\boldsymbol{H}$ is the atmosphere-optical system OTF matrix, $\boldsymbol{O}$ is the object spectrum vector, and $\boldsymbol{N}$ is an additive noise vector [9]. While sharing the linear degradation model, LMV and LS methods differ in their error minimization schemes.

The LMV method is based on the first and second statistical moments of the desired parameter and disturbances. This LMV scheme uses the linear estimator

[20]

$$I_W = W I_i \tag{2.29}$$

where I_W is a vector containing the final weighted image spectrum and W is the weighting matrix. The goal is to derive an expression for W that minimizes the error variance between the original object spectrum, O, and final weighted image spectrum, I_W such that

$$\tilde{O} = O - I_W \tag{2.30}$$

is as small as possible. Unfortunately, this optimization problem is ill-defined because the error variance is a matrix. The alternative is to minimize the sum of the variances in each component of O. This alternative leads to the following expression for the optimal frame weighting matrix

$$W = V_O H^T [H V_O H^T + V_N]^{-1} \tag{2.31}$$

where V_O is the variance matrix of the object spectrum and V_N is the variance matrix of the noise. Equation 2.31 is difficult to implement due to the fact that neither H nor V_O is perfectly known. In addition, this calculation is computationally intense due to the size of the matrices and vectors.

In contrast to the LMV method, the LS method does not require any stochastic information about the parameters or disturbances. For their LS derivation, Melsa and Cohn [20] minimize the following quadratic performance index:

$$J(\hat{O}) = \frac{1}{2}(I_i - H\hat{O})^T(I_i - H\hat{O}) \tag{2.32}$$

where $\hat{O}$ is an estimate of the object spectrum. The $\hat{O}$ that minimizes $J(\hat{O})$ of Equation 2.32 is given by

$$\hat{O}_{LS} = (H^T H)^{-1} H^T I_i \tag{2.33}$$

and is known as the least squares estimator. By assuming that I_W of Equation 2.29 is the least squares estimator, it is possible to derive the following equation for W:

$$W = (H^T H)^{-1} H^T \tag{2.34}$$

As with the LMV method, lack of knowledge of H is the primary drawback to operational use of the LS method.

Due to the difficulty in generating an optimal solution by either of these methods, more intuitive techniques for generating frame weights will be exploited in this thesis.

2.7.2 Intuitive Frame Weighting. Even though deriving an optimal W_i is beyond the scope of this thesis effort, it is still possible to apply frame weighting via a more intuitive approach. Unlike the LMV and LS methods, the goal of this approach is to improve image spectrum SNR not generate an optimal O estimate.

In this simplified approach, the frame weights, W_i, are constants and related to the quality metric value via a weighting function. A weighting function translates a given frame quality into a single weight such that

$$W_i = f_w(S_i) \tag{2.35}$$

where f_w is a frame weighting function and S_i is the quality metric value for the ith frame. The frame weighting function must fulfill the following requirements:

1. Apply frame weights between zero and one.

2. Apply frame weights close to or equal to one for high resolution frames and weights close to or equal to zero for low resolution frames

3. Maintain a close proportional relationship between frame weight value and frame quality metric value. Depending on the particular weighting function imple-

mentation, maintaining this relationship may be difficult in cases where all frames in an ensemble are either very good or very bad. Hence, intuitive frame weighting is not optimal and does not necessarily minimize any error metric as would be possible with a LMV or LS approach.

2.8   Image Sharpening through Deconvolution

As discussed in a previous section, linear reconstruction incorporating frame selection uses quality based selection and averaging to overcome randomness in the measured images. The new, averaged image has a higher image spectrum SNR but is still blurred due to attenuation of the high spatial frequencies by the atmosphere-optical system OTF. This blurred image can be sharpened by deconvolving the average PSF from the image after averaging [31]. Two possible schemes for this purpose are the inverse filter and pseudo Wiener filter.

2.8.1   Inverse Filter.   The inverse filter is based on the most simple of principles, directly reversing the process by which the image was made to return to an accurate estimate of the original object. Based on a linear systems model and Fourier optics [10], the image was created via

$$I(u,v) = H(u,v)O(u,v) + N(u,v) \qquad (2.36)$$

where $I(u,v)$ is the degraded image, $O(u,v)$ is the original object, $H(u,v)$ is the atmosphere-optical system OTF, and $N(u,v)$ is an additive noise term. In the absence of noise, returning to the original object involves solving Equation 2.36 for $O(u,v)$. Unfortunately, the noise term, $N(u,v)$, will not allow a direct return to the original object spectrum. This leads to the following formulation for the inverse filter:

$$\tilde{O}(u,v) = \frac{I(u,v)}{\tilde{H}(u,v)} \qquad (2.37)$$

where $\tilde{O}(u,v)$ is an estimate of the original object spectrum and $\tilde{H}(u,v)$ is an estimate of the OTF [9]. In many atmospheric imaging applications, $\tilde{H}(u,v)$ is provided by imaging a reference point source, such as a star near the desired object [31]. This filtering scheme is criticized for heavily amplifying high frequency noise [31].

The inverse filter can be modified to better handle noise effects. One such modified inverse filter [31] creates an estimated object spectrum in exactly the same manner as Equation 2.37 with three modifications:

1. $\tilde{O}(u,v)$ is set to zero for spatial frequencies where $\tilde{H}(u,v)$ is zero to restrict division by zeros in Equation 2.37. This technique eliminates spatial frequencies from the image that are not in $\tilde{H}(u,v)$.

2. Any value $\tilde{O}(u,v)$ with value greater than $\tilde{O}(u=0,v=0)$ is reduced to $\tilde{O}(u=.0,v=0)$. This method deals with the unphysical situation where spatial frequencies with $(u,v) > (0,0)$ have higher amplitude than the DC component of the image.

3. A circularly symmetric triangle filter with a user defined cutoff frequency is applied to the output after steps 1 and 2. This filter handles noise outside the passband of the optical system.

The modified inverse filter has been applied to experimental data from an adaptive optics system [31]. While it is not a minimum error method, the modified inverse filter can provide excellent results for the human visual system [31].

2.8.2 Weiner Filter. Unlike the modified inverse filter, the Weiner filter is an optimal deconvolution scheme in a constrained least squares sense [9]. The governing equation is

$$\tilde{O}(u,v) = \frac{I(u,v)\tilde{H}^*(u,v)}{|\tilde{H}(u,v)|^2 + \frac{S_n(u,v)}{S_o(u,v)}} \tag{2.38}$$

where $\tilde{H}^*(u,v)$ is the complex conjugate of the estimated atmosphere-optical system OTF, $S_n(u,v)$ is the power spectrum of the noise, and $S_o(u,v)$ is the power spectrum

of the object [9]. The formulation of Equation 2.38 is not readily applicable to an operational environment due to the need for knowledge of $S_o(u, v)$. A directly applicable form of the Weiner filter, the pseudo Weiner filter, circumvents this limitation via the modified expression

$$\tilde{O}(u, v) = \frac{I(u, v)\tilde{H}^*(u, v)}{|\tilde{H}(u, v)|^2 + \frac{\alpha}{SNR(u,v)}} \tag{2.39}$$

where $SNR(u, v)$ is the image spectrum SNR and α is a user selected parameter [31]. The ratio $\frac{\alpha}{SNR(u,v)}$ controls the amount of noise reduction or "smoothing" at each spatial frequency. Notice when $\alpha = 0$ the pseudo Weiner filter becomes an inverse filter. Therefore, the fact that a large value of $SNR(u, v)$, indicating low noise, results in inverse filter-like characteristics appeals to common sense.

The Weiner filter tends to result in overly-smoothed estimates of the object [31]. As indicated in an earlier section, some research indicates that the mean squared error metric may not provide the best images for human visual system consumption [18, 24].

2.9   Limits of Current Knowledge

Based on the work of Stoudt and others, frame weighting appears to be a promising technique to improve linearly reconstructed images, especially dim objects. In order to fully assess its potential, the following limitations in our current level of understanding of both frame selection and frame weighting must be overcome.

As noted previously, Stoudt examined frame selection performance on a limited set of independent parameters for one adaptive optics system implementation establishing the trade between image blurring and SNR. Unfortunately, our understanding of the limitations of frame selection under dim object conditions is incomplete. In addition, the SNR performance trade off between the photon noise limited and OTF variance limited situations is not adequately understood for frame selection.

This chapter has established that frame selection improves the image spectrum SNR of reconstructed images. As discussed above, these SNR improved images are often deconvolved with an estimate of the average atmosphere-optical system OTF to boost high spatial frequencies and increase resolution. In many cases, a bright point source, such as a star, will be used as this OTF estimate. In order for the point source to perform as an adequate OTF estimate, the average system PSFs of reference point source and image must be similar. None of the previous research efforts has examined the effect of frame selection on the average system PSF. This gap in our knowledge is a key point. Without a similarity between reference point source and image PSFs, it is not possible to fully realize improved resolution from the SNR improved, frame selected images.

Finally, while some performance bounds have been established for frame selection, no such studies have been conducted for frame weighting of short exposure images.

2.10 Summary

Atmospheric turbulence imposes a fundamental limit on optical system performance. Adaptive optics enhance image resolution, but cannot completely eliminate turbulence induced phase aberrations. Post-detection processing of adaptive optics compensated images is needed to further enhance image quality. Frame selection is a promising post-detection processing technique that offers significant improvement in image spectrum SNR over a substantial range of performance conditions and object brightness. A complete investigation of frame selection performance over a wide range of conditions is presented in this thesis. This effort includes demonstrating the superiority of images after frame selection and sharpening with deconvolution techniques. In addition, frame weighting is examined as a possible method for improving the image quality of dim objects. The methodology for conducting this investigation is developed in the next chapter.

III. Methodology

3.1 Introduction

Chapter two provided a brief overview of the atmospheric imaging problem and several possible solutions. The Air Force uses one of these solutions, adaptive optics (AO), to compensate for the random phase aberrations due to atmospheric turbulence. Unfortunately, AO cannot completely compensate for all phase fluctuations due to the atmosphere [34]. Instead, residual phase aberrations corrupt the AO compensated wavefront which results in a degraded image. To improve this degraded image, some form of post-detection processing is needed. The previous chapter showed that researchers have improved images from passive optics systems using a technique known as frame selection [4, 8, 23]. In addition, recent research at the Air Force Institute of Technology (AFIT) has shown that images from AO systems can also be improved using frame selection [32]. In order to fully benefit from this promising technique, it is important to understand its performance limits. A methodology for studying frame selection performance limits and another alternative post-processing technique, frame weighting, is developed in this chapter. Section 3.2 defines the terminology to be used throughout the remainder of this investigation. Section 3.3 justifies the use of the S_{S1} frame quality metric. Section 3.4 establishes the basic image model. Section 3.5 justifies the use of computer simulation for both frame selection and frame weighting studies. Section 3.6 justifies the use of image spectrum statistics as a performance metric. Section 3.7 identifies the independent variables associated with these experiments. Finally, section 3.8 introduces additional information associated with the collection and processing of actual Air Force Maui Optical Station (AMOS) data.

3.2 Terminology

A working knowledge of the terms and concepts associated with a research investigation is essential for complete understanding of the work. This section is organized according to general, frame selection, and frame weighting terminology categories.

3.2.1 General Terminology.

The following terminology is of a general nature and applies to both frame selection and frame weighting.

Composite image: an image resulting from re-centering and averaging multiple short exposure images (frames) of the same object.

Compensated image: a single image produced by an AO system. Multiple compensated images of the same object can be used to produce a composite image with improved resolution.

Deconvolved image: an image whose high spatial frequency content has been boosted by using one of many deconvolution techniques such as the inverse and pseudo-Weiner filters [31].

Quality metric: an algorithm which results in a single numerical value when applied to an image. Quality metric magnitude is directly related to a designated quality or feature.

3.2.2 Frame Selection Terminology.

The following terminology applies to frame selection.

Frame selection rule: a three-step process for choosing a subset of images for further processing.

1. Calculate a frame quality metric value for each frame in the data set.

2. Sort the images in the data set from highest to lowest based on the quality metric value.

3. Select the highest value images for processing.

Frame selection rate (FSR): the ratio of the number of frames M in the selected subset to the number of frames N in the original ensemble. Therefore,

$$FSR = \frac{M}{N}, \quad M < N. \tag{3.1}$$

The FSR is usually expressed as a percentage value. An FSR of 50 percent means the selected subset consists of the "best" 50 percent of the frames from the original data set based on the frame quality metric values.

3.2.3 Frame Weighting Terminology. The following terminology applies to frame weighting.

Frame weight: a single numerical value assigned to each frame in the ensemble. Frame weight values must adhere to the following mathematical rule:

$$0 \leq W \leq 1, \tag{3.2}$$

where W is a constant frame weight value. Larger frame weights are associated with the best frames in a data set. Smaller weights are associated with the worst frames. The designations "best" and "worst" are related to the quality metric value.

Frame weighting function: an equation, algorithm, or other scheme which translates a given frame quality to a single frame weight.

Frame weighting rule: a three-step process for calculating frame weights for each image in the data set in preparation for further processing.

1. Calculate a frame quality metric value for each frame in the ensemble.

2. Sort the images in the ensemble from highest to lowest based on the quality metric value.

3. Calculate a frame weight value for each image based on either a quality-based or function-based frame weighting scheme.

Quality-based frame weighting: a frame weighting scheme that applies weights which are directly proportional to the quality metric numerical values.

Function-based frame weighting: a frame weighting scheme which applies weights based on a pre-defined function and the relative quality ranking of the frames. Weights are only indirectly related to actual quality metric numerical values.

Weighted image: image processed using frame weighting.

Now that terminology pertaining to the frame selection and frame weighting techniques has been established, it is necessary to justify the use of the of a quality metric and establish appropriate system models.

3.3 S_{S1} Quality Metric

In Chapter two, a set of sharpness functions developed by Muller and Buffington [22] were introduced. These functions reach their maximum value for unaberrated images. One of these sharpness functions, S_1, is defined as:

$$S_1 = \int \int i^2(x,y)dxdy, \tag{3.3}$$

where $i(x,y)$ is the measured image and (x,y) are image plane coordinates. Stoudt [32] established a modified frequency domain version of Equation 3.3 by applying Parseval's theorem [2] such that:

$$S_{S1} = \int \int S_{OTF}(u,v)|I(u,v)|^2 dudv, \tag{3.4}$$

where $I(u,v)$ is the Fourier transform of $i(x,y)$, $S_{OTF}(u,v)$ is the support of the optical transfer function (OTF), and (u,v) is a spatial frequency. Since frequency components beyond the extent S_{OTF} are obviously manifestations of noise, S_{S1} has

improved noise reduction capabilities when compared to the original S_1 sharpness function. Stoudt's work indicated that the S_{S1} quality metric yielded superior image spectrum SNR performance when compared to the other quality metrics in his study [32]. Based on this fact, the S_{S1} quality metric is used for all applications of frame selection and frame weighting.

3.4 System Models

The linear, shift invariant model for an imaging system, as presented by Goodman [10], is utilized in this thesis. In the absence of noise, an image is created by the convolution of the original object and the point spread function (PSF) such that

$$i(x, y) = o(x, y) * h(x, y), \tag{3.5}$$

where $i(x, y)$ is the noiseless image, $o(x, y)$ is the object intensity, $h(x, y)$ is the PSF, and $*$ indicates the two dimensional convolution operation. Taking the Fourier transform of both sides of Equation 3.5 yields

$$I(u, v) = H(u, v)O(u, v), \tag{3.6}$$

where $O(u, v)$ is the Fourier transform or object spectrum of $o(x, y)$ and $H(u, v)$ is the Fourier transform of the PSF or the OTF. Equation 3.6 allows image formation to be performed without the computational difficulties associated with convolution.

The model of Equations 3.5 and 3.6 must account for noise effects. Noise degrades a compensated image formed through atmospheric turbulence due to sources of randomness in the image formation process. Two sources of randomness are: (1) randomness due to fluctuations in the instantaneous OTF and (2) randomness due to random arrival time and location of image photo-events. This noise process is known as a doubly stochastic Poisson random process [11].

Turbulence causes a random aberration in the telescope pupil. As noted in chapter two, an AO system cannot completely compensate for this effect resulting in a random, residual phase aberration, $\epsilon_i(x, y)$. If the telescope is diffraction limited without atmospheric turbulence, the instantaneous OTF due to $\epsilon_i(x, y)$ is [10]

$$H_i(u, v) = \frac{1}{N} \int \int P(x, y) P(x - u\lambda f, y - v\lambda f) \exp\{j[\epsilon_i(x, y) - \epsilon_i(x - u\lambda f, y - v\lambda f)]\} dx dy,$$
(3.7)

where $P(x, y)$ is the telescope pupil function, λ is the mean wavelength, f is the focal length of the imaging system, and N is given by:

$$N = \int \int | P(x, y) |^2 \, dx dy.$$
(3.8)

Equation 3.7 clearly shows that the instantaneous OTF due to atmospheric turbulence, $H_i(u, v)$, is a random process [11]. In turn, this random OTF forms an image, via Equation 3.6, which is also a random quantity.

The number and arrival locations of photo-events are random and governed by Poisson statistics [11]. The standard model for a photon-limited image is

$$i(x, y) = \sum_{n=1}^{K} \delta(x - x_n, y - y_n),$$
(3.9)

where K is the total number of photo-events in the image plane, and (x_n, y_n) is the location of the nth photo-event [11]. Since this study is particularly concerned with the image spectrum, the Fourier transform of Equation 3.9 is provided as

$$I(u, v) = \sum_{n=1}^{K} e^{-j2\pi(u x_n + v y_n)}.$$
(3.10)

Image spectrum signal-to-noise ratio (SNR) is key to objective performance analysis of the frame selection and frame weighting techniques. The standard ex-

pression for single frame image spectrum SNR is defined as [13, 28]:

$$SNR_1(u,v) = \frac{\mid E[I(u,v)] \mid}{\sqrt{Var[I(u,v)]}}, \qquad (3.11)$$

where $E[\cdot]$ is the expectation operator, and $Var[I(u,v)]$ is the variance of the measured image spectrum. SNR_1 can be viewed as an indicator of the precision of image information at a given spatial frequency. Using Equation 3.11 and conventional techniques for analyzing doubly stochastic Poisson random processes, the single frame image spectrum SNR becomes:

$$SNR_1(u,v) = \frac{\overline{K} \mid O_n(u,v) \mid\mid E[H(u,v)]\rangle \mid}{\sqrt{\overline{K} + \overline{K}^2 \mid O_n(u,v) \mid^2 Var[H(u,v)] + P\sigma^2}}, \qquad (3.12)$$

where $\overline{K}$ is the average number of photo-events per image, $O_n(u,v)$ is the object spectrum normalized to unity at $(u,v) = (0,0)$, $Var[H(u,v)]$ is the variance of the OTF, P is the number of pixels in the image spectrum array, and σ is the standard deviation of the CCD camera rms read noise [28].

Two limiting conditions on Equation 3.12 are of interest when determining the performance limits of the frame selection technique [35]. If the OTF is deterministic, Equation 3.12 reduces to the photon noise limited case

$$SNR_1(u,v) = \sqrt{\overline{K}} \mid O_n(u,v) \mid\mid E[H(u,v)] \mid. \qquad (3.13)$$

On the other hand, as the average number of photo-events per image approaches infinity, Equation 3.12 reduces to the OTF variance limited case

$$SNR_1(u,v) = \frac{\mid E[H(u,v)] \mid}{\sqrt{Var[H(u,v)]}}. \qquad (3.14)$$

It is possible to make a more accurate determination of the signal in the presence of noise through averaging multiple realizations of the desired image [1]. The

SNR of a composite image created by averaging N uncorrelated short exposure images is

$$SNR_N(u,v) = \sqrt{N} SNR_1(u,v), \qquad (3.15)$$

where N is the number of short exposure images averaged to create the composite image.

3.5 Computer Simulation

Computer simulation is a critical tool in establishing performance limits on the frame selection technique. This tool allows convenient manipulation of key independent parameters allowing accurate performance bounds to be established with relative ease. In addition, the frame selection and frame weighting rules are nonlinear. Therefore, a convenient expression that predicts image quality improvement using these techniques does not exist.

The computer simulation code used in this thesis was developed by Michael C. Roggemann [30] and further modified by Craig A. Stoudt [32]. The code incorporates a random phase screen generator to model atmospheric turbulence, a wavefront sensor model, a deformable mirror model, a tilt correction system model, and a charge-coupled device (CCD) camera model. Frame selection or frame weighting specific code is included as separate subroutines. Due to computer disk space limitations, both the frame selection and frame weighting techniques require two computer runs to implement. The first run computes the S_{S1} quality metric value for each short exposure image created by the simulation. These quality metric values are stored in a file. The second run reads the quality metric file and sorts these values from highest to lowest. The frame selection routines continue by calculating a minimum quality metric value based on the FSR indicated by the user. Then, the second run recreates the short exposure images from the first run and averages only the images with quality metric value greater than or equal to the minimum value. In contrast, the frame weighting routines use the sorted quality metric array to assign

constant-valued weights to each short exposure image. Then, as with frame selection, the second run recreates the short exposure images from the first run. However, all frames are weighted and then averaged to create a weighted composite image.

The code is used to accomplish three main objectives: establish objective performance limits on the frame selection technique as a function of key independent parameters, conduct a subjective comparison study of image quality with and without the benefits of frame selection, and conduct a preliminary investigation of simple frame weighting techniques. Image spectrum statistics, such as the image spectrum SNR, are the primary objective indicators of technique performance. The next section explores these performance metrics in detail.

3.6 Performance Metrics

Performance metrics allow for comparison between composite images processed with and without the frame selection or frame weighting techniques. The primary performance metric is the image spectrum SNR.

3.6.1 Image Spectrum SNR. Single frame image spectrum SNR, SNR_1, and multi-frame SNR, SNR_N, are positive, real, two-dimensional functions. Direct comparison of two-dimensional functions is difficult. Fortunately, Fourier image spectra exhibit a high degree of radial symmetry. This fact allows for the application of radial averaging on the SNR_1 and SNR_N functions such that

$$\overline{SNR_1(\rho)} = \frac{1}{2\pi\rho} \int_0^{2\pi} SNR_1(\rho, \theta)d\theta \tag{3.16}$$

and

$$\overline{SNR_N(\rho)} = \frac{1}{2\pi\rho} \int_0^{2\pi} SNR_N(\rho, \theta)d\theta \tag{3.17}$$

where $SNR_1(\rho, \theta)$ and $SNR_N(\rho, \theta)$ are expressed in polar coordinates. Comparison between two $\overline{SNR(\rho)}$ functions is made even more convenient through the use of the

radially averaged SNR gain function, $G(\rho)$. $G(\rho)$ is defined as

$$G(\rho) = \frac{\overline{SNR_M(\rho)}}{\overline{SNR_N(\rho)}}, \quad M \leq N, \tag{3.18}$$

where $\overline{SNR_M(\rho)}$ is the radially averaged image spectrum SNR of a composite image using the frame selection or frame weighting technique, $\overline{SNR_N(\rho)}$ is the radially averaged image spectrum SNR of a composite image formed using all the frames in the data set, M is the number of frames in the frame selection or frame weighting subset, and N is the number of frames in the complete data set. $G(\rho)$ allows easy visualization of the relative gain or loss in composite image SNR that results from the application of these techniques. Values above 1.0 at a given radial frequency indicate a gain in SNR and an improved image while values below 1.0 indicate a loss and a degraded image.

3.6.2 Noise Equivalent Frequency Cutoff. Another important performance metric that allows comparison of the signal quality of a composite image at high spatial frequencies is the noise equivalent frequency cutoff, η. As noted in Equation 3.6, the OTF acts as a filter which limits the Fourier spectrum. In fact, the Fourier spectrum of an image formed by passing through a diffraction-limited circular pupil must be zero outside the OTF radius. In contrast, noise typically exhibits a broader frequency spectrum. In general, there will exist a frequency where signal and noise spectra are equal. This frequency is the noise equivalent cutoff, η, and is defined as

$$\eta = \rho \text{ such that } \overline{SNR_1(\rho)} = 1.0. \tag{3.19}$$

η is the highest spatial frequency where the signal is known with a minimum degree of certainty. This performance metric will be used to support conclusions obtained via the image spectrum SNR.

3.6.3 Visual Image Comparison. Deconvolved images will be compared with and without application of the frame selection technique. Unlike the image spectrum SNR and noise equivalent cutoff frequency metrics, image comparison will be subjective. Deconvolved images will include simulated binary stars and a representative satellite model.

Now that the three performance metrics, $G(\rho), \eta$, and subjective visual image comparison have been defined, it is necessary to reexamine key equations associated with the image spectrum SNR to identify the independent parameters.

3.7 Independent Parameters

In section 3.4, the composite image spectrum SNR for averaging a set of N short exposures, $SNR_N(u,v)$, and the single frame image spectrum SNR for a short exposure, $SNR_1(u,v)$, were developed. The key parameters that influence image spectrum SNR are found in Equation 3.12 which is repeated below:

$$SNR_1(u,v) = \frac{\overline{K} \mid O_n(u,v) \mid \mid E[H(u,v)] \mid}{\sqrt{\overline{K} + \overline{K}^2 \mid O_n(u,v) \mid^2 Var[H(u,v)] + P\sigma^2}}, \qquad (3.20)$$

where $\overline{K}$ is the average number of photo-events per image, $O_n(u,v)$ is the object spectrum normalized to unity at $(u,v) = (0,0)$, $Var[H(u,v)]$ is the variance of the OTF, P is the number of pixels in the image spectrum array, and σ is the standard deviation of the CCD camera rms read noise [28].

3.7.1 Data Set Size, N, M. The number of short exposure images in a data set has a direct relationship to the SNR as indicated by Equation 3.15. Taken alone, this equation seems to indicate that larger data sets produce higher SNR. However, the number of images in a data set is limited by the apparent speed and rotational motion of the object as it moves across the sky. For example, a star may appear stationary with respect to the night sky allowing tens of thousands of images to be taken. In contrast, an artificial satellite may pass through the field-of-view

of a ground-based telescope in a matter of minutes, limiting the number of frames collected to a few hundred. Frame selection results in an even smaller subset of images, M, which has a direct effect on image spectrum SNR. Both N and M can be selected in the simulation by indicating N and the FSR.

3.7.2 Average Photo-events, $\overline{K}$. The average number of photo-events per image is directly related to the visual magnitude of the object, exposure time, mean imaging wavelength, and size of the telescope aperture minus any obstructions. The apparent visual magnitude, m_ν, allows astronomers to compare object brightness in the night sky [21]. A step in visual magnitude indicates a corresponding factor 2.5 change in brightness with smaller values of m_ν indicating brighter objects. Visual Magnitude of common sky objects are shown in Table 3.1 [21]. The visual magnitude

Table 3.1   Visual Magnitude of Common Sky Objects

OBJECT	m_ν
Sun	-26.7
Full Moon	-12.5
Venus	-4.3
Jupiter	-2.3
Sirius	-1.58
Polaris	+2.2
Typical Artificial Satellite	-0.96

of an object can be selected in the simulation by changing the value of $\overline{K}$ and another parameter, $\overline{K_W}$, the average number of photo-events across a single wavefront sensor subaperture per integration time. Stoudt noted that m_ν had the greatest affect on frame selection performance of all the independent parameters in his study [32].

3.7.3 $E[H(u,v)]$ and $Var[H(u,v)]$. The mean and variance of the system OTF depends, primarily, on the strength of the atmospheric turbulence or seeing conditions. Therefore, for the purposes of this thesis effort, the mean and variance

of the system OTF will be considered to be most directly related to the r_o parameter. As such, the simulation allows direct input of an appropriate r_o value. Stoudt noted that seeing conditions have a direct effect on frame selection performance [32].

3.7.4 Object Spectrum, $O_n(u,v)$. Unfortunately, SNR is dependent on the object spectrum which presents a potential problem when attempting to draw universal conclusions from the study of a single object. The simulation of point sources allows some relief from this problem due to their similarity to one another. In fact, star images have been seen in the pertinent literature [4, 8, 23]. However, the Air Force is primarily interested in imaging extended objects such as satellites. Therefore, care must be exercised when drawing conclusions for all extended objects after detailed examination of only one satellite model.

3.7.5 CCD Camera Noise. CCD cameras in use today introduce Gaussian additive read noise to the images. This noise is a function of the number of pixels in the image, P, and the noise variance per pixel, σ^2. The quantity σ^2 is dependent on the hardware available. Typical values for high quality, commercially available, CCD cameras range from 10-15 electrons per pixel [32]. The number of pixels is also important. Using the minimum number of pixels possible will reduce CCD noise effects. Stoudt developed a realistic CCD camera noise model which allows input of the σ^2 parameter [32].

3.8 AMOS Data

This thesis effort incorporates the first application of the frame selection technique to actual satellite data. The data was collected using the AMOS 1.6 meter telescope and compensated imaging system depicted in Figure 3.1 [31]. The AMOS telescope is a closed-tube cassegrain device on an equitorial mount. The telescope and mount are set on a rotating turntable to allow a third rotation axis. The Cassegrain design of the telescope includes a 1.57 meter clear aperture with a 33.5

centimeter central obscuration. Tilt is removed from the collimated wavefront with a flat mirror. Counter-rotating prisms correct the collimated incoming light beam for atmospheric dispersion. The beam is then split to the wavefront sensor (WFS) and imaging portions of the system. The WFS uses a pair of shearing interferometers with 152 subapertures in the telescope pupil. The deformable mirror (DM) is a monolithic piezoelectric device with 168 actuators. The WFS and DM combine to compensate for atmospheric turbulence effects in real time. The detector used to collect these images was a Photometrics CH200 camera head with a class-1 Kodak KAF 1400 chip. The detector utilizes a 1317 x 1035 pixel array which was windowed in hardware and software to a final 128 x 128 pixel image. Dark frame and flat field data were collected to properly calibrate for camera bias and noise.

The data consisted of satellite images and star references. The star references were collected to provide an estimate of the atmosphere-optical system OTF for later deconvolution. Processing of AMOS data for incorporation in this thesis consisted of the following steps:

1) Use AMOS image viewing software known as ALFY to view satellite images. Select 20, 40, 60, 80, and 100 frame satellite data sets. Each data set starts with the same beginning frame. Also collect satellite dark frames and flat fields.

2) Average all frames in each complete satellite data set and compare image spectrum SNR. Select the data set size with the highest overall SNR for frame selection processing. An example is shown in Figure 3.2. This step optimizes the data set size to eliminate the degrading effects of rotational motion as the satellite passes across the sky.

3) Perform frame selection on the optimum data set from step 2 using the REDSEL frame selection code. Compare image spectrum SNR using FSRs of 100, 70, 50, and 30 percent.

4) View reference star images. Select reference star data set, dark frames, and flat fields.

5) Perform frame selection on the reference star data set using the REDSEL frame selection code. Compare image spectrum SNR using FSRs of 100, 70, 50, and 30 percent.

6) Deconvolve satellite images using the modified inverse filter or pseudo-Weiner filter. Satellite and star references used for deconvolution had identical FSRs.
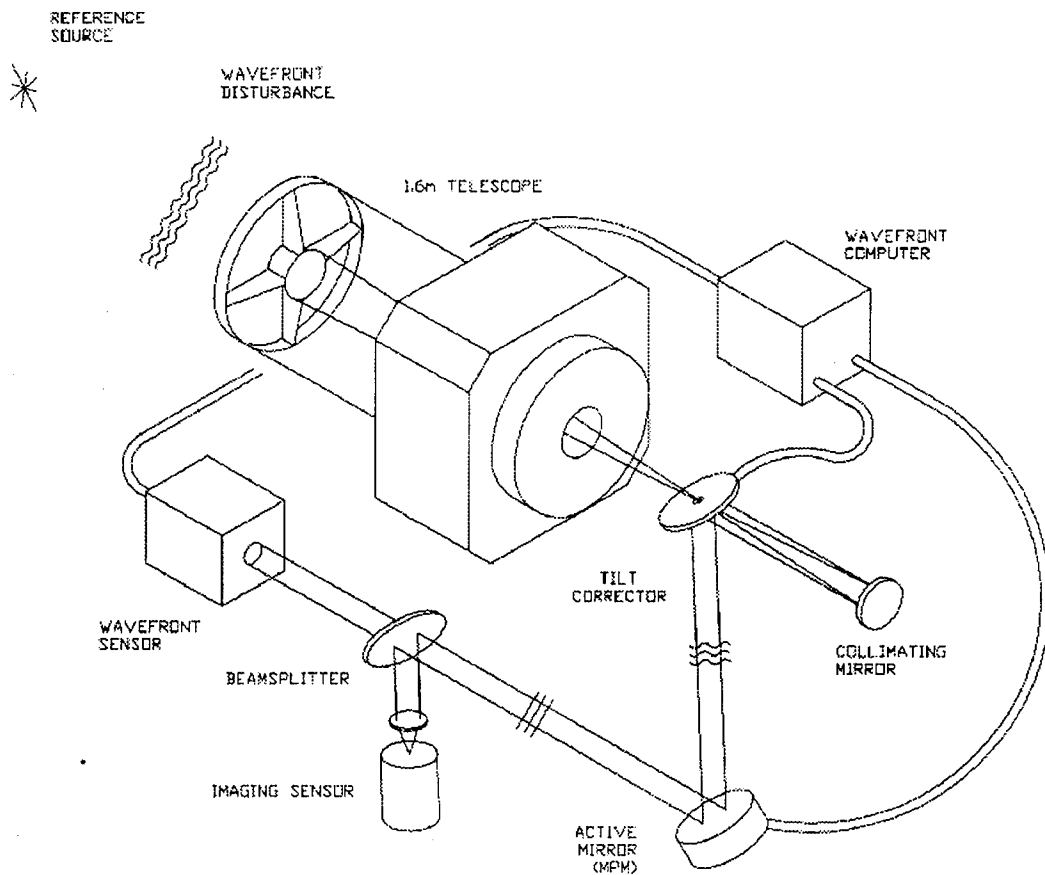
REFERENCE
SOURCE

WAVEFRONT
DISTURBANCE

1.6m TELESCOPE

WAVEFRONT
COMPUTER

TILT
CORRECTOR

COLLIMATING
MIRROR

WAVEFRONT
SENSOR

BEAMSPLITTER

IMAGING SENSOR

ACTIVE
MIRROR
(MPM)

Figure 3.1   Block Diagram of the AMOS Adaptive Optics System
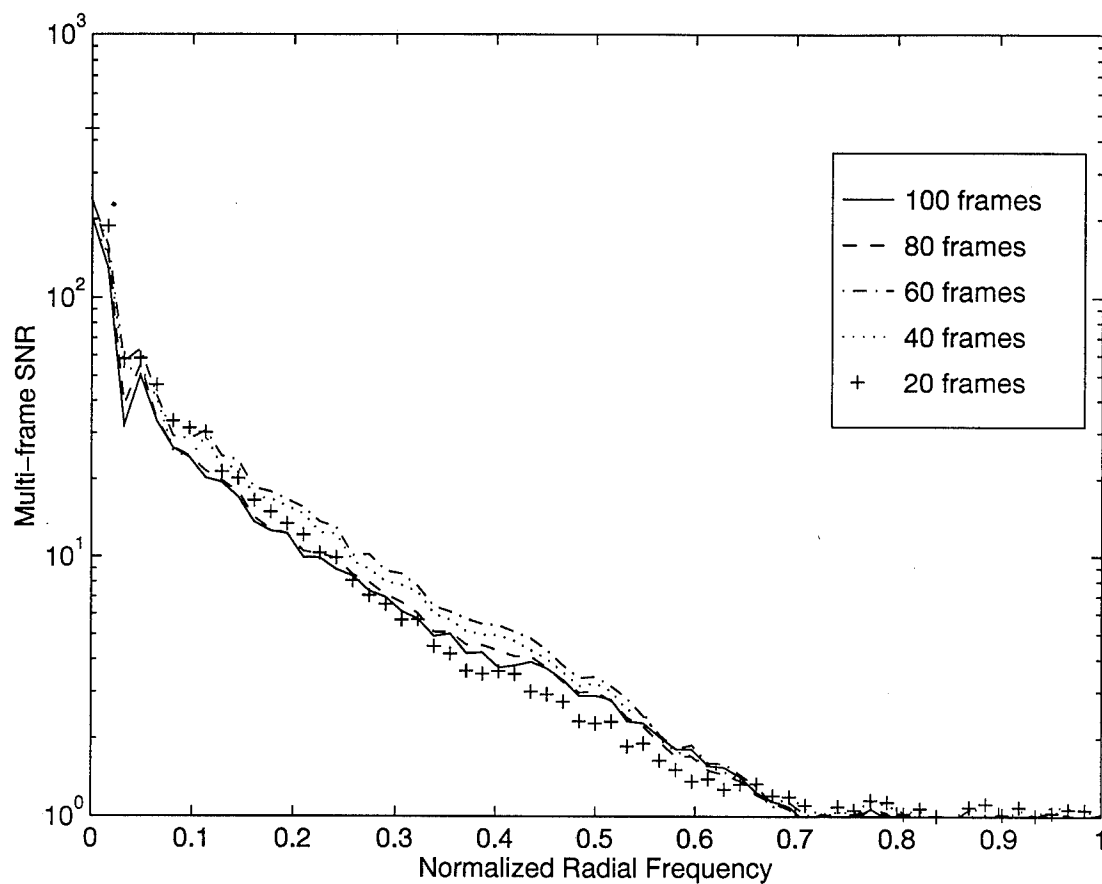
Figure 3.2 An Example of a Multi-frame Image Spectrum SNR Plot Used to Determine the Optimum Data Set Size for Frame Selection Processing of AMOS Data. Optimum Data Set Size = 60 frames, Object = Hubble Space Telescope, Exposure Time = 60 milliseconds, Data Collected 23 Jun 94.

3.9 Summary

This chapter provided the basic terminology used in frame selection and frame weighting, established a single frame quality metric, outlined the performance metrics used to evaluate improvements in the composite images, and identified the key independent parameters. In addition, data reduction considerations pertaining to AMOS images were discussed. The results of five experiments will be presented in the next chapter.

IV. Analysis Results

4.1 Introduction

This chapter consists of five experiments designed to establish frame selection performance limits, demonstrate the superiority of deconvolved images after application of the frame selection technique, explore image reconstruction via frame weighting, and demonstrate frame selection on actual Air Force Maui Optical Site (AMOS) satellite and reference star imagery. Chapter three developed the methodology to conduct this investigation. The frame selection rule was defined as a three step process in which a quality metric is calculated for each frame in the data set, the images are sorted from best to worst based on the quality metric value, and those images with highest quality metric value are averaged to create a composite image. Selection is based on a user-defined frame selection rate (FSR). The FSR was defined as the ratio of the number of frames selected to the number of frames in the original data set. The frame weighting rule is identical to the frame selection rule except in the last step. In contrast to frame selection, the frame weighting technique does not discard lower quality frames. Instead, this method applies a weight either via a quality-based or function-based weighting scheme. The weighted frames are then averaged to form a composite image. The S_{S1} quality metric is defined as

$$S_{S1} = \int \int S_{OTF}(u,v)|I(u,v)|^2 du dv \tag{4.1}$$

and is a variant of the S_1 quality metric developed by Muller and Buffington [22]. Due to its superior performance in the Stoudt investigation [32], the S_{S1} quality metric was used for all experiments in this thesis. Independent parameters and performance metrics were also outlined in the previous chapter. To bound frame selection performance, demonstrate subjective visual image improvement, and investigate the frame weighting technique, five experiments were performed.

Experiment One establishes the limits of the frame selection technique as a function of the independent parameters. The radially averaged signal-to-noise ratio (SNR) gain function, $G(\rho)$, and the noise equivalent frequency cutoff, η, are the performance metrics. Experiment Two establishes the effect of frame selection on the effective average point spread function (PSF) as a function of the independent parameters. Experiment Three uses simulation to conduct a subjective visual comparison of point source and satellite objects with and without frame selection processing. Experiment Four consists of a limited feasibility investigation of several frame weighting schemes. $G(\rho)$ is the performance metric. Experiment Five demonstrates frame selection on actual AMOS imagery. $G(\rho)$ and subjective visual comparison of images are the performance metrics.

Some information is already available due to previous research associated with the frame selection technique [4, 8, 23, 32]. This information is used to bound this study.

4.1.1 Independent Parameters. Chapter Three identified the following independent parameters that impact image spectrum SNR: data set size (N), frame selection rate (FSR), the average number of photo-events per image ($\overline{K}$), object spectrum $O(u, v)$, atmospheric seeing conditions (r_o), and the charge coupled device (CCD) detector noise characteristics (P, σ^2). Thanks primarily to the work of Stoudt [32], the following restrictions and emphasis were placed on each parameter in order to better bound the study:

1. Data set size, N, was 500 frames for all simulation runs. Data set size was optimized for AMOS data as noted in Chapter Three.

2. Frame selection rate, FSR, is a free parameter in this study.

3. Average number of photo-events per image, $\overline{K}$, is a free parameter in this study. The minimum apparent visual magnitude of an object, m_ν, that yields im-

proved image spectrum SNR after frame selection processing is a key performance limit investigated in Experiment One.

4. Objects will consist of a simulated point source and satellite. The satellite model is a CAD rendering of a typical space satellite as shown in Figure 4.1. The satellite was modeled as being 12 meters in length and in an orbit 500 kilometers above the surface of the earth.

5. Atmospheric seeing condition, r_o, is a free parameter in this study. A wide variety of seeing conditions are modeled.

6. Number of pixels, P, is fixed at 256^2 by the simulation image output size.

7. CCD rms read noise variance, σ^2, is fixed at 15 electrons per pixel to reflect a realistic, state-of-the-art detector unless otherwise noted.

4.1.2 Adaptive Optics (AO) System Parameters. The simulation experiments utilized two AO system configurations. The two systems differ only in the deformable mirror (DM) actuator spacing. AO case 1 has the DM actuator spacing tied closely to wavefront sensor (WFS) subaperture size (DM actuator spacing = 11 centimeters, WFS subaperture size = 10 centimeters). AO case 2 has the DM actuator spacing larger than the WFS subaperture size (DM actuator spacing = 22 centimeters, WFS subaperture size = 10 centimeters). The addition of AO case 2 allowed a greater ability to study performance of frame selection on partially compensated AO systems. All other parameters were common to both system configurations. The simulated AO system had a 1 meter diameter telescope with no central obscuration. The imaging and wavefront sensing wavelength was 500 nanometers. The fractional bandwidth of the telescope was modeled as 10 percent. Transmission efficiency from the top of the atmosphere to the wavefront sensor and imaging camera was 50 percent. The simulation modeled an intensity splitter to send 40 percent of photons to the image plane and 60 percent to the wavefront sensor.
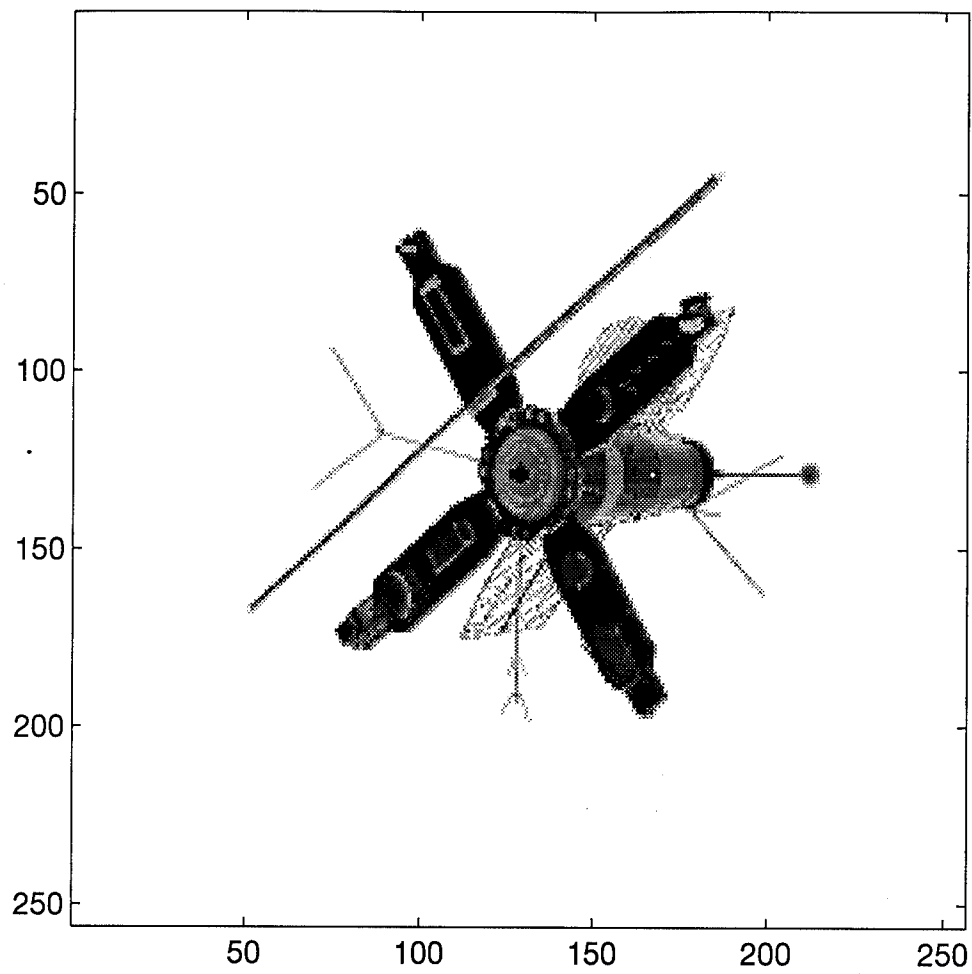
Figure 4.1   CAD Rendering of a Typical Satellite for Use in Computer Simulation

This is the primary experiment to establish performance limits on the frame selection technique as a function of the key parameters. First, the fundamental limit on the frame selection rule, photon noise, is used to predict SNR performance. Then, theoretical predictions are verified using computer simulation with the image spectrum SNR as the primary performance metric.

4.2.1 Theoretical Performance Limits. Recall the single frame image spectrum SNR expression from Chapter Three:

$$SNR_1(u,v) = \frac{\overline{K} \mid O_n(u,v) \mid \mid E[H(u,v)] \mid}{\sqrt{\overline{K} + \overline{K}^2 \mid O_n(u,v) \mid^2 Var[H(u,v)] + P\sigma^2}}, \qquad (4.2)$$

where $\overline{K}$ is the average number of photo-events per image, $O_n(u,v)$ is the object spectrum normalized to unity at $(u,v) = (0,0)$, and $Var[H(u,v)]$ is the variance of the optical transfer function (OTF) [28]. By multiplying numerator and denominator of Equation 4.2 by $\overline{K}^{-1}$, this expression becomes,

$$SNR_1(u,v) = \frac{\mid O_n(u,v) \mid \mid E[H(u,v)] \mid}{\sqrt{\overline{K}^{-1} + \mid O_n(u,v) \mid^2 Var[H(u,v)] + \overline{K}^{-2} P\sigma^2}}. \qquad (4.3)$$

Close examination of the denominator of Equation 4.3 reveals three sources of randomness, photon noise, noise associated with atmosphere-optical system OTF variance, and CCD camera noise effects.

Photon noise is associated with the random number and arrival time of photons in the image plane. It is directly related to the $\bar{K}^{-1}$ term in Equation 4.3. In this case, if the object is sufficiently dim ($\bar{K}$ small) or the OTF is deterministic, photon noise will dominate the expression, reducing Equation 4.3 to

$$SNR_1(u,v) = \sqrt{\overline{K}} \mid O_n(u,v) \mid \mid E[H(u,v)] \mid . \qquad (4.4)$$

Notice that the $Var[H(u,v)]$ term does not appear in Equation 4.4. AO systems and post-detection processing schemes, such as frame selection, sharpen images by reducing the OTF variance, $Var[H(u,v)]$. With photon noise as the dominant effect, this quantity plays a limited role in the image spectrum SNR calculation. In other words, AO and frame selection cannot improve a photon noise limited image.

On the other hand, the randomness of the OTF may dominate the SNR. When the OTF variance is the dominant effect, Equation 4.3 becomes

$$SNR_1(u,v) = \frac{|\,E[H(u,v)]\,|}{\sqrt{Var[H(u,v)]}}. \tag{4.5}$$

Equation 4.5 represents the condition in which frame selection can best improve image spectrum SNR.

CCD camera noise effects are closely related to photon noise in that they both depend on the average number of photo-events available in the image plane. As Equation 4.3 indicates, CCD camera noise plays an increasingly important role as $\overline{K}$ decreases. Figure 4.2 is an SNR gain plot versus radially averaged normalized spatial frequency showing three values of σ^2 for a relatively bright point source, $m_\nu = +2$. The horizontal axis is normalized to the diffraction limited cutoff of the optical system. Notice that the three gain curves are virtually identical supporting the conclusion that CCD noise effects are minimal for bright objects. However, Figure 4.3 shows that CCD noise significantly degrades a dim point source, $m_\nu = +8$.

With photon noise and OTF variance established as primary limits on the image spectrum SNR, it is possible to use the transition between these two states as a predictor of frame selection performance. The goal is a set of theoretical plots which aid in the visualization of the relative dominance of various noise effects. Due to their mutual dependence on the average number of photo-events, $\overline{K}$, photon noise

and CCD camera noise will be grouped as a measurement noise term defined as

$$\text{Measurement Noise} = \overline{K}^{-1} + \overline{K}^{-2} P \sigma^2. \qquad (4.6)$$

The OTF variance caused by atmospheric turbulence will be known as OTF noise such that

$$\text{OTF Noise} = \mid O_n(u, v) \mid^2 Var[H(u, v)]. \qquad (4.7)$$

Figure 4.4 provides an example of this method for a point source, AO case 1, for a noiseless CCD array ($\sigma^2 = 0$ electrons per pixel). The vertical axis allows direct comparison of the measurement noise and OTF noise quantities. The solid horizontal lines provide measurement noise levels associated with the stated apparent visual magnitude, m_ν. The family of curves represent the OTF noise for discrete r_o values. The relative position of measurement noise lines of visual magnitude and OTF noise curves indicate the dominance of the respective noise effect. For example, Figure 4.4 shows a measurement noise line associated with $m_\nu = +10$ below the four OTF noise curves. In this case, the image spectrum SNR of a $m_\nu = +10$ object can be improved using frame selection processing. Plots similar to Figure 4.4 will be used in this experiment to provide a theoretical basis for the experimental observations made using computer simulation.
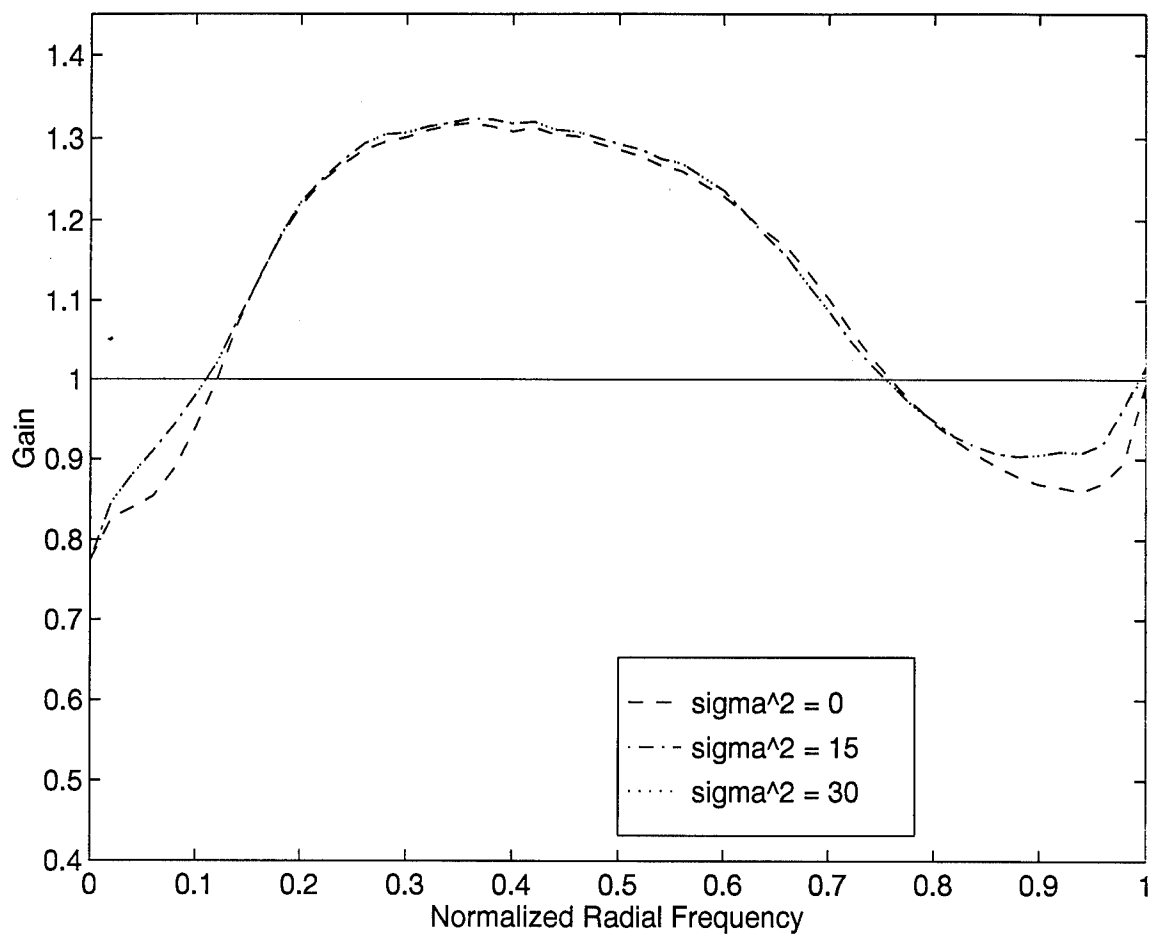
Figure 4.2   Gain Curves Showing the Minimal Effects of CCD Camera Noise for a
Bright Point Source. $r_o = 10$cm, $m_\nu = +2$, FSR = 60 percent, AO Case
1
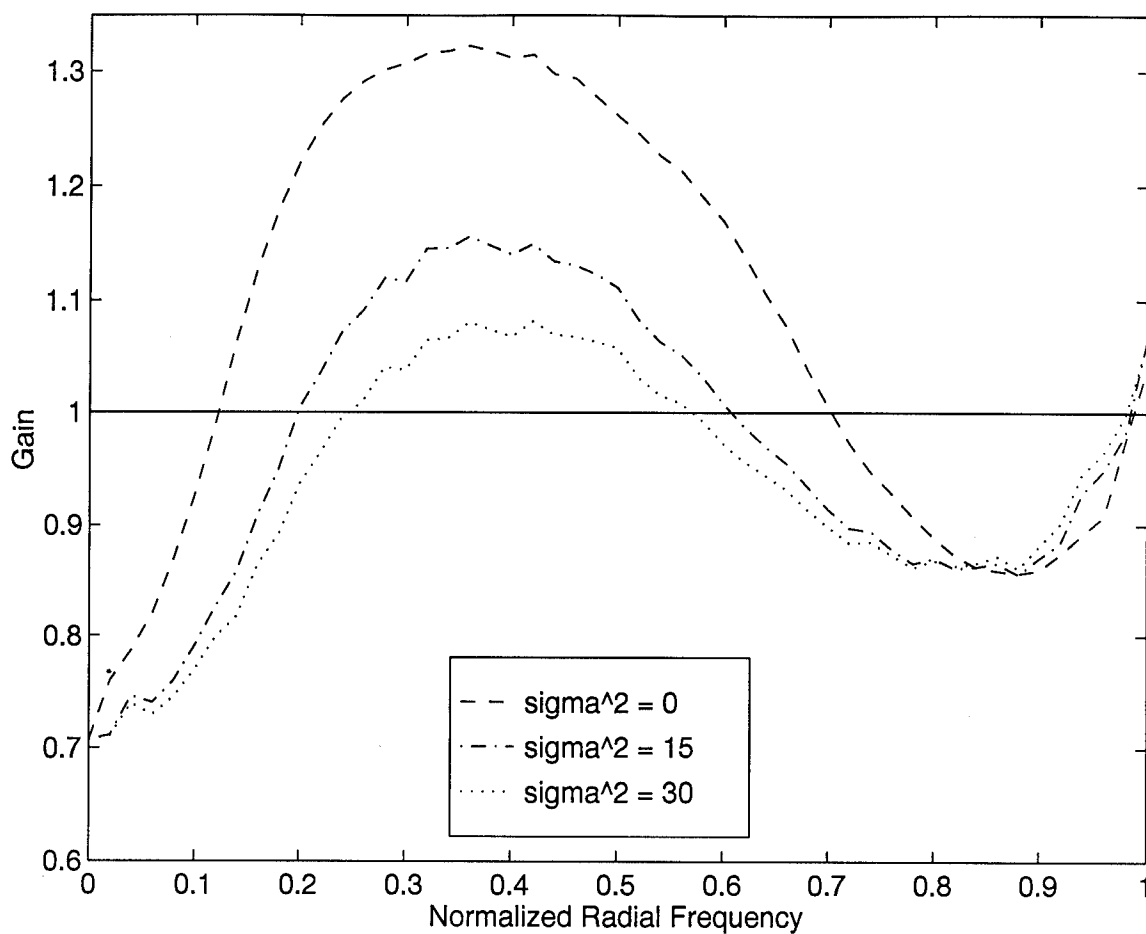
Figure 4.3   Gain Curves Showing the Effects of CCD Camera Noise for a Dim Point
Source. $r_o = 10$cm, $m_\nu = +8$, FSR = 60 percent, AO Case 1
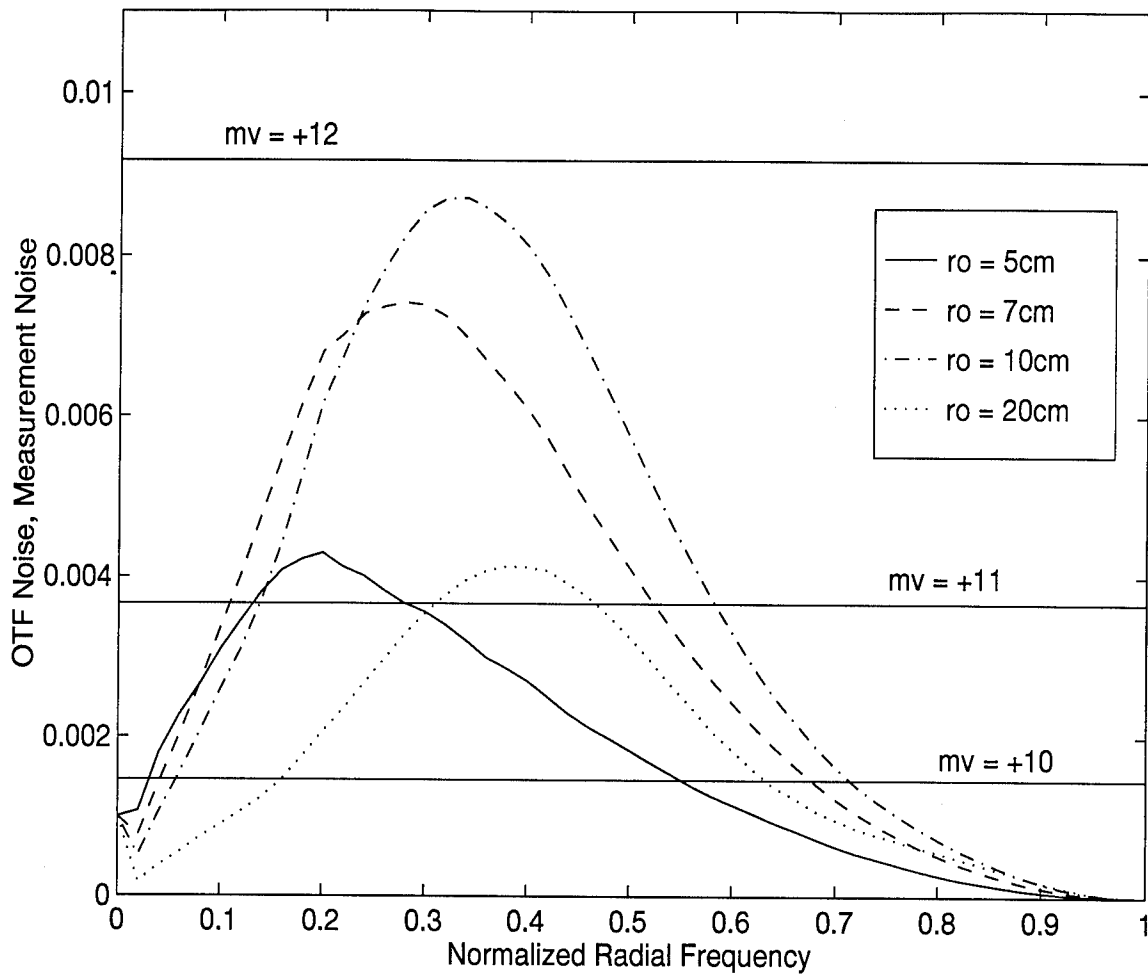
Figure 4.4   Measurement Noise and OTF noise as a Function of Spatial Frequency, AO Case 1, Point Source. Curves Indicate the Relative Dominance of Photon Noise and OTF Noise for Various r_o Values. $\sigma^2 = 0$ electrons per pixel

4.2.2 Simulation Results. The following four cases: point source-fully compensated AO, point source-partially compensated AO, satellite model-fully compensated AO, and satellite model-partially compensated AO provide representative data used to establish key performance limits associated with the frame selection technique. Additional SNR gain plots are found in Appendix A.

4.2.2.1 Point Source-Fully Compensated AO. This case investigates frame selection performance limits associated with a fully compensated AO system imaging a point source object. This data is considered fully compensated because r_o, the AO system subaperture dimension, and the AO system actuator spacing are all approximately the same size. AO case 1 was used to generate all plots in this section.

Figure 4.5 depicts a typical set of SNR gain curves as a function of spatial frequency for the 70, 50, and 30 percent FSRs where $m_\nu = +2$ and $r_o = 10$ centimeters. At the 50 percent selection rate, a gain in SNR occurs over 60 percent of the diffraction limited frequency range with the greatest improvement in the mid spatial frequencies. The peak gain occurs at 40 percent of the diffraction limit and represents just over a 30 percent gain in SNR. As is typical of gain curves associated with this case, reducing the FSR results in a general reduction in the improved frequency range. At the same time, lower FSRs produce greater losses at low and high frequencies. This degradation in SNR performance is due to an insufficient number of frames in the subset to adequately reduce photon noise through averaging. This result reestablishes Stoudt's conclusion that there exists an optimal FSR for image spectrum SNR performance [32].

With this key conclusion revisited, it is now possible to use theoretical data such as that in Figure 4.4 to accurately bound performance for the key independent parameters, m_ν and r_o. Figure 4.6 provides measurement noise and OTF noise data as a function of spatial frequency. The difference between Figures 4.4 and 4.6

4-11

is that the latter models a detector with CCD rms read noise variance, σ^2, equal to 15 electrons per pixel. Notice the significant impact of CCD camera noise for this theoretical plot when compared to Figure 4.4. Figure 4.6 indicates a general change from OTF noise to measurement noise dominance for objects of brightness $m_\nu = +7 - +8$. In addition, the $r_o = 10$ centimeter curve has the largest peak value which is associated with the greatest OTF variance. Greater OTF variance can yield a corresponding increase in SNR gain in conjunction with improvements in the mean OTF. Therefore, one possible interpretation of this theoretical data predicts the greatest SNR gain when $r_o = 10$ centimeters. Finally, it is apparent that OTF variance is reduced for very poor and very good seeing conditions. This suggests possible upper and lower performance bounds on the r_o parameter.

Computer simulation can be used to validate these predictions. Figure 4.7 depicts SNR gain curves as a function of spatial frequency for $m_\nu = +6, 7, 8$, and 10 with $r_o = 10$ centimeters and FSR = 50 percent. Peak SNR gain is clearly reduced when $m_\nu = +8$ and totally eliminated as brightness is further decreased. Figures 4.6 and 4.7 establish $m_\nu = +8$ as the minimum object brightness necessary for the frame selection rule to increase SNR for a point source and a fully compensated AO system.

At this point, it is necessary to relax restrictions on the r_o parameter in order to gain insight into its effect on frame selection performance. First, Figure 4.8 depicts SNR gain curves associated with $r_o = 5, 7, 10$, and 20 centimeters where $m_\nu = +2$ and FSR = 50 percent. The $r_o = 10$ centimeter curve provides the maximum SNR gain as predicted by the theoretical plot of Figure 4.6. In addition, the $r_o = 5$ and 20 centimeter SNR gain curves show the least gain as predicted by their smaller OTF variance. Figure 4.9 is similar to the previous plot but examines very poor and exceptional seeing conditions to determine potential frame selection performance at these extremes. The data clearly shows a minimum r_o value of approximately 4 centimeters. This minimum value is more a function of the AO system limitations than

4-12

the frame selection technique. However, Figure 4.9 also shows a general degradation of SNR gain as seeing conditions improve. While degradation in SNR gain occurs as seeing conditions improve, gain continues to average approximately 20 percent over the mid-spatial frequencies for the $r_o = 30$ centimeter case. Therefore, it is possible to conclude that frame selection will improve image spectrum SNR, to some extent, even under exceptional seeing conditions.
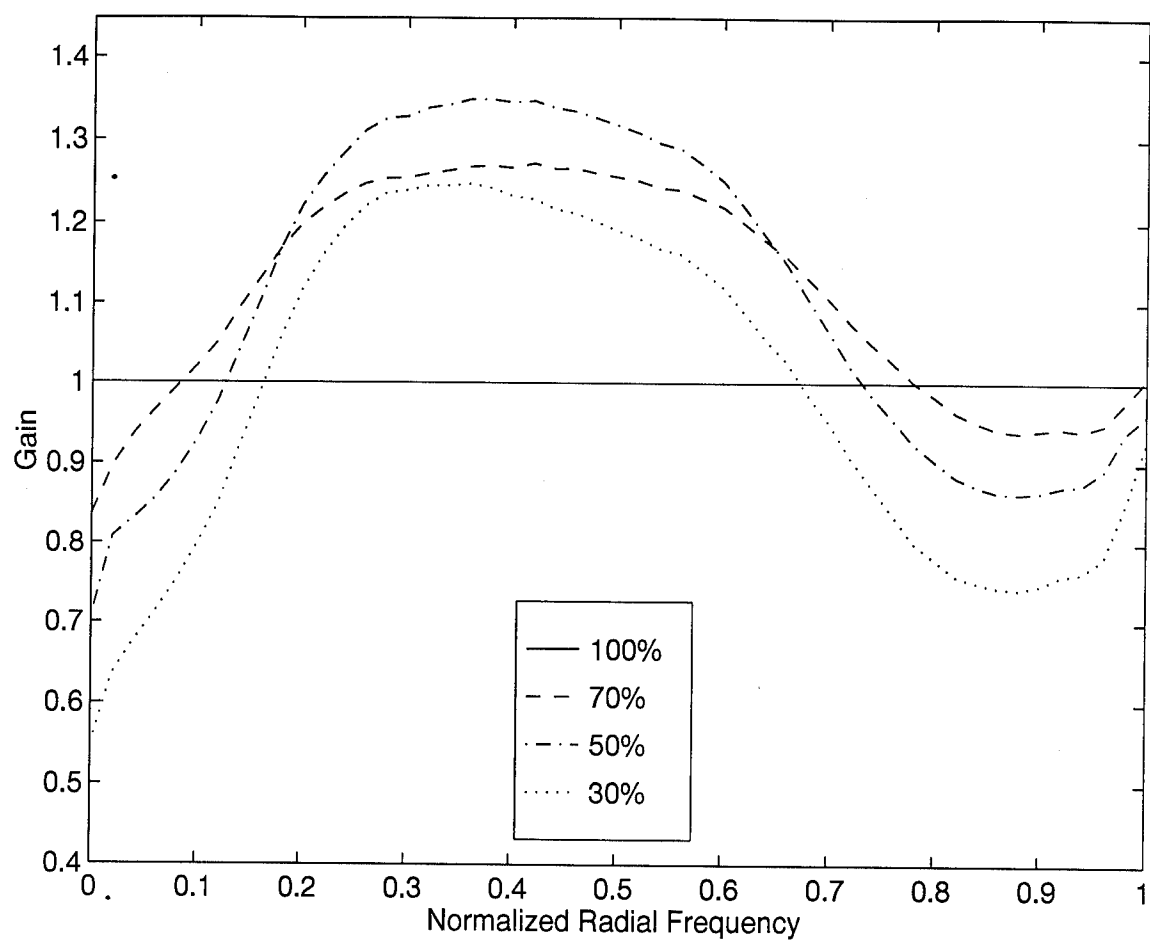
Figure 4.5   Gain Curves Establishing Improved Image Spectrum SNR for Fully Compensated AO, AO Case 1, Point Source. $r_o = 10$ cm, $m_\nu = +2$, $\sigma^2 = 15$ electrons per pixel
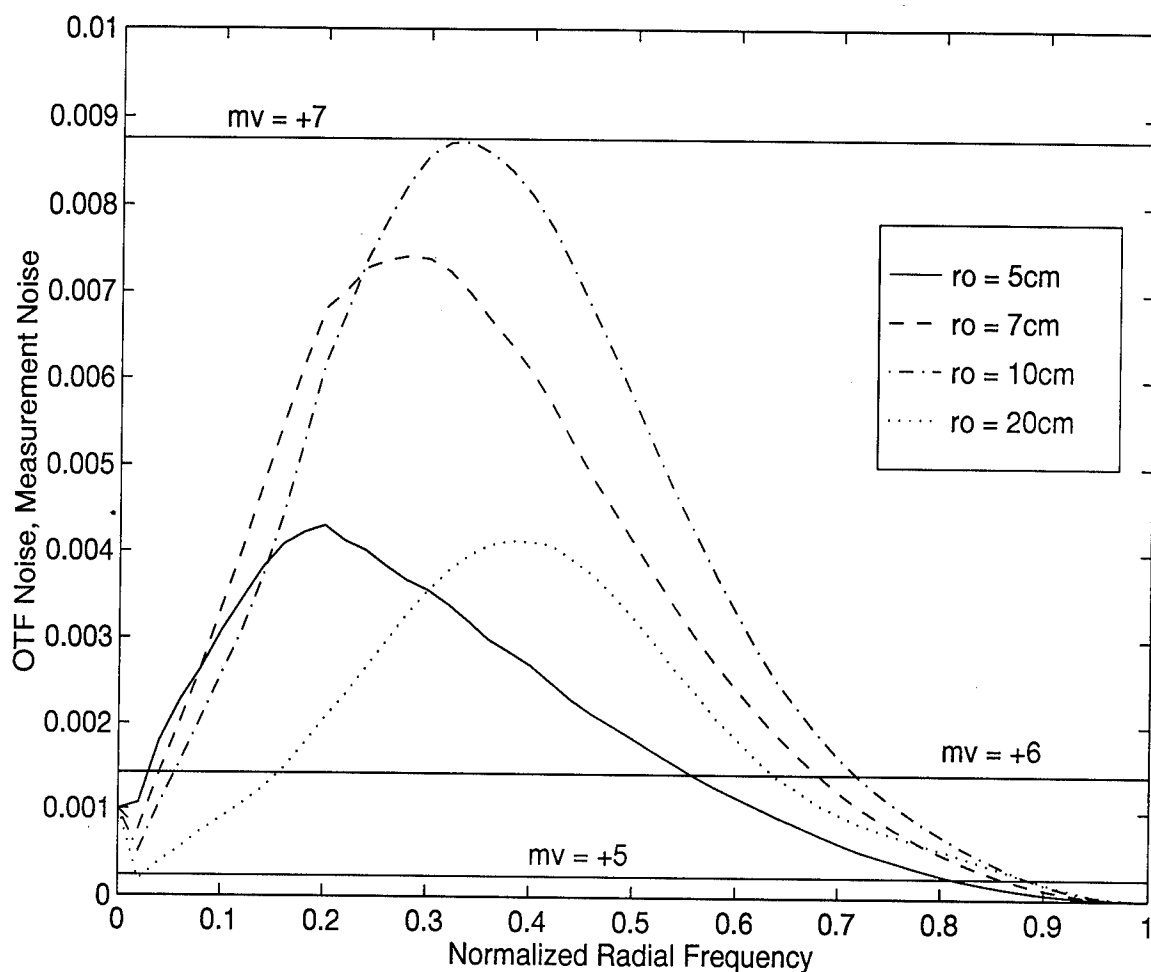
Figure 4.6 Measurement Noise and OTF Noise as a Function of Spatial Frequency, AO Case 1, Point Source. Curves Indicate the Relative Dominance of Measurement Noise and OTF Noise for Various r_o Values. $\sigma^2 = 15$ electrons per pixel
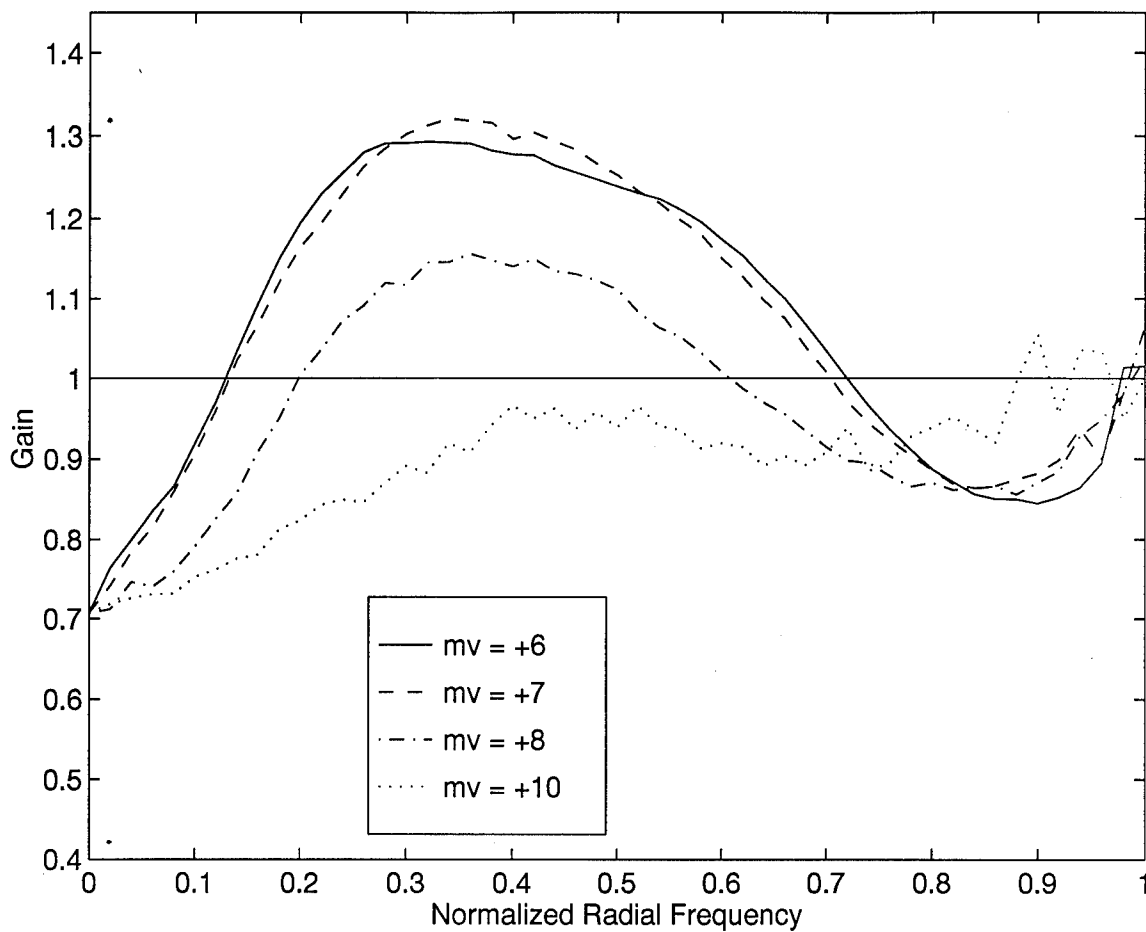
Figure 4.7   Gain Curves Establishing Minimum m_ν for Image Improvement Using Frame Selection, Fully Compensated AO, AO Case 1, Point Source. $r_o = 10$ cm, FSR = 50 percent, $\sigma^2 = 15$ electrons per pixel. Minimum m_ν for frame selection $= +8$
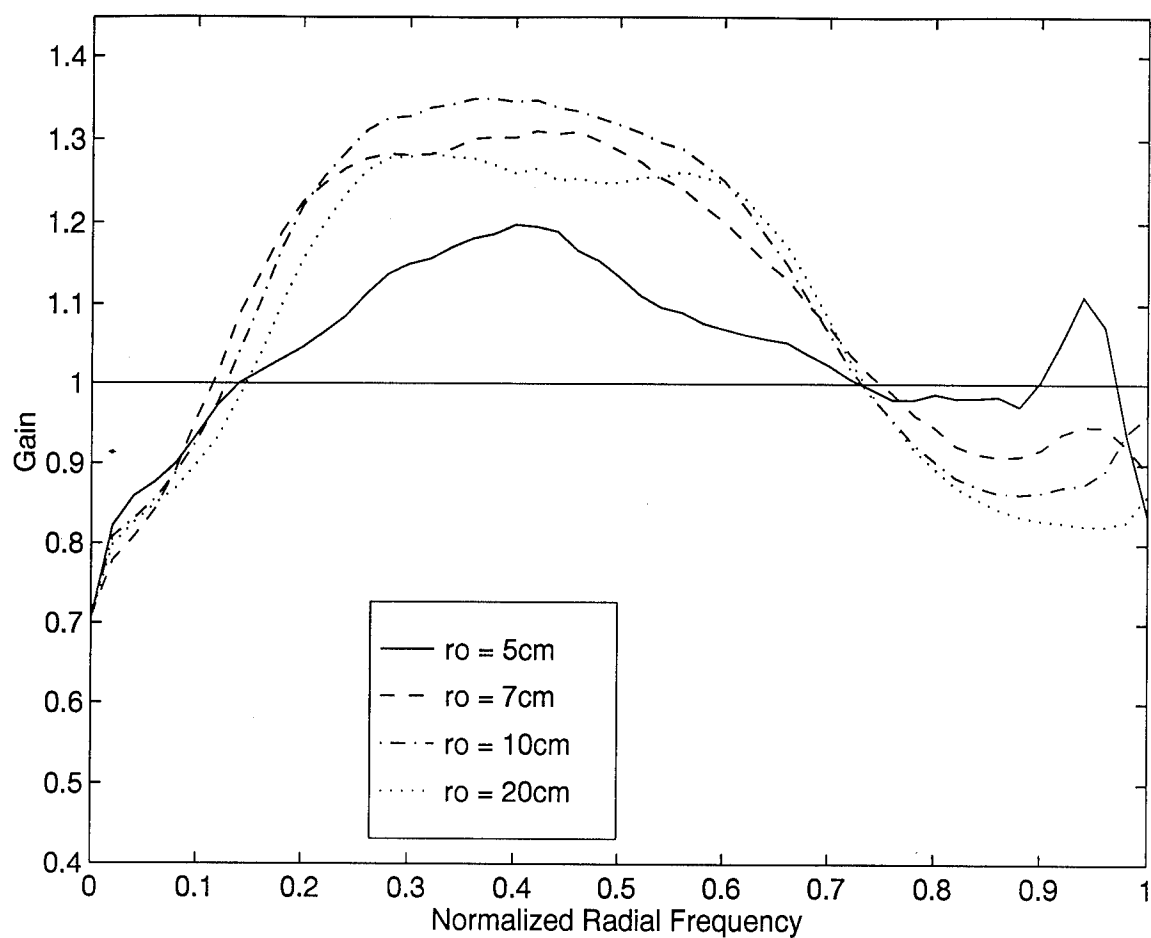
Figure 4.8   Gain as a Function of Spatial Frequency for $r_o = 5, 7, 10, 20$ cm, AO
Case 1, Point Source. Gain Curves Indicate Best Frame Selection Per-
formance for $r_o = 10$ cm. $m_\nu = +2$, FSR = 50 percent, $\sigma^2 = 15$
electrons per pixel
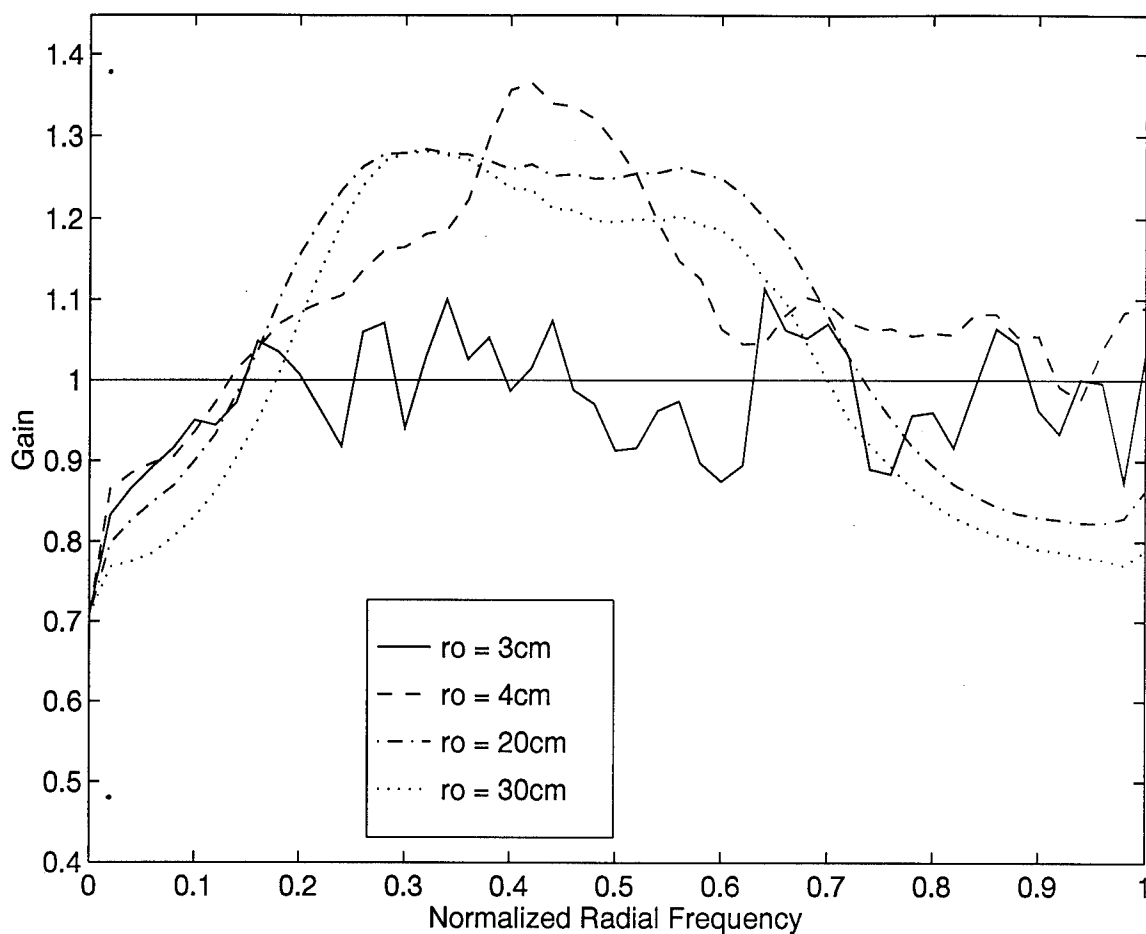
Figure 4.9 Gain as a Function of Spatial Frequency for $r_o = 3, 4, 20, 30$ cm, AO Case 1, Point Source. Gain Curves Establish Bounds on r_o for the Frame Selection Technique. $m_\nu = +2$, FSR = 50 percent, $\sigma^2 = 15$ electrons per pixel. Minimum $r_o = 4$ cm

4.2.2.2 Point Source-Partially Compensated AO. The previous section established performance limits on two key parameters, m_ν and r_o, for a fully compensated AO system with 11 centimeter spacing between DM actuators. As noted in Chapter Two, a DM with a large number of actuators is complex and expensive to build. Recent research suggests that adequate performance for many applications is possible with fewer DM actuators [28, 29, 34]. This case investigates frame selection performance limits associated with a less complex AO system imaging a point source object. The data is considered partially compensated because r_o is much less than the DM actuator spacing used in AO case 2 ($r_o = 10$ centimeters, DM actuator spacing = 22 centimeters). The wavefront sensor subaperture size retains the previous dimensions. The AO case 2 system was used to generate all plots in this section.

Figure 4.10 depicts a set of SNR gain curves as a function of spatial frequency for the 70, 50, and 30 percent FSRs where $m_\nu = +2$ and $r_o = 10$ centimeters. At the 50 percent selection rate, the peak gain occurs at 35 percent of the diffraction limit and represents just over a 25 percent gain in SNR. This gain is 5 to 10 percent less than that of the previous fully compensated system. In contrast, all three frame selection rates maintain nearly the same bandwidth for SNR gains and losses when compared to the fully compensated case. Therefore, the net result of employing fewer actuators is a simple reduction in SNR gain compared to the fully compensated case.

To illustrate another effect, Figure 4.11 shows the noise equivalent cutoff frequency, η, for both AO case 1 and 2. Note that frame selection has a much more pronounced effect on η for AO case 2. In fact, η is 45 percent less for AO case 2 for a 100 percent FSR. This η differential is reduced to less than 10 percent for a 30 percent FSR. Frame selection seems to have the capability to improve the mid to high spatial frequency information degraded by using fewer DM actuators.

The theoretical plot of Figure 4.12 shows a marked reduction in the OTF noise curves for $r_o = 5, 7$, and 10 centimeters. In these partially compensated cases, OTF

variance has been reduced. This reduction in OTF variance is due to inadequate AO compensation resulting in an increased number of highly attenuated realizations of the instantaneous OTF. If the instantaneous OTF approaches this attenuated case more often, OTF variance is reduced. This lower OTF variance translates to increased measurement noise dominance and less potential for frame selection to benefit the composite image. As in the previous section, Figure 4.12 can be used to make theoretical predictions regarding performance of the frame selection technique for the m_ν and r_o parameters. Once again, a minimum m_ν of approximately +7-+8 is necessary to avoid the measurement noise limited condition. The theoretical data also predicts the greatest SNR gain when $r_o = 10$ centimeters.

The simulation validates these predictions in Figures 4.13 and 4.14. Figure 4.13 shows that SNR gain is clearly reduced for the $m_\nu = +8$ case. The $m_\nu = +7$ curve provides the minimum visual magnitude for net SNR gain across the normalized frequency band. Notice in Figure 4.14 the distinct drop off in SNR gain for $r_o = 5$ and 7 centimeters reflecting their drop in OTF variance. The $r_o = 10$ centimeter case maintains the greatest SNR gain but only by a small margin.
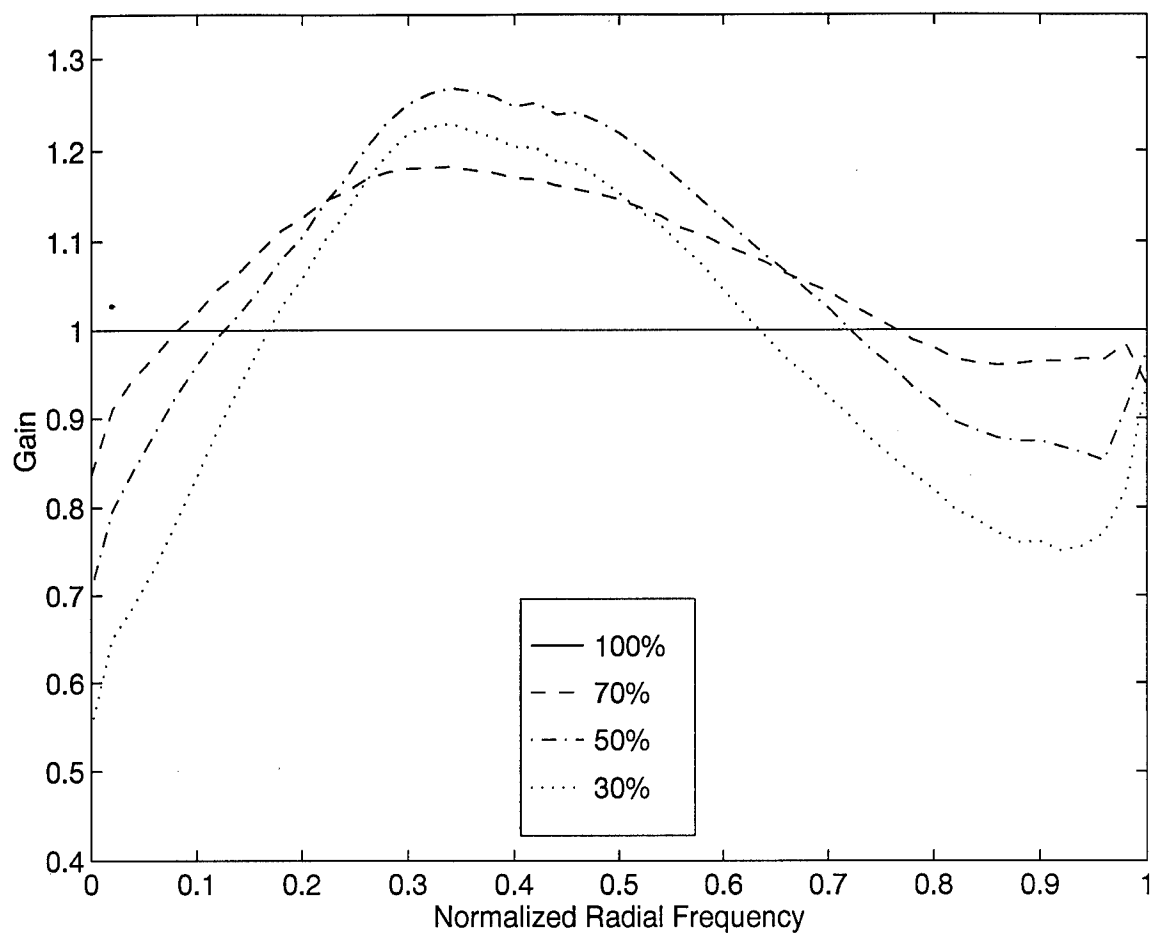
Figure 4.10   Gain Curves Establishing Improved Image Spectrum SNR for Partially Compensated AO, AO Case 2, Point Source. $r_o = 10$ cm, $m_\nu = +2$, $\sigma^2 = 15$ electrons per pixel
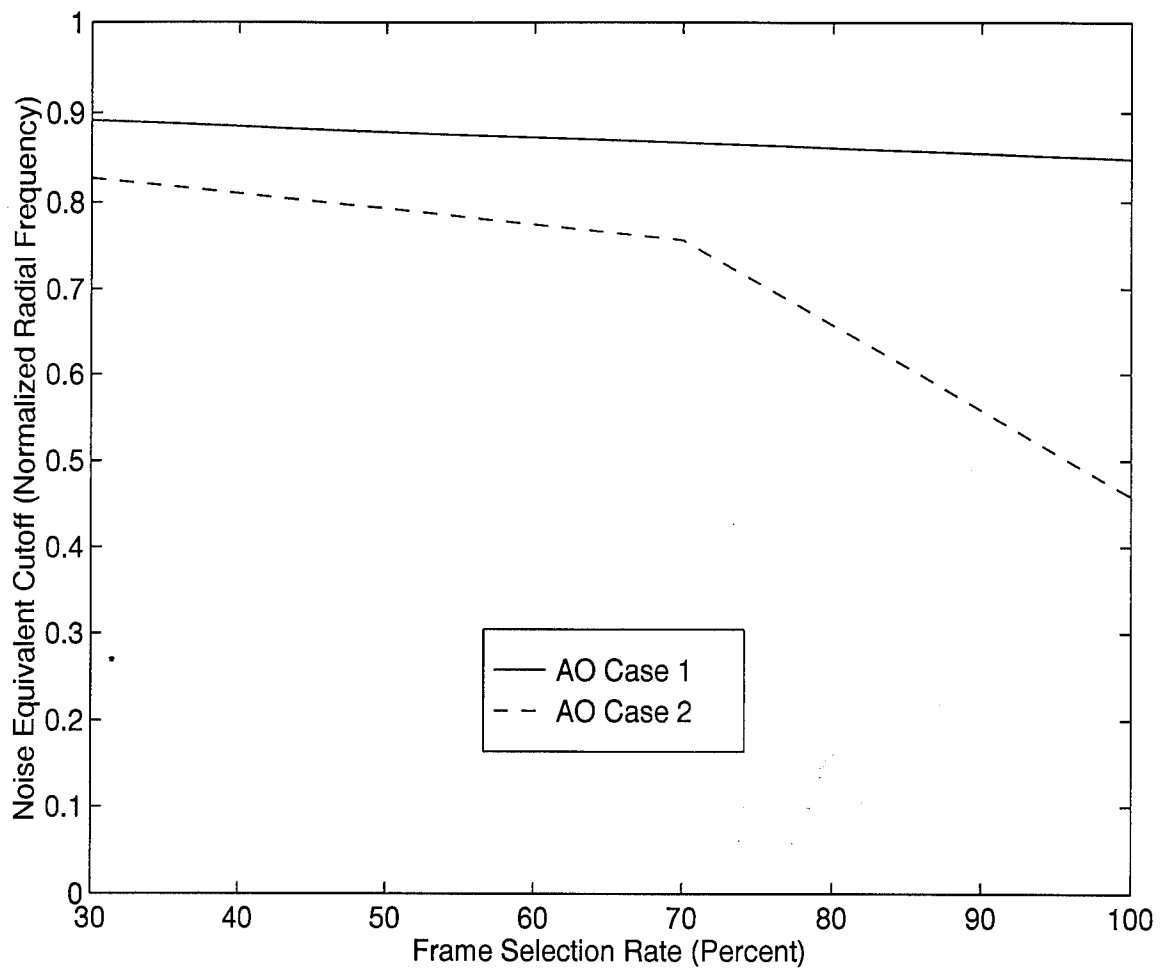
Figure 4.11 η as a Function of FSR for both AO Case 1 and 2, Point Source. $r_o = 10$ cm, $m_\nu = +2$, $\sigma^2 = 15$ electrons per pixel
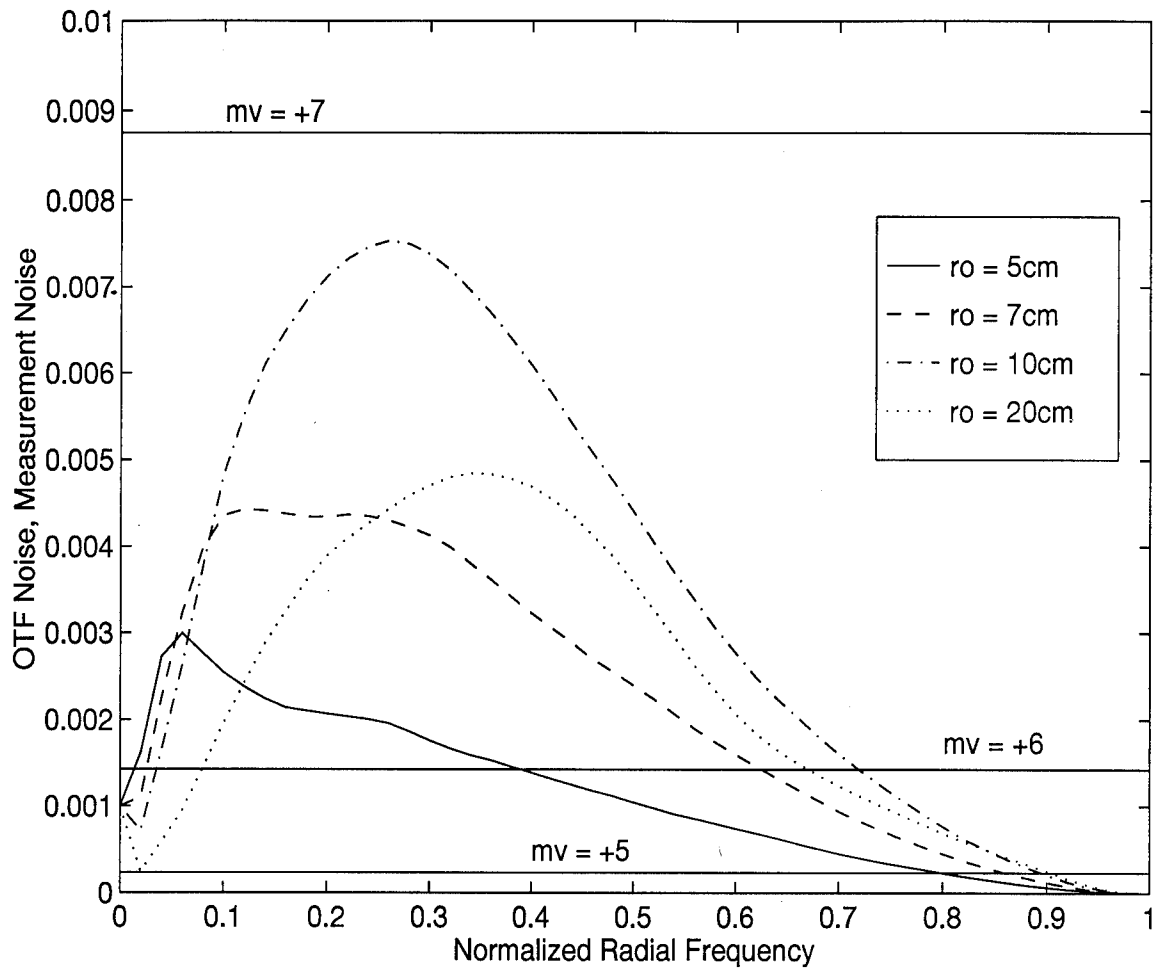
Figure 4.12   Measurement Noise and OTF Noise as a Function of Spatial Frequency
AO Case 2, Point Source. Curves Indicate the Relative Dominance of
Measurement Noise and OTF Noise for Various r_o Values. $\sigma^2 = 15$
electrons per pixel
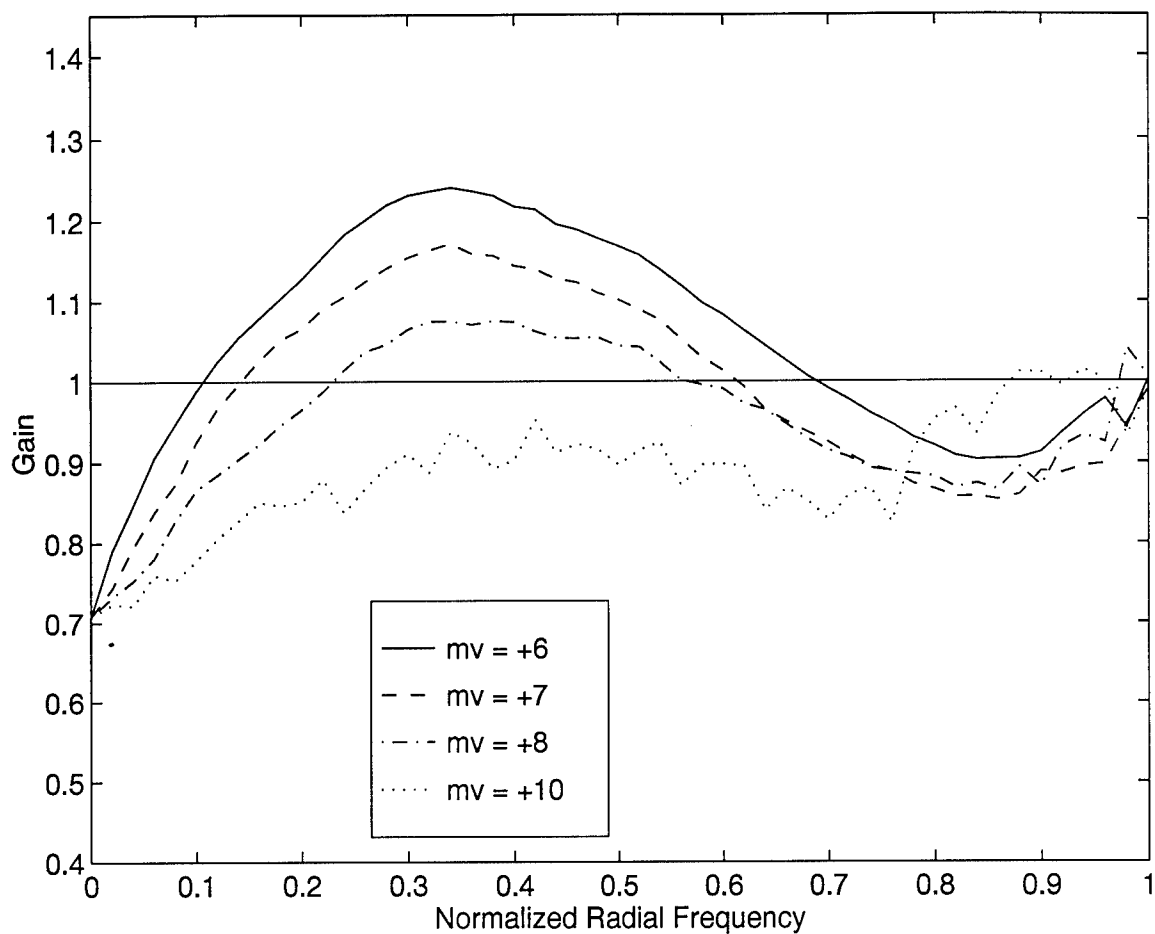
Figure 4.13   Gain Curves Establishing Minimum m_ν for Image Improvement Using Frame Selection, Partially Compensated AO, AO Case 2, Point Source. $r_o = 10$ cm, FSR = 50 percent, $\sigma^2 = 15$ electrons per pixel. Minimum m_ν for frame selection = +7
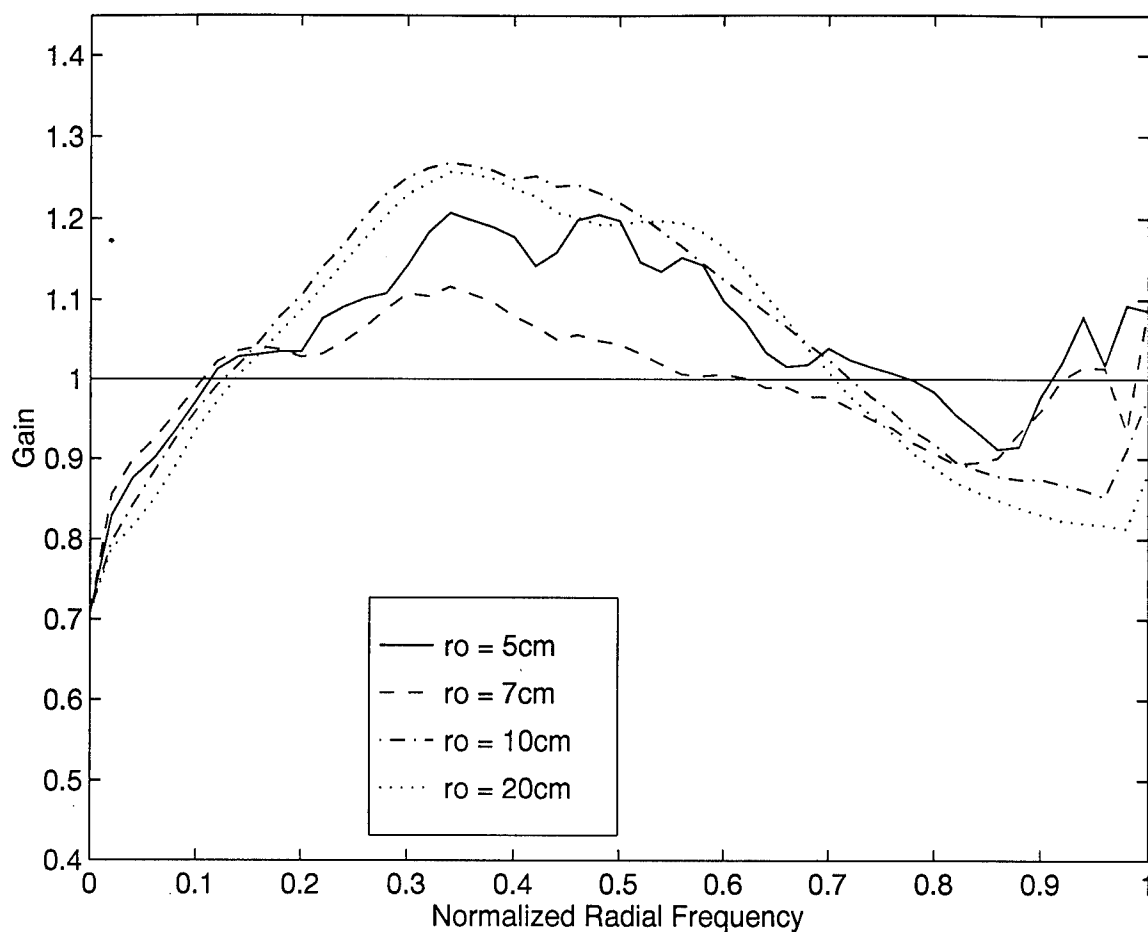
Figure 4.14   Gain as a Function of Spatial Frequency for $r_o = 5, 7, 10, 20$ cm, AO
Case 2, Point Source. Gain Curves Indicate Best Frame Selection Per-
formance for $r_o = 10$ cm. $m_\nu = +2$, FSR = 50 percent, $\sigma^2 = 15$
electrons per pixel

4.2.2.3 Satellite Model-Fully Compensated AO. The previous sections dealt exclusively with point source objects. However, the Air Force requires knowledge of frame selection performance limits for extended objects, such as satellites. Recalling Equation 4.2, note that the single frame SNR is a function of the product of the mean OTF and the object spectrum. For a point source, the normalized object frequency spectrum is one, containing all frequencies. This fact sets up the OTF as the dominant term in the product. In the case of the satellite, the object spectrum falls off much faster than the OTF, which means that the object spectrum becomes the dominant term in determining image spectrum SNR. It is this dependence on the object spectrum that forces a separate study of frame selection for the satellite model.

Figure 4.15 depicts a typical set of SNR gain curves as a function of spatial frequency for the 70, 50, and 30 percent FSRs where $m_{\nu} = +2$ and $r_o = 10$ centimeters. At the 70 percent selection rate, a gain in SNR occurs over just less than 60 percent of the diffraction limited frequency range. The peak gain occurs at 20 percent of the diffraction limit and represents just over a 15 percent gain in SNR. The 70 percent FSR case yields a 15 percent loss at DC and as much as an 8 percent loss at high spatial frequencies. Lower FSRs produce greater losses at low and high frequencies. As with the point source, this degradation in SNR performance for lower FSRs is due to an insufficient number of frames in the subset to adequately reduce photon noise through averaging. In general, the satellite model provides less SNR gain than the point source for identical independent parameters. This is due to the SNR limitations associated with the satellite model object spectrum noted above.

Figure 4.16 illustrates the dramatic difference in noise plots between the point source and satellite model. First, the peaks of the OTF noise curves are an order of magnitude less for the satellite model than for the point source indicating a much higher minimum object brightness to avoid the measurement noise limited condition. In fact, this theoretical plot predicts a minimum m_{ν} of approximately +3 to +4 for

this satellite model. Next, it is important to note the nature of these OTF noise curves. As expected, the satellite model object spectrum clearly dominates the OTF noise quantity, which restricts the curves to low spatial frequencies. This dominance tends to shift the peak SNR gains to lower spatial frequencies.

The simulation validates these predictions in Figures 4.17 through 4.19. Figure 4.17 provides clear proof that the frame selection technique requires a minimum visual magnitude of approximately $m_\nu = +4$ for this scenario. Notice in Figure 4.18 that $r_o = 7$ centimeters provides the largest SNR gain for this satellite model. It is important to note that imaging different extended objects may result in a variety of results as different object spectrums alter the balance between measurement noise and OTF noise. Finally, Figure 4.19 indicates that this satellite model needs a minimum $r_o = 4$ centimeters to perform beneficial frame selection. In addition, note that the net SNR gain across the normalized frequency band is marginal for exceptional seeing conditions ($r_o = 20$ and 25 centimeters). This performance is slightly worse than that seen for point source objects.
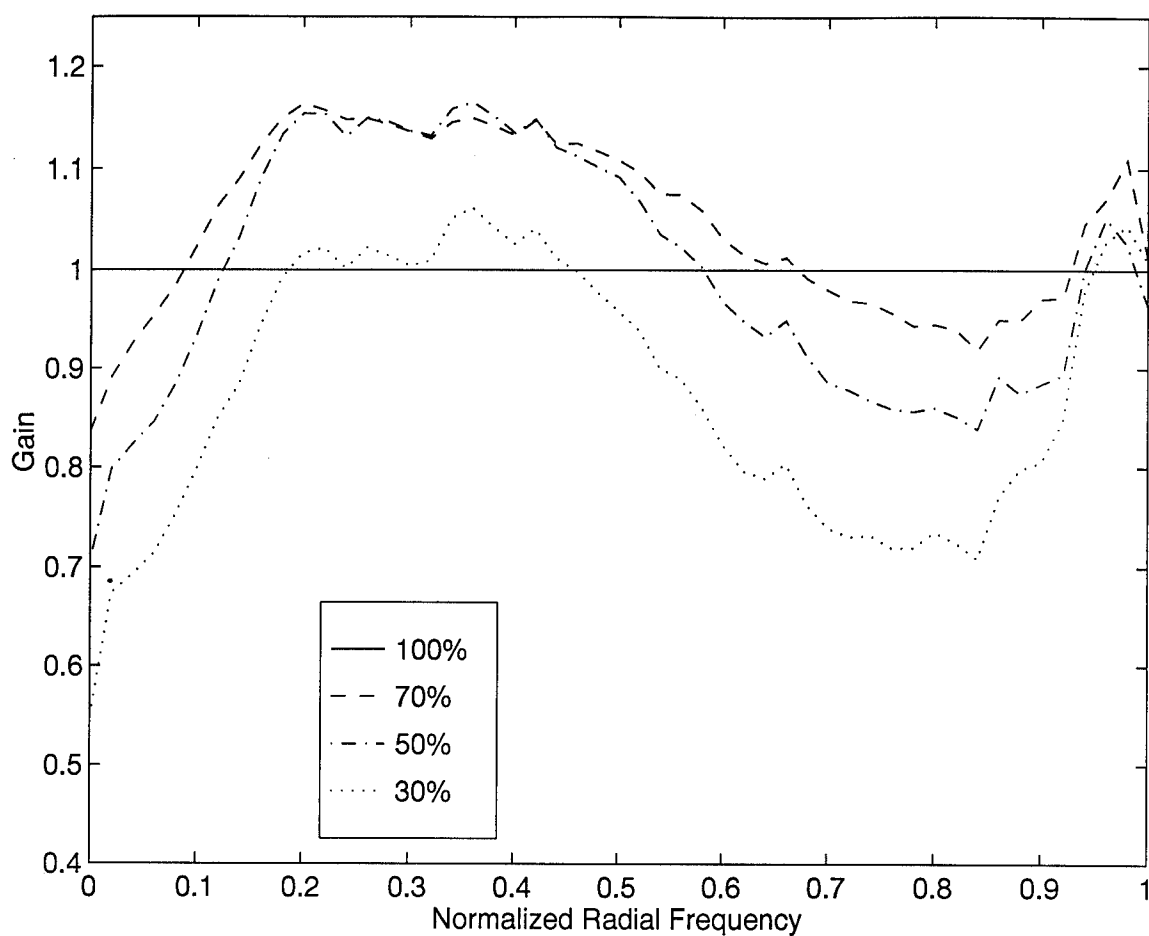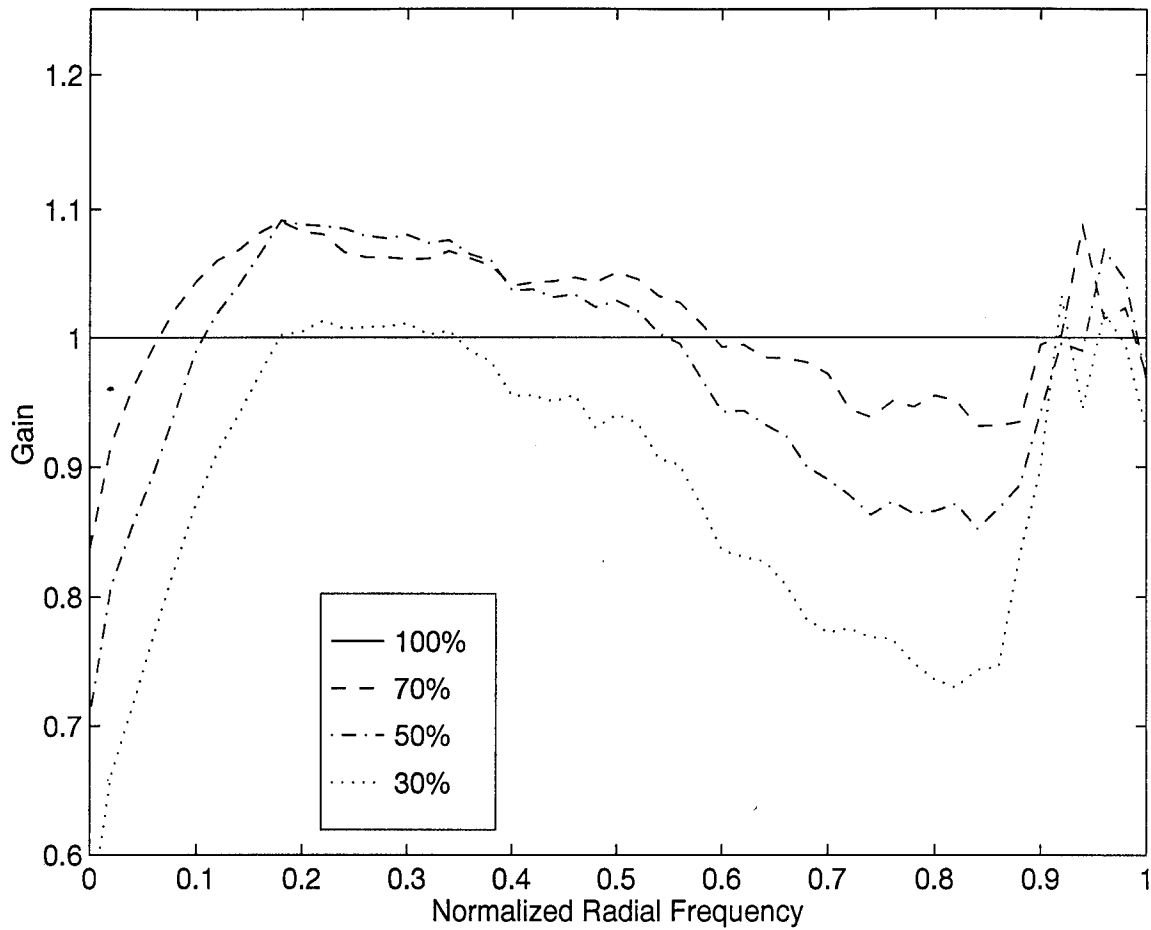
Figure 4.15   Gain Curves Establishing Improved Image Spectrum SNR for Fully Compensated AO, AO Case 1, Satellite Model. $r_o = 10$ cm, $m_\nu = +2$, $\sigma^2 = 15$ electrons per pixel
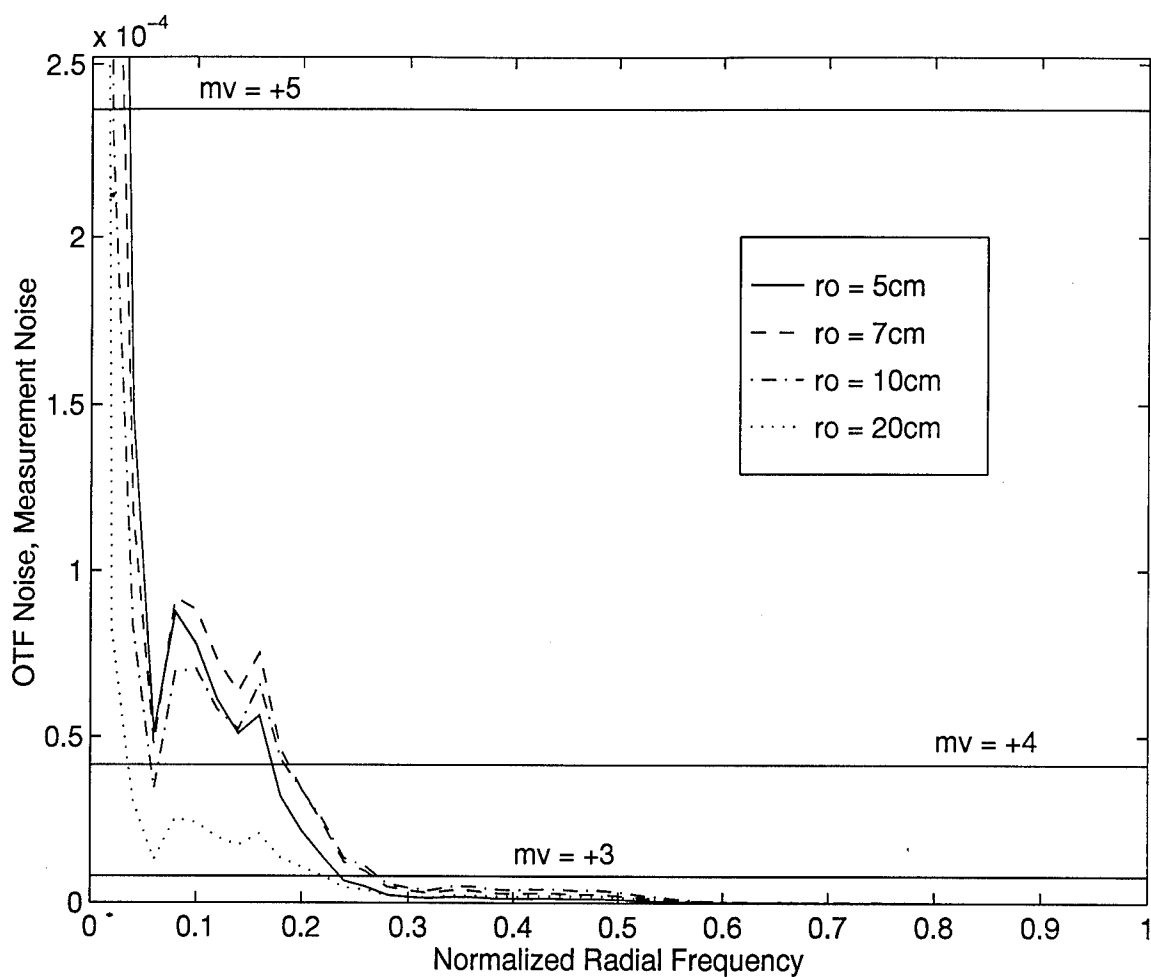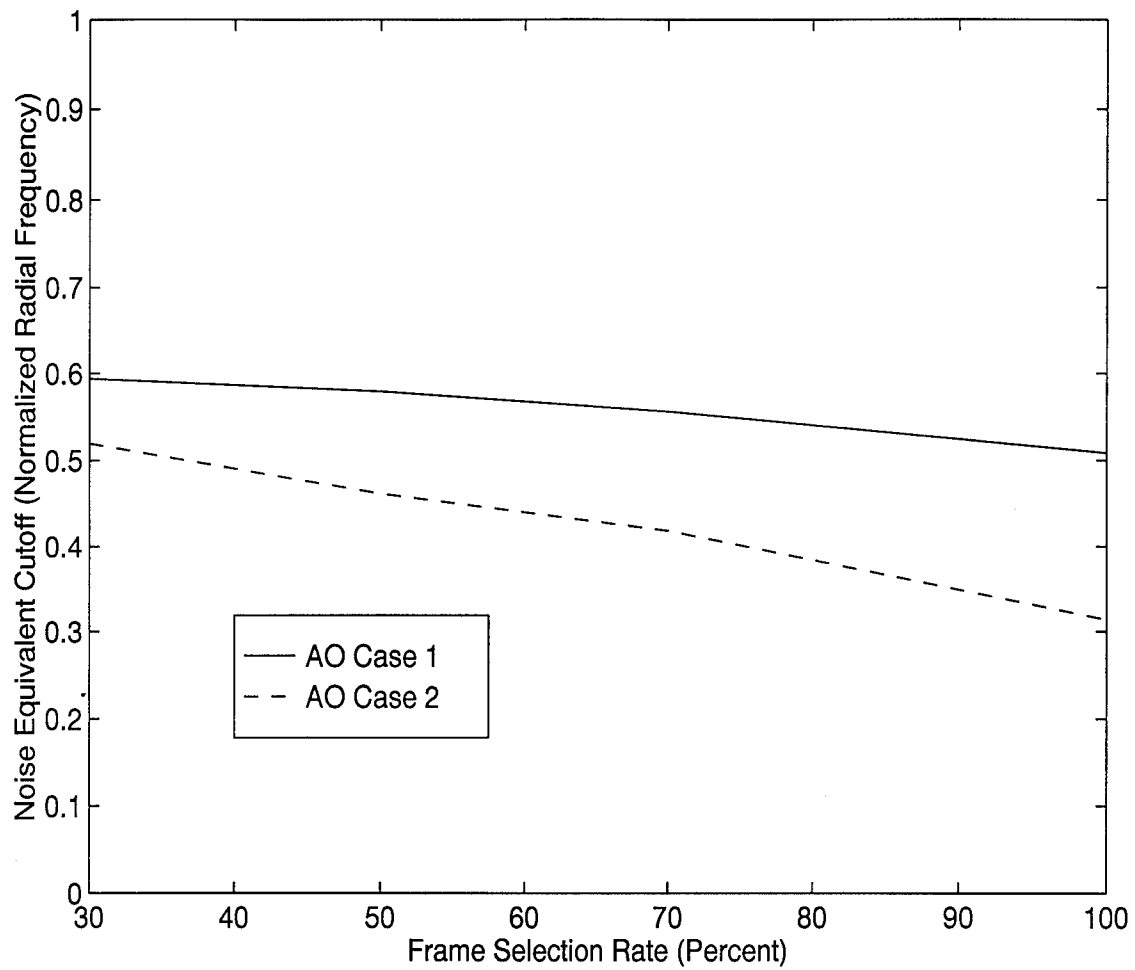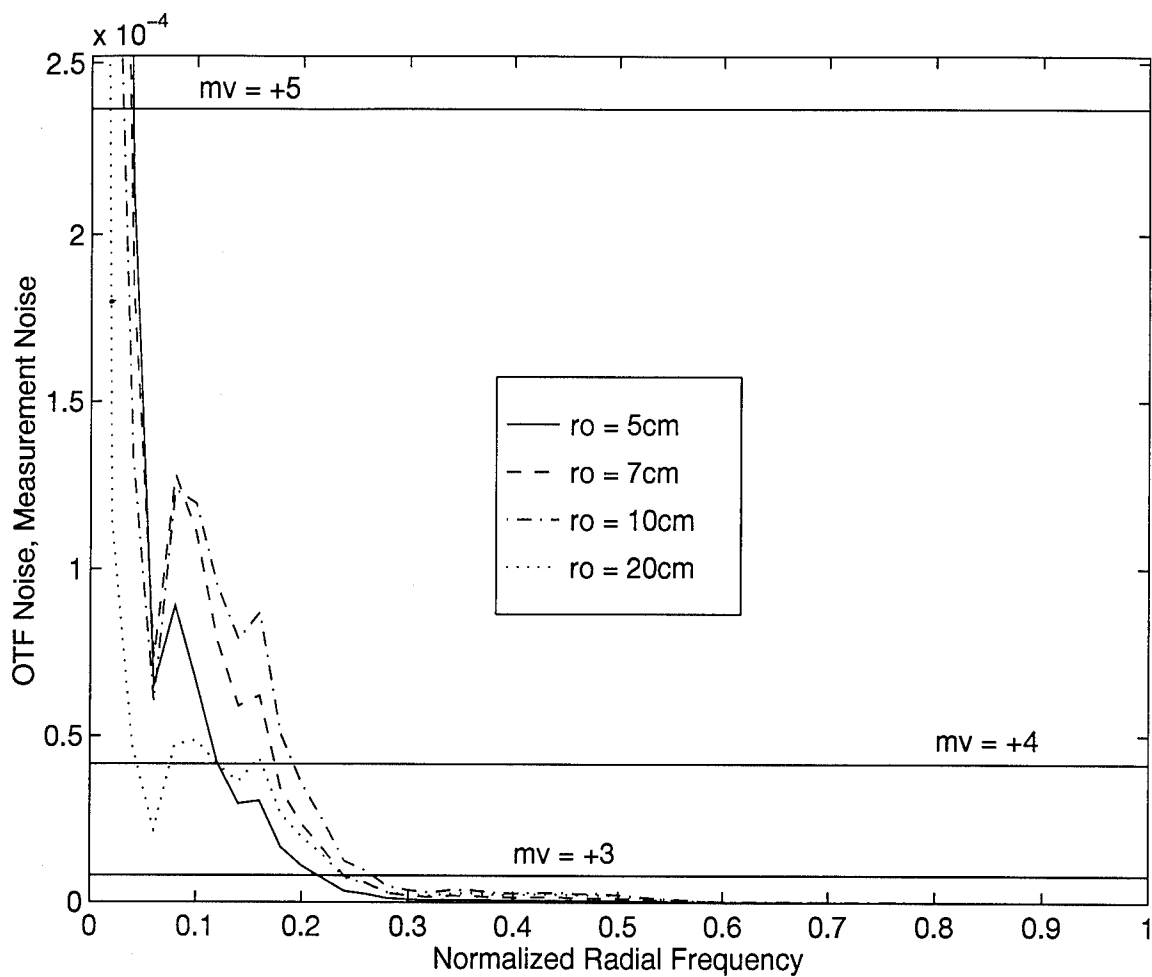
Figure 4.16   Measurement Noise and OTF Noise as a Function of Spatial Frequency AO Case 1, Satellite Model (Scaled View). Curves Indicate the Relative Dominance of Measurement Noise and OTF Noise for Various r_o Values. $\sigma^2 = 15$ electrons per pixel
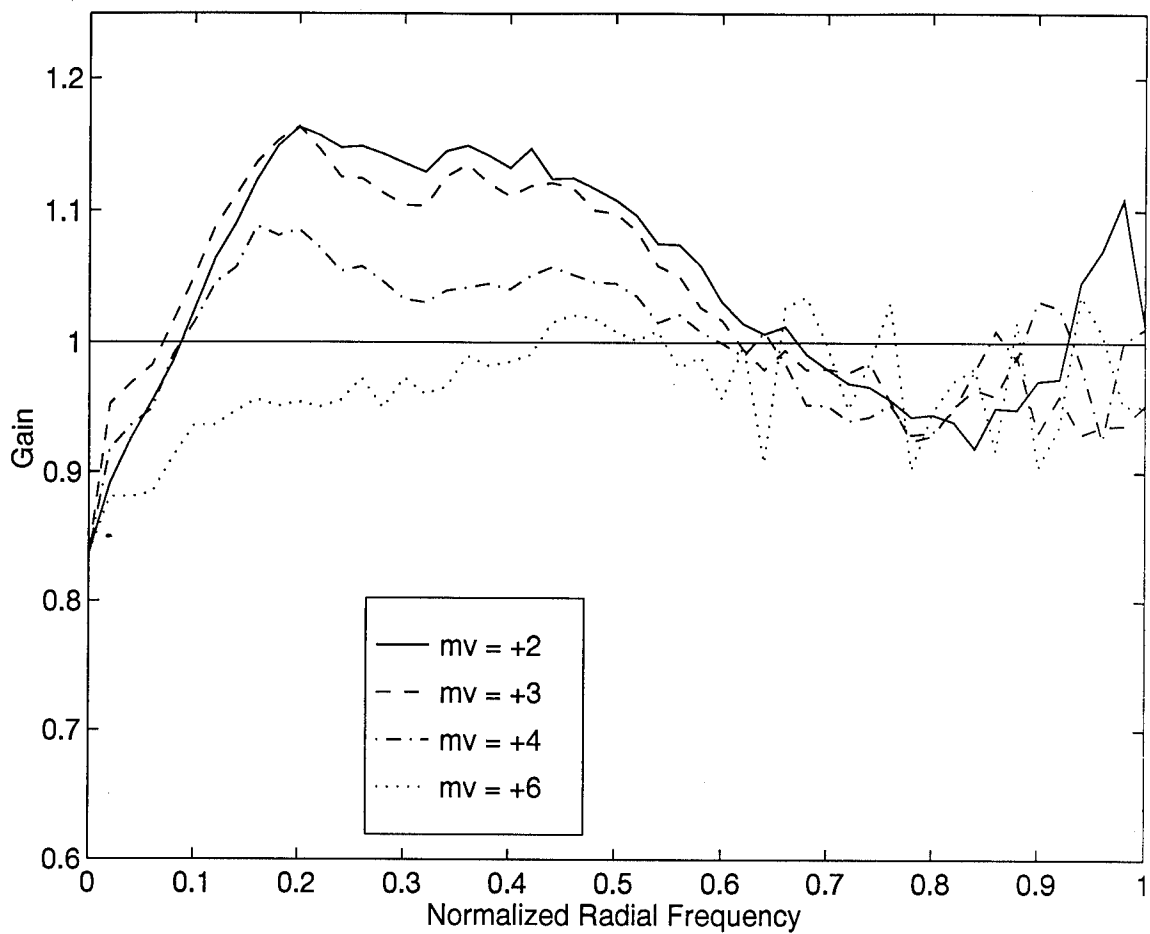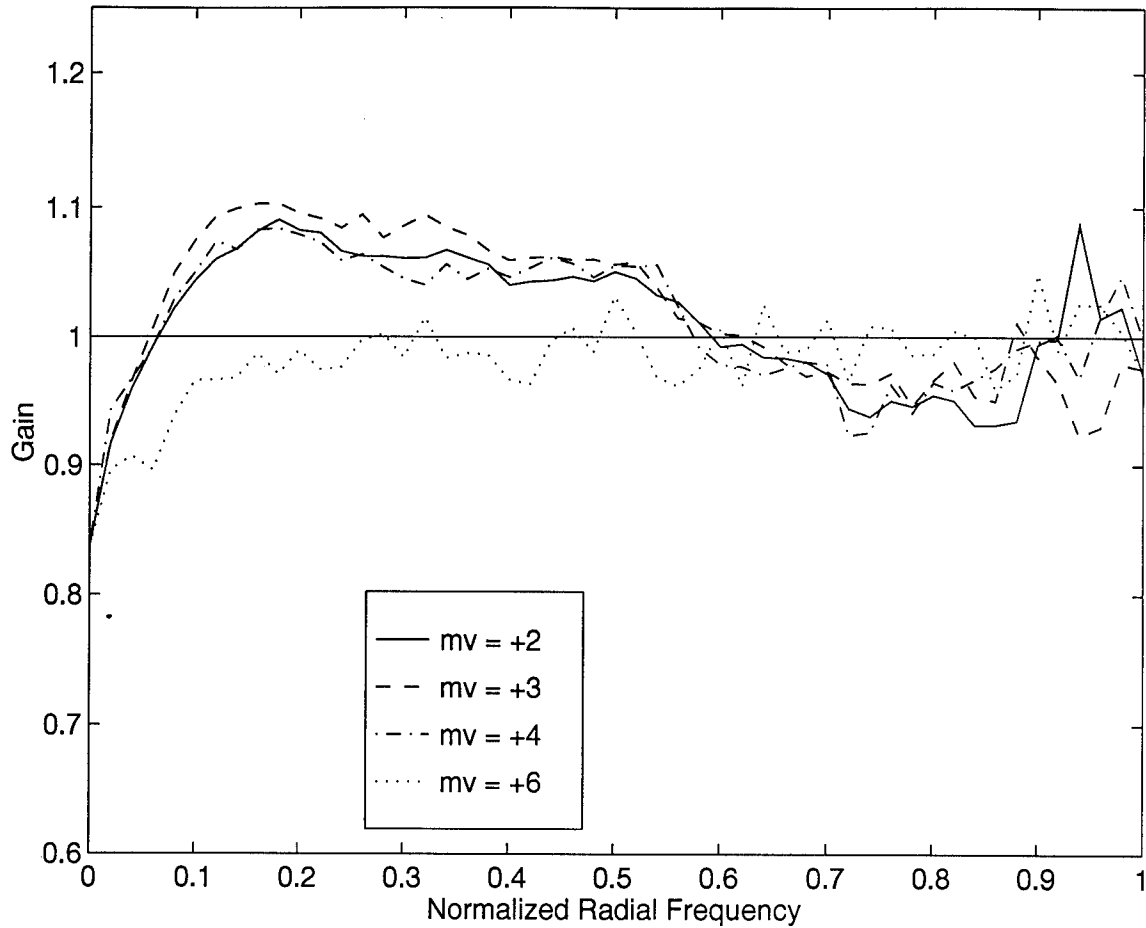
Figure 4.17   Gain Curves Establishing Minimum m_ν for Image Improvement Using
Frame Selection, Fully Compensated AO, AO Case 1, Satellite Model.
$r_o = 10$ cm, FSR = 70 percent, $\sigma^2 = 15$ electrons per pixel. Minimum
m_ν for frame selection = +4
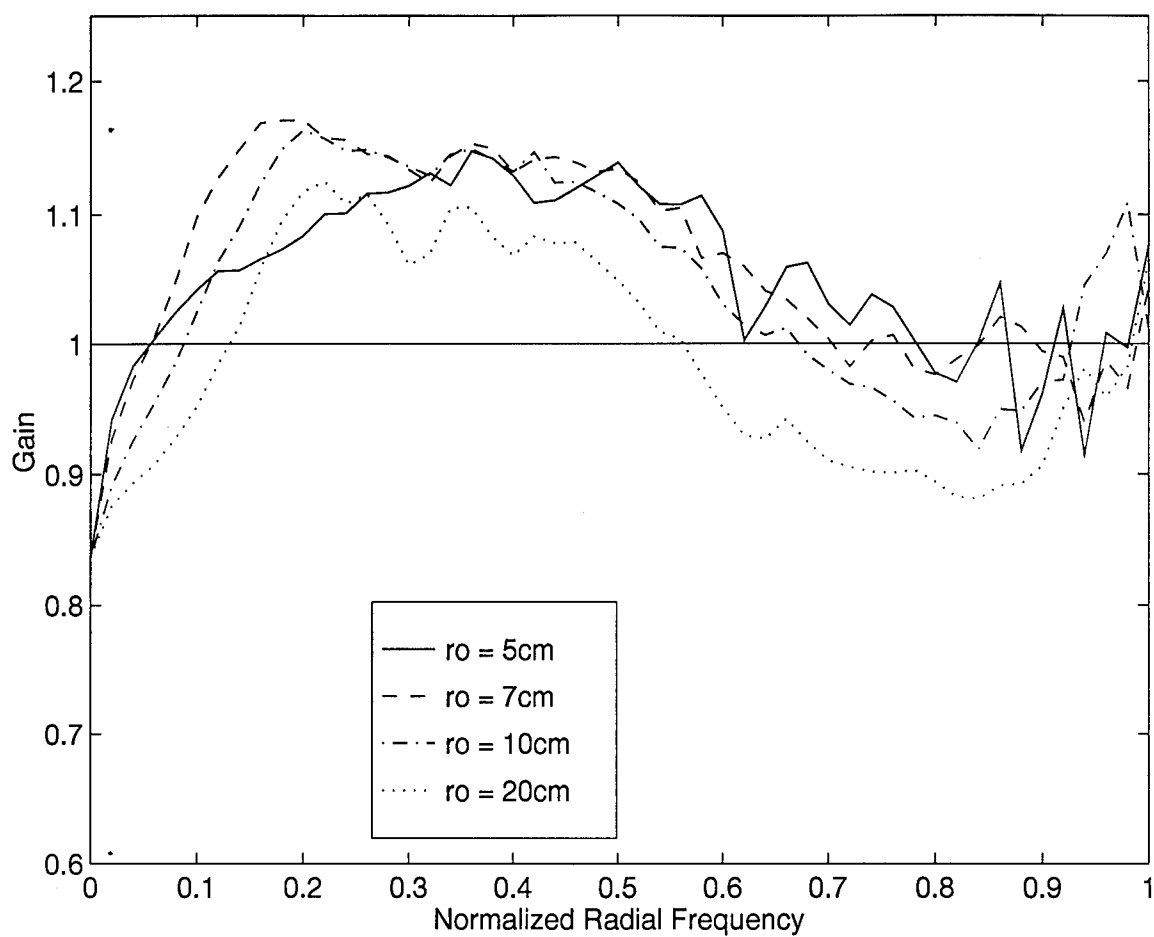
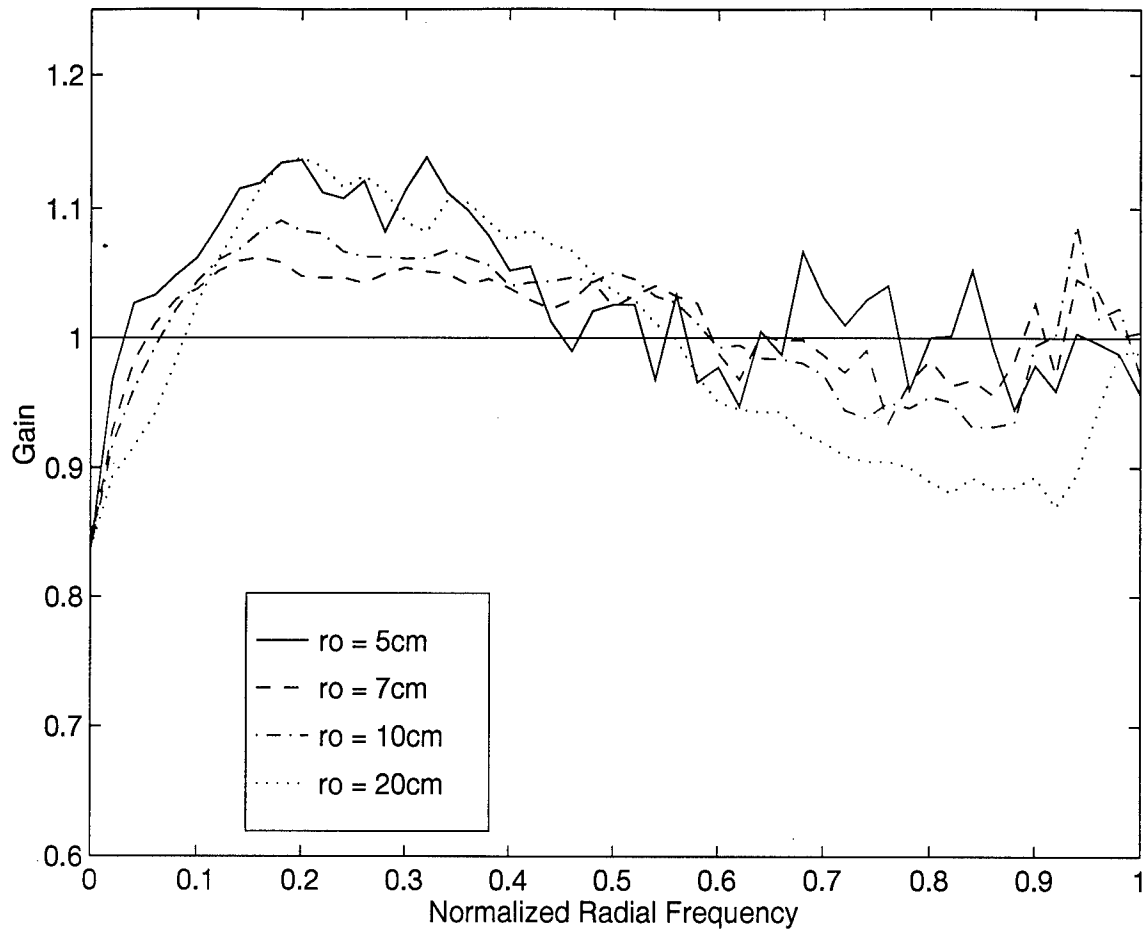Figure 4.18   Gain as a Function of Spatial Frequency for $r_o = 5, 7, 10, 20$ cm, AO Case 1, Satellite Model. Gain Curves Indicate Best Frame Selection Performance for $r_o = 7$ cm. $m_\nu = +2$, FSR = 70 percent, $\sigma^2 = 15$ electrons per pixel
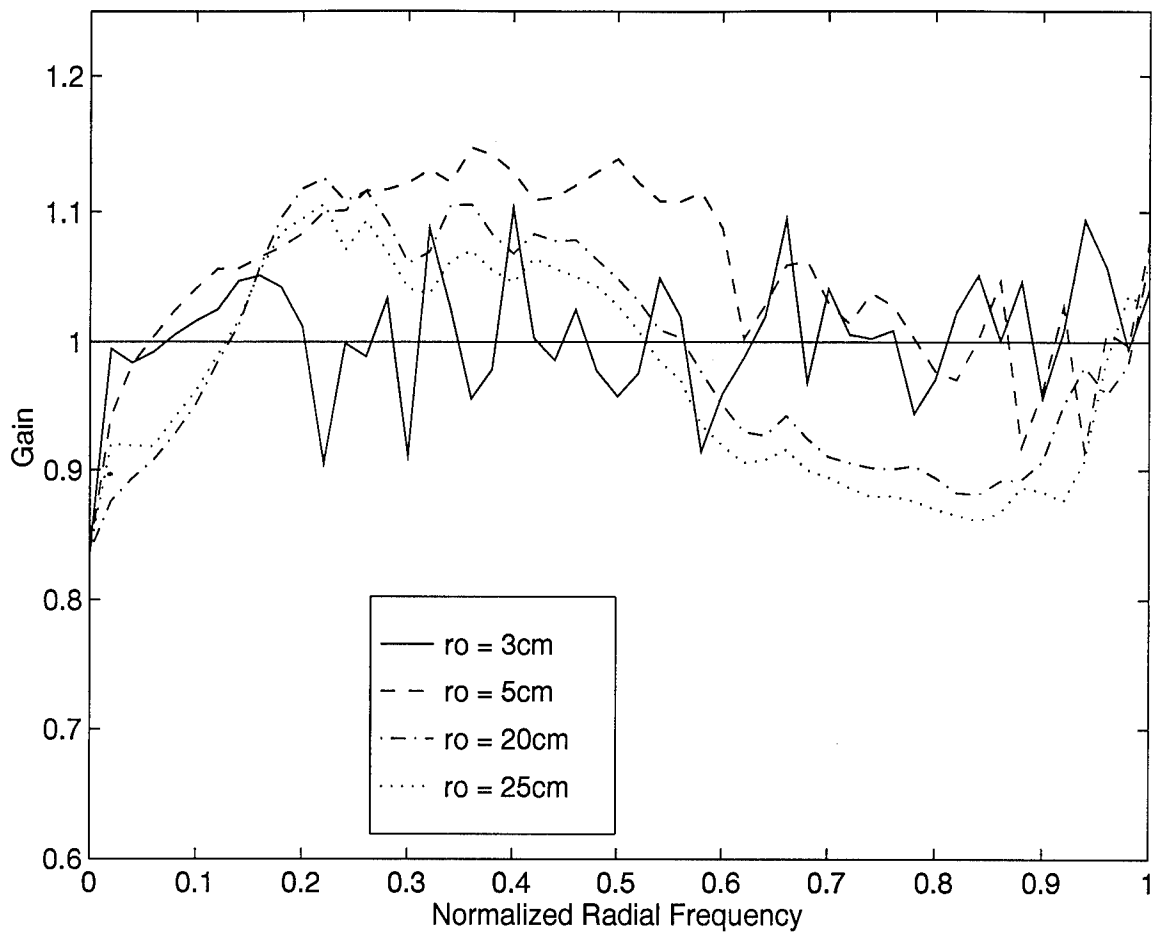
Figure 4.19   Gain as a Function of Spatial Frequency for $r_o = 3, 5, 20, 25$ cm, AO
Case 1, Satellite Model. Gain Curves Establish Bounds on r_o for Frame
Selection. $m_\nu = +2$, FSR = 70 percent, $\sigma^2 = 15$ electrons per pixel,
Maximum $r_o = 20 - 25$ cm, Minimum $r_o = 4$ cm

4.2.2.4 Satellite Model-Partially Compensated AO. This last case investigates frame selection performance limits associated with the AO case 2 system imaging the satellite object. Figure 4.20 depicts a set of SNR gain curves as a function of spatial frequency for the 70, 50, and 30 percent FSRs where $m_\nu = +2$ and $r_o = 10$ centimeters. Once again, gain is greatly reduced as fewer actuators are used. The best overall gain occurs using the 70 percent selection rate. With the 70 percent selection rate, the peak gain occurs at 18 percent of the diffraction limit and represents less than a 10 percent gain in SNR. This gain is 8 percent less than that of the AO case 1 system. As expected, the net result of employing fewer actuators is a reduction in SNR gain for a partially compensated value of r_o. In this case, the residual phase aberration from the AO system severely degrades enough frames to prevent frame selection from boosting SNR to the level of the fully compensated case shown in the previous section. In other words, if most of the frames in a data set are poor, what is there to throw away?

Figure 4.21 shows the noise equivalent cutoff frequency, η, for both AO case 1 and 2. In contrast to the point source, frame selection has only a slightly more pronounced effect on η for AO case 2 due to the limited high spatial frequency content of the satellite model object spectrum. As in the previous section, Figure 4.22 can be used to make theoretical predictions regarding performance of the frame selection technique for the m_ν and r_o parameters. A minimum m_ν of approximately +4 is necessary to avoid the measurement noise limited condition. In this case, the theoretical data also predicts the widest frequency band of SNR gain greater than one when $r_o = 10$ centimeters.

Figure 4.23 shows that the $m_\nu = +4$ curve provides the minimum visual magnitude for SNR gain. This limit is identical to that seen for AO case 1. Notice in Figure 4.24 that the results are inconclusive for this partially compensated imaging system and satellite model. No conclusions can be made regarding the r_o parameter from this data.

Figure 4.20   Gain Curves Establishing Improved Image Spectrum SNR for Partially Compensated AO, AO Case 2, Satellite Model. $r_o = 10$ cm, $m_\nu = +2$, $\sigma^2 = 15$ electrons per pixel

Figure 4.21 η as a Function of FSR for both AO Case 1 and 2, Satellite Model. $r_o = 10$ cm, $m_\nu = +2$, $\sigma^2 = 15$ electrons per pixel

Figure 4.22   Measurement Noise and OTF Noise as a Function of Spatial Frequency AO Case 2, Satellite Model (Scaled View). Curves Indicate the Relative Dominance of Measurement Noise and OTF Noise for Various r_o Values. $\sigma^2 = 15$ electrons per pixel

Figure 4.23   Gain Curves Establishing Minimum m_ν for Image Improvement Using Frame Selection, Partially Compensated AO, AO Case 2, Satellite Model. $r_o = 10$ cm, FSR = 70 percent, $\sigma^2 = 15$ electrons per pixel. Minimum m_ν for frame selection = +4

Figure 4.24 Gain as a Function of Spatial Frequency for $r_o = 5, 7, 10, 20$ cm, AO Case 2, Satellite Model. $m_\nu = +2$, FSR = 70 percent, $\sigma^2 = 15$ electrons per pixel

4.2.3 Conclusions. The results of this section are significant because they establish general performance limits for frame selection as a function of the seeing conditions, r_o, and object brightness, m_ν. Point source objects must be brighter than visual magnitude +7 to +8 for frame selection to provide significant SNR gain. The satellite model required visual magnitude greater than +4. These limits were largely repeatable for both full and partial AO compensation cases. This minimum brightness restriction is due to the fundamental limit imposed by photon noise and CCD camera noise as shown by theoretical plots indicating the relative dominance of measurement noise and OTF noise effects. CCD camera noise has a significant impact on the performance limits associated with frame selection processing. However, when bright objects are imaged, this noise effect is minimal. Finally, frame selection provides the largest SNR gain for image data sets collected under average seeing conditions.

4.3 Experiment Two

Experiment One established performance limits on the frame selection technique as a function of the independent parameters. These limits are based on the image spectrum SNR as the primary performance metric. However, the Air Force desires visually improved images of extended objects, typically satellites. Therefore, it is critical to understand the effect of frame selection on current operational image collection techniques.

Operational imagery collected by AMOS is processed using an image reconstruction method to overcome randomness in the data then sharpened using deconvolution [31]. As discussed in Chapter Two, deconvolution techniques rely on an accurate estimate of the effective average PSF, usually provided by imaging a bright reference star. In order for deconvolution to achieve optimal performance, the effective average PSF available from the reference star must be similar to the effective average PSF associated with the satellite. As noted in Chapter Three, the frame selection rule is nonlinear. Therefore, its effect on the PSF cannot be readily predicted. The question then becomes, "Will the effective average PSF of a point source be similar to the effective average PSF of an extended object after application of the frame selection rule?"

The purpose of this experiment is to investigate the effect of frame selection on the effective average PSF as a function of the independent parameters and establish the similarity of PSFs for point source and extended objects. First, it is important to examine the PSF as it relates to the parameters r_o, m_ν, and FSR.

4.3.1 PSF versus Independent Parameters. The primary goal of this section is to confirm that frame selection does not significantly alter known characteristics of the PSF for standard linear reconstruction. When all frames in the data set are used to form the composite image, better seeing conditions result in a narrowing of the PSF and less image blurring. Figures 4.25 and 4.26 confirm this trend when

frame selection is applied to a point source and satellite, respectively. As noted by Stoudt [32], lowering the FSR results in a gradual narrowing of the PSF due to the elimination of the worst manifestations of the atmospheric turbulence. This fact is reaffirmed in Figures 4.27 and 4.28. Finally, the PSF is not changed for various levels of object brightness as depicted in Figures 4.29 and 4.30.

4.3.2 PSF Comparison: AO Case 1. As noted above, frame selection appears to affect the effective average PSF in an expected way as a function of r_o, FSR, and m_ν. This section establishes the high degree of similarity between point source and satellite model PSFs for the AO case 1 system. Three example cases are shown in Figures 4.31 through 4.33 where point source and satellite model average PSFs are plotted for poor, average, and above average seeing conditions. The FSR is fixed at 70 percent for all cases to reflect the optimum FSR for this satellite model. The key observation is that the PSFs are virtually identical. Figure 4.31 shows the most difference between point source and satellite model PSFs for $r_o = 5$ centimeters. However, this difference is small enough so as to be insignificant in the application of deconvolution.

4.3.3 PSF Comparison: AO Case 2. This section investigates PSF similarity between the point source and satellite model objects for the AO case 2 system. The same three example cases as shown in the previous section are depicted in Figures 4.34 through 4.36. Point source and satellite model average PSFs are plotted for poor, average, and above average seeing conditions. FSR is fixed at 70 percent. As before, the PSFs are nearly identical for all three cases. The average PSFs for the $r_o = 5$ and 10 centimeter cases exhibit widening when compared to AO case 1, but the $r_o = 20$ centimeter plots do not. This observation is due to the fact that the DM actuator spacing is approximately the same as the 20 centimeter r_o value allowing full AO compensation to occur while using the AO case 2 system. When $r_o = 5$ and 10 centimeters, only partial AO compensation occurs.

4.3.4   Conclusions.   The similarity between point source and satellite model effective average PSFs after frame selection is documented in this experiment. This conclusion is significant because it allows the optimal use of deconvolution techniques to sharpen composite images after frame selection processing. In Experiment Three, this important conclusion is applied to simulated binary stars and the satellite model to demonstrate visual improvements in images after deconvolution.
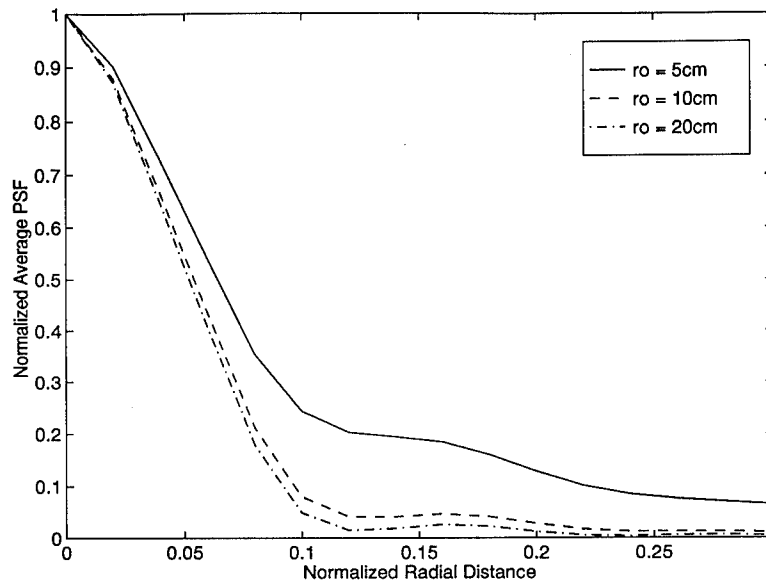
Figure 4.25   PSF as a Function of Radial Distance for Various r_o Values, AO Case 1, Point Source. FSR = 50 percent, $m_\nu = +2$
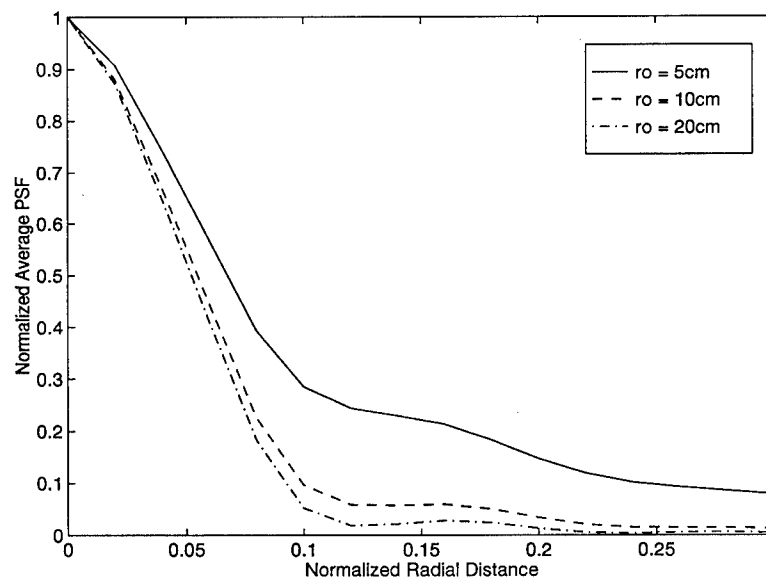
Figure 4.26   PSF as a Function of Radial Distance for Various r_o Values, AO Case 1, Satellite Model. FSR = 70 percent, $m_\nu = +2$
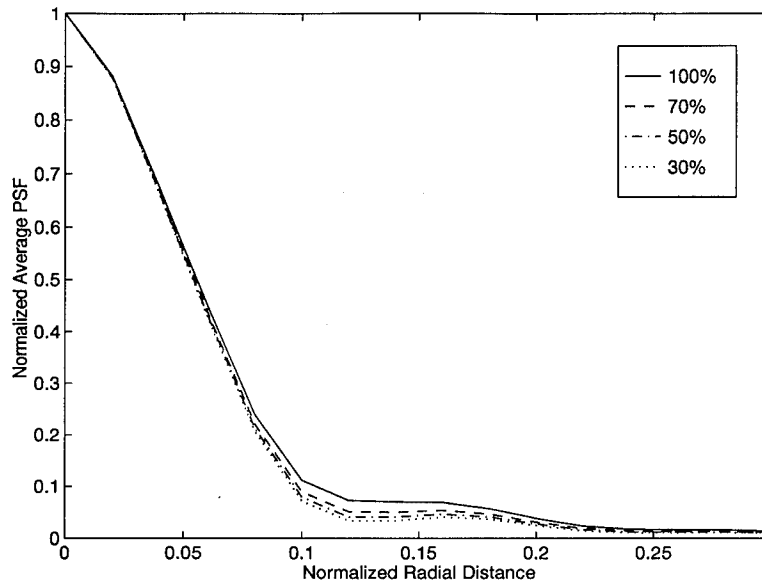
Figure 4.27   PSF as a Function of Radial Distance for FSR $= 100, 70, 50, 30$ percent, AO Case 1, Point Source. $r_o = 10$ cm, $m_\nu = +2$
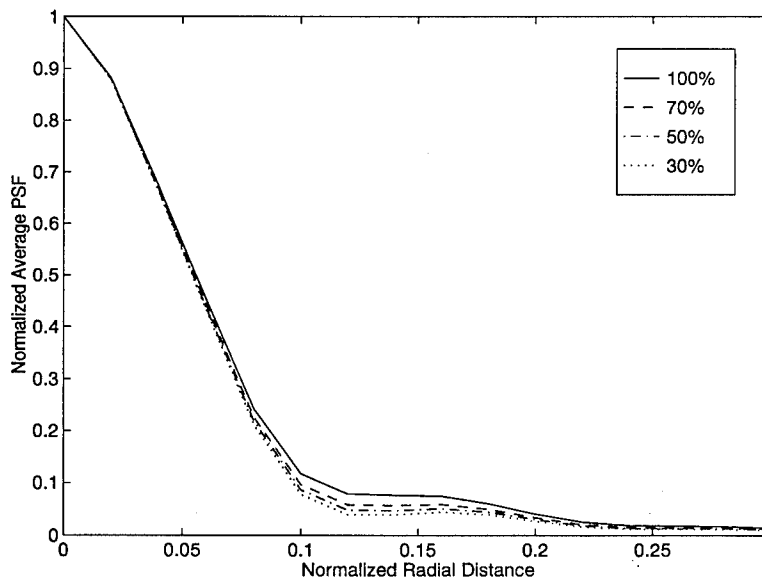
Figure 4.28   PSF as a Function of Radial Distance for FSR $= 100, 70, 50, 30$ percent, AO Case 1, Satellite Model. $r_o = 10$ cm, $m_\nu = +2$
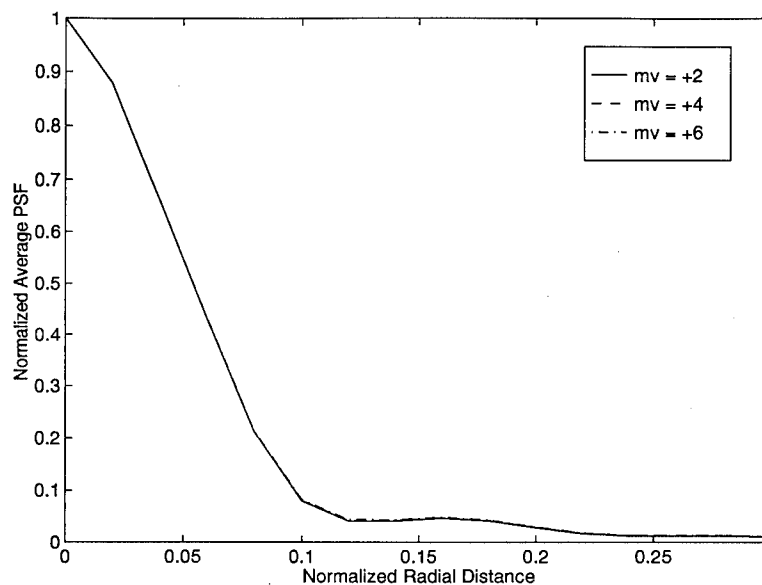
Figure 4.29   PSF as a Function of Radial Distance for Various m_ν Values, AO Case 1, Point Source. $r_o = 10$ cm, FSR = 50 percent
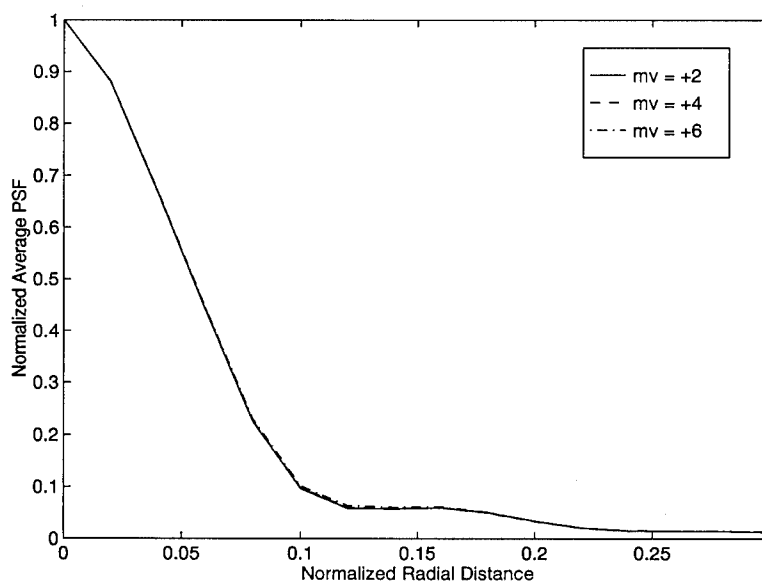
Figure 4.30   PSF as a Function of Radial Distance for Various m_ν Values, AO Case 1, Satellite Model. $r_o = 10$ cm, FSR = 70 percent
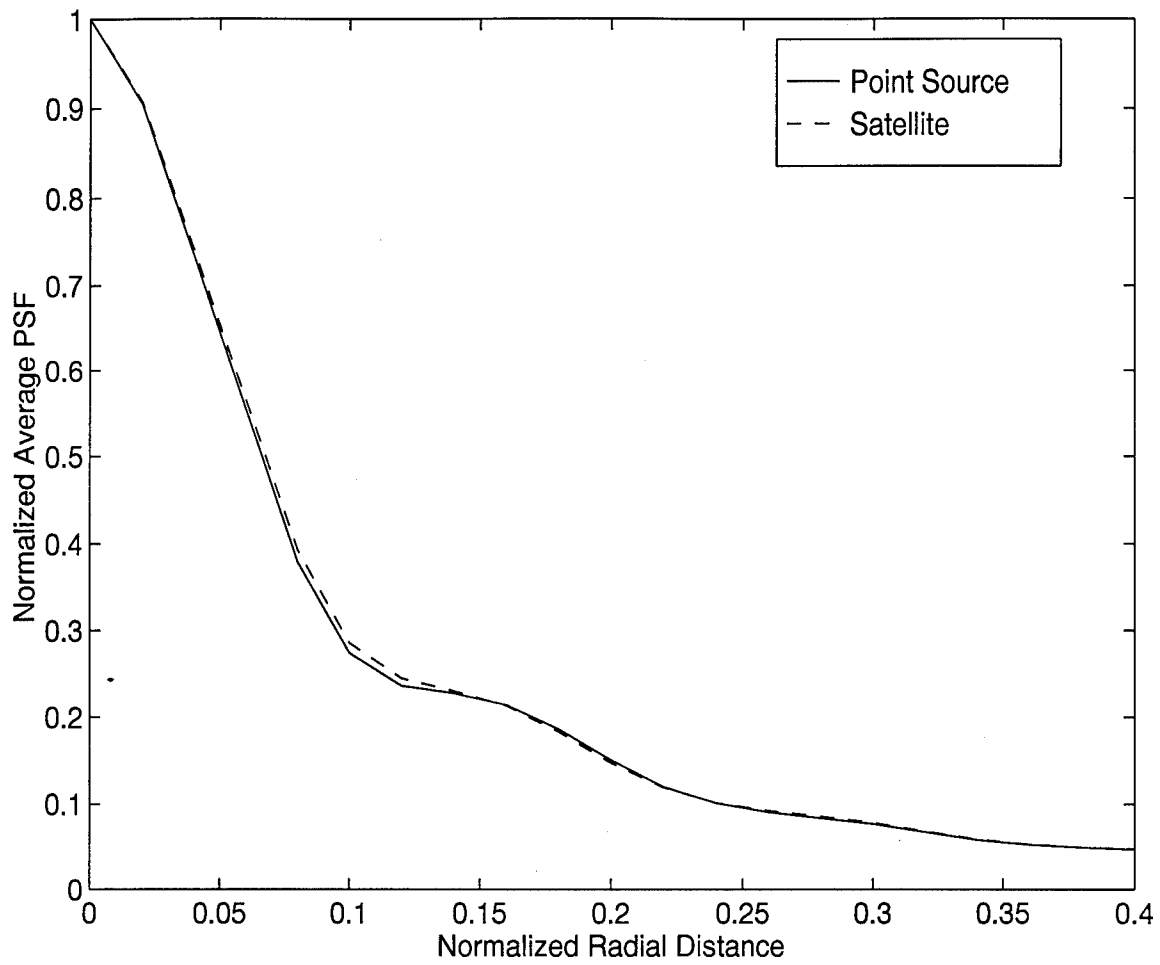
Figure 4.31   PSF as a Function of Radial Distance, AO Case 1. Comparison Plot Showing that Point Source and Satellite Model PSFs are Nearly Identical. $r_o = 5$ cm, $m_\nu = +2$, FSR = 70 percent
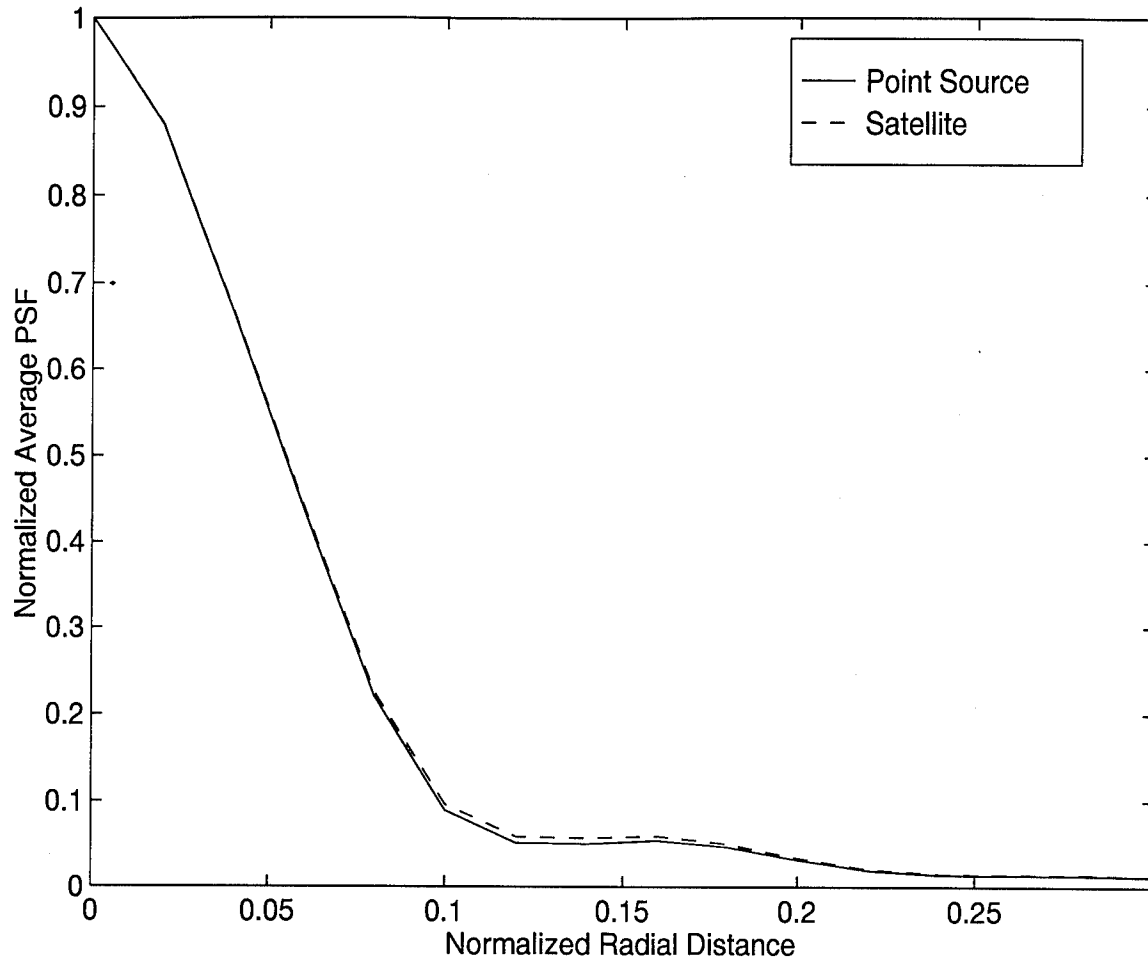
Figure 4.32   PSF as a Function of Radial Distance, AO Case 1. Comparison Plot Showing that Point Source and Satellite Model PSFs are Nearly Identical. $r_o = 10$ cm, $m_\nu = +2$, FSR = 70 percent
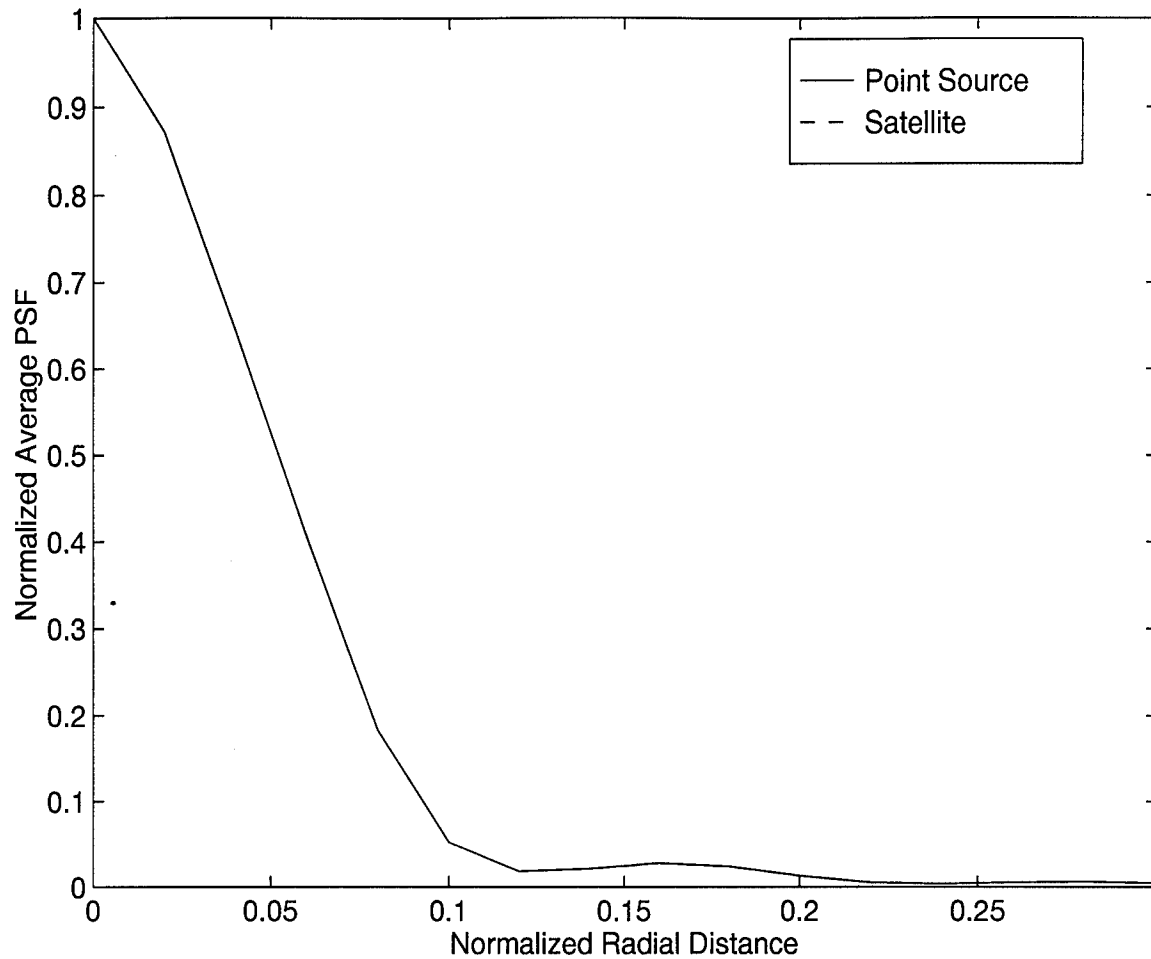
Figure 4.33   PSF as a Function of Radial Distance, AO Case 1. Comparison Plot
Showing that Point Source and Satellite Model PSFs are Identical.
$r_o = 20$ cm, $m_\nu = +2$, FSR = 70 percent
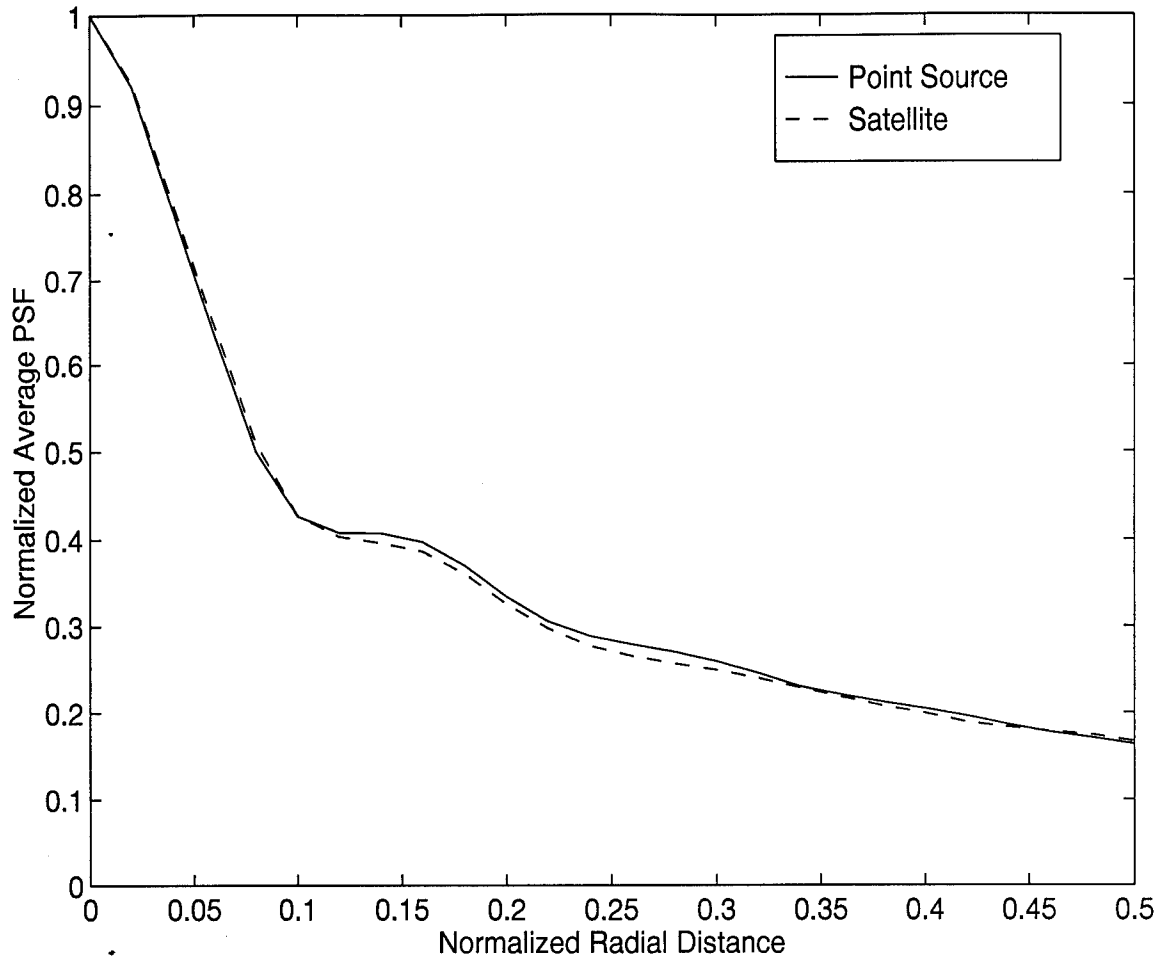
Figure 4.34   PSF as a Function of Radial Distance, AO Case 2. Comparison Plot
Showing that Point Source and Satellite Model PSFs are Nearly Iden-
tical. $r_o = 5$ cm, $m_\nu = +2$, FSR $= 70$ percent
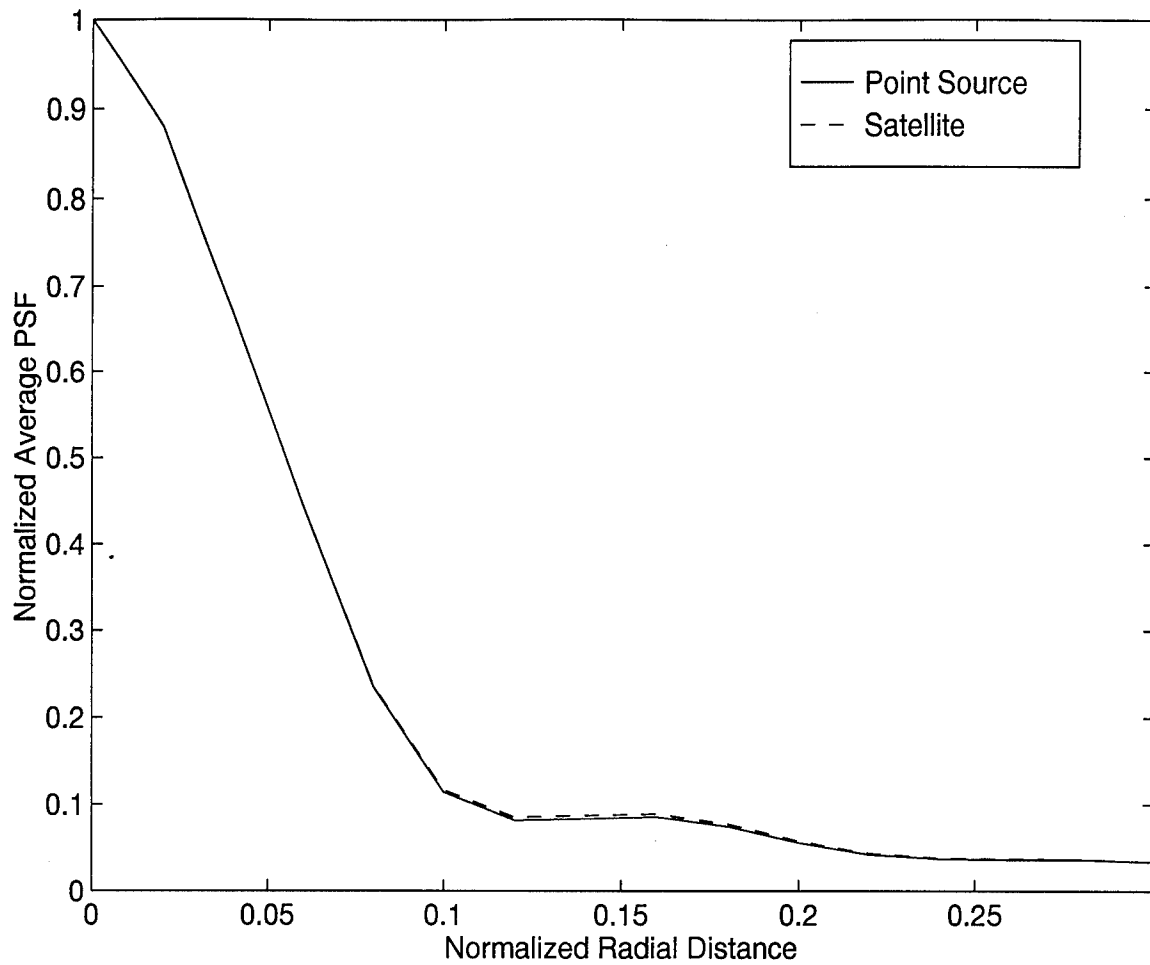
Figure 4.35   PSF as a Function of Radial Distance, AO Case 2. Comparison Plot Showing that Point Source and Satellite Model PSFs are Nearly Identical. $r_o = 10$ cm, $m_\nu = +2$, FSR = 70 percent
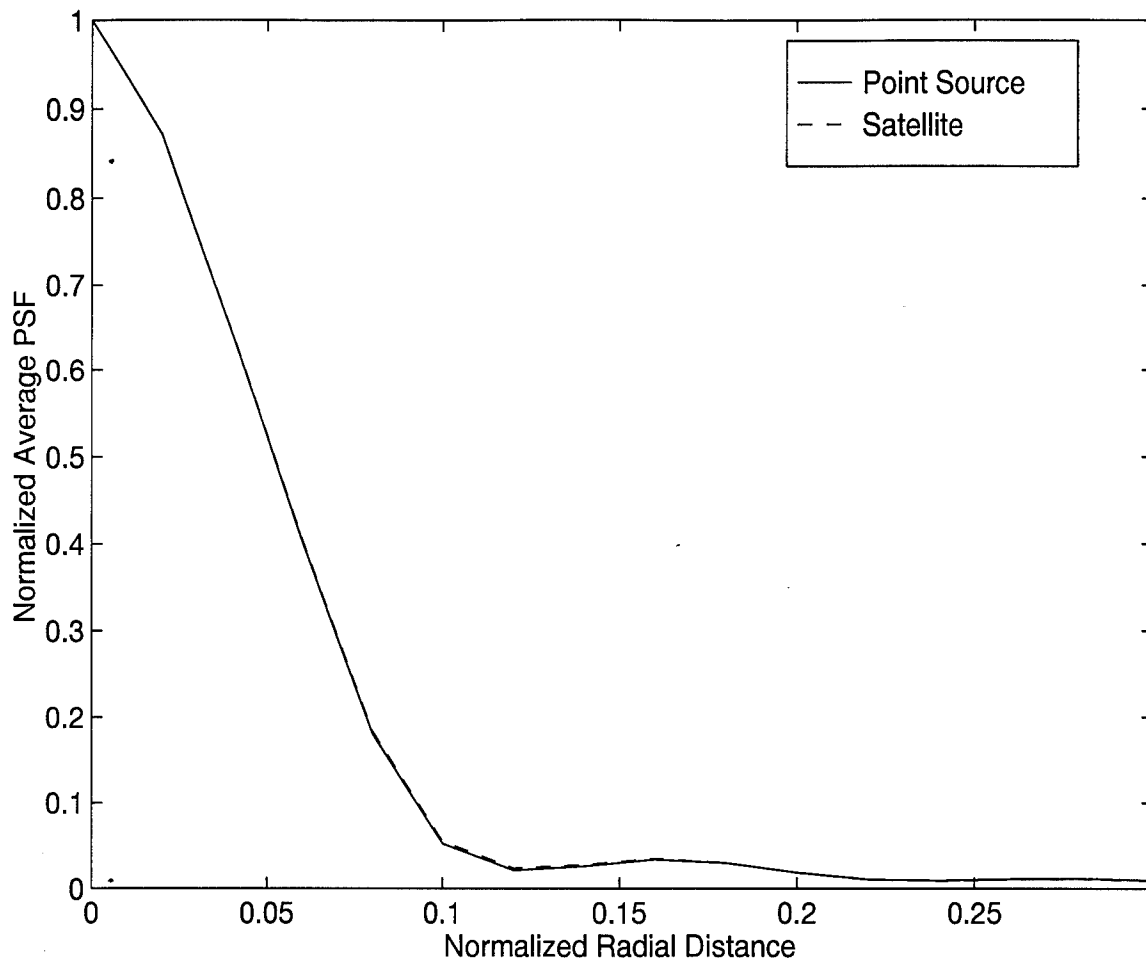
Figure 4.36 PSF as a Function of Radial Distance, AO Case 2. Comparison Plot Showing that Point Source and Satellite Model PSFs are Nearly Identical. $r_o = 20$ cm, $m_\nu = +2$, FSR = 70 percent

4.4 Experiment Three

As concluded in the previous experiment, the effective average PSFs for point source and satellite model objects are virtually identical. This conclusion allows deconvolution techniques to be used on images after frame selection processing without degradation due to an inaccurate PSF estimate. This experiment documents the first attempt to compare deconvolved images with and without frame selection.

The demonstration consists of deconvolving both simulated binary stars and the satellite model. First, SNR gain curves are used to determine the FSR offering the highest gain over the largest spatial frequency band. The pseudo-Weiner filter is then used to deconvolve the FSR = 100 percent (standard linear reconstruction) and optimum FSR cases for comparison. Recall Chapter Two and the following Equation for the pseudo-Weiner filter:

$$\tilde{O}(u,v) = \frac{I(u,v)\tilde{H}^*(u,v)}{|\tilde{H}(u,v)|^2 + \frac{\alpha}{SNR(u,v)}} \tag{4.8}$$

where $\tilde{O}(u,v)$ is the estimated object spectrum, $I(u,v)$ is the measured image spectrum, $\tilde{H}(u,v)$ is the estimated atmosphere-optical system OTF, $SNR(u,v)$ is the image spectrum SNR, α is a user-selected parameter, and $*$ denotes the complex conjugate of a quantity [31]. For the binary star cases, the α parameter was decreased until the primary and secondary stars achieved complete separation. A center slice of the image plane showing primary and secondary star component irradiance and broadening was used as the primary means of comparison before and after frame selection processing. For the satellite case, the α parameter was decreased until the images reached maximum sharpness as determined by subjective visual image observation. Subjective visual image comparison was the final means of determining the highest resolution image.

4.4.1 Simulated Binary Star. The simulated binary star used for this demonstration had a 1 microradian angular separation between primary and secondary components. Two cases were observed as noted in Table 4.1.

Table 4.1   Simulated Binary Star Cases

CASE	r_o (cm)	m_ν PRIMARY	m_ν SECONDARY
Full AO (AO Case 1)	10	+2	+3
Partial AO (AO Case 1)	5	+6	+7

Figure 4.37 shows a three dimensional surface plot of the fully compensated binary star case after averaging all frames in the data set. Note that the adaptive optics and standard linear reconstruction have reduced noise effects to a minimum. Figure 4.38 provides gain curves for FSRs 70, 50, and 30 percent. FSR = 50 percent provides the maximum SNR gain at mid spatial frequencies. Therefore, this FSR is chosen for comparison against the FSR = 100 percent case. Figure 4.39 reveals a center slice plot of the FSR = 100 and 50 percent binary star images before deconvolution. The plots are normalized to the irradiance of the FSR = 50 percent binary star image. Note that the 50 percent image provides an approximate 15 percent increase in irradiance for the primary component and a 5 percent increase in the secondary component. In addition, the 50 percent image is closer to complete separation of the primary and secondary components. Figure 4.40 shows a center slice for the same case after deconvolution with the pseudo-Weiner filter, $\alpha = 0.5$. The 50 percent image exhibits slightly more irradiance in both primary and secondary. More importantly, the image after frame selection is narrower in both the primary and secondary components. This increased narrowing indicates less blurring in the FSR = 50 percent image. The frame selection technique has produced a sharper binary star image.

The partially compensated AO case provides similar results. Figure 4.41 shows a three dimensional surface plot for this case when FSR = 100 percent. As expected,

more blurring has occurred for these degraded seeing conditions. Figure 4.42 provides SNR gain curves which show the FSR = 30 percent case providing the maximum SNR gain at mid spatial frequencies. However, this case also yields a significant SNR loss for spatial frequencies 68 to 88 percent of the diffraction limit. Therefore, the FSR = 50 percent case was used for this comparison. Figure 4.43 depicts a center slice plot comparison before deconvolution. Figure 4.44 depicts greater irradiance and less blurring in both components for the FSR = 50 percent image after deconvolution with a pseudo-Weiner filter, $\alpha = 0.001$.

4.4.2 Simulated Satellite Image. As demonstrated with the simulated binary stars in the previous section, SNR gain due to the application of frame selection can be translated into tangible image improvements after deconvolution. It has been shown that extended objects exhibit less SNR gain than point source objects when frame selection is used to reconstruct images [32]. The question is "Will frame selection provide visual improvements over standard linear reconstruction for extended objects?"

Figure 4.45 shows SNR gain curves for the satellite model, $r_o = 5cm$, $m_\nu = +2$. As noted in Experiment One, these poor seeing conditions constitute a difficult test for frame selection. The FSR = 50 percent case produces the maximum SNR gain for the mid spatial frequencies. Therefore, this case will be used for this visual image comparison demonstration. Figures 4.46 and 4.47 show reconstructed satellite images before deconvolution for the 100 and 50 percent cases, respectively. Note the slight increase in outline sharpness in the FSR = 50 percent image. Figures 4.48 and 4.49 reveal the same images after deconvolution with the pseudo-Weiner filter, $\alpha = 0.01$. The FSR = 50 percent image seems to have more detail in the upper left and lower left solar panels.

4.4.3 Conclusions. Frame selection can provide visually superior images for point sources as demonstrated in this experiment. The simulated binary stars

after frame selection processing and deconvolution provided greater irradiance and less blurring than those reconstructed with all the frames in the data set. Frame selection provided improvements in the satellite model image, but the differences were more subtle than those seen with binary stars.
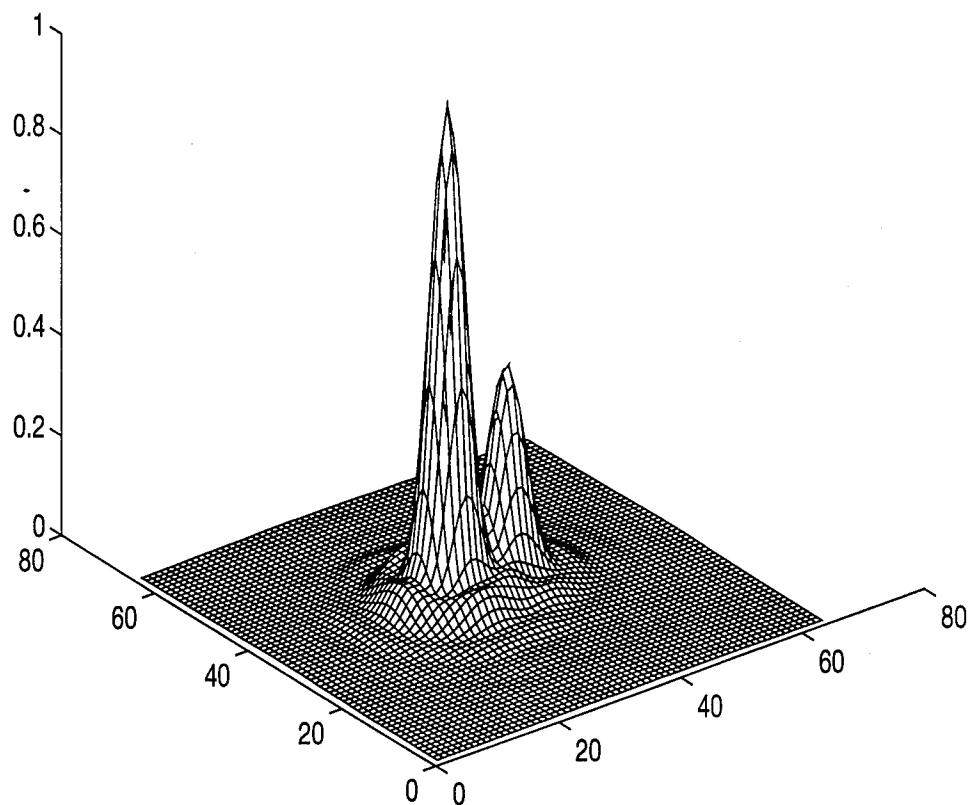
Figure 4.37   Three Dimensional Simulated Binary Star Before Deconvolution, Fully
Compensated AO, AO Case 1. $r_o = 10$ cm, m_ν Primary = +2, m_ν
Secondary = +3, Angular Separation Between Primary and Secondary
= 1 microradian, FSR = 100 percent, $\sigma^2 = 15$ electrons per pixel
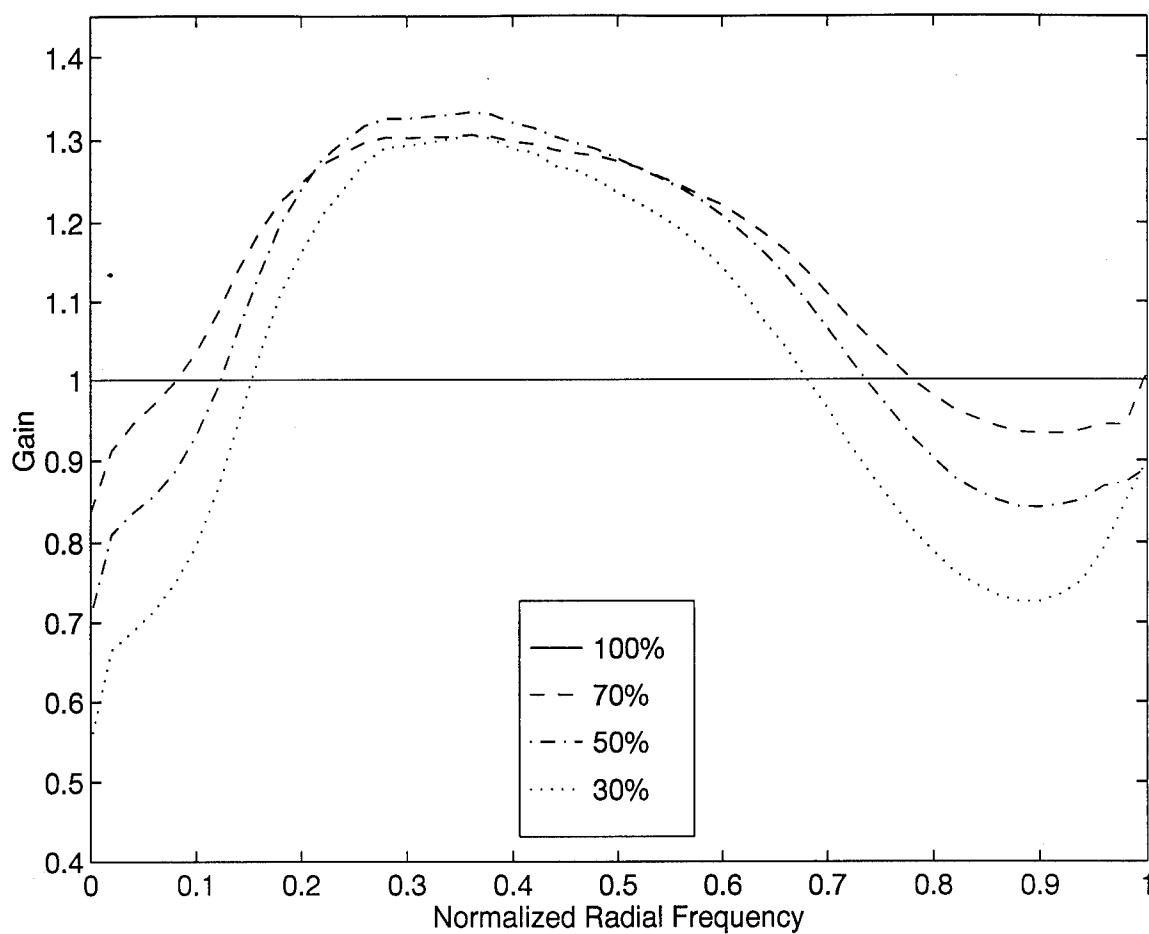
Figure 4.38 Gain Curves Establishing Optimum FSR = 50 percent, Fully Compensated AO, AO Case 1. r_o = 10 cm, m_ν Primary = +2, m_ν Secondary = +3, Angular Separation Between Primary and Secondary = 1 microradian, σ^2 = 15 electrons per pixel

Figure 4.39   Center Slice Plots of Binary Star Showing Improvement Due to Frame Selection Before Deconvolution, Fully Compensated AO, AO Case 1. Slices Normalized to Peak Value of FSR = 50 percent Slice
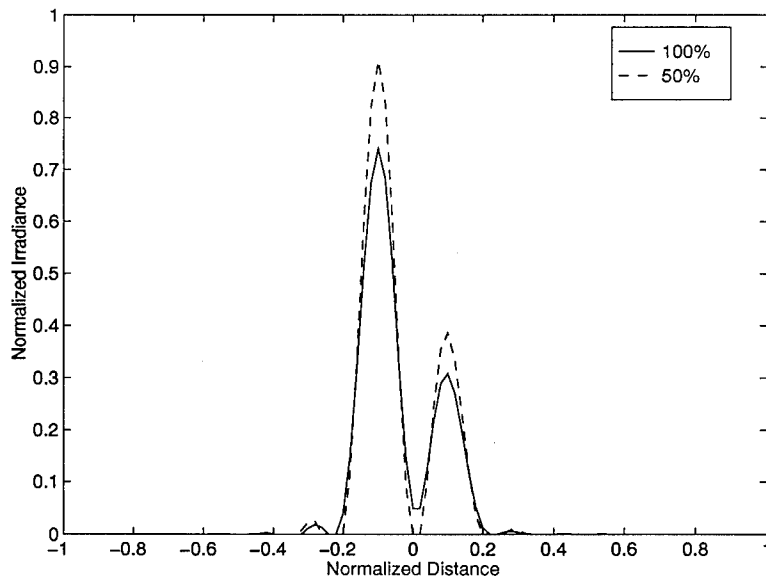
Figure 4.40   Center Slice Plots of Binary Star Showing Improvement Due to Frame Selection After Deconvolution with Pseudo-Weiner Filter ($\alpha = 0.5$), Fully Compensated AO, AO Case 1. Slices Normalized to Peak Value of FSR = 50 percent Slice
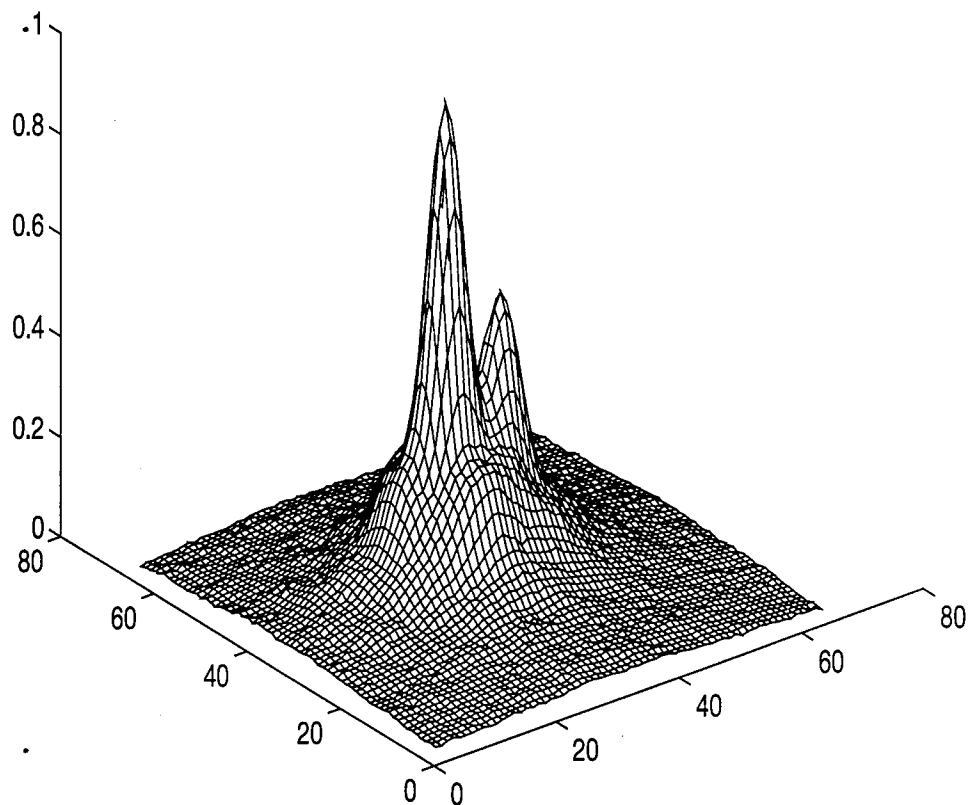
Figure 4.41   Three Dimensional Simulated Binary Star Before Deconvolution, Partially Compensated AO, AO Case 1. $r_o = 5$ cm, m_ν Primary $= +6$, m_ν Secondary $= +7$, Angular Separation Between Primary and Secondary $= 1$ microradian, FSR $= 100$ percent, $\sigma^2 = 15$ electrons per pixel
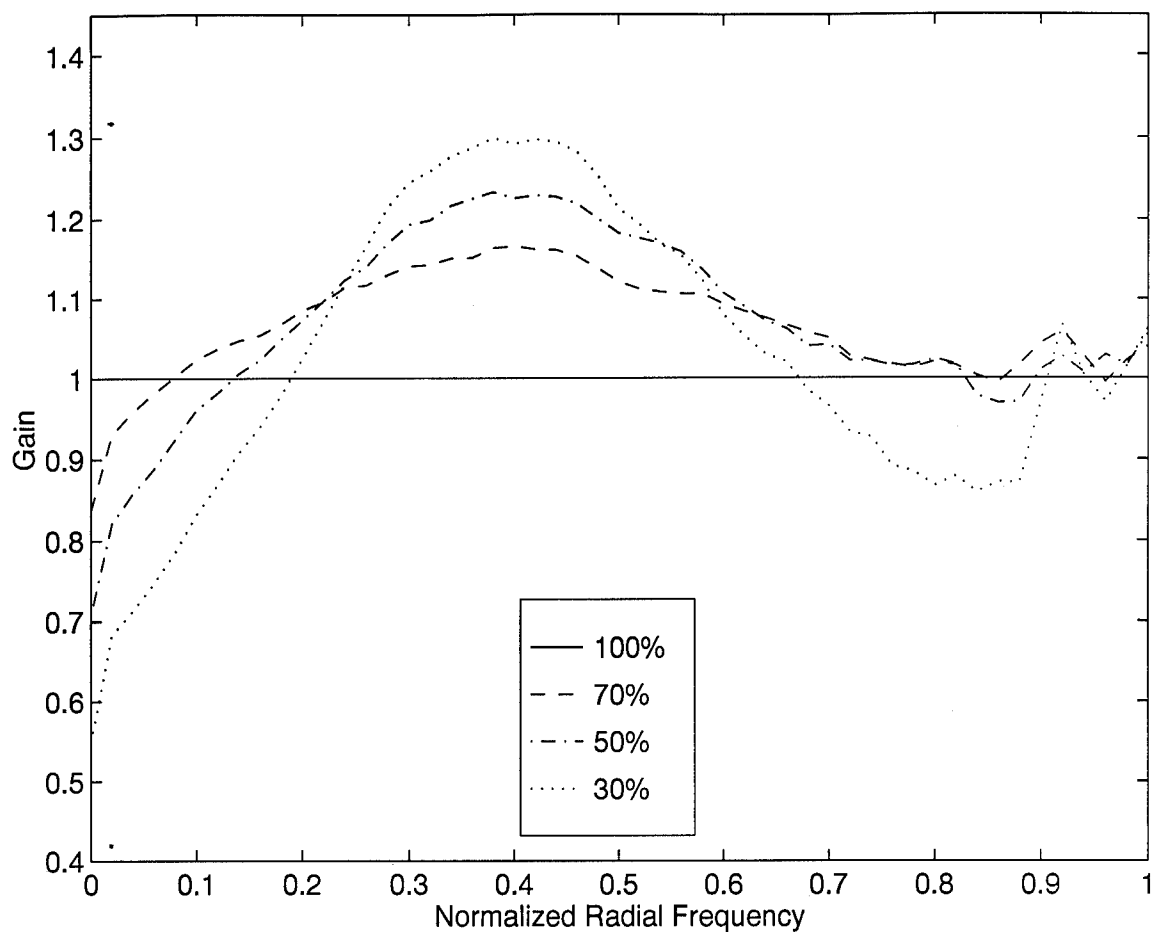
Figure 4.42   Gain Curves Establishing Optimum FSR = 50 percent, Partially Compensated AO, AO Case 1. $r_o = 5$ cm, m_ν Primary = +6, m_ν Secondary = +7, Angular Separation Between Primary and Secondary = 1 microradian, $\sigma^2 = 15$ electrons per pixel
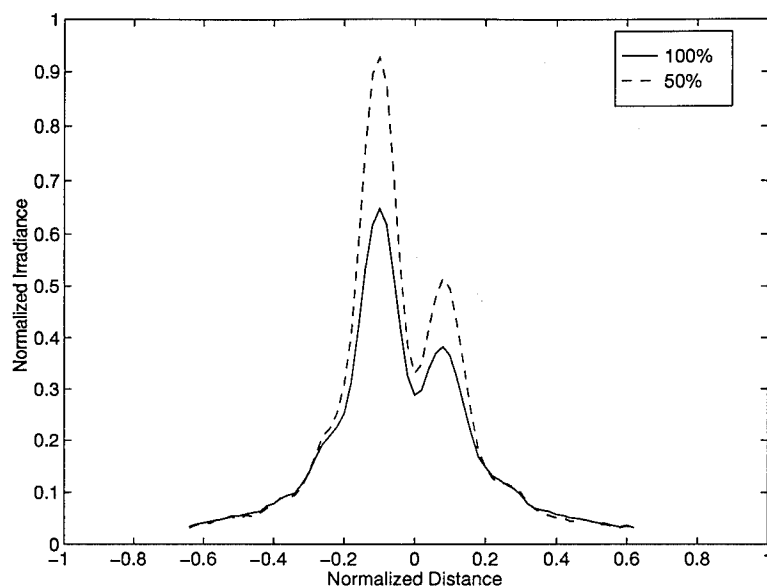
Figure 4.43   Center Slice Plots of Binary Star Showing Improvement Due to Frame
Selection Before Deconvolution, Partially Compensated AO, AO Case
1. Slices Normalized to Peak Value of FSR = 50 percent Slice
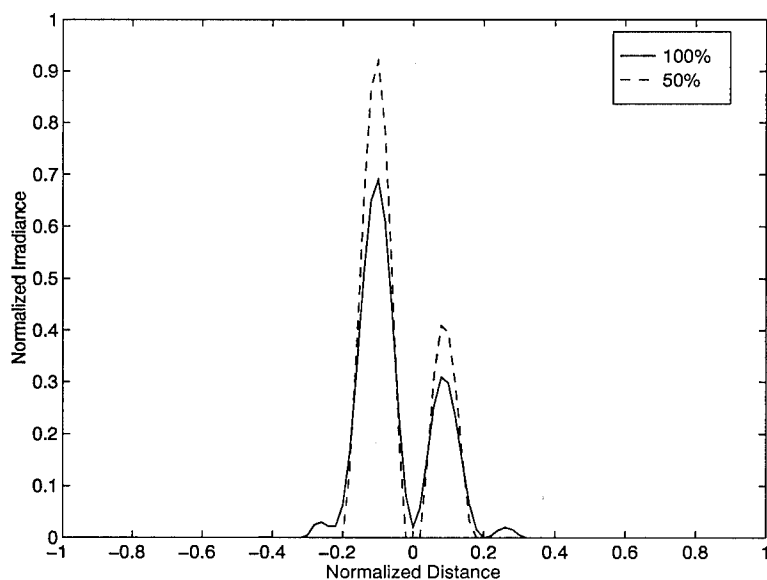
Figure 4.44   Center Slice Plots of Binary Star Showing Improvement Due to Frame
Selection After Deconvolution with Pseudo-Weiner Filter ($\alpha = 0.001$),
Partially Compensated AO, AO Case 1. Slices Normalized to Peak
Value of FSR = 50 percent Slice
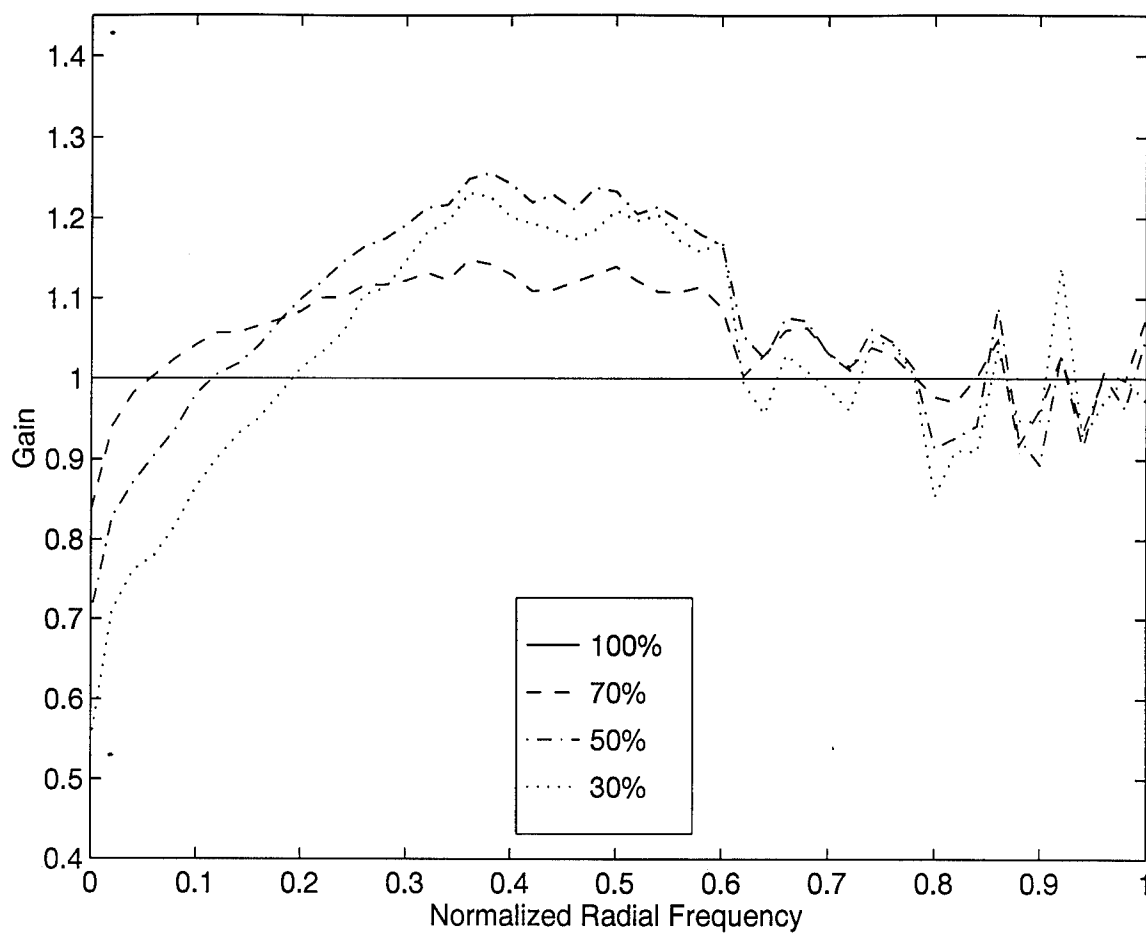
Figure 4.45 Gain Curves Establishing Optimum FSR = 50 percent, AO Case 1. $r_o = 5$ cm, $m_\nu = +2$, $\sigma^2 = 15$ electrons per pixel
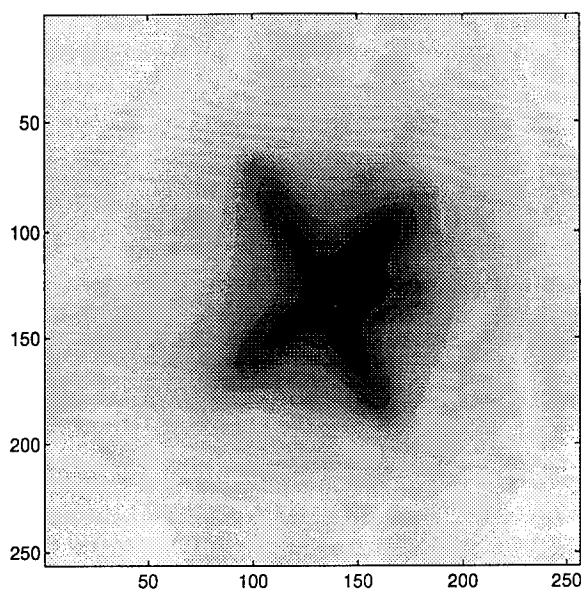
Figure 4.46 Simulated Satellite Image Before Deconvolution, AO Case 1. FSR = 100 percent, $r_o = 5$ cm, $m_\nu = +2$, $\sigma^2 = 15$ electrons per pixel
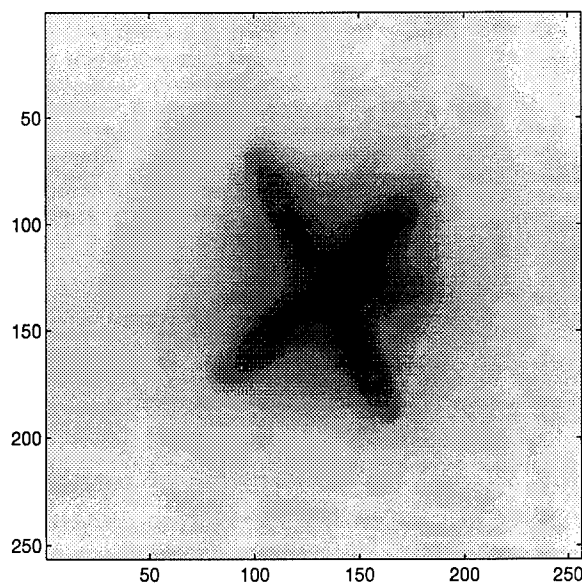
Figure 4.47 Simulated Satellite Image Before Deconvolution, AO Case 1. FSR = 50 percent, $r_o = 5$ cm, $m_\nu = +2$, $\sigma^2 = 15$ electrons per pixel
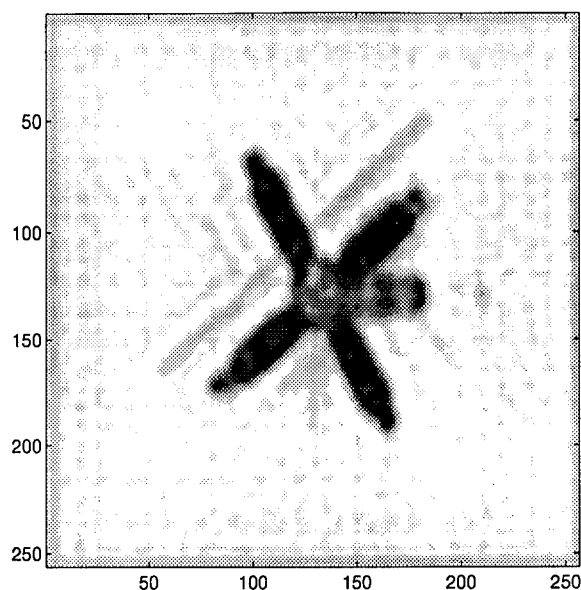
Figure 4.48   Simulated Satellite Image After Deconvolution with a Pseudo-Weiner
Filter ($\alpha = 0.01$), AO Case 1. FSR = 100 percent, $r_o = 5$ cm, $m_\nu = +2$,
$\sigma^2 = 15$ electrons per pixel
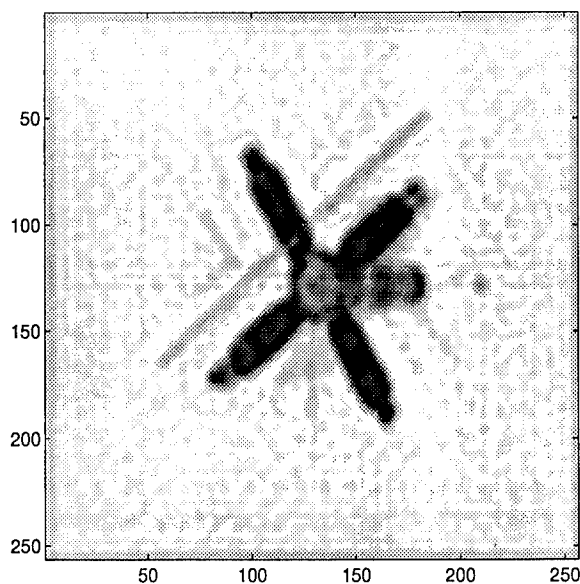
Figure 4.49   Simulated Satellite Image After Deconvolution with a Pseudo-Weiner
Filter ($\alpha = 0.01$), AO Case 1. FSR = 50 percent, $r_o = 5$ cm, $m_\nu = +2$,
$\sigma^2 = 15$ electrons per pixel

Frame selection processing has been shown to improve images using both the image spectrum SNR [32] and visual image comparison. However, photon noise poses a fundamental limit on this technique. This experiment documents the initial investigation of a new, related image reconstruction technique, frame weighting, which may boost the image spectrum SNR of dim objects and complement frame selection.

Recalling Chapter Two, frame weighting is defined by

$$I_W(u,v) = \frac{1}{N} \sum_{i=1}^{N} W_i I_i(u,v), \tag{4.9}$$

where $I_W(u,v)$ is the average image frequency spectrum of the weighted image, W_i is a frame weight associated with the ith frame, $I_i(u,v)$ is the image frequency spectrum of an individual frame, N is the number of frames in the entire data set, and (u,v) is a spatial frequency. A weight, W_i, is assigned to each frame such that:

1. Frame weights are between zero and one.

2. Frame weights are close to or equal to one for high resolution frames and are close to or equal to zero for low resolution frames.

For the purposes of this experiment, weights are assigned using two approaches: quality-based frame weighting and function-based frame weighting. Quality-based frame weighting is implemented via the following:

$$W_i = \left(\frac{S_i}{S_{max}}\right)^{\beta}, \tag{4.10}$$

where S_i is the quality metric value associated with the ith frame, S_{max} is the quality metric value associated with the best frame in the data set, and β is a user selected parameter. Frame weights derived using the quality-based approach maintain an exact proportional relationship with the original quality metric values. The β pa-

rameter is used to adjust the weighting distribution for better SNR performance. An example of quality-based frame weighting distributions for selected β parameters is shown at 4.50 where lower frame order numbers denote lower quality. In contrast, function-based frame weighting uses the relative quality ranking from the frame quality metric to fit weights via a pre-defined weighting function. Frame weights are no longer proportional to the quality metric values but are tied only to the relative quality ranking within the data set. In this thesis, three weighting distribution functions are investigated: exponential, Gaussian, and linear as depicted in Figure 4.51. SNR gain plots are compared for the point source and satellite model in the following sections.

4.5.1 Point Source. Frame weighting for point source objects is discussed in this section. Two r_o values were investigated, 5 and 10 centimeters, representing poor and average seeing conditions. The object visual magnitude, m_ν, was also assigned two values, +2 and +8, representing a standard and dim object. Figure 4.52 depicts the quality-based weighting distributions for $r_o = 10$ centimeters and $m_\nu = +2$. As the information from Experiment One predicts, average seeing conditions provide significant variance in frame quality due to increased OTF variance. Figure 4.53 shows the SNR gain curves for this case. Each curve is referenced against the SNR produced when all frames in the data set are used in the image reconstruction (FSR = 100 percent). Note the significant SNR loss at low spatial frequencies. This loss is indicative of almost all cases examined in this frame weighting investigation. Also, note that larger β values further degrade SNR performance. Larger values of β do not always provide worse performance as will be seen in later cases. Function-based frame weighting attains approximately the same level of performance as the quality-based approach as shown in Figure 4.54. Using this case as an example, frame weighting does not hold promise for average seeing conditions and relatively bright point source objects.

4-66

The next case reveals more interesting results as r_o is reduced to 5 centimeters and the object visual magnitude is adjusted to $m_\nu = +8$. Recalling Experiment One, $m_\nu = +8$ is sufficiently dim to be a borderline case between measurement noise and OTF noise dominance of the image spectrum SNR expression. Figure 4.55 depicts the quality-based weighting distributions for this case. Notice, frame quality does not vary as much for these poor seeing conditions when compared to the previous case. Once again, this reduced image quality variance is consistent with the observations in Experiment One. In contrast to the results above, Figure 4.56 reveals SNR gain at mid spatial frequencies for quality-based frame weighting. This SNR gain reaches a maximum at 40 percent of the diffraction limit and represents a 10 percent gain over the FSR = 100 percent case. In addition, note that the low spatial frequency losses have been reduced as compared to the previous results. These low frequency losses are now comparable with those exhibited by frame selection. However, Figure 4.56 also shows that frame selection still outperforms quality-based frame weighting in the mid spatial frequencies. Conversely, function-based frame weighting does outperform frame selection at mid spatial frequencies as depicted in Figure 4.57. Notice that the Gaussian distribution function outperforms the FSR = 50 percent case from about 25 to 90 percent of the diffraction limit. However, this same weighting distribution also shows a huge SNR loss at low spatial frequencies. This significant low frequency SNR loss may make image reconstruction difficult.

Frame weighting provides improved SNR performance for point source objects but only under poor seeing conditions and with dim objects. The potential use of this technique may be further limited by huge SNR losses at low spatial frequencies. The next section documents similar analysis for the satellite model.

4.5.2 Satellite Model. The results for the satellite model follow the same general trends established for the point source. Therefore, only one case, $r_o = 5$ centimeters and $m_\nu = +4$, will be examined. Figure 4.58 shows the quality-based weighting distributions. As expected, frame quality variance is fairly low.

Figure 4.59 depicts the SNR gain curves for quality-based frame weighting. Notice the $\beta = 2.5$ case does provide some gain at mid spatial frequencies but only with substantial loss at low frequencies. Once again, the Gaussian distribution function provides good peak SNR gain as shown in Figure 4.60. The maximum SNR gain for the Gaussian distribution function reaches over 20 percent which outperforms frame selection under these conditions as shown in Experiment One. As before, this respectable gain at mid spatial frequencies is balanced by huge losses at low frequencies.

4.5.3 Conclusions. These frame weighting schemes offer improved SNR performance for poor seeing conditions and dim objects at mid spatial frequencies. One possible limiting factor is the huge SNR loss at low frequencies observed for almost all conditions. Typical image spectrum SNR values are very large at low frequencies (on the order of 20,000 for average seeing conditions). When a constant weight is applied, these low frequencies are reduced by a large absolute amount when compared to mid and high spatial frequencies. Recall the defining expression for image spectrum SNR from Chapter 3:

$$SNR_1(u, v) = \frac{\mid E[I_i(u, v)] \mid}{\sqrt{Var[I_i(u, v)]}}. \tag{4.11}$$

Applying a frame weight to a low spatial frequency results in a large reduction in the numerator of Equation 4.11. When compared to the FSR = 100 percent case, a huge SNR loss is noted. At mid and high spatial frequencies, smaller absolute losses are noted in the numerator of Equation 4.11 which are more than offset by reductions in image spectrum variance. Hence, SNR gain is produced under some conditions. One possible solution to this problem is to apply weights only to the mid and high spatial frequencies. The implementation of this solution is left to future experimentation.

4-68
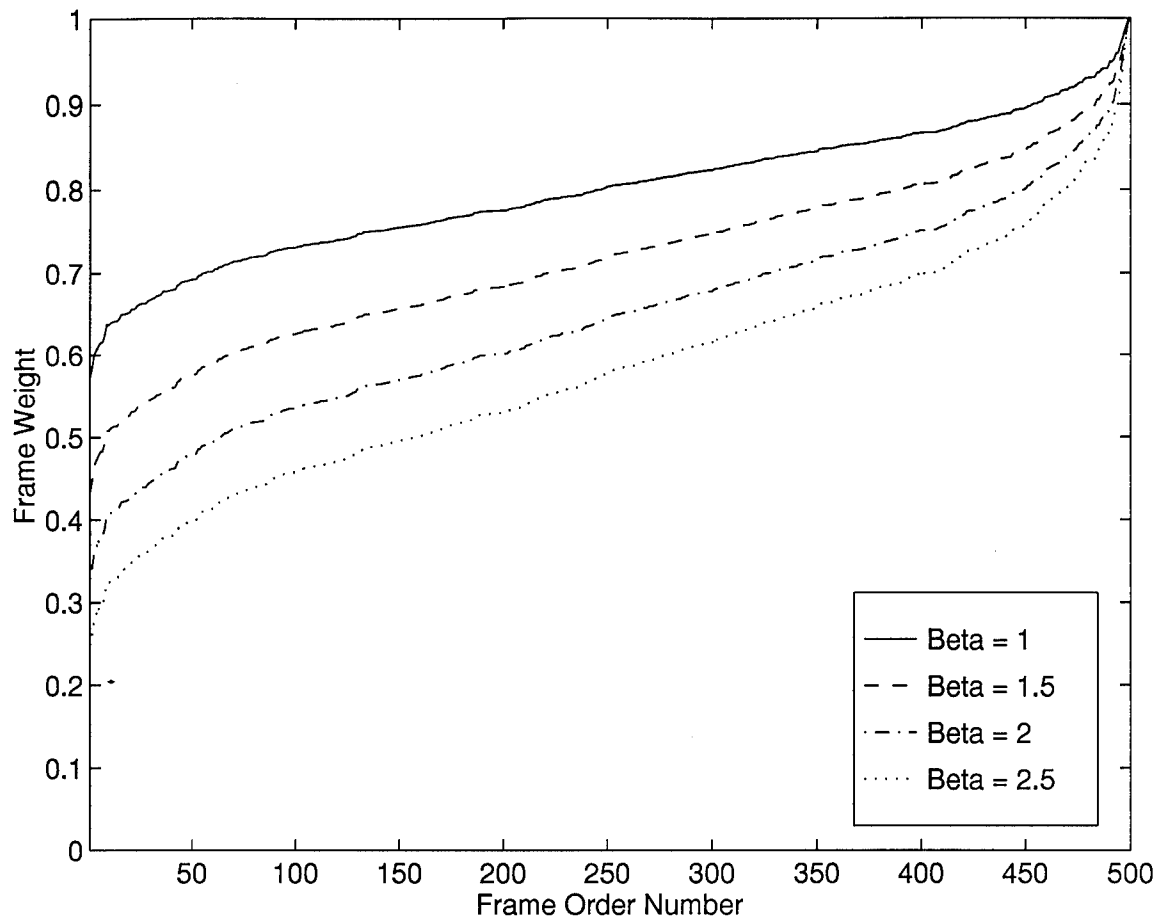
Figure 4.50   Example of Quality-Based Weighting Distributions versus Frame Order
Number as a Function of the β Parameter. $r_o = 10$ cm, $m_\nu = +2$,
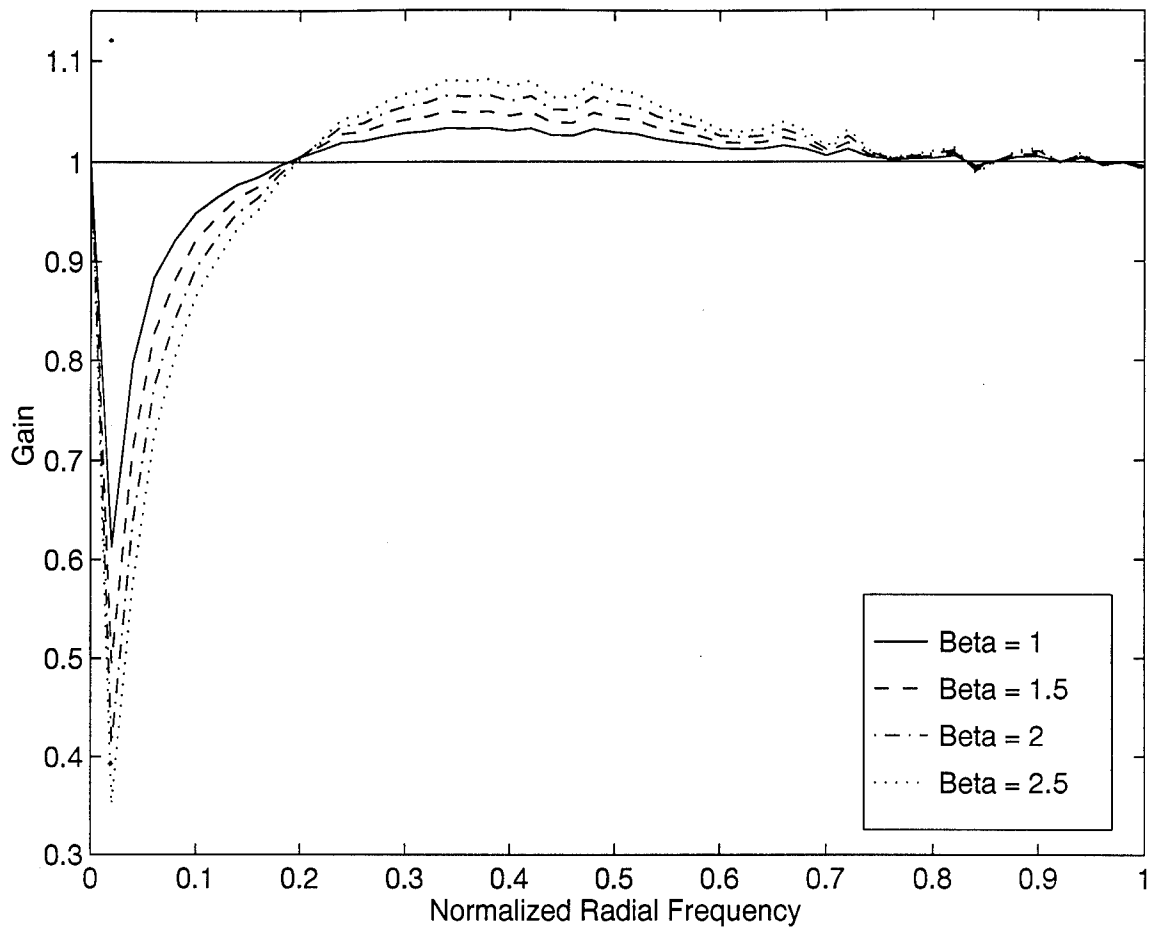Satellite Model, AO Case 1
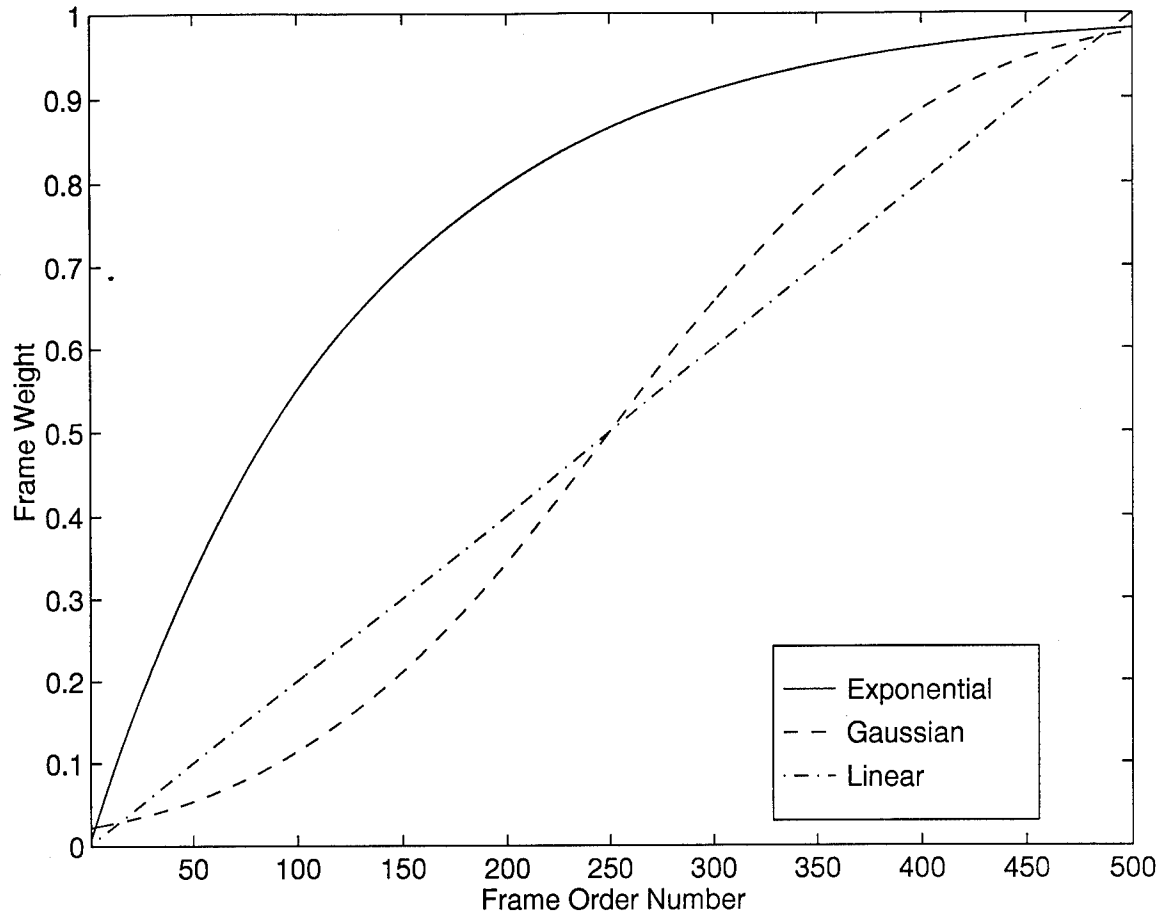
Figure 4.51   Experimental Weighting Function Distributions versus Frame Order Number
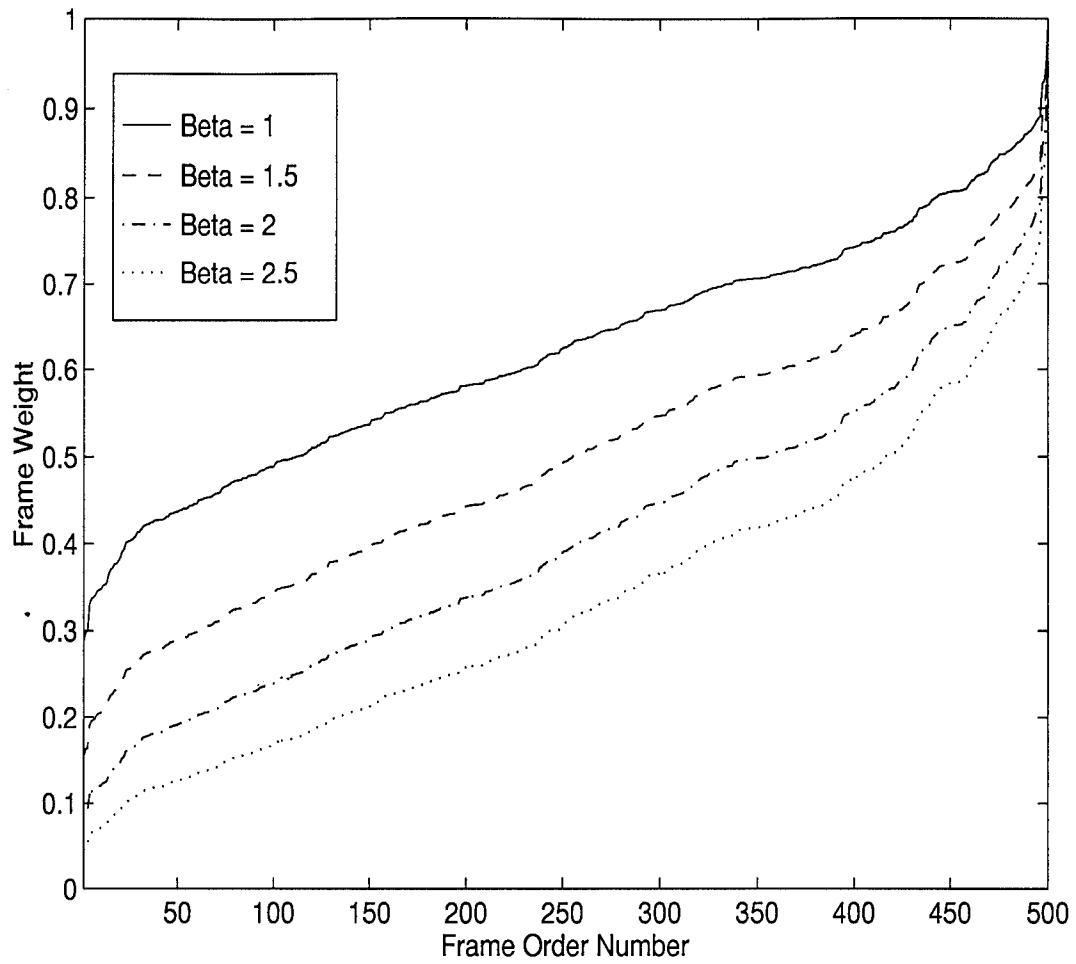
Figure 4.52   Quality-Based Weighting Distributions versus Frame Order Number as a Function of the β Parameter. $r_o = 10$ cm, $m_\nu = +2$, Point Source, AO Case 1
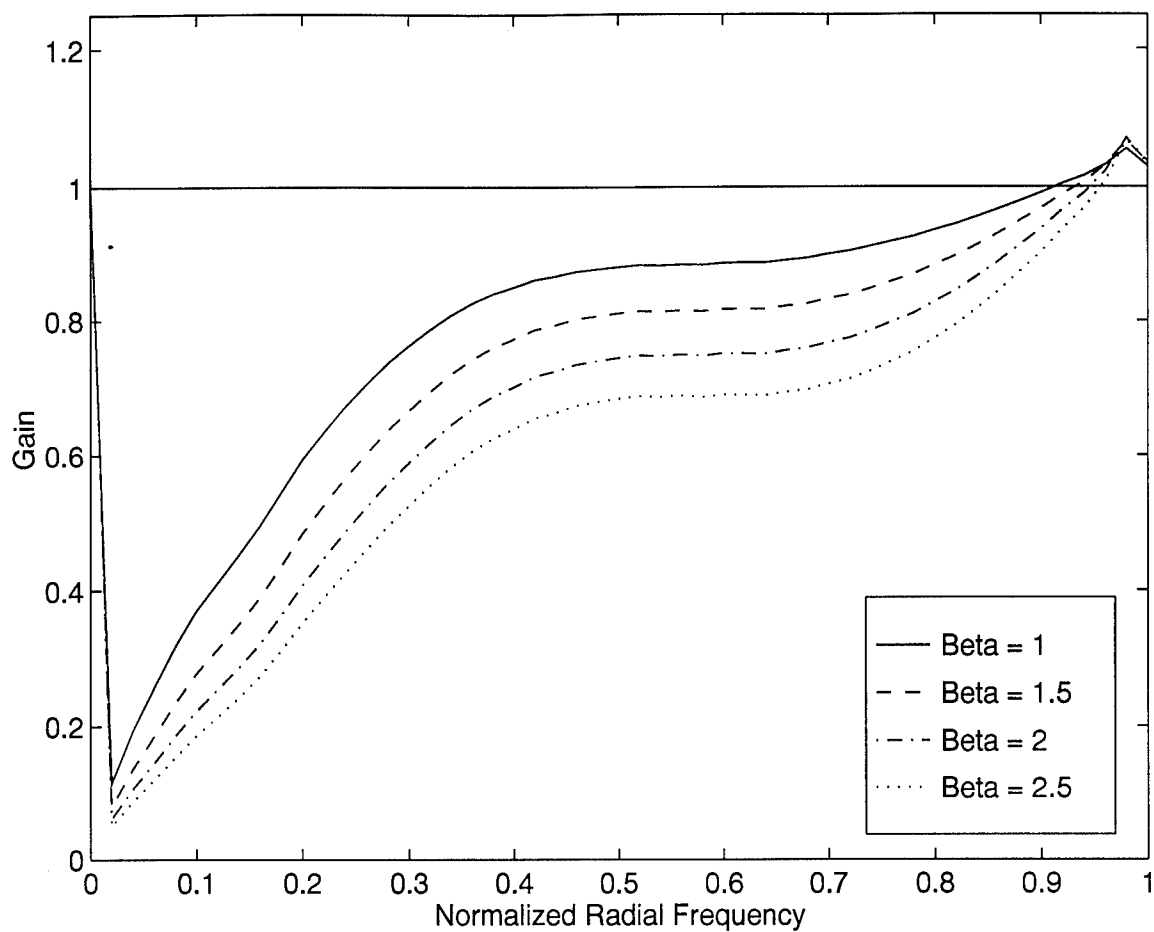
Figure 4.53   Quality-Based Weighting Gain Curves Referenced Against the FSR = 100 percent Case Showing SNR Penalty at Low Spatial Frequencies. $r_o = 10$ cm, $m_\nu = +2$, Point Source, AO Case 1
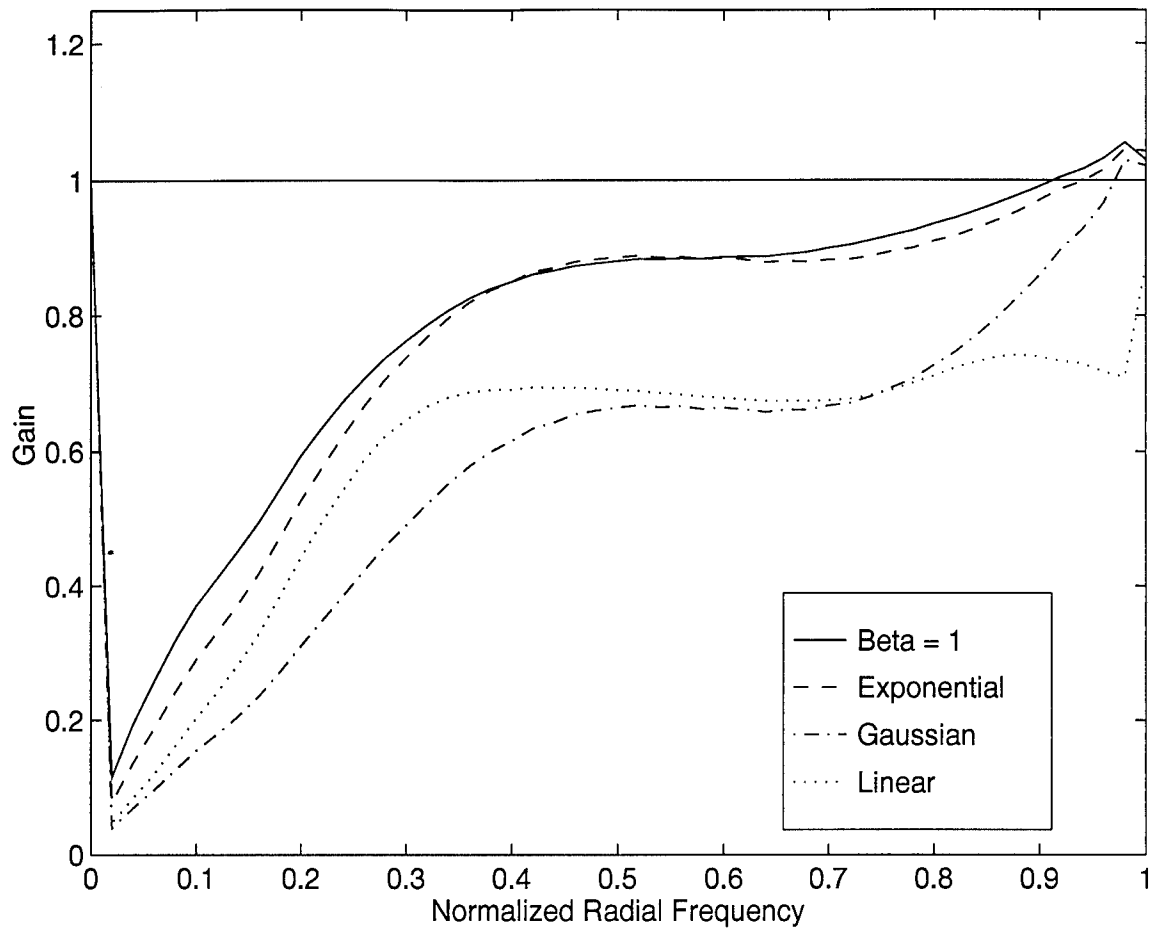
Figure 4.54 Function-Based Gain Curves Referenced Against the FSR = 100 percent Case Showing Performance of Function-Based Frame Weighting. $r_o = 10$ cm, $m_\nu = +2$, Point Source, AO Case 1
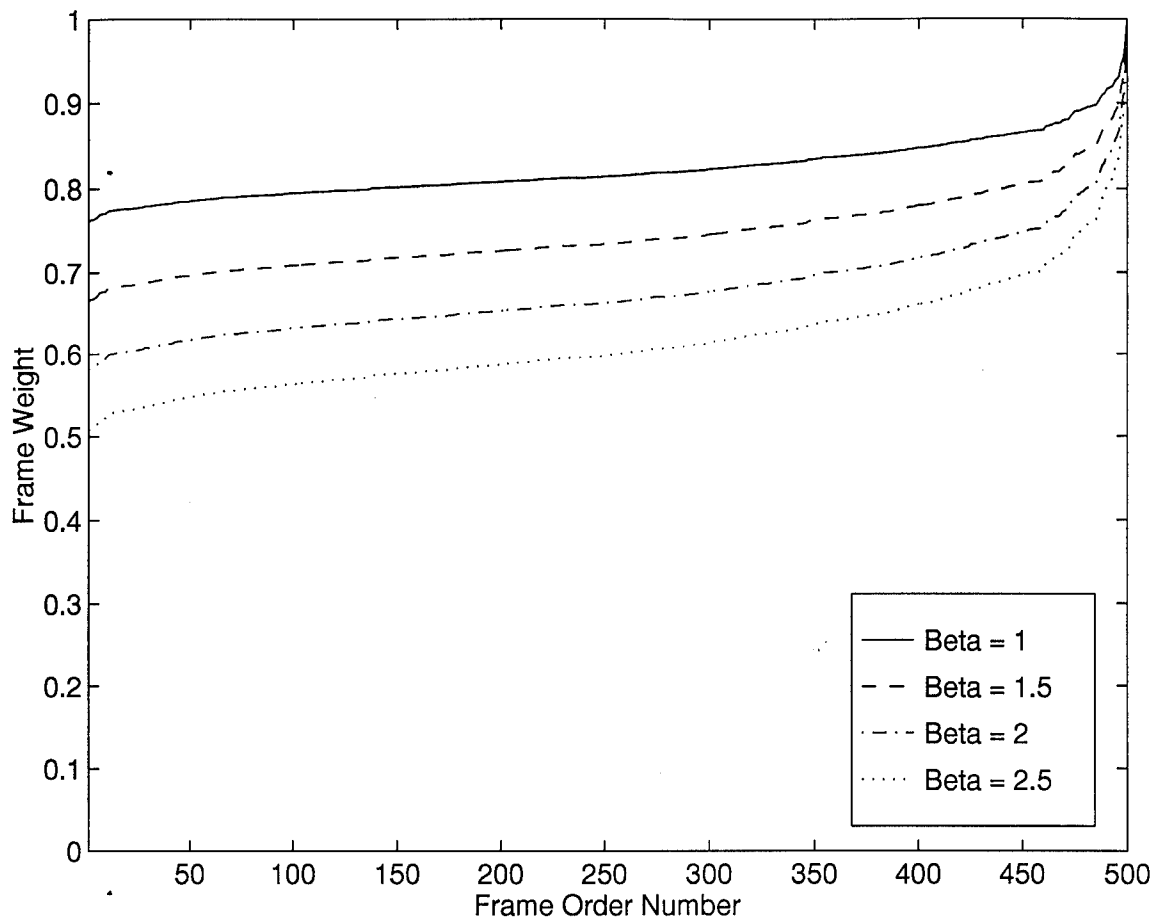
Figure 4.55   Quality-Based Weighting Distributions versus Frame Order Number as a Function of the β Parameter. $r_o = 5$ cm, $m_\nu = +8$, Point Source, AO Case 1

4-74
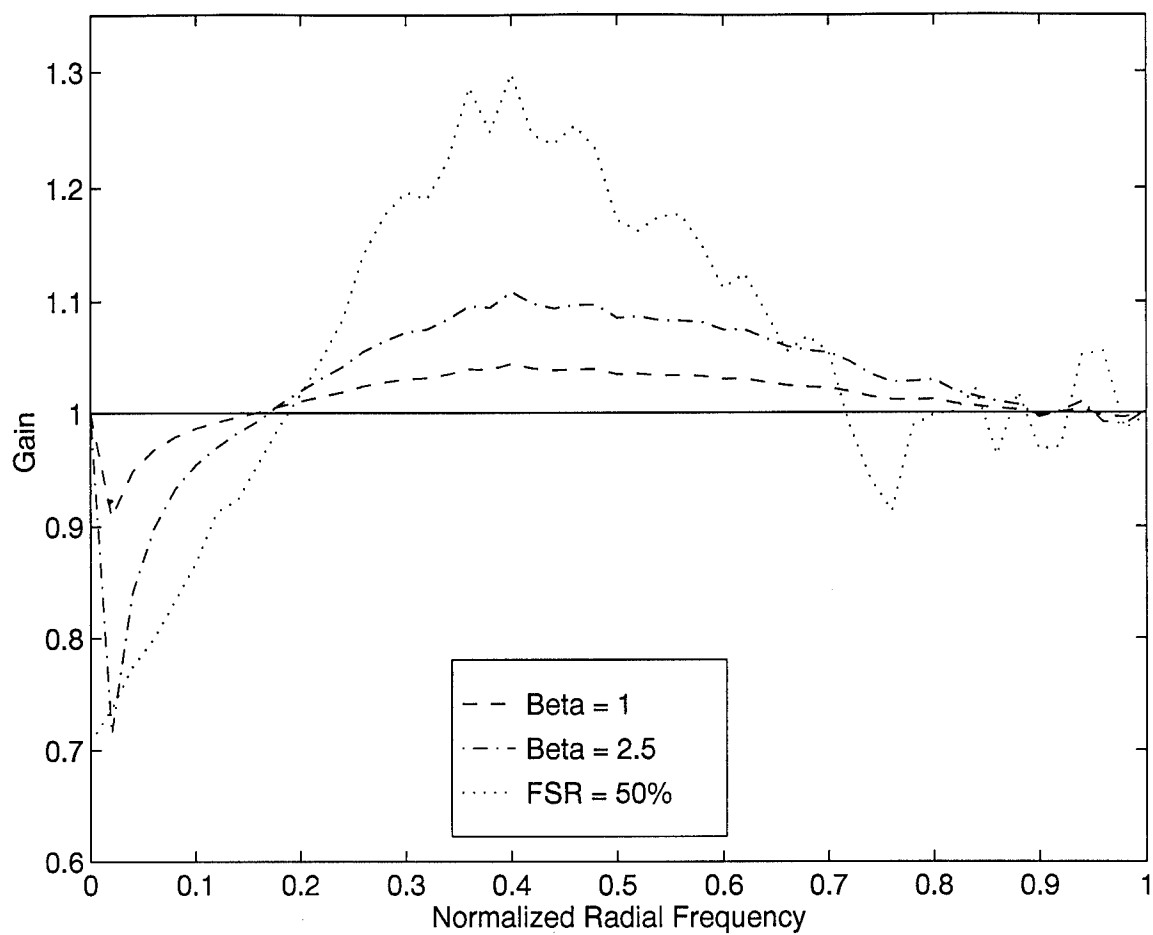
Figure 4.56   Quality-Based Gain Curves Referenced Against the FSR $= 100$ percent
Case Showing Quality-Based Frame Weighting versus Frame Selection.
$r_o = 5$ cm, $m_\nu = +8$, Point Source, AO Case 1
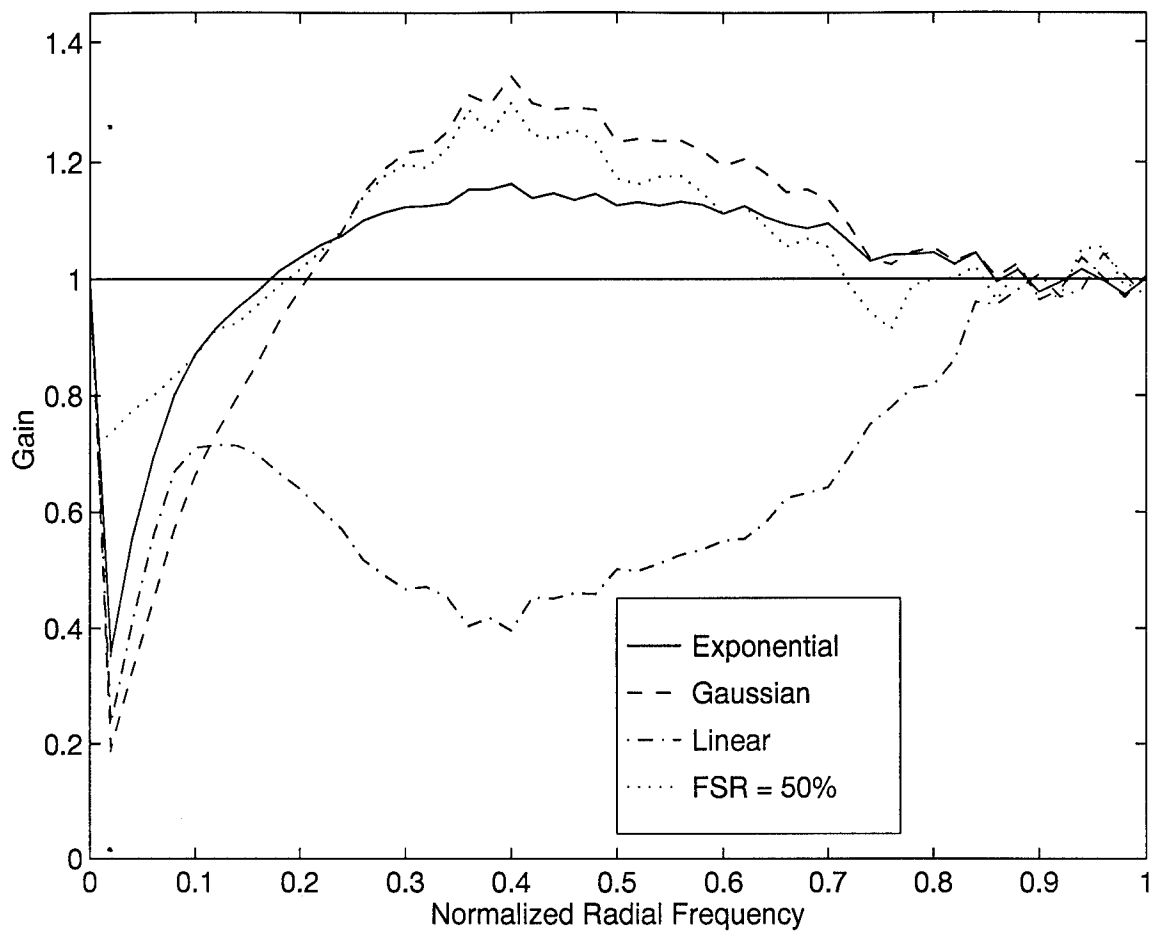
Figure 4.57   Function-Based Gain Curves Referenced Against the FSR = 100 percent Case Showing Function-Based Frame Weighting versus Frame Selection. $r_o = 5$ cm, $m_\nu = +8$, Point Source, AO Case 1
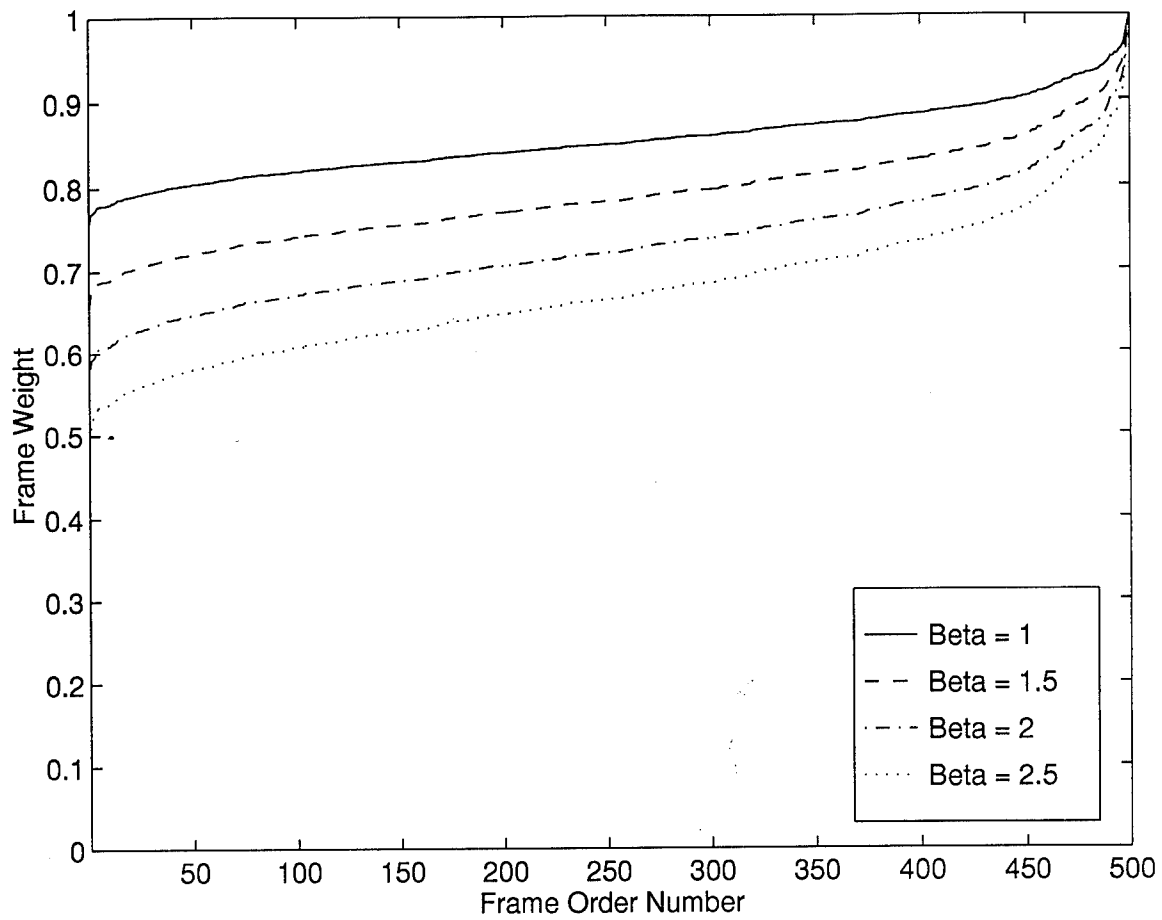
Figure 4.58   Quality-Based Weighting Distributions versus Frame Order Number as a Function of the β Parameter. $r_o = 5$ cm, $m_\nu = +4$, Satellite Model, AO Case 1

Figure 4.59   Quality-Based Weighting Gain Curves Referenced Against the FSR =
100 percent Case. $r_o = 5$ cm, $m_\nu = +4$, Satellite Model, AO Case 1
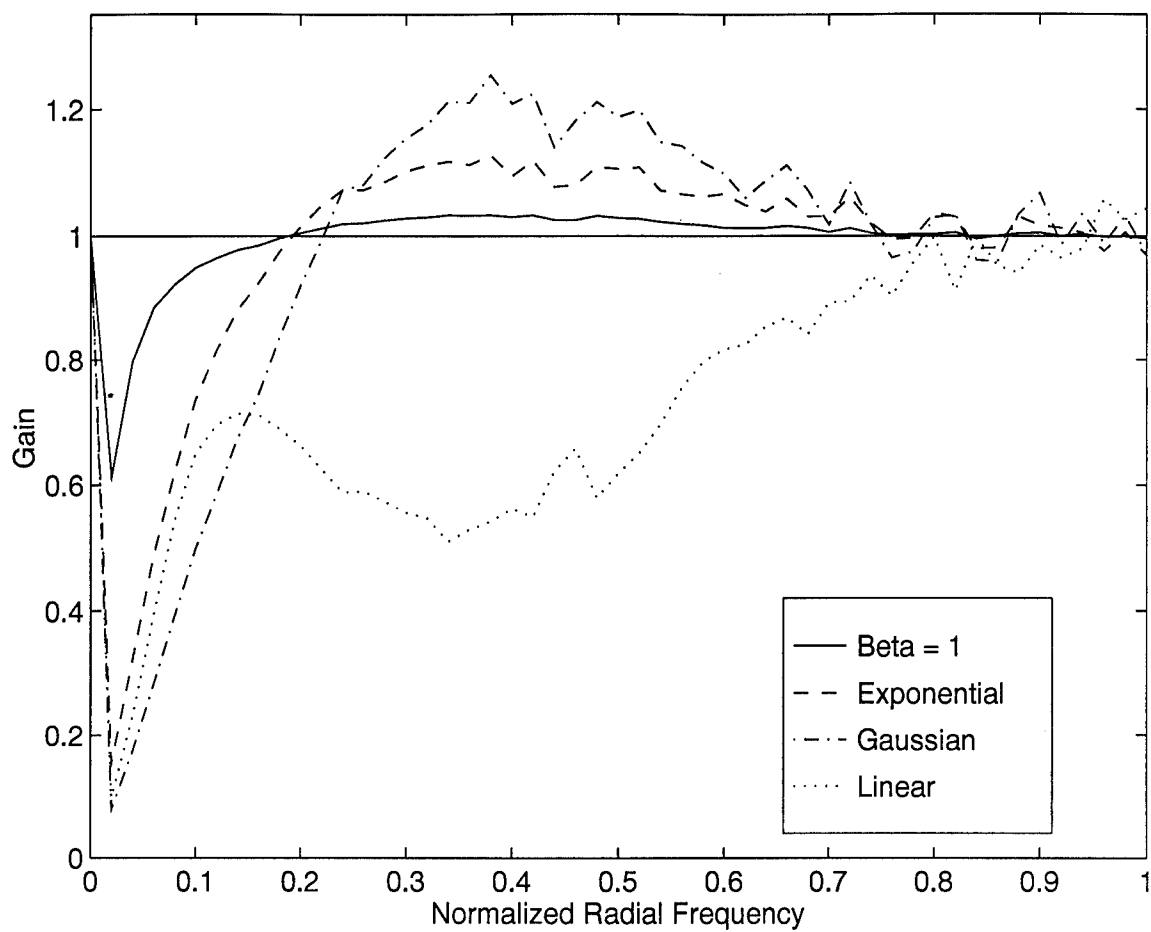
Figure 4.60   Function-Based Weighting Gain Curves Referenced Against the FSR
= 100 percent Case. $r_o = 5$ cm, $m_\nu = +4$, Satellite Model, AO Case 1

4.6 Experiment Five

This experiment investigates frame selection performance on actual space imagery from AMOS. Reference star and satellite data are examined.

4.6.1 Raw Data. AMOS provided raw imagery on 8 millimeter data tape. Each tape contained satellite images, reference star images, dark frames, and flat fields. The images were processed as described in chapter three. Five data tapes were analyzed as part of this investigation. The content of each tape is summarized in Tables 4.2 and 4.3 below. No accurate r_o information was available for any of the data.

Table 4.2 AMOS Satellite Data

TAPE	OBJECT	EXP. (ms)	PHOTO-EVENTS	DATA SET SIZE
1	68700	99	14211800	60
2	68496 HST	60	9388770	60
3	68899	99	602053	60
4	64872	60	4876170	20
5	62633 HST	99	22388100	80

Table 4.3 AMOS Star Reference Data

TAPE	STAR	EXP. (ms)	PHOTO-EVENTS	DATA SET SIZE
1	HR5340	99	1950590	100
2	HR8414	60	1171630	100
3	HR5933	99	711670	100
4	HR8079	60	Unavailable	Unavailable
5	HR8684	99	605835	50

4.6.2 Reference Star Results. First, consider frame selection performance on reference star data. Figures 4.61 and 4.62 illustrate improvement in image spectrum SNR similar to simulated point source data. An FSR of 70 percent provides an

4-80

average 10-15 percent gain between 10 and 40 percent of the diffraction limit. This optimum FSR falls within the expected 60-75 percent rate established in previous work [32]. This case illustrates the potential for SNR gain on actual point source imagery.

Overall, the AMOS data did not show the impressive performance gains seen on simulated point source data. Figures 4.63 and 4.64 illustrate a more typical case with SNR loss at both low and high spatial frequencies and only minimal SNR gain between 50 and 70 percent of the diffraction limit. Lower than expected performance is most likely due to the long exposure times used by the AMOS facility. Fried suggested 10 milliseconds as a suitable exposure time to "freeze" a single realization of the atmospheric turbulence [6]. Exposure times on the order of 60-100 milliseconds combine several realizations of the atmospheric turbulence thereby eliminating the opportunity to discard the worst degrading effects.

4.6.3 Satellite Results. AMOS satellite imagery is subject to the same limitations in regard to exposure time as discussed for reference stars. However, it is still possible to demonstrate some level of performance gain as shown in Figures 4.65 and 4.66. An FSR of 70 percent provides an average 5-10 percent SNR gain across all spatial frequencies.

The ultimate goal of this technique is to provide visually improved images. As discussed previously, providing examples of visually improved satellite images is difficult due to the lack of an objective performance metric. Figures 4.67 through 4.72 provide a subjective example of visual image improvement. Figures 4.67 and 4.68 establish SNR gain using the 70 percent FSR for spatial frequencies greater than 40 percent of the diffraction limit. Figure 4.69 shows the average image using all frames in the data set and Figure 4.70 shows the average image using the best 70 percent of the frames in the data set. There is no visual difference between these two images. Both images have had their high spatial frequency content severely attenuated by

the atmosphere-optical system OTF. To observe any improvement, these averaged images must be deconvolved with an estimate of the OTF. Figure 4.71 shows the 100 percent FSR image after deconvolution with a modified inverse filter incorporating a 32 pixel radius cone filter while Figure 4.72 shows the 70 percent FSR image after the same process. The 70 percent FSR image is visibly sharper at both the lower right and upper left corners of the image when compared to the 100 percent FSR case.

4.6.4 Conclusions. This experiment was only partly successful in demonstrating improved AMOS imagery due to frame selection. While examples of improved image spectrum SNR for both reference star and satellite were noted, these results were not repeatable across the available data (See Appendix C). Poor performance of the frame selection technique was due primarily to the relatively long exposure lengths used in AMOS data collection. AMOS makes use of 60 and 99 millisecond exposure lengths to compensate for optical system losses inherent in the 1.6 meter telescope design. Long exposures violate the basic tenet of this technique: the ability to discriminate and eliminate the worst manifestations of atmospheric turbulence by discarding the lowest quality frames. Frame selection must utilize data collected with sufficiently short exposure lengths to produce expected performance gains.
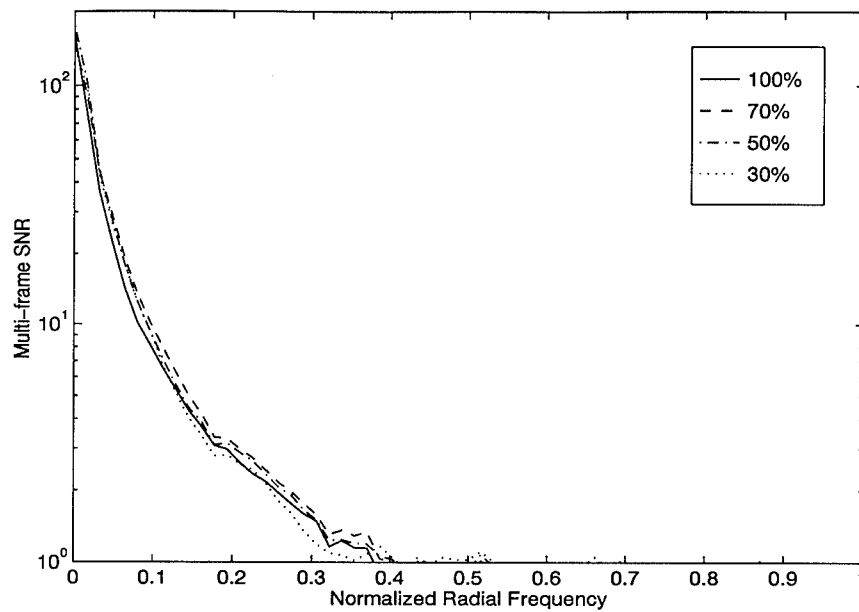
Figure 4.61   Multi-frame Image Spectrum SNR, AMOS Tape 5, Reference Star
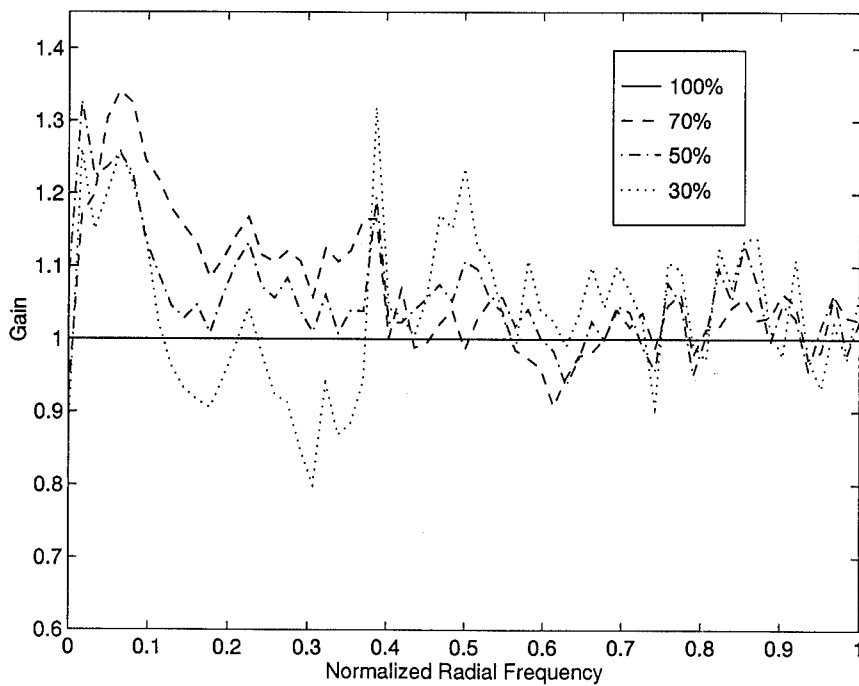
Figure 4.62   Gain Curves, AMOS Tape 5, Reference Star
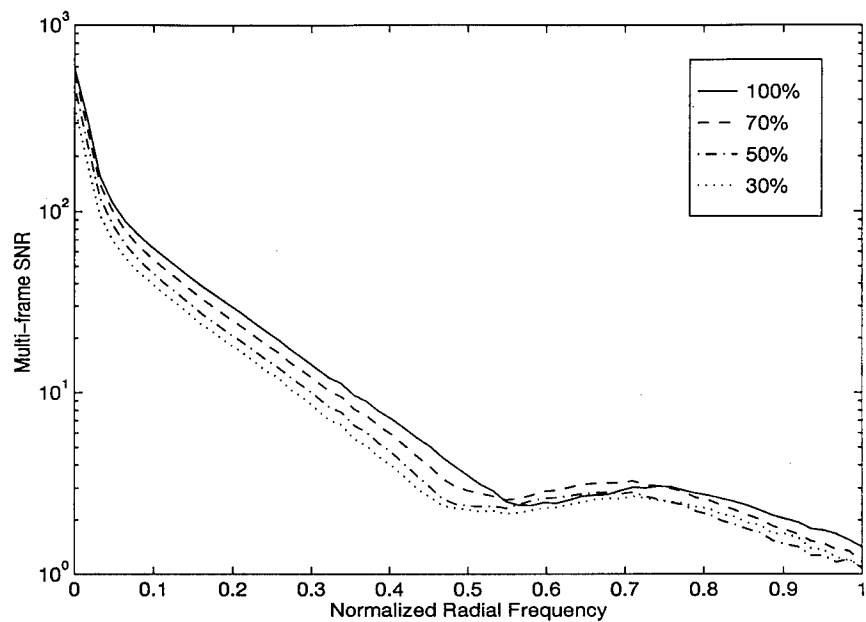
Figure 4.63   Multi-frame Image Spectrum SNR, AMOS Tape 2, Reference Star
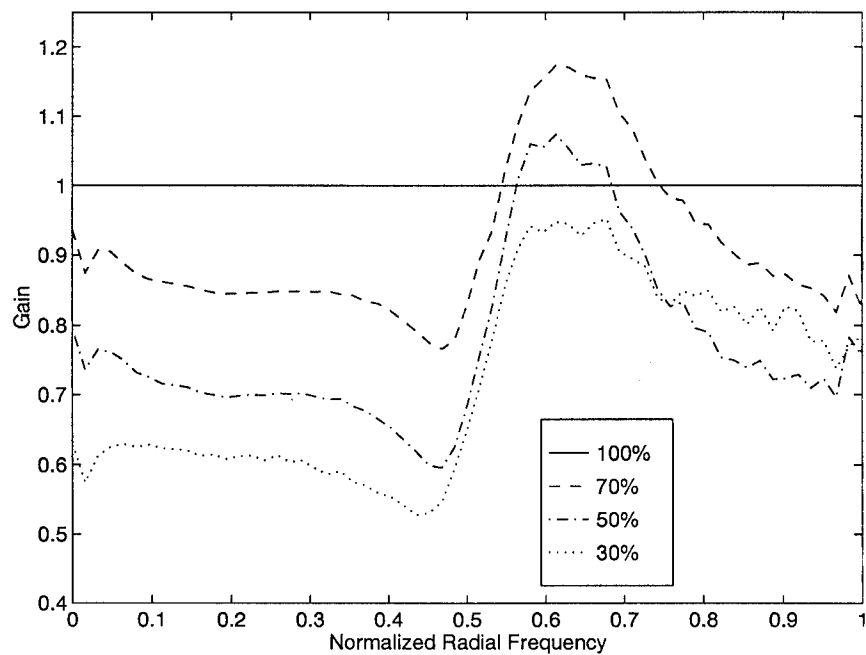
Figure 4.64   Gain Curves, AMOS Tape 2, Reference Star
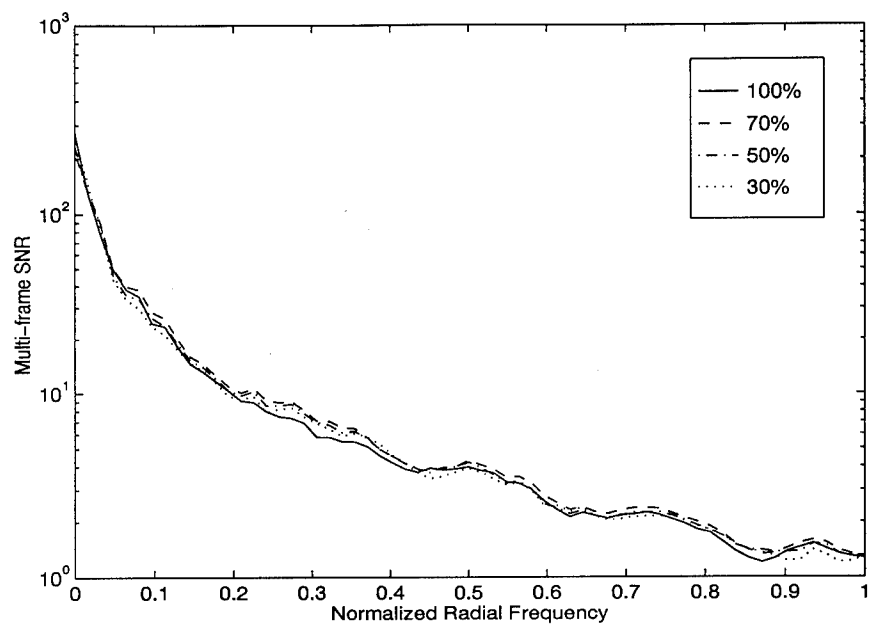
Figure 4.65   Multi-frame Image Spectrum SNR, AMOS Tape 3, Satellite
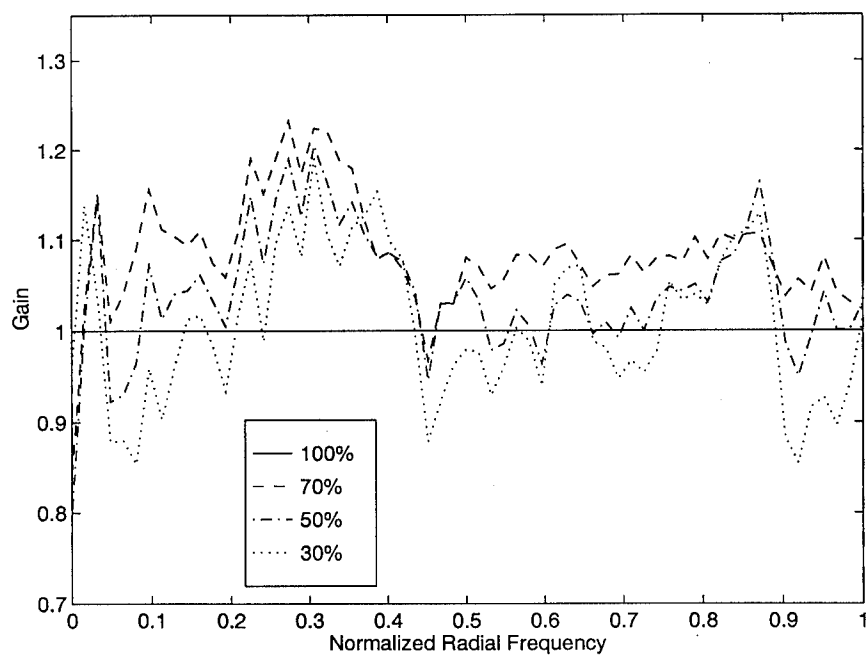
Figure 4.66   Gain Curves, AMOS Tape 3, Satellite
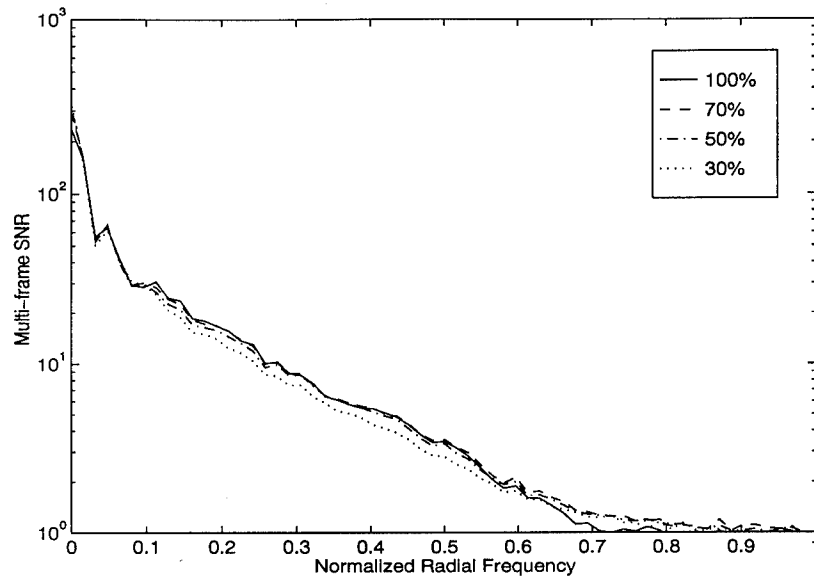
Figure 4.67   Multi-frame Image Spectrum SNR, AMOS Tape 2, Hubble Space
Telescope
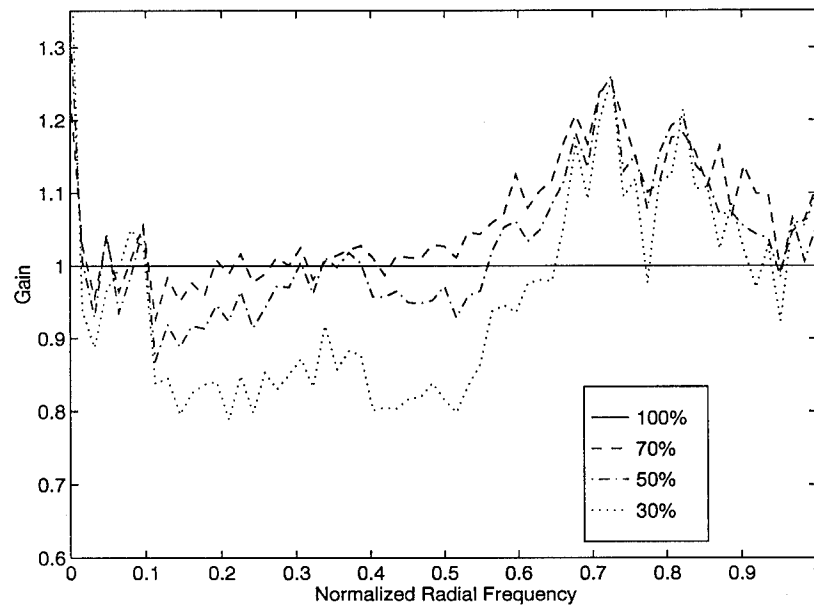
Figure 4.68   Gain Curves, AMOS Tape 2, Hubble Space Telescope
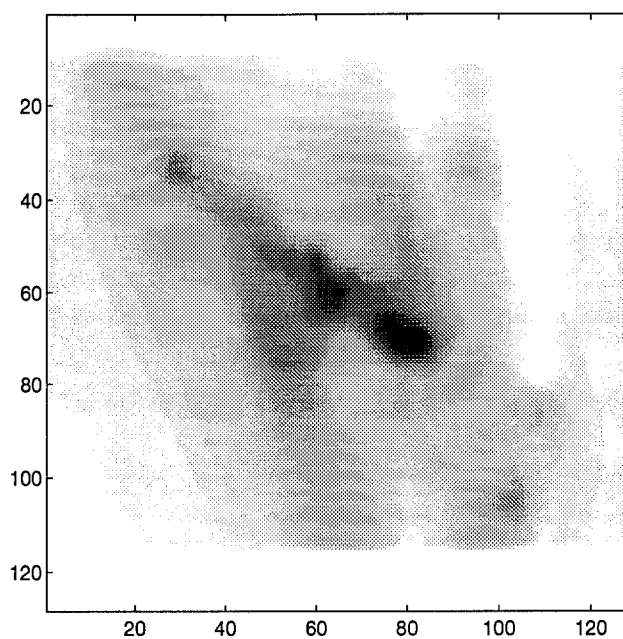
Figure 4.69   Hubble Space Telescope Composite Image, AMOS Tape 2, Data Set
Size = 60 frames, FSR = 100 percent
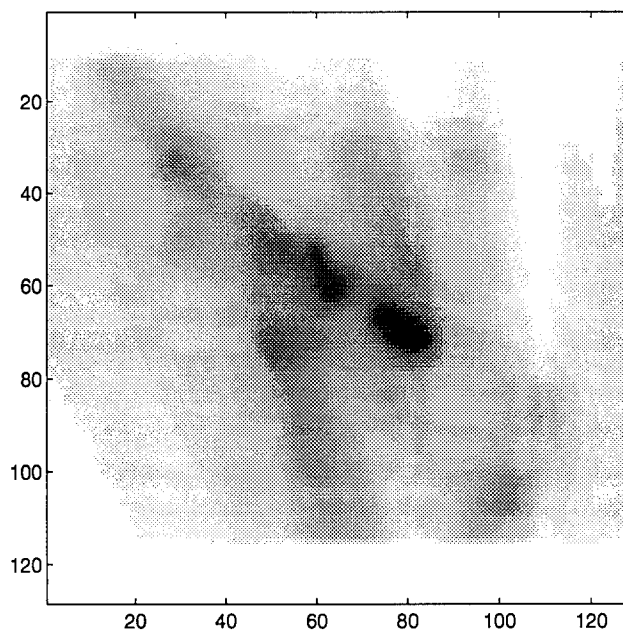
Figure 4.70   Hubble Space Telescope Composite Image, AMOS Tape 2, Data Set
Size = 60 frames, FSR = 70 percent
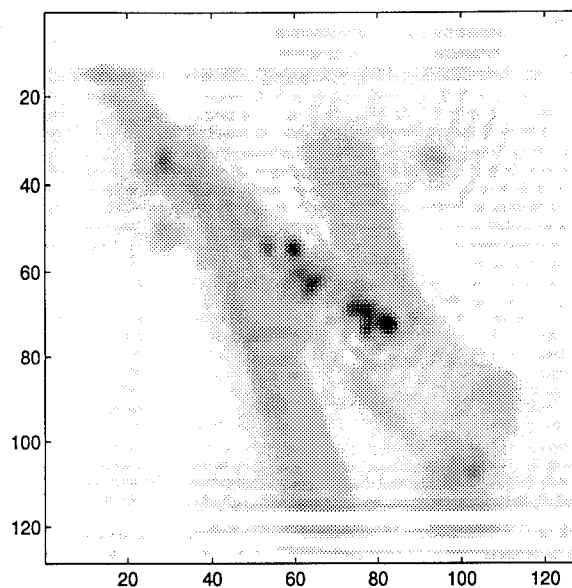
Figure 4.71   Deconvolved Hubble Space Telescope Composite Image, AMOS Tape 2, Data Set Size = 60 frames, FSR = 100 percent, Modified Inverse Filter, mtf = 32 pixels
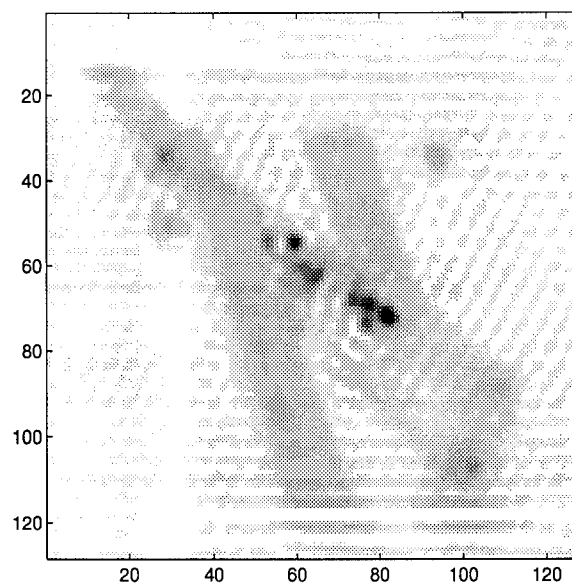
Figure 4.72   Deconvolved Hubble Space Telescope Composite Image, AMOS Tape 2, Data Set Size = 60 frames, FSR = 70 percent, Modified Inverse Filter, mtf = 32 pixels

4.7 Summary

This chapter establishes performance limits for frame selection processing as a function of key independent parameters. Using the fact that photon noise imposes a fundamental limit on SNR, theoretical noise plots were generated which predict the minimum object brightness required to produce SNR gain when compared to the FSR = 100 percent case. The minimum brightness for a point source object was visual magnitude +7 to +8, while the satellite required a minimum visual magnitude of +4. These same theoretical noise plots showed that frame selection provides the most benefit to data sets collected under average seeing conditions in most cases. CCD camera noise effects were seen to have a large influence on the establishment of performance limits for dim objects. The effective average PSF was observed to be virtually identical for point source and satellite objects after the application of frame selection. This similarity allowed the successful utilization of deconvolution techniques to sharpen these images. The visual superiority of images benefiting from frame selection processing was demonstrated on simulated binary stars and the satellite model. Frame weighting was seen to be significantly inferior to frame selection for average seeing conditions and bright objects. However, some SNR improvements were noted for poor seeing conditions and dim objects. Almost all frame weighting test cases exhibited significant SNR losses at low spatial frequencies when compared to the FSR = 100 percent case. These losses may limit the utility of frame weighting. Finally, frame selection was demonstrated on AMOS imagery. Improvements in SNR were noted for both reference stars and satellites, but this performance was not consistent. The long exposure times used by AMOS for data collection do not allow the "freezing" of individual realizations of the atmospheric turbulence which significantly degrades the predictable performance of the frame selection technique.

V. Conclusions and Recommendations

5.1 Introduction

This investigation began due to the need to answer performance questions raised by previous research associated with the frame selection technique [32]. A complete understanding of the limitations associated with this technique is critical to its application to U. S. Air Force imaging problems. In addition, it was desirable to demonstrate that signal-to-noise (SNR) gain due to frame selection processing translates to visually improved images. A new image reconstruction technique, frame weighting, was investigated. Finally, frame selection was demonstrated on actual Air Force Maui Optical Site (AMOS) imagery. This chapter presents a summary of the accomplishments documented in this thesis and provides recommendations for further research in this area.

5.2 Conclusions

1. The transition between measurement noise limited and optical transfer function (OTF) noise limited imaging can be used to provide a theoretical predictor of frame selection performance. Previous research established that photon noise sets a fundamental limit on frame selection performance [32]. Frame selection provides improved image spectrum SNR by discarding the worst manifestations of atmospheric turbulence. This results in reduced image spectrum variance and higher SNR. When objects are sufficiently dim, photon and charge-coupled device (CCD) camera noise effects dominate the single frame SNR expression. All available frames in the data set are needed to reduce this effect through averaging. Therefore, frame selection cannot provide image improvement. These facts were used to generate theoretical noise plots illustrating the influence of the seeing conditions, expressed by r_o, and the object visual magnitude, m_ν, on the transition to measurement noise limited imaging. These theoretical noise plots proved excellent predictors of frame selec-

tion performance limits as related to these parameters. For point source objects, the minimum visual magnitude for SNR gain due to frame selection was $m_\nu = +7-8$ depending on the adaptive optics (AO) system modeled. An example extended object, a satellite model, required a much brighter minimum visual magnitude of $m_\nu = +4$. In general, average seeing conditions, represented by $r_o = 10$ centimeters, benefited the most from frame selection processing. This increased SNR gain is due, in part, to larger OTF variance for average seeing conditions when compared to poor or very good conditions. Finally, CCD camera noise effects play a significant role in establishing frame selection performance limits.

2. Point spread functions (PSFs) are nearly identical for point source and extended objects after frame selection processing. This fact allows the optimal use of deconvolution techniques, such as inverse and Weiner filters, to sharpen images after frame selection. This thesis documents the successful demonstration of visual image improvements due to frame selection.

3. The utility of the frame weighting approach developed in this thesis is limited. This frame weighting technique demonstrated greater SNR gain than frame selection for poor seeing conditions and dim objects. However, large signal losses at low frequencies may make image reconstruction difficult. Further research is needed to examine this potential drawback to the technique.

4. Short exposure times are necessary to get the full, predictable benefits of frame selection processing on real imagery. Improvements in SNR gain were demonstrated as part of this thesis for reference star and satellite objects collected by the AMOS facility. Experiments using this data were not readily repeatable due to the 60-99 millisecond exposure times used for image collection. Long exposure times violate the advantage of this technique: the ability to discriminate and eliminate the worst manifestations of atmospheric turbulence by discarding the lowest quality frames. Frame selection must utilize data collected with sufficiently short exposure lengths to produce expected performance gains.

5.3 Recommendations for Further Research

1. To date, frame selection has only been demonstrated in conjunction with the linear reconstruction of AO compensated images. Speckle interferometry may benefit from forming the average energy spectrum and phase spectrum from only the highest quality frames in a data set. A successful demonstration of frame selection-speckle processing could result in a parallel study documenting the performance limits of the new technique.

2. Frame selection should be fully demonstrated on real data collected with adequately short exposure times. This data could be obtained from another Air Force facility such as the Starfire Optical Range (SOR) 3.5 meter telescope. Short exposure times will allow a convincing evaluation of frame selection performance on real imagery.

3. A mathematically optimal frame weighting scheme should be investigated. Chapter Two outlined two common approaches to solving problems of this type within a linear algebra framework, linear minimum variance and least squares optimization. Drawbacks were associated with computational difficulties and a lack of knowledge of OTF statistics. If these problems can be overcome, significant image improvements may be available.

4. Simple, intuitive frame weighting should be reexamined in an attempt to overcome the large low spatial frequency signal losses that are a side effect of this technique. If this problem is overcome, frame weighting can provide a simple complementary method to frame selection for poor seeing conditions and dim objects.

5. Image spectrum SNR provides a convenient engineering metric to measure improvements in an image. However, the Air Force is only interested in visual image improvements as they affect the gathering of information on objects in space. A study of Air Force image assessment techniques may yield information that will

provide an objective performance metric for image improvement that is directly tied to human visual system performance.

Appendix A. Frame Selection Simulation Results

This appendix contains additional gain curves for Experiment One, Chapter Four.
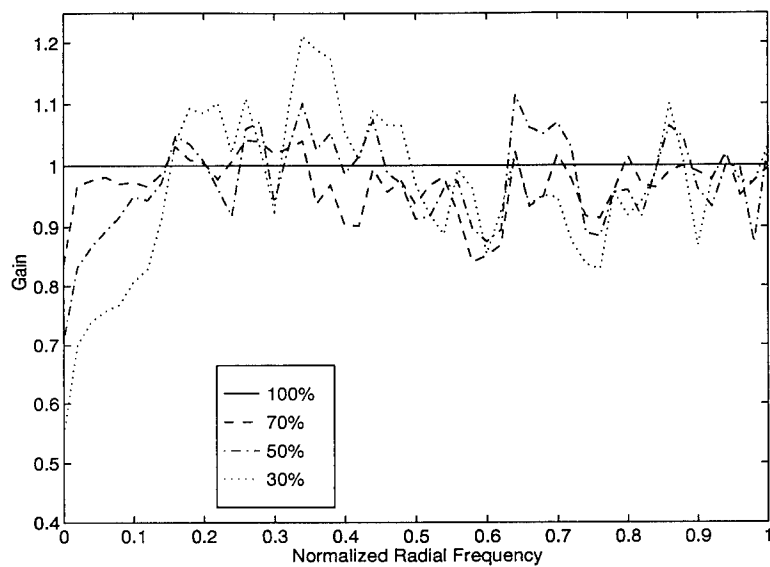
Figure A.1   Gain Curves, Point Source, AO Case 1, $r_o = 3$ cm, $m_\nu = +2$
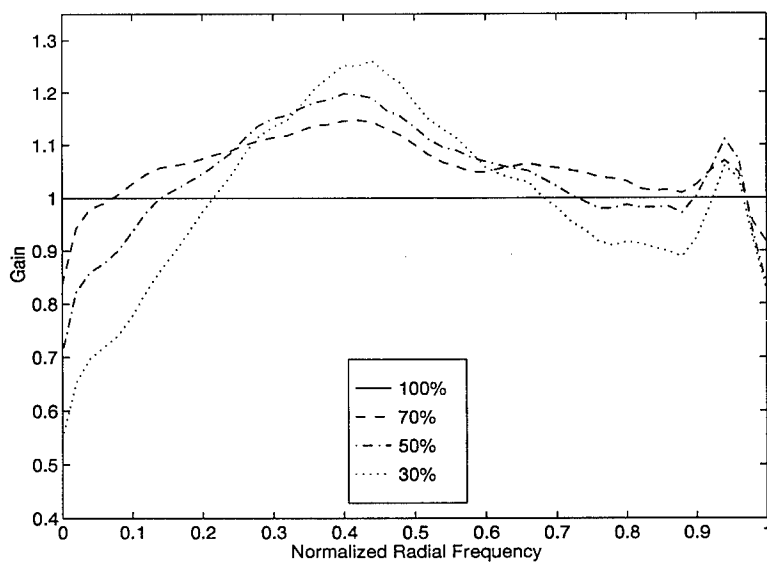
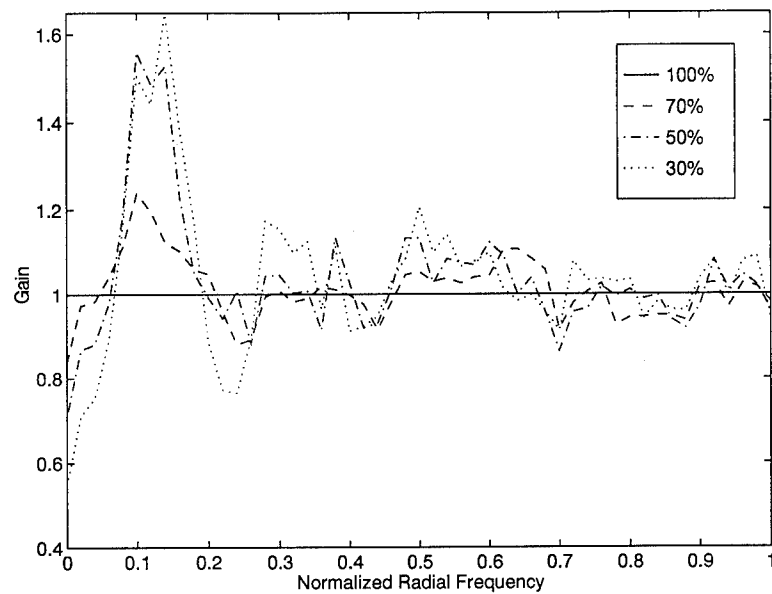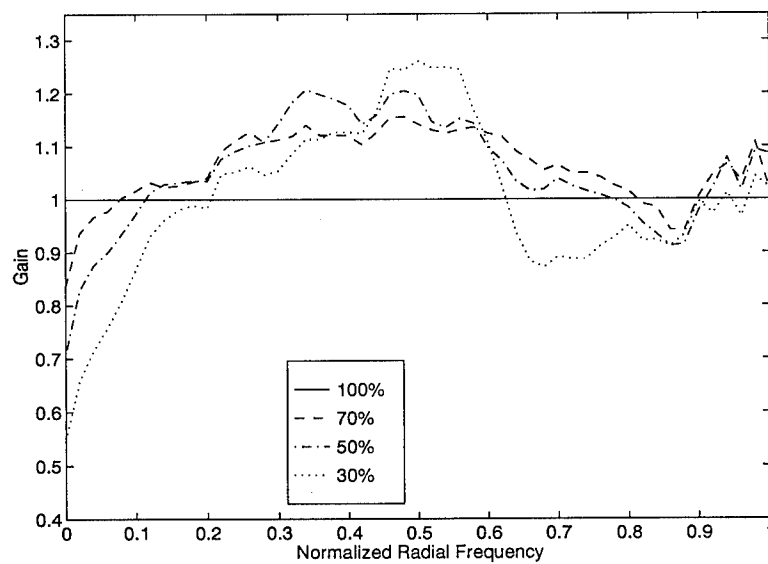Figure A.2   Gain Curves, Point Source, AO Case 1, $r_o = 5$ cm, $m_\nu = +2$
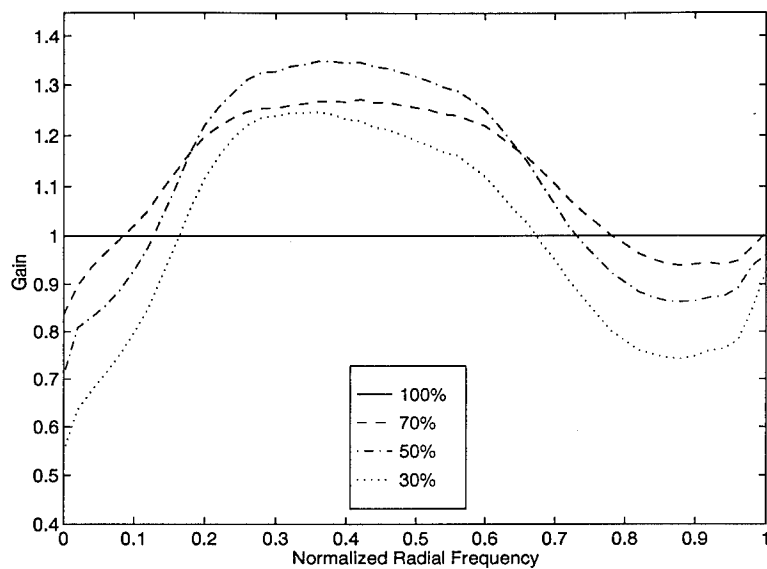
Figure A.3   Gain Curves, Point Source, AO Case 1, $r_o = 10$ cm, $m_\nu = +2$
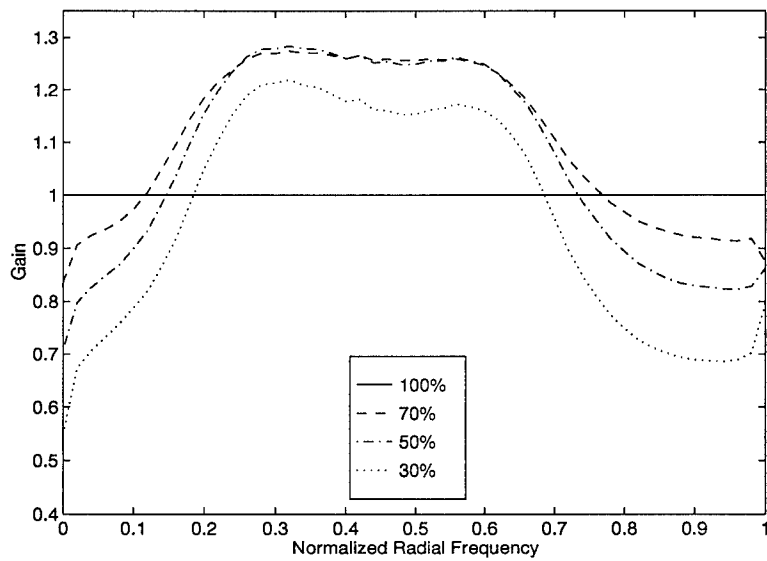
Figure A.4   Gain Curves, Point Source, AO Case 1, $r_o = 20$ cm, $m_\nu = +2$
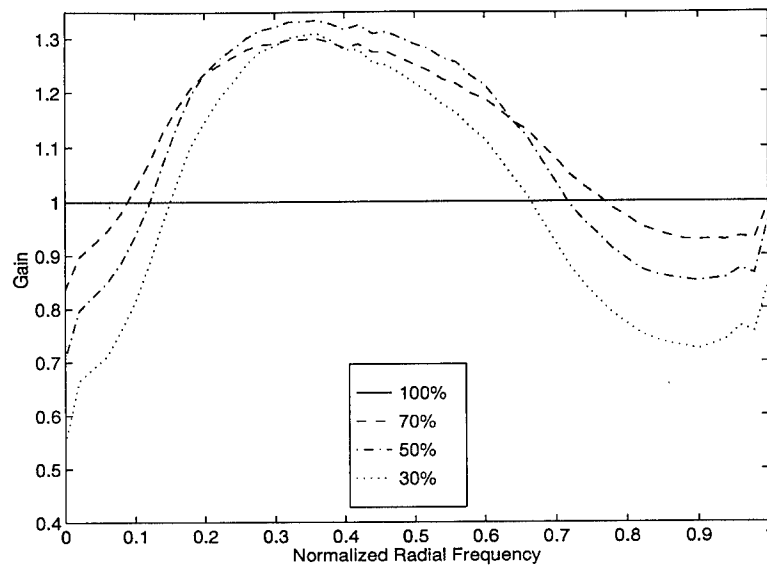
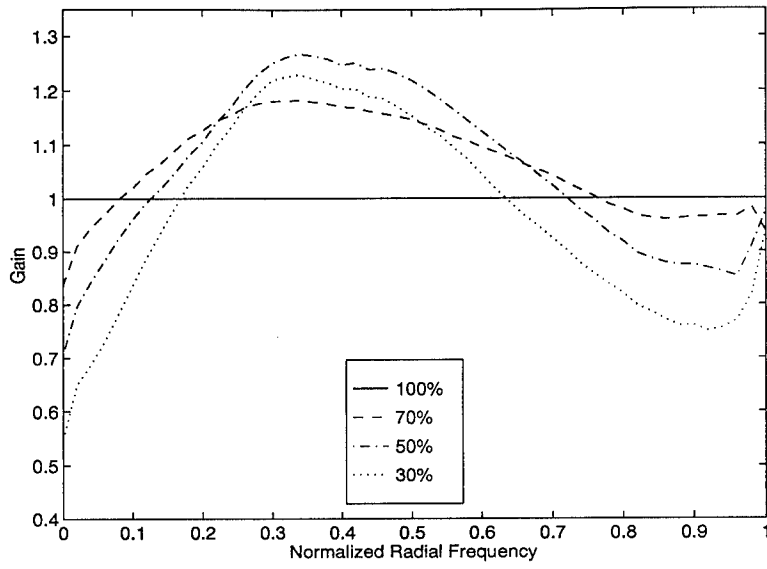Figure A.5   Gain Curves, Point Source, AO Case 1, $r_o = 10$ cm, $m_\nu = +3$
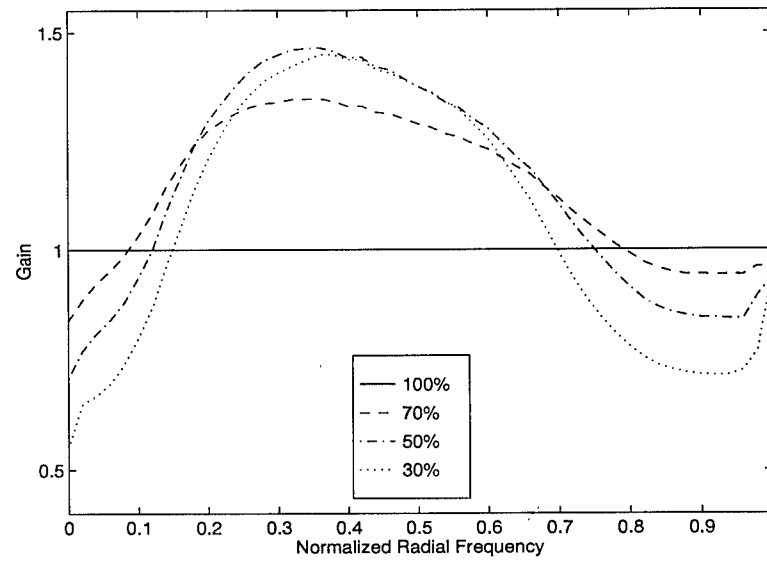
Figure A.6   Gain Curves, Point Source, AO Case 1, $r_o = 10$ cm, $m_\nu = +4$
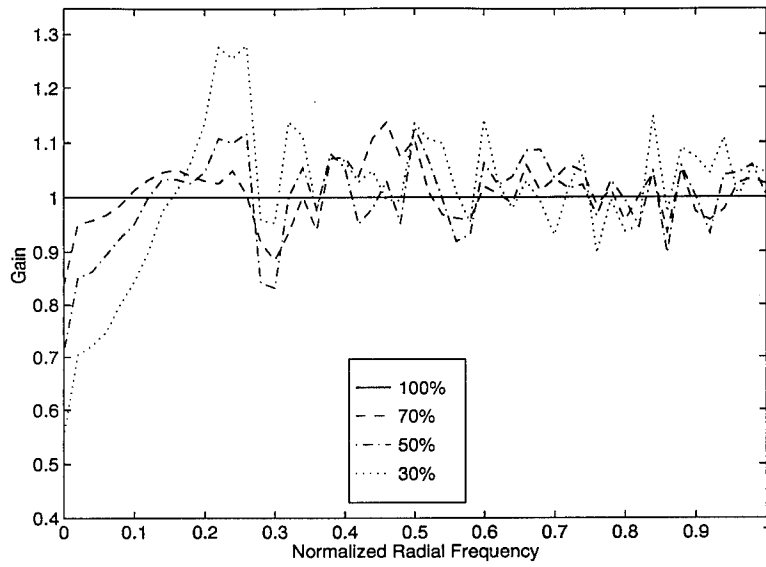
Figure A.7   Gain Curves, Point Source, AO Case 1, $r_o = 3$ cm, $m_\nu = +6$
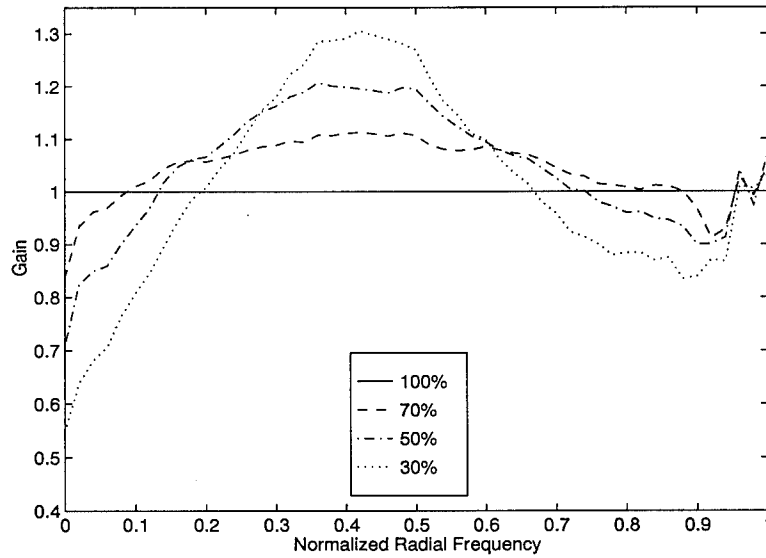
Figure A.8   Gain Curves, Point Source, AO Case 1, $r_o = 5$ cm, $m_\nu = +6$
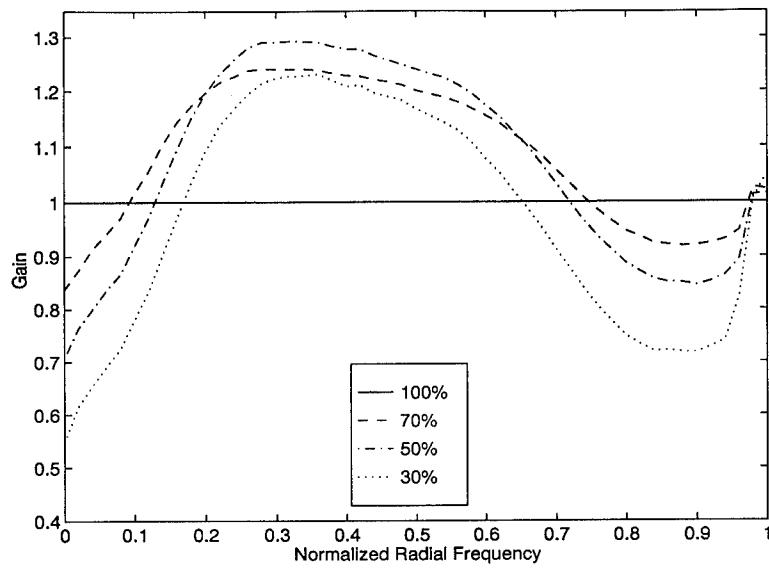
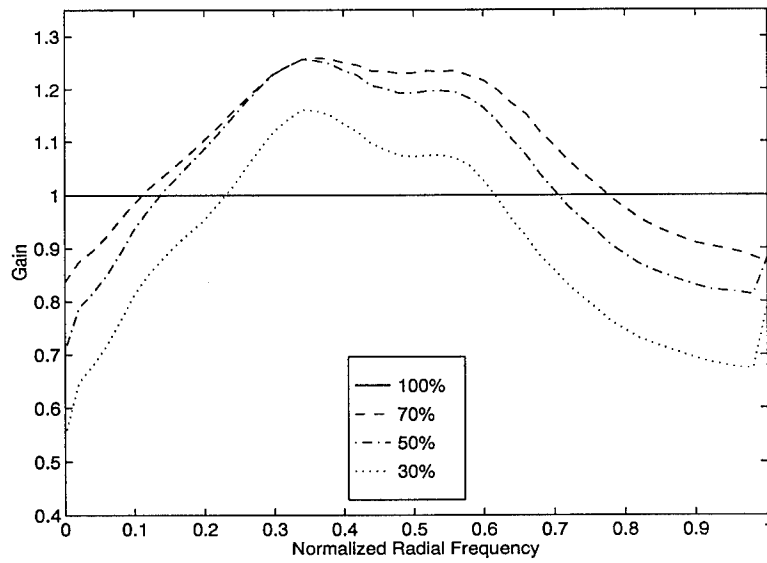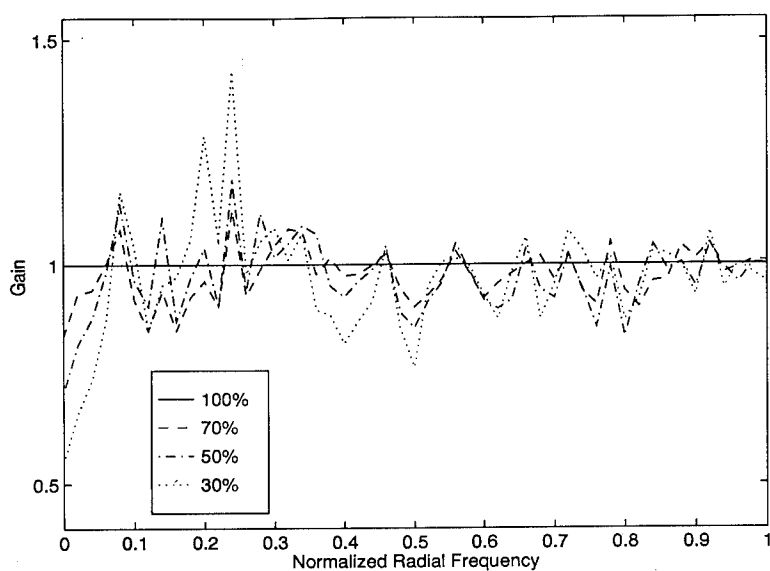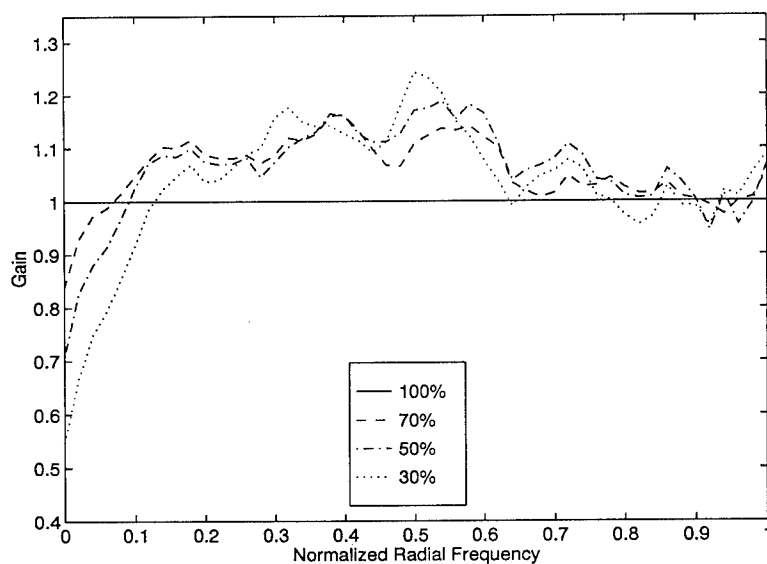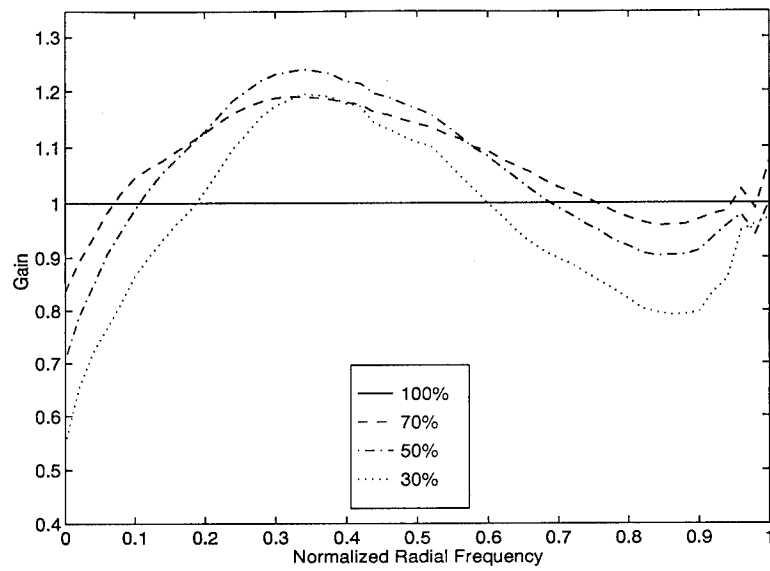Figure A.9   Gain Curves, Point Source, AO Case 1, $r_o = 10$ cm, $m_\nu = +6$
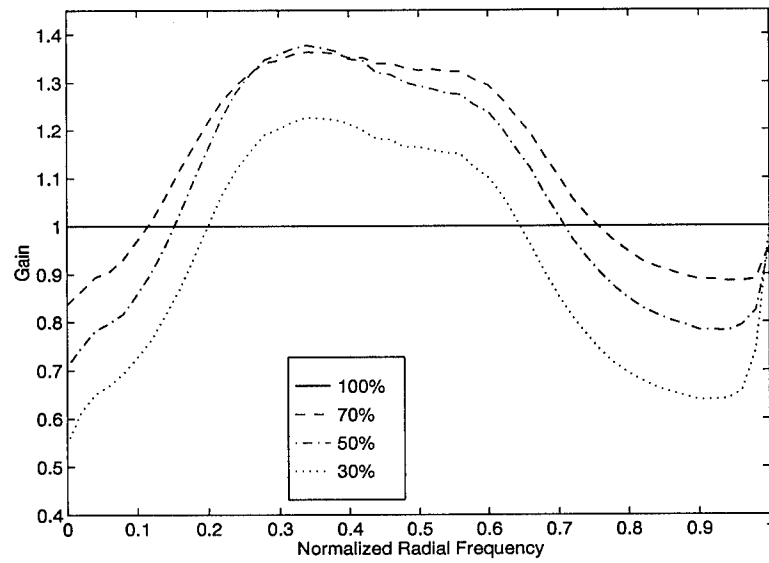
Figure A.10   Gain Curves, Point Source, AO Case 1, $r_o = 20$ cm, $m_\nu = +6$

A.2   Point Source-AO Case 2
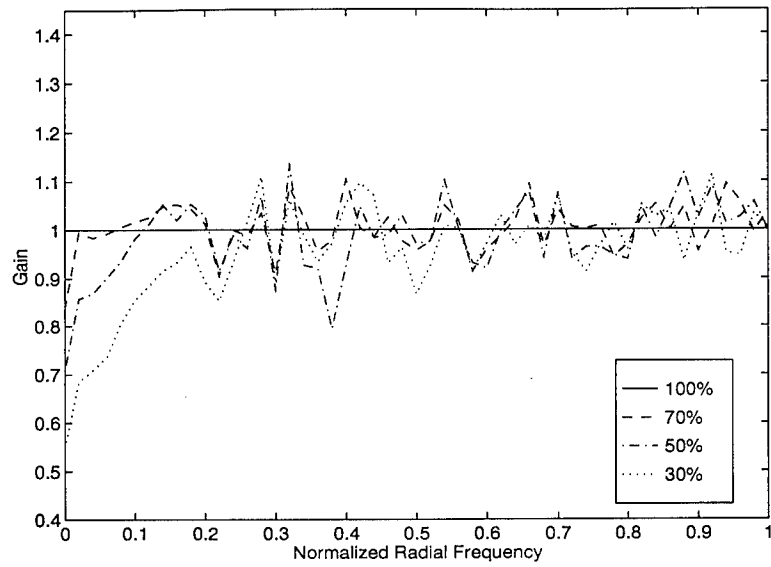
Figure A.11   Gain Curves, Satellite Model, AO Case 1, $r_o = 3$ cm, $m_\nu = +2$
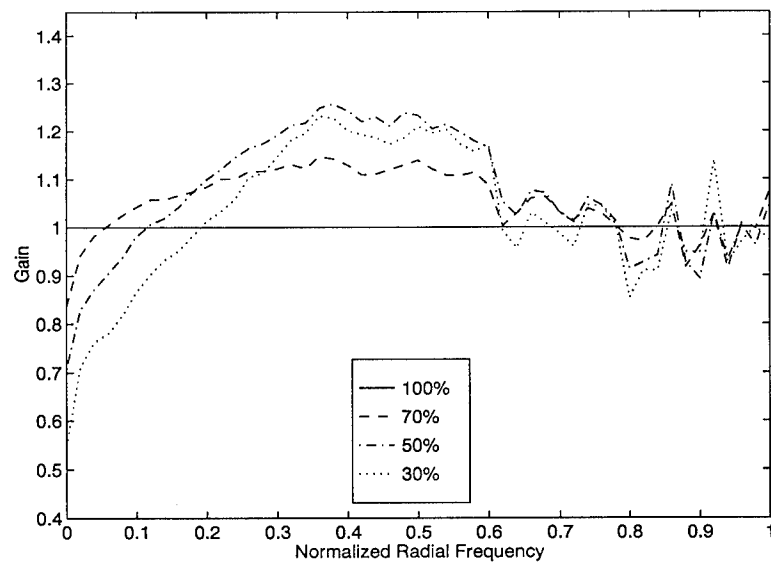
Figure A.12   Gain Curves, Satellite Model, AO Case 1, $r_o = 5$ cm, $m_\nu = +2$
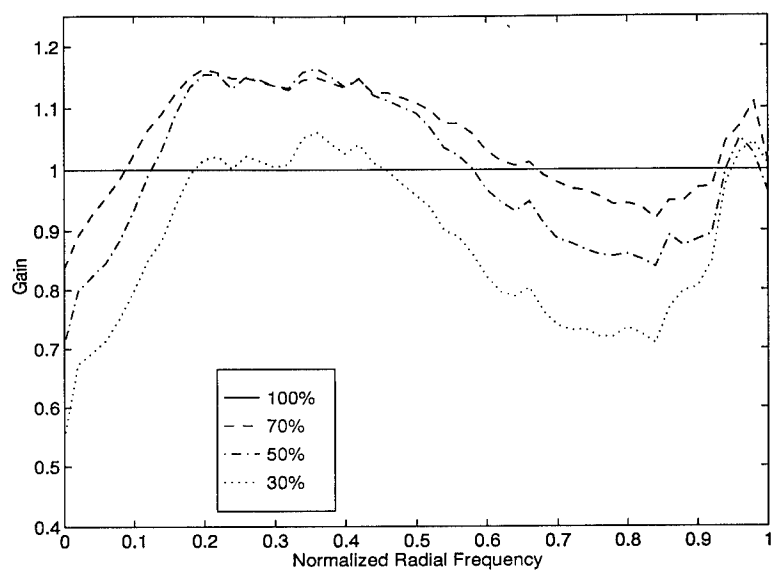
Figure A.13   Gain Curves, Satellite Model, AO Case 1, $r_o = 10$ cm, $m_\nu = +2$
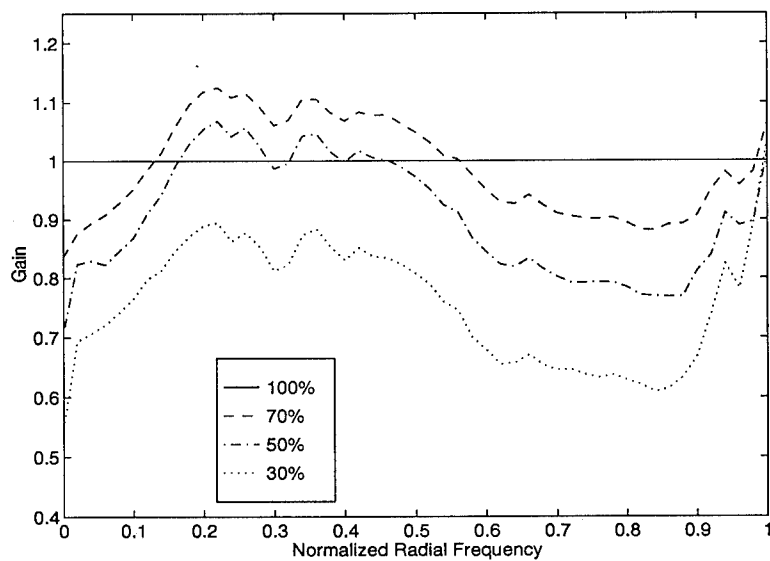
Figure A.14   Gain Curves, Satellite Model, AO Case 1, $r_o = 20$ cm, $m_\nu = +2$
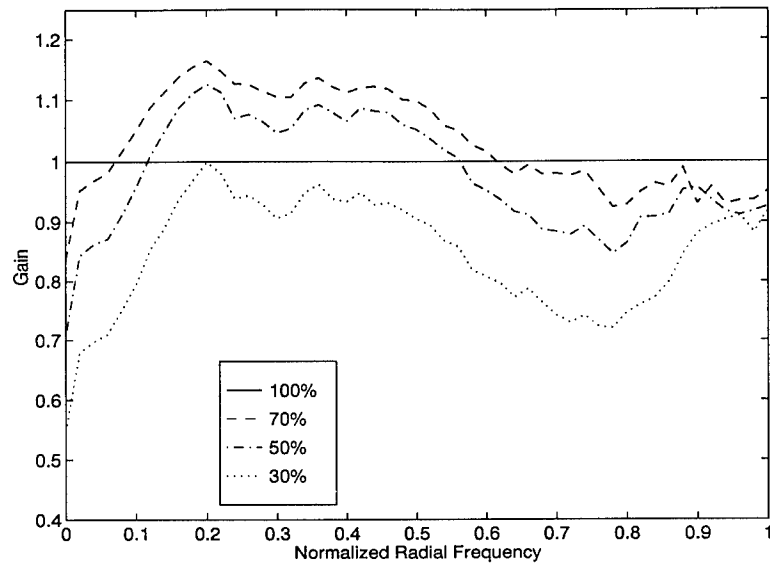
Figure A.15   Gain Curves, Satellite Model, AO Case 1, $r_o = 10$ cm, $m_\nu = +3$
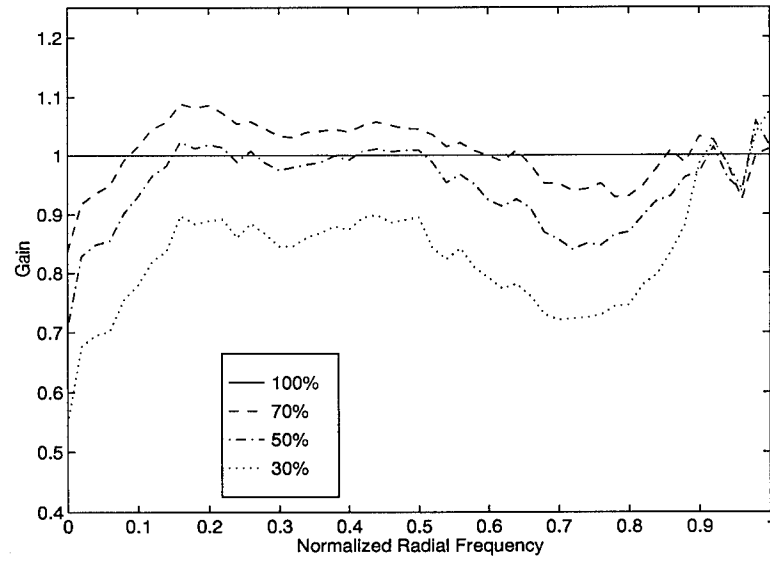
Figure A.16   Gain Curves, Satellite Model, AO Case 1, $r_o = 10$ cm, $m_\nu = +4$
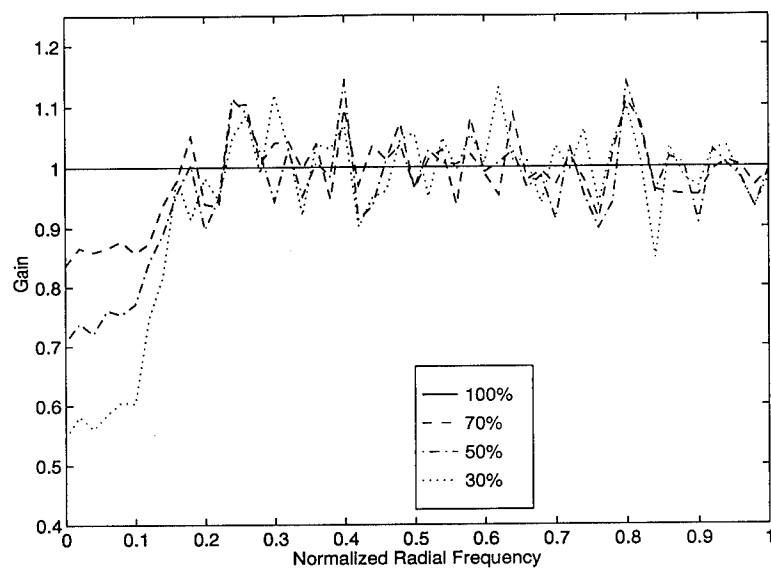
Figure A.17   Gain Curves, Satellite Model, AO Case 1, $r_o = 3$ cm, $m_\nu = +6$
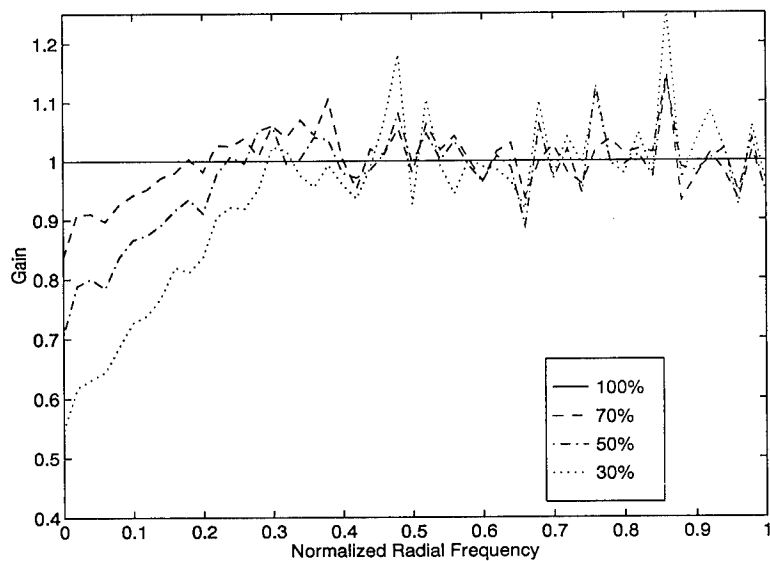
Figure A.18   Gain Curves, Satellite Model, AO Case 1, $r_o = 5$ cm, $m_\nu = +6$
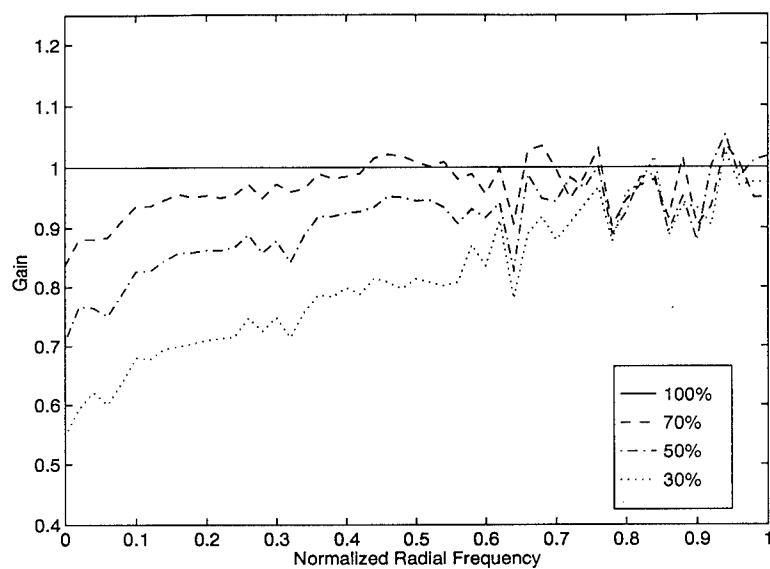
Figure A.19   Gain Curves, Satellite Model, AO Case 1, $r_o = 10$ cm, $m_\nu = +6$
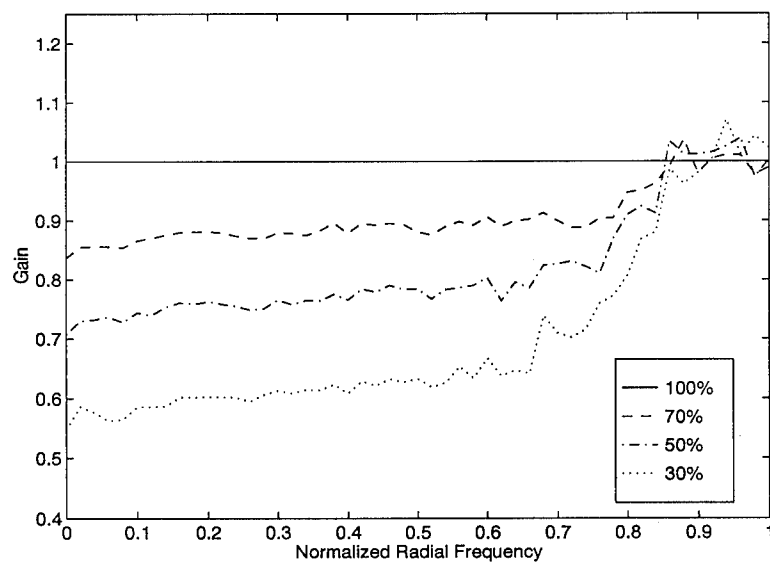
Figure A.20   Gain Curves, Satellite Model, AO Case 1, $r_o = 20$ cm, $m_\nu = +6$

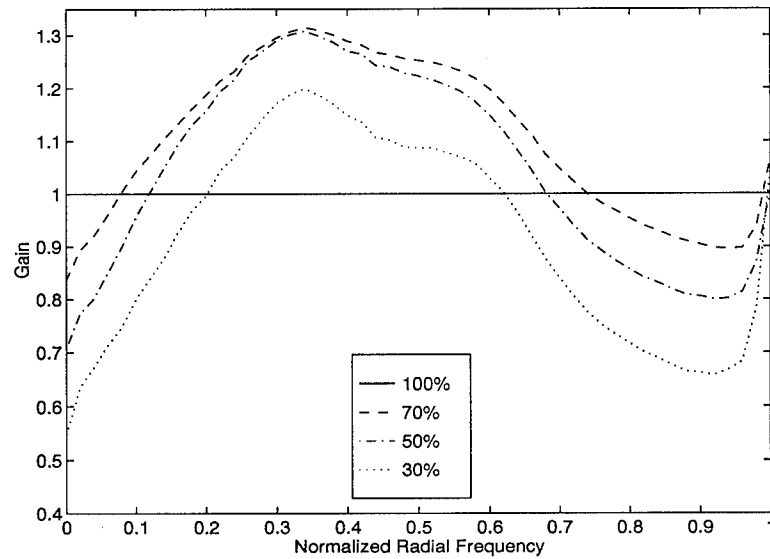Figure A.21   Gain Curves, Point Source, AO Case 2, $r_o = 3$ cm, $m_\nu = +2$

Figure A.22   Gain Curves, Point Source, AO Case 2, $r_o = 5$ cm, $m_\nu = +2$

Figure A.23   Gain Curves, Point Source, AO Case 2, $r_o = 10$ cm, $m_\nu = +2$

Figure A.24   Gain Curves, Point Source, AO Case 2, $r_o = 20$ cm, $m_\nu = +2$

Figure A.25 Gain Curves, Point Source, AO Case 2, $r_o = 3$ cm, $m_\nu = +6$

Figure A.26 Gain Curves, Point Source, AO Case 2, $r_o = 5$ cm, $m_\nu = +6$

Figure A.27   Gain Curves, Point Source, AO Case 2, $r_o = 10$ cm, $m_\nu = +6$

Figure A.28   Gain Curves, Point Source, AO Case 2, $r_o = 20$ cm, $m_\nu = +6$
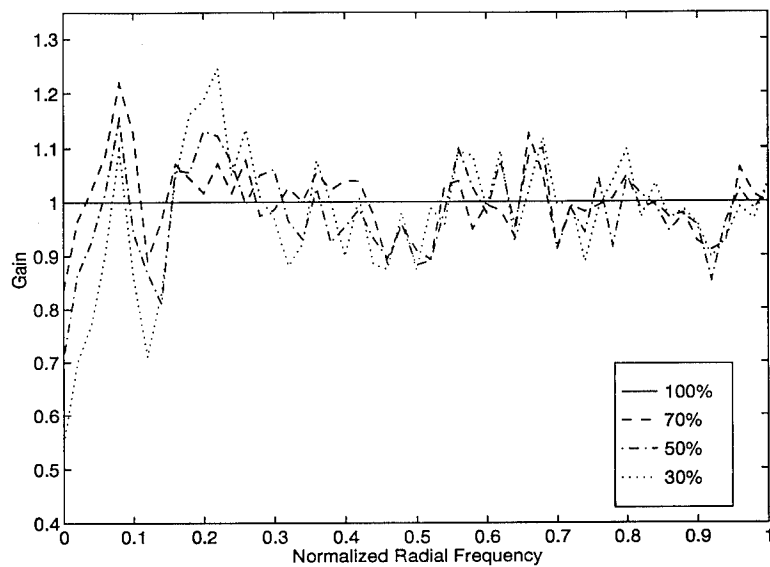
Figure A.29   Gain Curves, Satellite Model, AO Case 2, $r_o = 3$ cm, $m_\nu = +2$
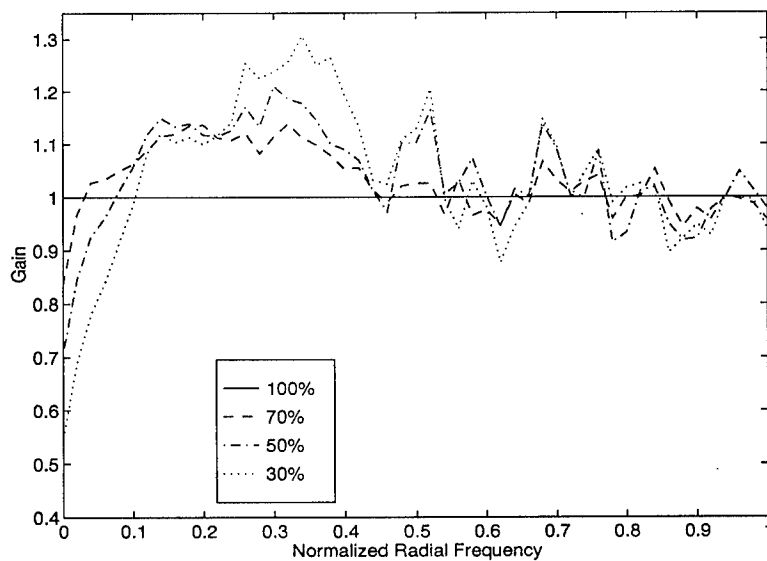
Figure A.30   Gain Curves, Satellite Model, AO Case 2, $r_o = 5$ cm, $m_\nu = +2$
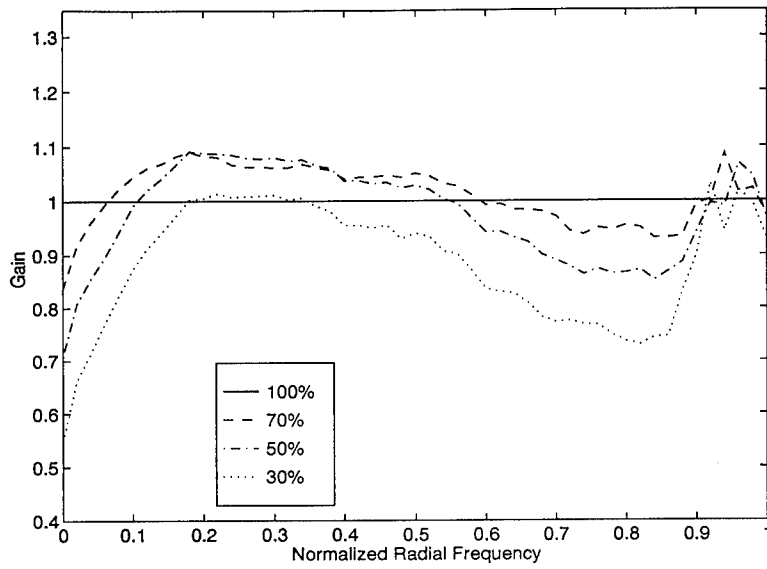
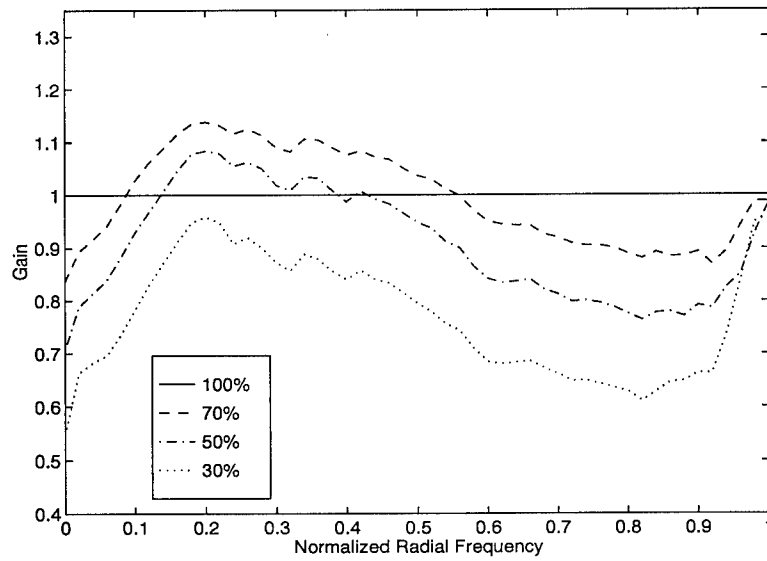Figure A.31   Gain Curves, Satellite Model, AO Case 2, $r_o = 10$ cm, $m_\nu = +2$

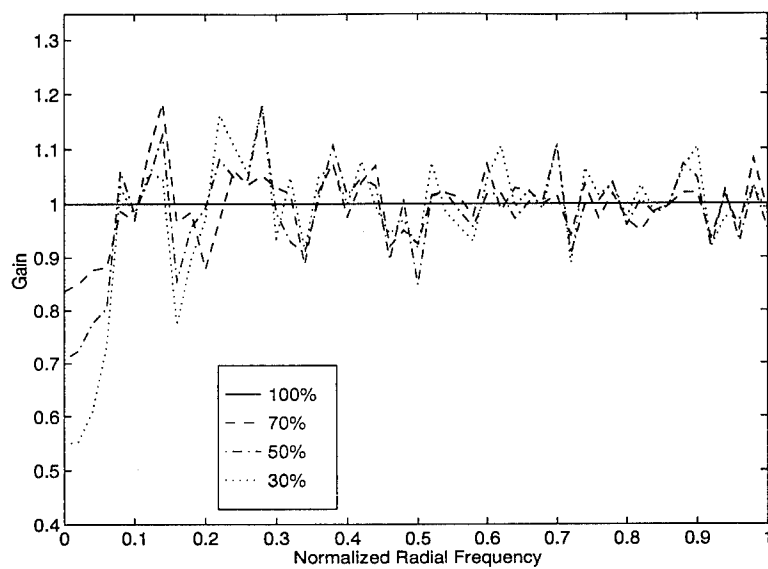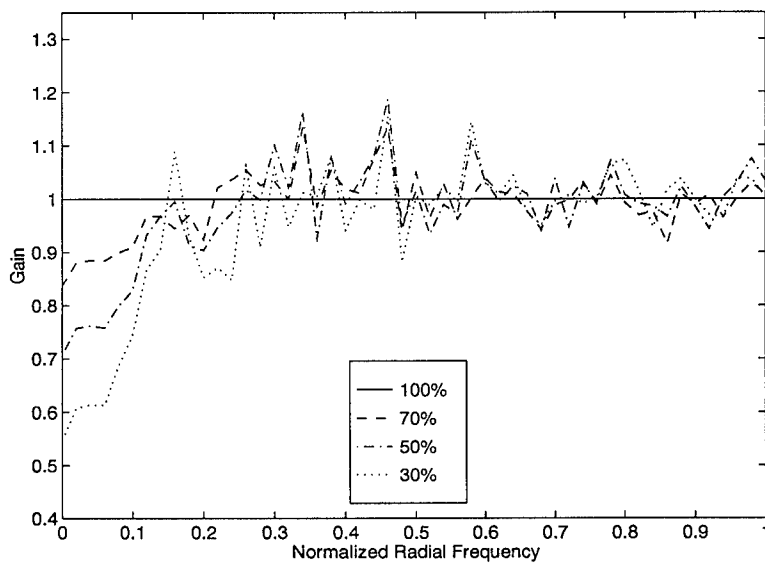Figure A.32   Gain Curves, Satellite Model, AO Case 2, $r_o = 20$ cm, $m_\nu = +2$

A-17

Figure A.33   Gain Curves, Satellite Model, AO Case 2, $r_o = 3$ cm, $m_\nu = +6$

Figure A.34   Gain Curves, Satellite Model, AO Case 2, $r_o = 5$ cm, $m_\nu = +6$
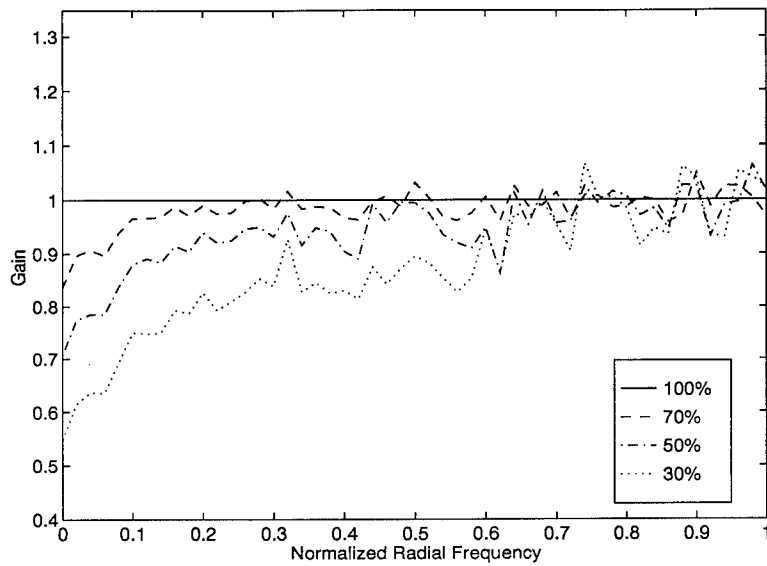
Figure A.35   Gain Curves, Satellite Model, AO Case 2, $r_o = 10$ cm, $m_\nu = +6$
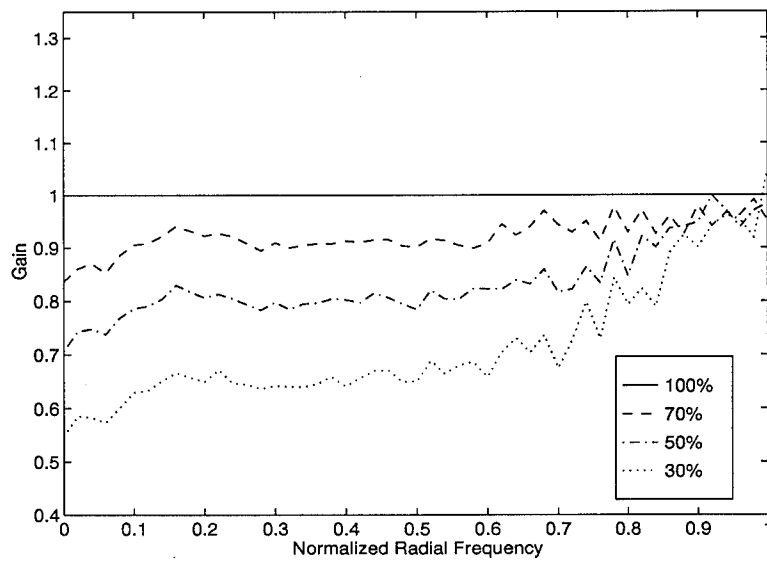

Figure A.36   Gain Curves, Satellite Model, AO Case 2, $r_o = 20$ cm, $m_\nu = +6$

Appendix B. Frame Weighting Simulation Results

This appendix contains additional frame weighting distributions and gain curves for Experiment Four, Chapter Four.
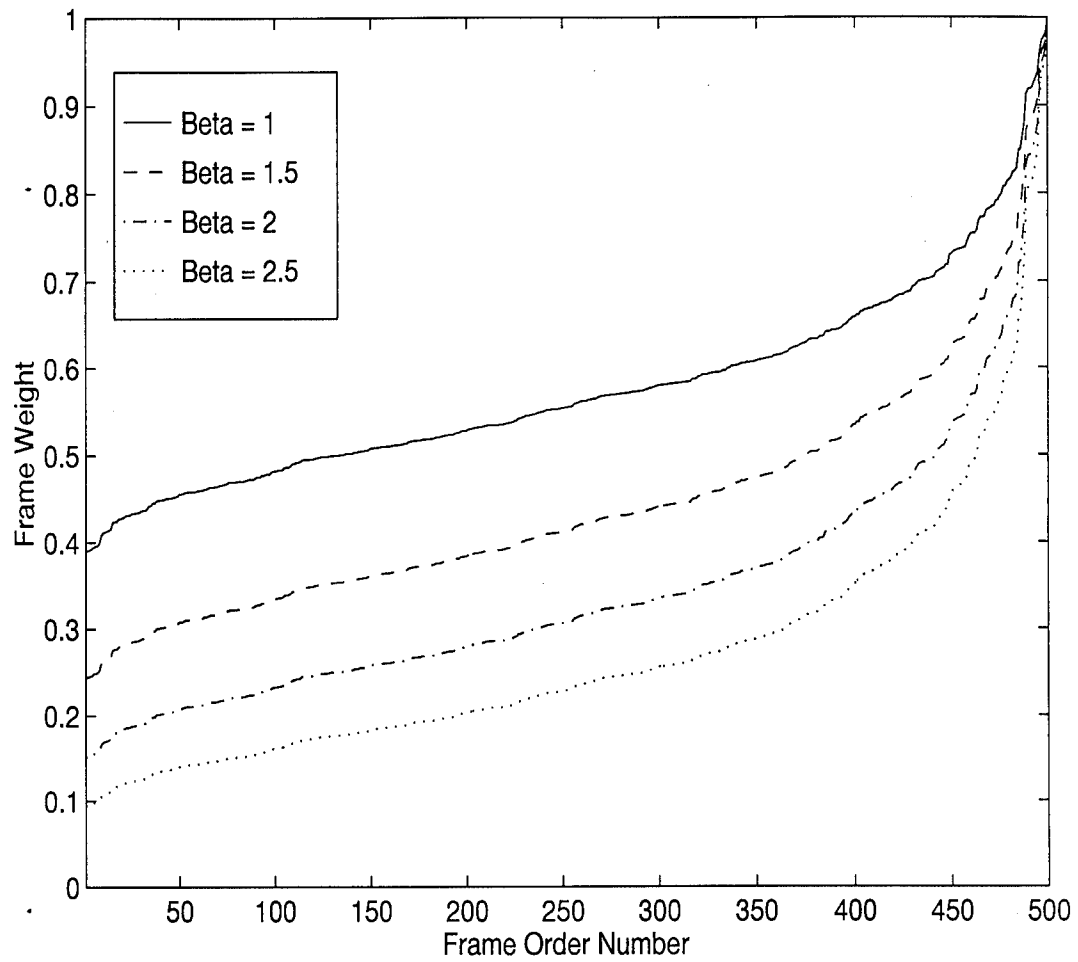
Figure B.1   Quality-Based Weighting Distributions versus Frame Order Number as a Function of the β Parameter. $r_o = 5$ cm, $m_\nu = +2$, Point Source, AO Case 1
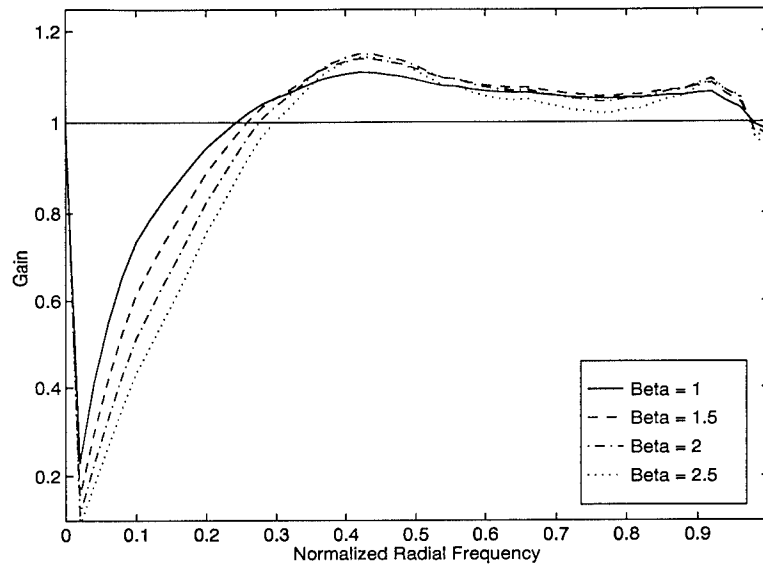
Figure B.2 Quality-Based Frame Weighting Gain Curves, $r_o = 5$ cm, $m_\nu = +2$, Point Source, AO Case 1

Figure B.3 Function-Based Frame Weighting Gain Curves, $r_o = 5$ cm, $m_\nu = +2$, Point Source, AO Case 1

Figure B.4 Quality-Based Weighting Distributions versus Frame Order Number as a Function of the β Parameter. $r_o = 10$ cm, $m_\nu = +8$, Point Source, AO Case 1

Figure B.5   Quality-Based Frame Weighting Gain Curves, $r_o = 10$ cm, $m_\nu = +8$, Point Source, AO Case 1
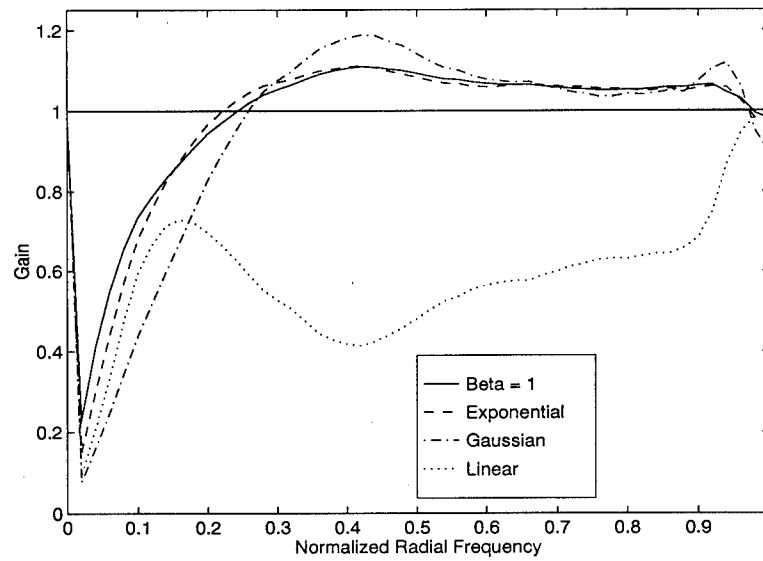

Figure B.6   Function-Based Frame Weighting Gain Curves, $r_o = 10$ cm, $m_\nu = +8$, Point Source, AO Case 1
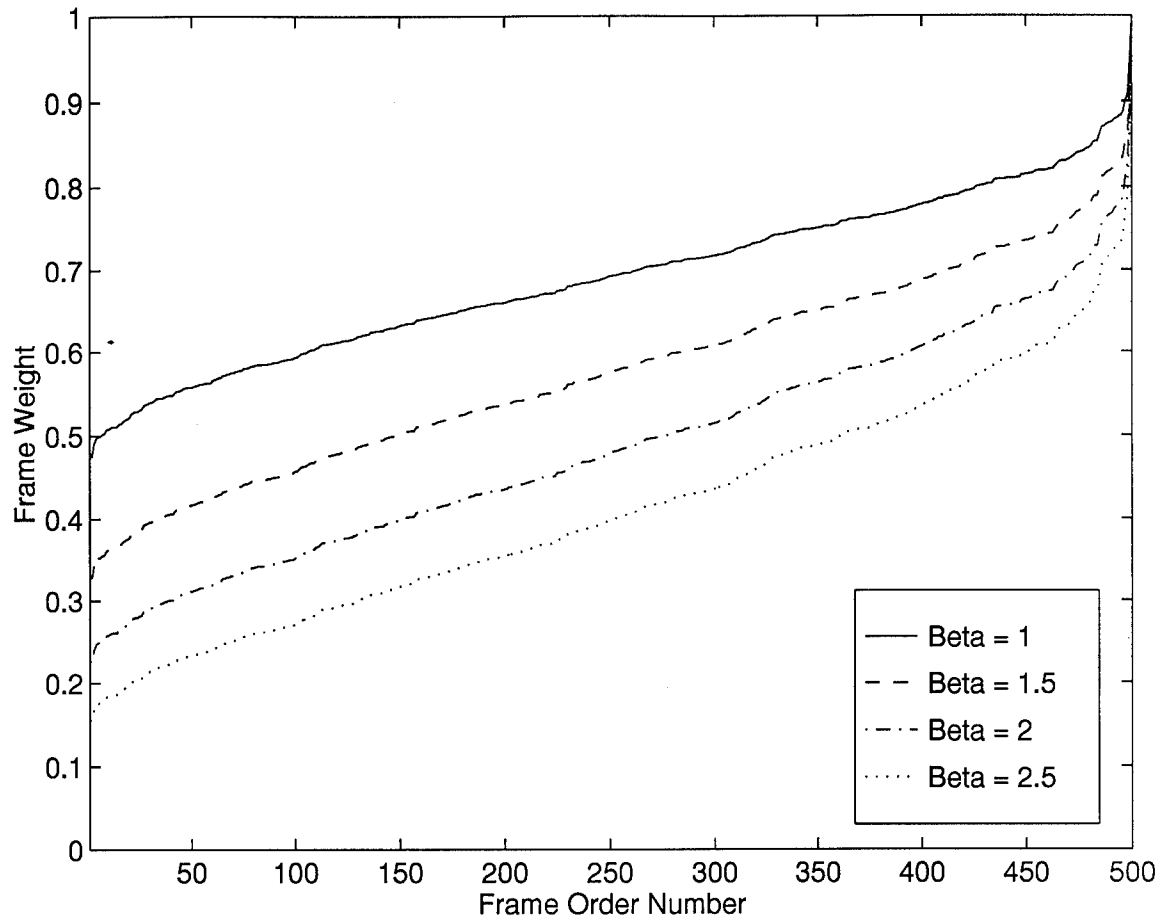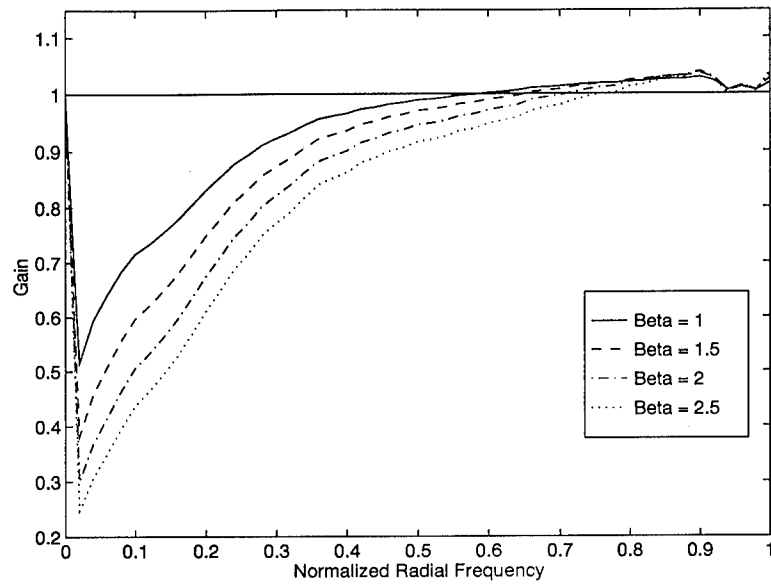
Figure B.7   Quality-Based Weighting Distributions versus Frame Order Number as a Function of the β Parameter. $r_o = 5$ cm, $m_\nu = +2$, Satellite Model, AO Case 1

Figure B.8   Quality-Based Frame Weighting Gain Curves, $r_o = 5$ cm, $m_\nu = +2$, Satellite Model, AO Case 1

Figure B.9   Function-Based Frame Weighting Gain Curves, $r_o = 5$ cm, $m_\nu = +2$, Satellite Model, AO Case 1
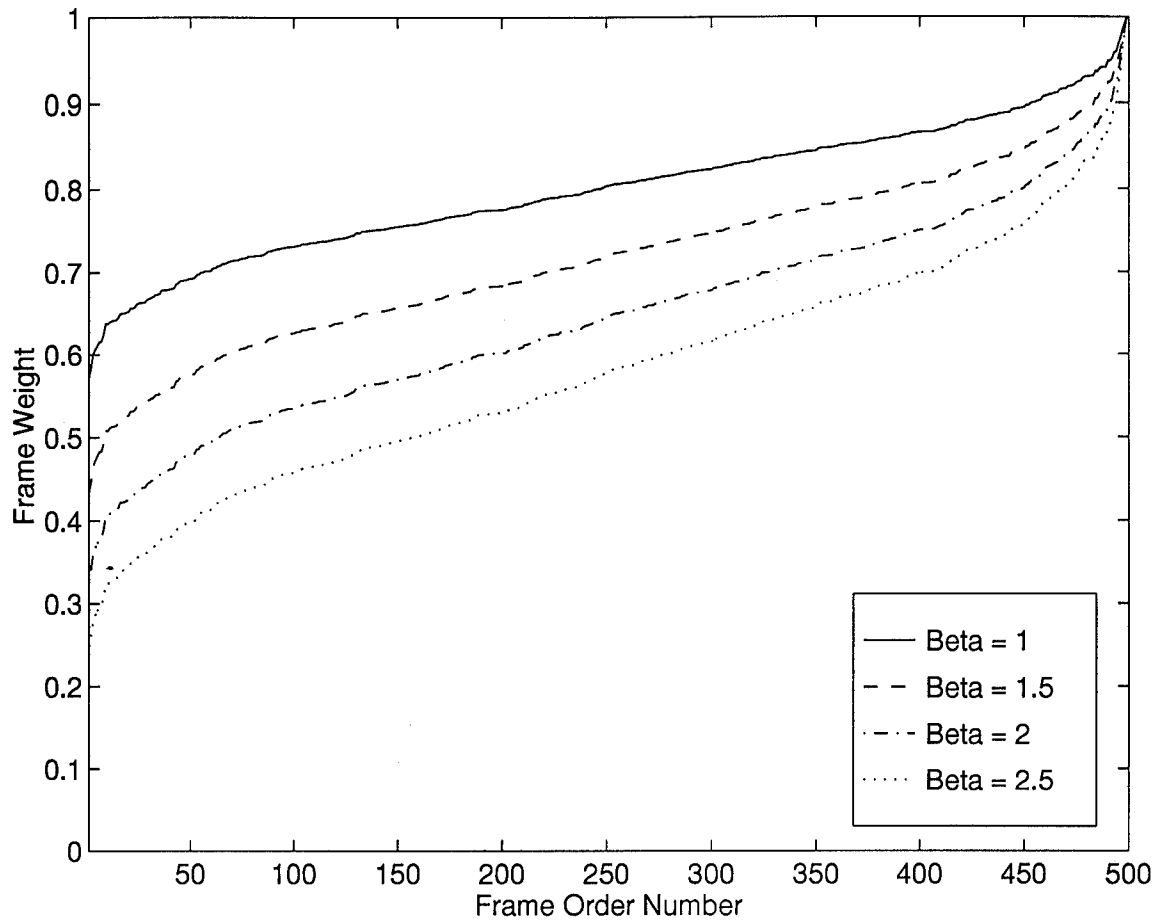
Figure B.10   Quality-Based Weighting Distributions versus Frame Order Number as a Function of the β Parameter. $r_o = 10$ cm, $m_\nu = +2$, Satellite Model, AO Case 1
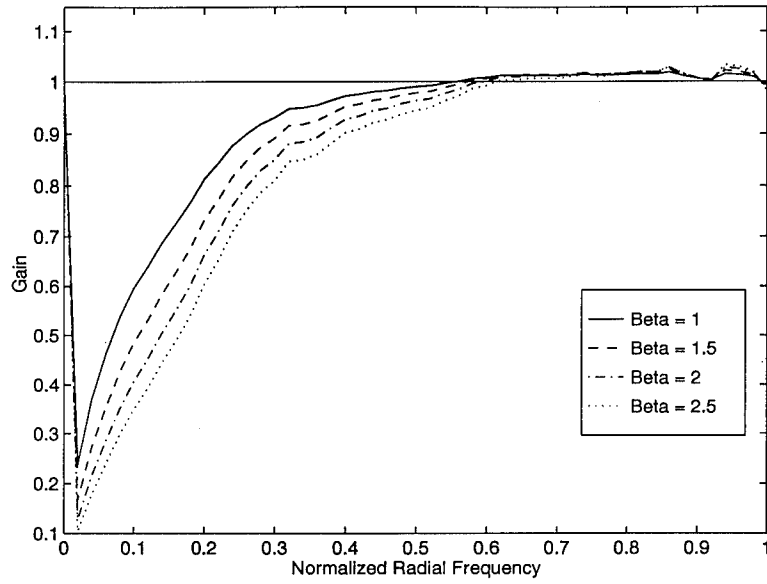
Figure B.11 Quality-Based Frame Weighting Gain Curves, $r_o = 10$ cm, $m_\nu = +2$, Satellite Model, AO Case 1
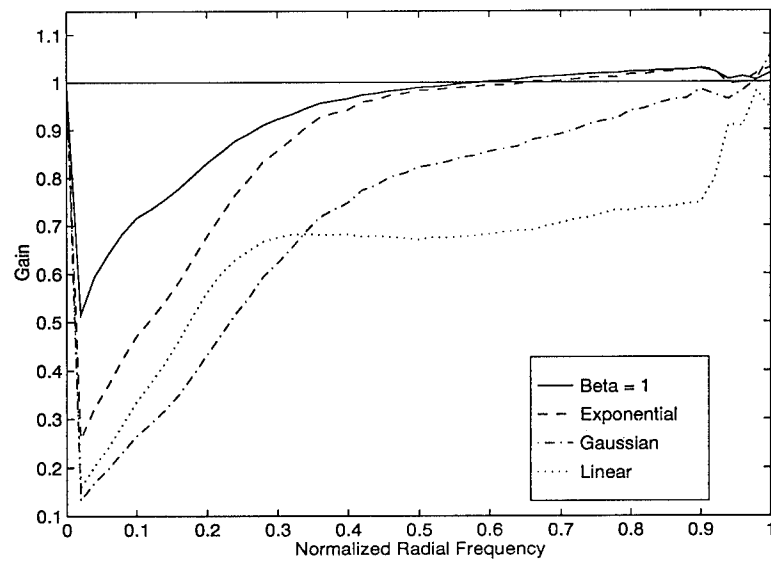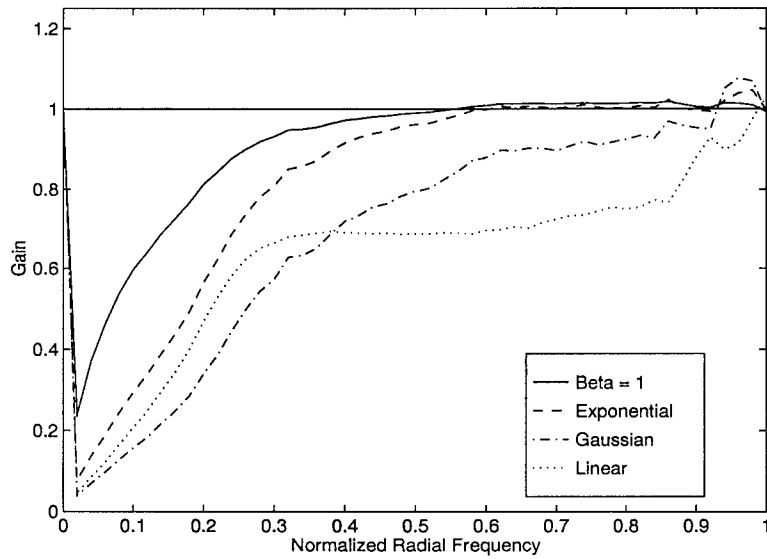

Figure B.12 Function-Based Frame Weighting Gain Curves, $r_o = 10$ cm, $m_\nu = +2$, Satellite Model, AO Case 1
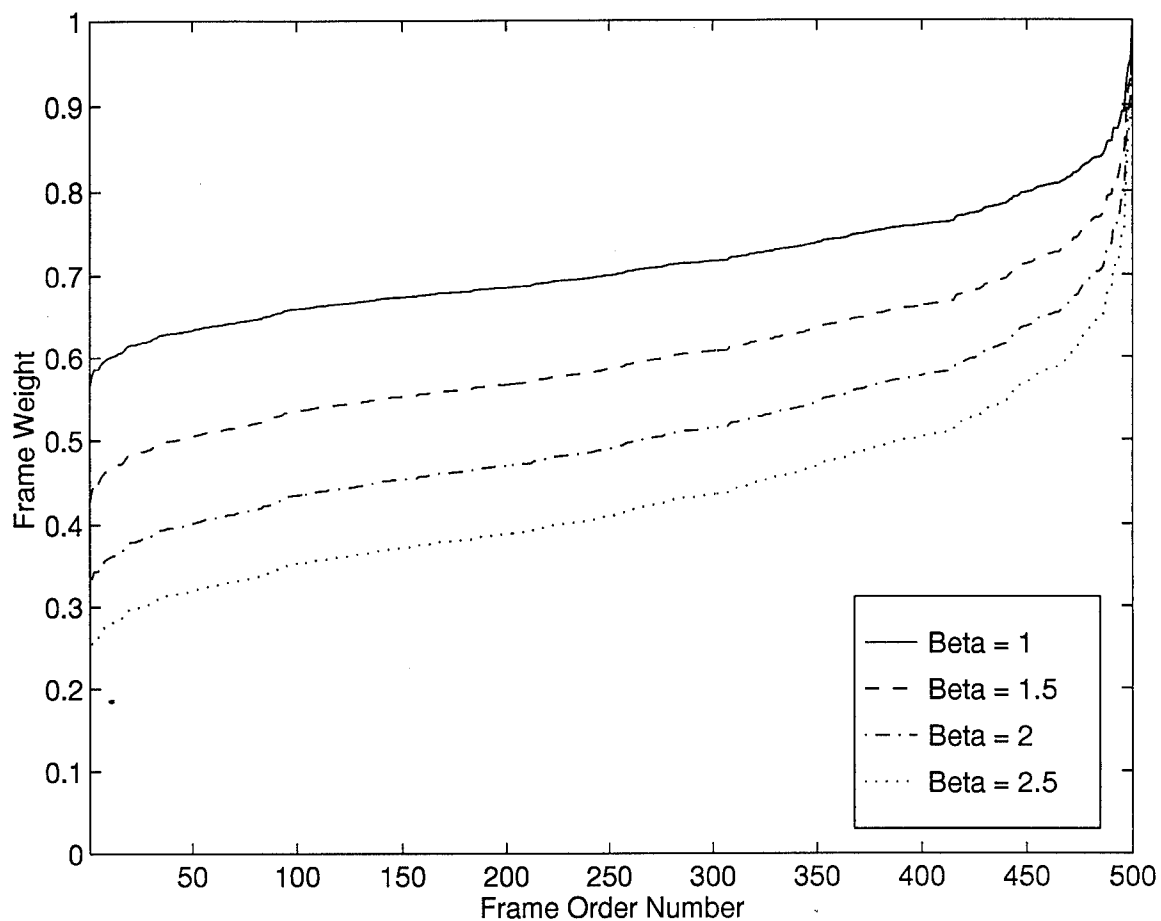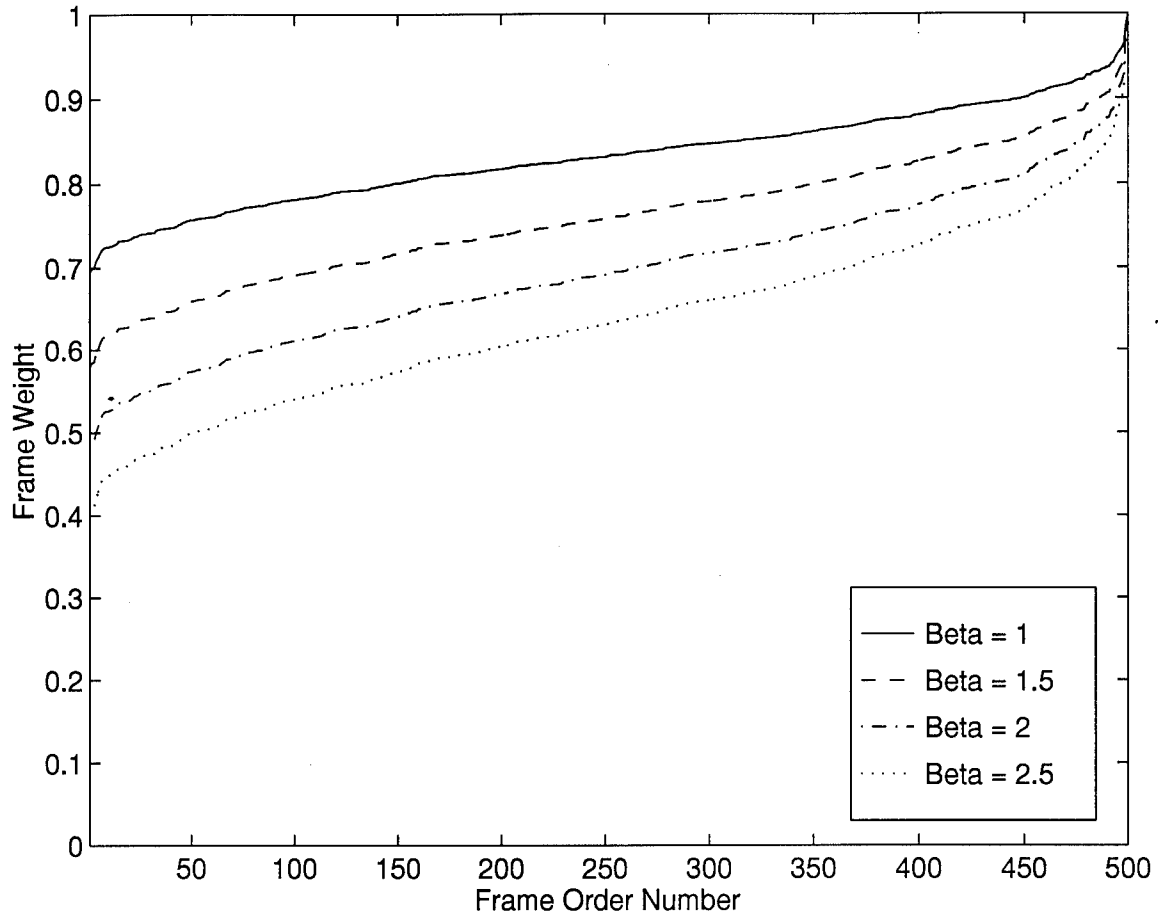
Figure B.13   Quality-Based Weighting Distributions versus Frame Order Number as a Function of the β Parameter. $r_o = 10$ cm, $m_\nu = +4$, Satellite Model, AO Case 1
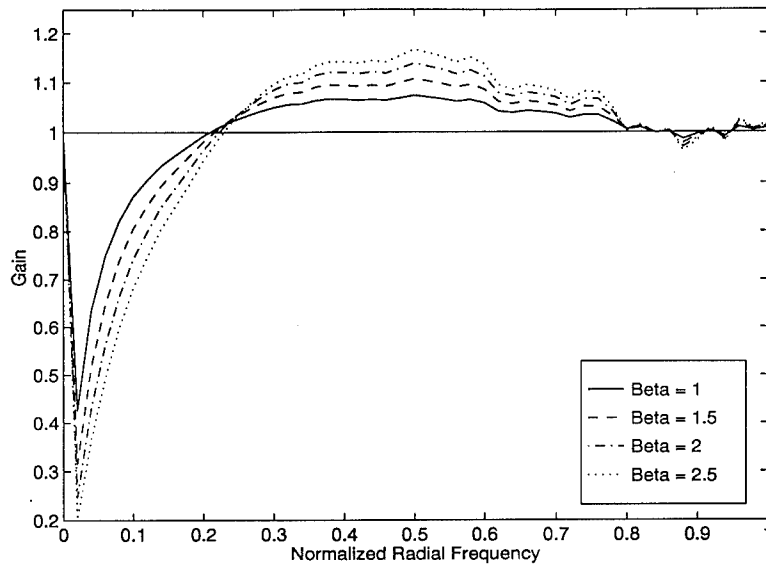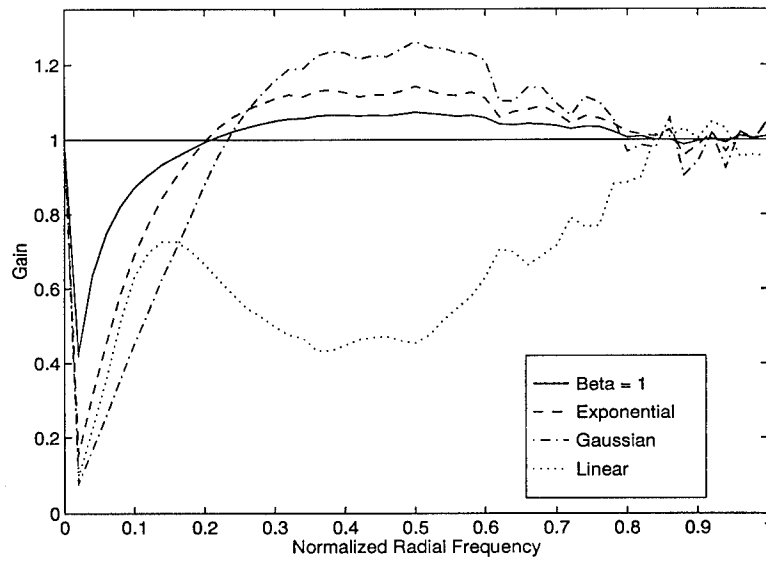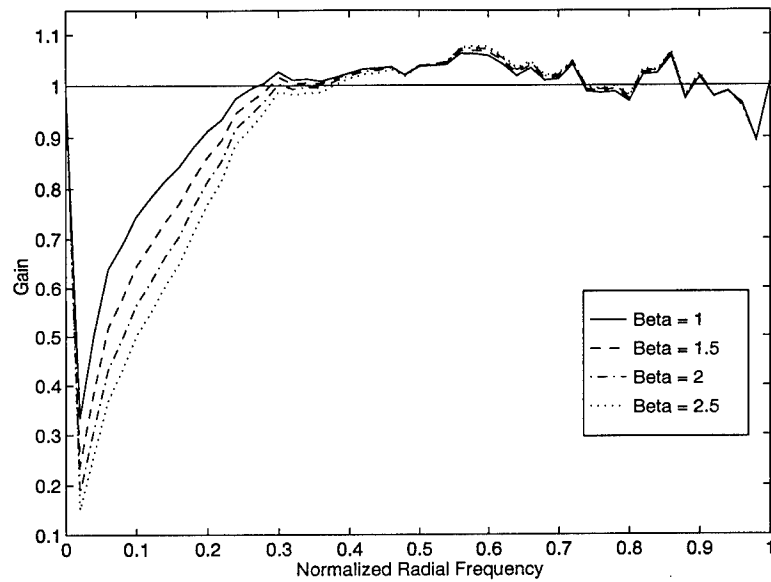
Figure B.14   Quality-Based Frame Weighting Gain Curves, $r_o = 10$ cm, $m_\nu = -4$, Satellite Model, AO Case 1
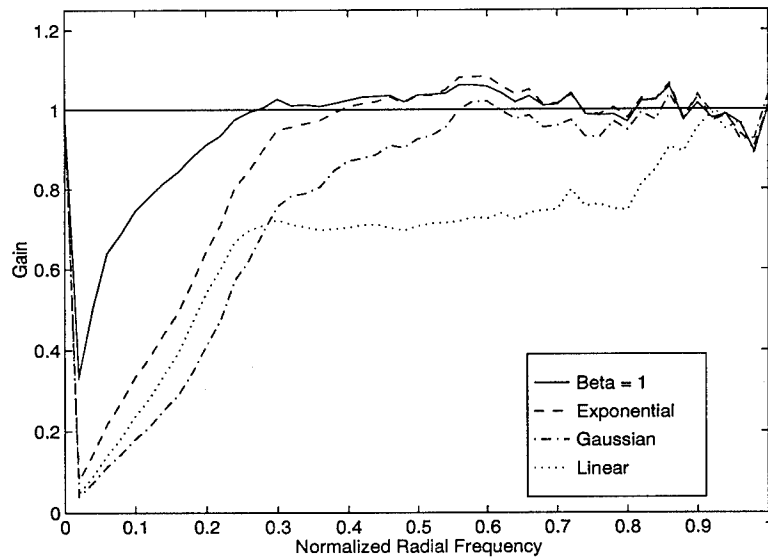
Figure B.15   Function-Based Frame Weighting Gain Curves, $r_o = 10$ cm, $m_\nu = -4$, Satellite Model, AO Case 1

B-11

Appendix C. Air Force Maui Optical Site (AMOS) Data Results

This appendix contains additional gain curves for Experiment Five, Chapter Four.
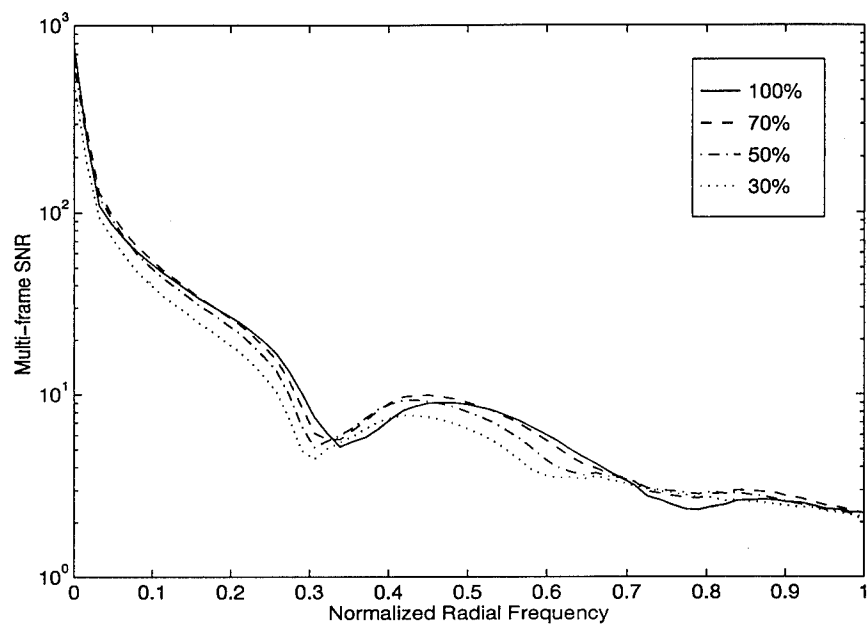
Figure C.1   Multi-frame Image Spectrum SNR, AMOS Tape 1, Reference Star
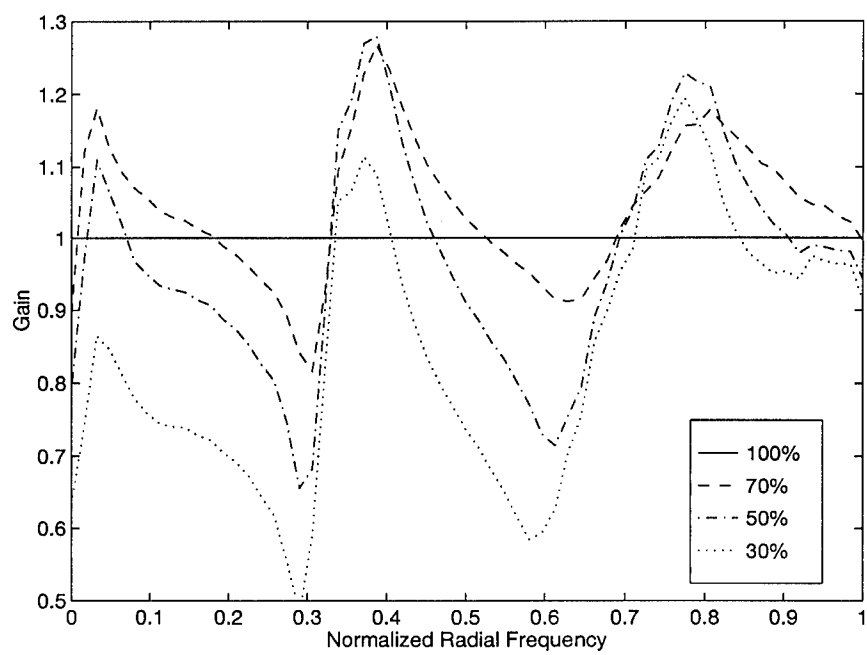
Figure C.2   Gain Curves, AMOS Tape 1, Reference Star
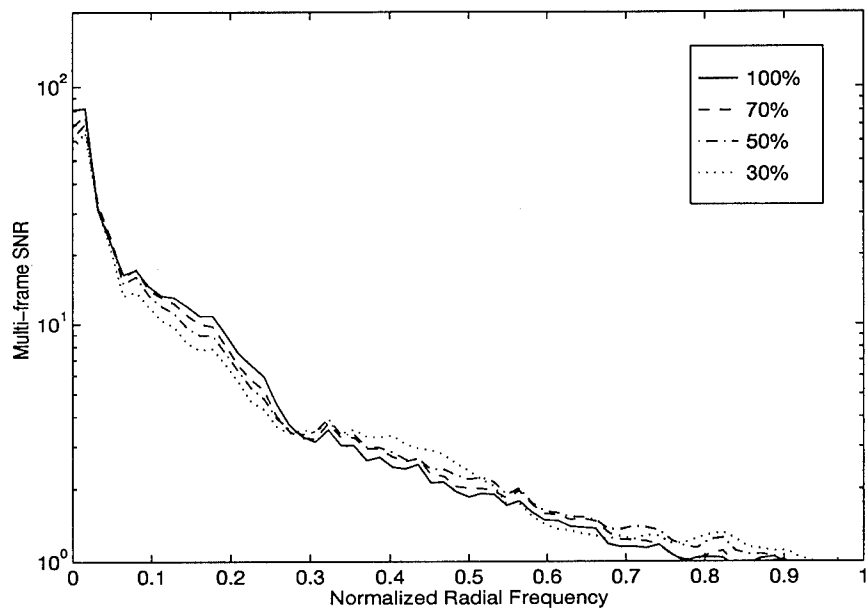
Figure C.3   Multi-frame Image Spectrum SNR, AMOS Tape 1, Satellite
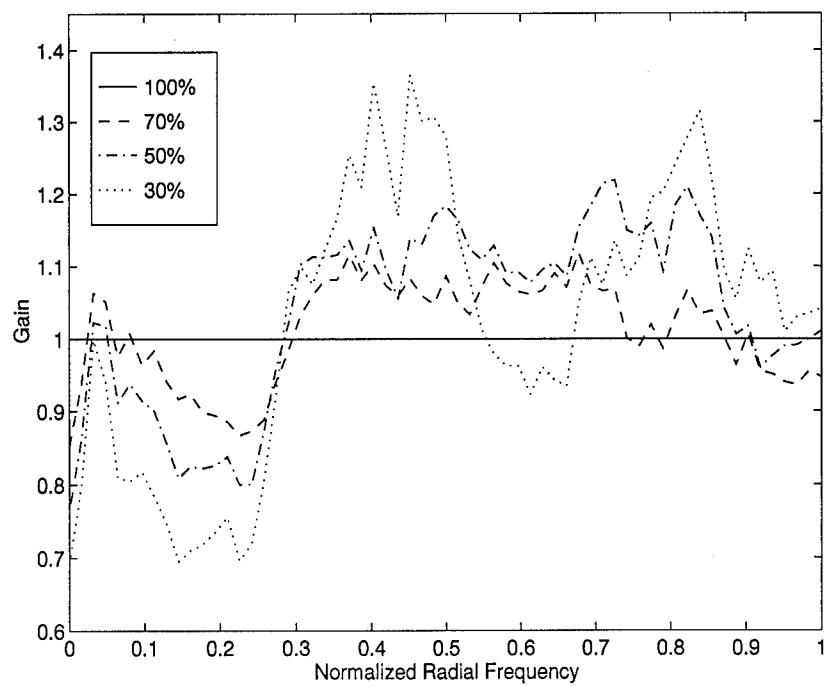
Figure C.4   Gain Curves, AMOS Tape 1, Satellite
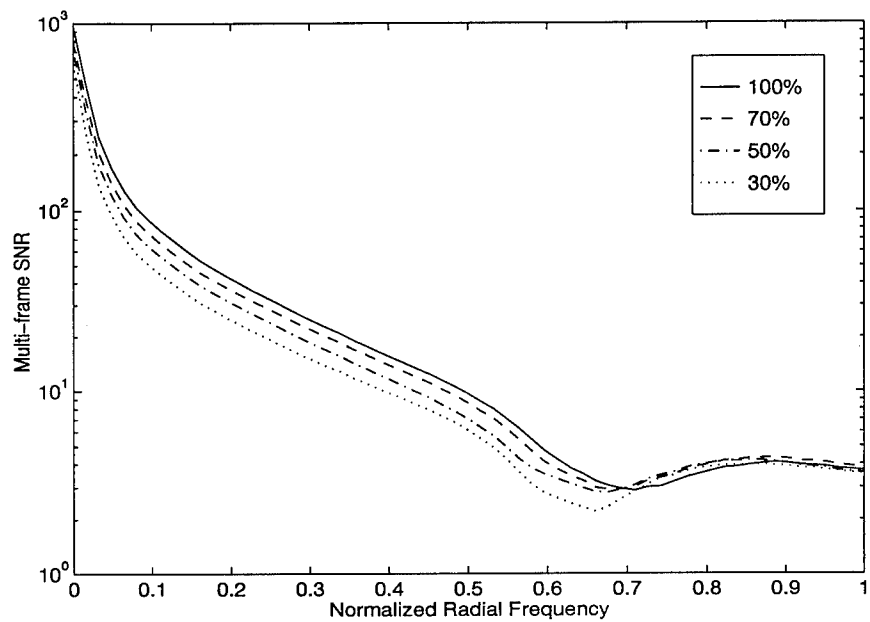
Figure C.5   Multi-frame Image Spectrum SNR, AMOS Tape 3, Reference Star
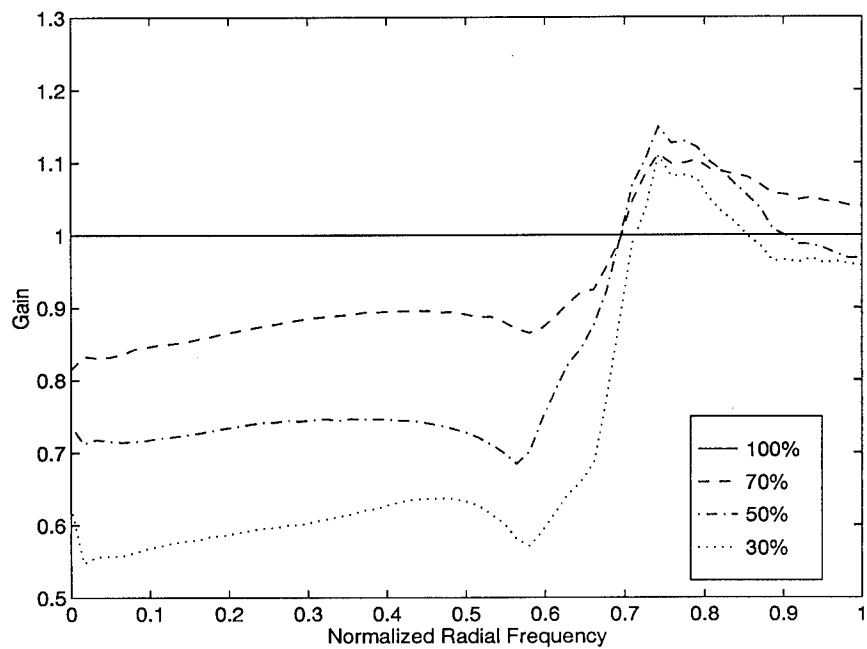
Figure C.6   Gain Curves, AMOS Tape 3, Reference Star
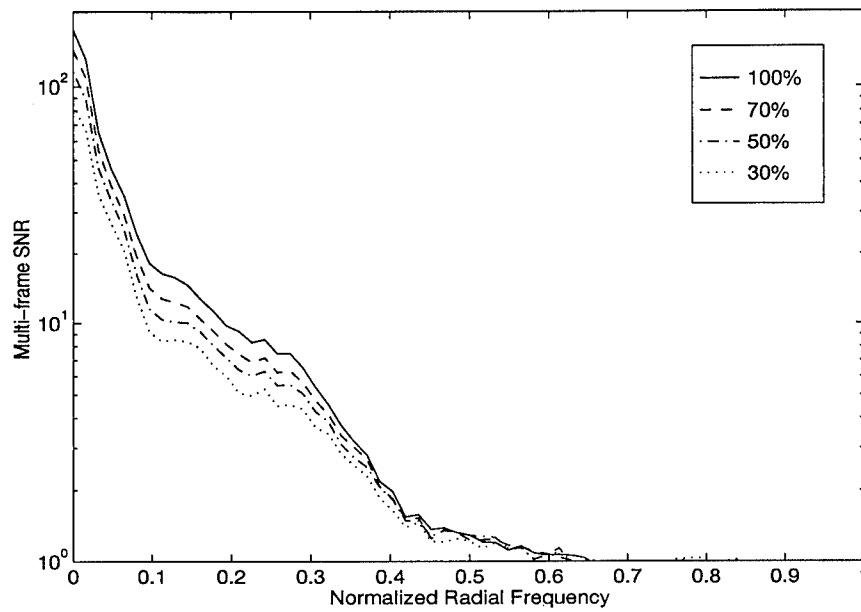
Figure C.7   Multi-frame Image Spectrum SNR, AMOS Tape 4, Satellite
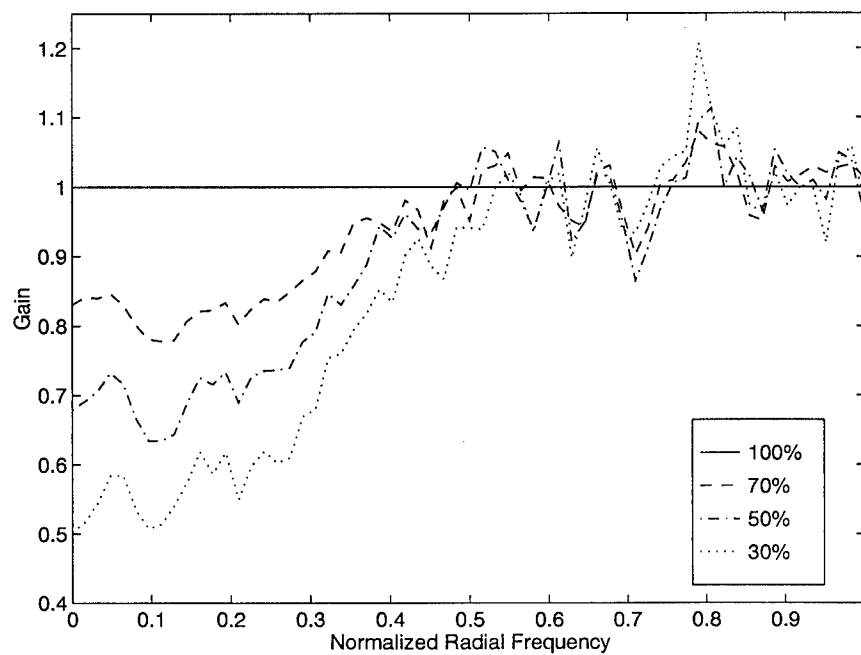
Figure C.8   Gain Curves, AMOS Tape 4, Satellite
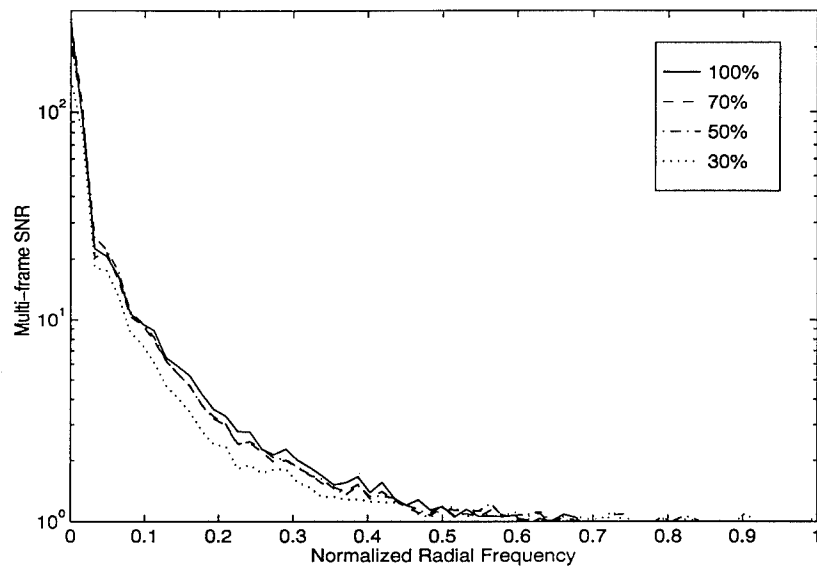
Figure C.9   Multi-frame Image Spectrum SNR, AMOS Tape 5, Hubble Space Telescope
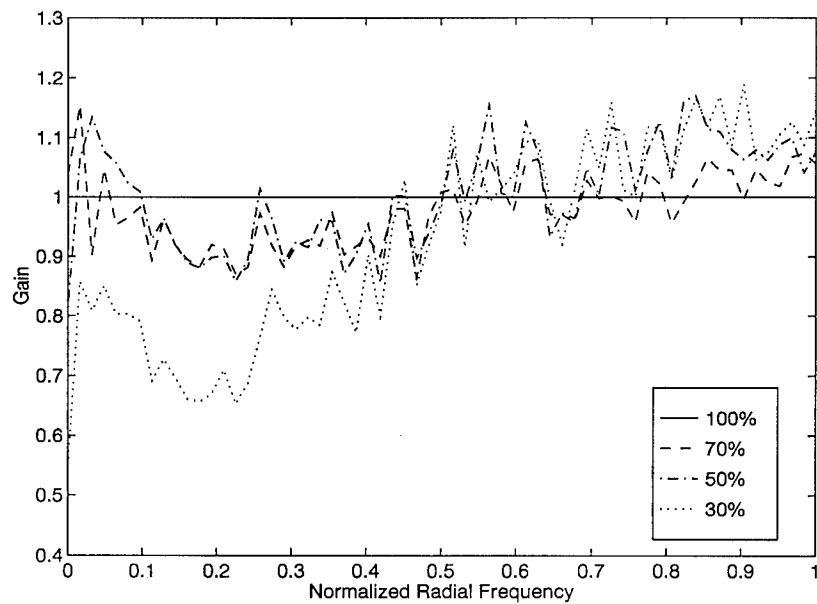
Figure C.10   Gain Curves, AMOS Tape 5, Hubble Space Telescope

Bibliography

1. Boyd, R. W. *Radiometry and Detection of Optical Radiation*. John Wiley and Sons, New York, 1983.

2. Carlson, A. B. *Communications Systems: An Introduction to Signals and Noise in Electrical Communications* (3rd Edition). McGraw-Hill Book Company, New York, 1986.

3. Corteggiani, J. P. J. Gay and Y. Rabbia. "Probability of Diffraction-Limited Images in Infrared through Turbulence-Experimental Results." *Scientific Importance of High Angular Resolution at Infrared and Optical Wavelengths*. 175–180. March 1981.

4. Devany, M. N. R. M. Redfern E. B. Ramirez R. G. Renasco P. O'Kane and F. Rosa. "Real-Time Image Sharpening." *Diffraction-Limited Imaging with Very Large Telescopes* edited by D. M. Alloin and J. M. Mariotti, 369–378, Kluwer Academic Publishers, 1989.

5. Fried, D. L. "Optical Resolution through a Randomly Inhomogeneous Medium for Very Long and Very Short Exposures," *Journal of the Optical Society of America, 56*(10):1372–1379 (October 1966).

6. Fried, D. L. "Probability of getting a lucky short-exposure image through turbulence," *Journal of the Optical Society of America, 68*(12):1651–1658 (December 1978).

7. Fried, D. L. "Post-detection wavefront distortion compensation." *Proceedings SPIE 828*. 127–133. 1987.

8. Fuensalida, J. J. F. Rosa and F. J. Fuentes. "Applications of image sharpening techniques," *Astronomy and Astrophysics, 191*:L13–L15 (1988).

9. Gonzalez, R. C. and R. E. Woods. *Digital Image Processing*. Reading, Massachusetts: Addison-Wesley Publishing Company, 1992.

10. Goodman, J. W. *Introduction to Fourier Optics*. San Francisco: McGraw-Hill Book Company, 1968.

11. Goodman, J. W. *Statistical Optics*. New York: John Wiley and Sons, 1985.

12. Hequet and Coupinout. "Gain en resolution par superposition de poses courtes recentrees et selectionees," *Journal of Optics (Paris), 16*(1):21–26 (1985).

13. Idell, P. S. and A. Webster. "Resolution limits for coherent optical imaging: signal-to-noise analysis in the spatial-frequency domain," *Journal of the Optical Society of America, 9*(1):43–56 (January 1992).

14. Knox, K. T. and B. J. Thompson. "Recovery of images from atmospherically degraded short exposure images," *Astrophysics Journal, 193*:L45–48 (1974).

15. Labeyrie, A. "Attainment of diffraction limited resolution in large telescopes by fourier analyzing speckle patterns in star images," *Astronomy and Astrophysics*, *6*:85–87 (1970).

16. Lohman, A. W. G. Weigelt and B. Wirnitzer. "Speckle masking in astronomy: triple correlation theory and applications," *Applied Optics*, *22*(4):4028–4037 (December 1983).

17. Mahajan, V. N. "Strehl ratio for primary aberrations: some analytical results for circular an annular pupils," *Journal of the Optical Society of America*, *72*(9):1258–1266 (September 1982).

18. Mannos, J. L. and D. K. Sakrison. "The effects of a visual fidelity criterion on the encoding of images," *IEEE Transactions on Information Theory, IT-20*, *4*:525–536 (July 1974).

19. Matson, C. L. "Weighted-least-squares phase reconstruction from the bispectrum," *Journal of the Optical Society of America*, *8*(12):1905–1913 (December 1991).

20. Melsa, J. L. and D. L. Cohn. *Decision and Estimation Theory*. New York: McGraw-Hill Book Company, 1978.

21. Menzel, D. H. *A Field Guide to the Stars and Planets*. Houghton-Mifflin Company, Boston, 1964.

22. Muller, R. A. and A. Buffington. "Real-time correction of atmospherically degraded telescope images through image sharpening," *Journal of the Optical Society of America*, *64*(9):1200–1210 (September 1974).

23. Nieto, J. L. A. Llebaria and S. di Serego Alighieri. "Photon-counting detectors in time-resolved imageing mode: image recentering and selection algorithms," *Astronomy and Astrophysics*, *178*:301–306 (1987).

24. Nill, N. B. "A visual model weighted cosine transform for image compression and quality assessment," *IEEE Transactions on Communications, COMM-33*, *6*:551–557 (June 1985).

25. O'Neill, E. L. *Introduction to Statistical Optics*. Reading, Mass.: Addison-Wesley Publishing Company, Inc., 1963.

26. Primot, J. G. Rousset and J. C. Fontanella. "Deconvolution from wavefront sensing: a new technique for compensating turbulence-degraded images," *Journal of the Optical Society of America*, *7*(9):1598–1608 (September 1990).

27. Roddier, F. "The Effects of Atmospheric Turbulence in Optical Astronomy." *Progress in Optics 19*, edited by E. Wolf, North-Holland, Amsterdam, 1981.

28. Roggemann, M. C. "Limited degree-of-freedom adaptive optics and image reconstruction," *Applied Optics*, *30*(29):4227–4233 (October 1991).

29. Roggemann, M. C. "Optical Performance of fully and partially compensated adaptive optics systems using least-squares and minimum variance phase reconstruction," *Computers and Electrical Engineering*, *18*:451–466 (1992).

30. Roggemann, M. C. and J. A. Meinhardt. "Image reconstruction by means of wave-front sensor measurements in closed-loop adaptive-optics systems," *Journal of the Optical Society of America*, *10*(9):1996–2007 (September 1993).

31. Roggemann, M. C. D. W. Tyler and M. F. Bilmont. "Linear Reconstruction of Compensated Images: Theory and Experimental Results," *Applied Optics*, *31*:7429–7441 (December 1992).

32. Stoudt, C. A. *Improved Quality of Reconstructed Images through Sifting of Data in Statistical Image Reconstruction*. MS Thesis, School of Engineering, Air Force Institute of Technology, Wright-Patterson AFB OH, December 1993.

33. Tatarskii, V. I. *Wave Propagation in Turbulent Medium*. McGraw-Hill Book Company, New York, 1961.

34. Welsh, B. M. and C. S. Gardner. "Performance analysis of adaptive-optics systems using laser guide stars and slope sensors," *Journal of the Optical Society of America*, *6*(12):1913–1923 (December 1989).

35. Welsh, B. M. and M. C. Roggemann. "Signal-to-noise comparison of deconvolution from wave front sensing with traditional linear and speckle image reconstruction." *Image Reconstruction and Restoration, SPIE Proceedings 2302-20*. July 1994.

Vita

Captain Stephen D. Ford was born in Grand Rapids, Michigan on September 6th, 1967. In 1985, he graduated from Lowell Senior High School in Lowell, Michigan, and then attended Michigan State University in East Lansing, Michigan from 1985 to 1989. While attending college, he enrolled in the Air Force Reserve Officer Training Corps leading to an Air Force commission in June of 1989. Second Lieutenant Ford then served as an electronics engineer at Wright Laboratory's Armament Directorate, Eglin Air Force Base, Florida. His duties included program management responsibility for the Ballistic Sight Technology Improving Night/Day Gunnery program which sought to improve the first burst accuracy of small crew-served weapons. In May of 1993, First Lieutenant Ford was reassigned to the Air Force Institute of Technology to pursue a Master of Science Degree in Electrical Engineering with a specialty in Electro-Optics. In January of 1995, Captain Ford will begin studies leading to a Doctor of Philosophy degree in Electrical Engineering also at the Air Force Institute of Technology.

Permanent address: 2839 Wabash Avenue
                       Grand Rapids, Michigan 49505

REPORT DOCUMENTATION PAGE

Public reporting burden for this collection of information is estimated to average 1 hour per response, including the time for reviewing instructions, searching existing data sources, gathering and maintaining the data needed, and completing and reviewing the collection of information. Send comments regarding this burden estimate or any other aspect of this collection of information, including suggestions for reducing this burden, to Washington Headquarters Services, Directorate for Information Operations and Reports, 1215 Jefferson Davis Highway, Suite 1204, Arlington, VA 22202-4302, and to the Office of Management and Budget, Paperwork Reduction Project (0704-0188), Washington, DC 20503.

1. AGENCY USE ONLY (Leave blank)	2. REPORT DATE December 1994	3. REPORT TYPE AND DATES COVERED Master's Thesis

4. TITLE AND SUBTITLE
Frame selection performance limits for statistical image reconstruction of adaptive optics compensated images

5. FUNDING NUMBERS

6. AUTHOR(S)
Stephen D. Ford, Capt, USAF

7. PERFORMING ORGANIZATION NAME(S) AND ADDRESS(ES)
Air Force Institute of Technology, WPAFB OH 45433-6583

8. PERFORMING ORGANIZATION REPORT NUMBER
AFIT/GEO/ENP/94D-03

9. SPONSORING/MONITORING AGENCY NAME(S) AND ADDRESS(ES)
Capt Andy Suzuki
PL/LIMA, 535 Lipoa Pkwy, Suite 200
Kihei, HI 96753

10. SPONSORING/MONITORING AGENCY REPORT NUMBER

11. SUPPLEMENTARY NOTES

12a. DISTRIBUTION/AVAILABILITY STATEMENT
Approved for Public Release; Distribution Unlimited

12b. DISTRIBUTION CODE

13. ABSTRACT (Maximum 200 words)
The U.S. Air Force uses adaptive optics systems to collect images of extended objects beyond the atmosphere. These systems use wavefront sensors and deformable mirrors to compensate for atmospheric turbulence induced aberrations. Adaptive optics greatly enhance image quality, however, wavefront aberrations are not completely eliminated. Therefore, post-detection processing techniques are employed to further improve the compensated images. Typically, many short exposure images are collected, recentered to compensate for tilt, and then averaged to overcome randomness in the images and improve signal-to-noise ratio. Experience shows that some short exposure images in a data set are better than others. Frame selection exploits this fact by using a quality metric to discard low quality frames. A composite image is then created by averaging only the best frames. Performance limits associated with the frame selection technique are investigated in this thesis. Limits imposed by photon noise result in a minimum object brightness of visual magnitude +8 for point sources and +4 for a typical satellite model. Effective average point spread functions for point source and extended objects after frame selection processing are almost identical across a wide range of conditions. This discovery allows the use of deconvolution techniques to sharpen images after using the frame selection technique. A new post-detection processing method, frame weighting, is investigated and may offer some improvement for dim objects during poor atmospheric seeing. Frame selection is demonstrated for the first time on actual imagery from an adaptive optics system. Data analysis indicates that signal-to-noise ratio improvements are degraded for exposure times longer than that allowed to "freeze" individual realizations of the turbulence effects.

14. SUBJECT TERMS
Frame Selection, Adaptive Optics, Image Processing

15. NUMBER OF PAGES
197

16. PRICE CODE

17. SECURITY CLASSIFICATION OF REPORT	18. SECURITY CLASSIFICATION OF THIS PAGE	19. SECURITY CLASSIFICATION OF ABSTRACT	20. LIMITATION OF ABSTRACT
UNCLASSIFIED	UNCLASSIFIED	UNCLASSIFIED	UL

The Report Documentation Page (RDP) is used in announcing and cataloging reports. It is important that this information be consistent with the rest of the report, particularly the cover and title page. Instructions for filling in each block of the form follow. It is important to *stay within the lines* to meet *optical scanning requirements.*

Block 1. Agency Use Only *(Leave blank).*

Block 2. Report Date. Full publication date including day, month, and year, if available (e.g. 1 Jan 88). Must cite at least the year.

Block 3. Type of Report and Dates Covered. State whether report is interim, final, etc. If applicable, enter inclusive report dates (e.g. 10 Jun 87 - 30 Jun 88).

Block 4. Title and Subtitle. A title is taken from the part of the report that provides the most meaningful and complete information. When a report is prepared in more than one volume, repeat the primary title, add volume number, and include subtitle for the specific volume. On classified documents enter the title classification in parentheses.

Block 5. Funding Numbers. To include contract and grant numbers; may include program element number(s), project number(s), task number(s), and work unit number(s). Use the following labels:

C	-	Contract	PR	-	Project
G	-	Grant	TA	-	Task
PE	-	Program Element	WU	-	Work Unit Accession No.

Block 6. Author(s). Name(s) of person(s) responsible for writing the report, performing the research, or credited with the content of the report. If editor or compiler, this should follow the name(s).

Block 7. Performing Organization Name(s) and Address(es). Self-explanatory.

Block 8. Performing Organization Report Number. Enter the unique alphanumeric report number(s) assigned by the organization performing the report.

Block 9. Sponsoring/Monitoring Agency Name(s) and Address(es). Self-explanatory.

Block 10. Sponsoring/Monitoring Agency Report Number. *(If known)*

Block 11. Supplementary Notes. Enter information not included elsewhere such as: Prepared in cooperation with...; Trans. of...; To be published in.... When a report is revised, include a statement whether the new report supersedes or supplements the older report.

Block 12a. Distribution/Availability Statement. Denotes public availability or limitations. Cite any availability to the public. Enter additional limitations or special markings in all capitals (e.g. NOFORN, REL, ITAR).

DOD - See DoDD 5230.24, "Distribution Statements on Technical Documents."
DOE - See authorities.
NASA - See Handbook NHB 2200.2.
NTIS - Leave blank.

Block 12b. Distribution Code.

DOD - Leave blank.
DOE - Enter DOE distribution categories from the Standard Distribution for Unclassified Scientific and Technical Reports.
NASA - Leave blank.
NTIS - Leave blank.

Block 13. Abstract. Include a brief *(Maximum 200 words)* factual summary of the most significant information contained in the report.

Block 14. Subject Terms. Keywords or phrases identifying major subjects in the report.

Block 15. Number of Pages. Enter the total number of pages.

Block 16. Price Code. Enter appropriate price code *(NTIS only).*

Blocks 17. - 19. Security Classifications. Self-explanatory. Enter U.S. Security Classification in accordance with U.S. Security Regulations (i.e., UNCLASSIFIED). If form contains classified information, stamp classification on the top and bottom of the page.

Block 20. Limitation of Abstract. This block must be completed to assign a limitation to the abstract. Enter either UL (unlimited) or SAR (same as report). An entry in this block is necessary if the abstract is to be limited. If blank, the abstract is assumed to be unlimited.